

Banded iron formations as critical paleomarine proxies

by

Leslie James Robbins

A thesis submitted in partial fulfillment of the requirements for the degree of

Doctor of Philosophy

Department of Earth and Atmospheric Sciences
University of Alberta

© Leslie James Robbins, 2018

Abstract

Banded iron formations (BIF) are a key chemical sedimentary record for examining the evolution of the early oceans, atmosphere, and biosphere. While the classic model suggests that BIF were deposited by either anoxygenic photoferrotrophs or oxygen producing cyanobacteria, recent studies have invoked an alternative depositional model reliant on the precipitation of a ferrous silicate precursor and the subsequent post-depositional oxidation of BIF by groundwater. Inspired by this suggestion, this work evaluates the proposed depositional model of BIF, the reliability of trace element signatures in these chemical sediments as ancient marine geochemical proxies, and aspects of ancient marine chemistry that may affect the interpretation of the paleo-seawater record. Hydrogeological and stratigraphic constraints from a simplistic box model indicate that the post-depositional oxidation of a ferrous silicate precursor phase to BIF, such as greenalite, is highly unlikely except under highly non-actualistic constraints such as grossly elevated oxygen levels in groundwater, untenable hydraulic gradients, and permeabilities inconsistent with the lithology of BIF. Therefore, an iron oxyhydroxide precursor phase is favoured and strongly suggests the influence of the biosphere in oxidizing ferrous iron, leading to BIF deposition. A statistical assessment of the trace element chemistry of BIF generated through complementary analytical techniques, namely bulk digestion high resolution inductively coupled plasma mass spectrometry (HR-ICP-MS) and laser ablation ICP-MS (LA-HR-ICP-MS), indicate that significant differences can exist in signals measured in BIF by these two methods. Bulk digestion analyses tend to produce more muted geochemical trends and may significantly mask certain geochemical signals that can be ascertained using an *in-situ* analysis of individual mineral grains by LA-HR-ICP-MS. In order to fully capture the wealth of information recorded by BIF, an approach that combines the two methodologies likely represents the best practice in the continued use of BIF as Archean to Paleoproterozoic marine archives. Finally, marine pH plays a fundamental role in controlling a number of processes that would have been operative in the ancient oceans including the authigenic precipitation of mineral phases, the surface reactivity of particle phases such as the iron oxyhydroxide precursor to BIF, and the speciation of trace elements in seawater. Thermodynamic calculations and flux estimates indicate that carbonate buffering in the early oceans should have been established within 0.1 to 10 million years, suggesting a relatively restricted range of pH conditions that would be favourable for iron oxyhydroxides to quantitatively, and reliably, capture the composition of the ancient water column.

Preface

This papers-based thesis represents the cumulative effort of several collaborative projects centered on the banded iron formations and Archean to Paleoproterozoic marine geochemistry. As the lead author of the four articles underlying the body of this work, I was intimately involved in all aspects of the research from the initial conception of the project to data collection, analysis, and interpretation, as well as authoring the corresponding manuscripts. This work was conducted under the supervision of Dr. Kurt Konhauser and Dr. Daniel Alessi at the University of Alberta and Dr. Stefan Lalonde at the European Institute for Marine Studies in Brest, France. To be explicit, my contribution to each chapter is outlined below.

Chapter 1 is an introductory chapter that draws on sections of a review paper published in *Earth-Sciences Reviews* for which I was the first author and is published as: Robbins et al. (2016) “Trace elements at the intersection of marine biological and geochemical evolution” *Earth-Science Reviews*, vol. 163, 323-348. As the lead author, I was responsible for the conception of the idea and the majority of the writing, with input from all the co-authors. Sections used in the introduction are inherently focused on banded iron formations and their trace element geochemistry.

Chapter 2 has been submitted to *Nature Geoscience* as: Robbins, L.J., Funk, S.P., Flynn, S.L., Warchola, T.J., Li, Z., Lalonde, S.V., Rostron, B., Smith, A.J.B., Beukes, N.J., Alessi, D.S., and Konhauser, K.O. Hydrogeological constraints on the post-secondary oxidation of Paleoproterozoic iron formation. I was responsible for the design of the study,

establishment of boundary conditions, and the initial formulation of the manuscript. S.P. Funk, B. Rostron, and I formulated the hydrogeological model, which was then executed by S.P. Funk. A.J.B. Smith and N.J. Beukes contributed the stratigraphic context of the Transvaal Supergroup. All authors contributed to the writing of the manuscript.

Chapter 3 has been prepared as a manuscript for submission as: Robbins, L.J., Konhauser, K.O., Warchola, T.J., Homann, M., Thoby, M., Foster, I., Mloszewska, A.M., Alessi, D.S., and Lalonde, S.V. A comparison of bulk versus laser ablation trace element analyses in banded iron formations: Insights into the mechanisms leading to compositional variability. I conducted the majority of banded iron formation analyses and the statistical assessment of the data. The study was designed by myself, S.V. Lalonde, and K.O. Konhauser. T.J. Warchola, M. Homann, and M. Thoby assisted with additional analyses, I. Foster provided analytical materials, and A. Mloszewska collected samples and provided geological context. The manuscript was written with input from all authors.

Chapter 4 has been prepared as a manuscript for submission as: Robbins, L.J., Lalonde, S.V., Flynn, S.V., Alessi, D.S., and Konhauser, K.O. New considerations on paleomarine pH conditions: carbonate buffering and thermodynamic calculations. The thermodynamic calculations and modeling was completed by myself, S.L. Flynn, and D.S. Alessi with input from K.O. Konhauser. The study was conceived by myself and S.V. Lalonde. I was responsible for preparing the manuscript with input from all authors.

“I think I have gone further this year, have lifted a little. I see things a little more as a whole, a little more complete. I am always watching for fear of getting feeble and *passé* in my work. I don't want to trickle out. I want to pour until the pail is empty, the last bit going out in a gush, not drops.”

- Emily Carr, September 23rd, 1936

Acknowledgements

One of the most enjoyable aspects of academics is the opportunity to work collaboratively in a collegial manner. Accordingly, I would like to extend my sincere thanks to all my co-authors whom I have had the good fortune to publish with and the members of my lab group at the University of Alberta. Special thanks to my supervisors, Dr. Kurt Konhauser and Dr. Daniel Alessi at the University of Alberta, and Dr. Stefan Lalonde at the European Institute of Marine Studies in Brest, France. I would also like to acknowledge the support of the other member of my supervisory committee including Dr. Murray Gingras. Finally, Dr. Bleuenn Guéguen is thanked for assistance with LA-HR-ICP-MS analyses performed at the European Institute for Marine Studies.

My doctoral research would not have been possible without the support of a Vanier Canada Graduate Scholarship, and a President's Doctoral Prize of Distinction at the University of Alberta. Additionally, my semester abroad at the European Institute of Marine Studies was supported by a Mobility Grant for Foreign Doctoral Students from the Université de Bretagne Occidentale.

Ultimately, none of this would not have been possible without the unwavering support of my family and friends.

Table of Contents

Chapter 1. Iron Formations as critical Precambrian archives: An introduction	1
1.1 Iron formations	1
1.2 Transition metals and oxidatively mobilized elements, their temporal patterns, and implications for changes in seawater chemistry	7
1.2.1 Nickel	7
1.2.2 Zinc	10
1.2.3 Cobalt	14
1.2.4 Copper	16
1.2.5 Vanadium	17
1.2.6 Chromium	18
1.2.7 Uranium	23
1.3 Summary	25
1.3.1 What this thesis entails	26
1.4 References	28
Chapter 2. Hydrogeological constraints on the post-secondary oxidation of Paleoproterozoic iron formation	52
2.1 Introduction	52
2.2 Methods	56
2.3 Results	61
2.4 Discussion	63
2.5 Conclusions	68
2.6 References	69
Chapter 3. A comparison of bulk versus laser ablation trace element analyses in banded iron formations: Insights into the mechanisms leading to compositional variability	84
3.1 Introduction	84
3.2 Banded iron formation samples and localities	87
3.2.1 Nuvvuagittuq Supracrustal Belt	87
3.2.2 Hamersley Basin	88
3.3 Methods	89
3.3.1 Sample preparation	89
3.3.2 LA-HR-ICP-MS operating conditions and data treatment	90
3.3.3 Bulk rock sample digestions and solution mode HR-ICP-MS	91
3.3.4 Statistical Analysis	92
3.4 Results	93
3.4.1 Bulk solution versus laser generated averages	93
3.4.2 Inter-deposit variability	95

3.4.3 Intra-deposit variability	98
3.4.3.1 Weeli Wolli Iron Formation	99
3.4.3.2 Joffre Member, Brockman Iron Formation	99
3.4.3.3 Dales Gorge Member, Brockman Iron Formation	100
3.4.3.4 Nuvvuagittuq Supracrustal Belt.....	101
3.4.4 Trace metal systematics.....	102
3.5 Discussion	103
3.5.1 Statistical reproducibility of bulk versus laser generated trace element concentrations	103
3.5.2 The origin of variability within the trace metal record	105
3.5.2.1 An environmental signal	107
3.5.2.2 Trace element removal pathways.....	112
3.5.2.3 Diagenesis.....	114
3.5.3 Implications for the interpretation of environmental signal in banded iron formations.....	116
3.5.4 A suggested methodology for future studies.....	118
3.6 Conclusions	119
3.7 References	121
Chapter 4. New considerations on Precambrian paleomarine pH conditions: carbonate buffering and thermodynamic calculations	163
4.1 Introduction	163
4.2 Methods.....	166
4.2.1 Ca ²⁺ concentration calculation	166
4.2.2 Calcium fluxes and timing necessary to develop carbonate buffering.....	168
4.2.3 Thermodynamic phase diagrams.....	169
4.3 Results and discussion	171
4.3.1 Carbonate thickness in the Archean and Paleoproterozoic	171
4.3.2 pH, Ca ²⁺ , and pCO ₂	172
4.3.3 Ca ²⁺ fluxes and establishment of carbonate buffering	174
4.3.4 Phase diagram pH implications and primary marine precipitates	175
4.3.5 The biosphere as a driver of carbonate precipitation	178
4.6 Conclusions	180
4.7 References	181
Chapter 5. Conclusions.....	198
5.1 The iron formation record and its interpretation.....	199
5.2 Future work	203
5.3 References	208
Bibliography	213
Appendix 1. Supplementary information for Chapter 2.....	251
A1.1 Sequence stratigraphy and iron formation mineralogy	251
A1.2 References	254

Appendix 2. Supplementary information for Chapter 3.....	258
Appendix 3. Supplementary Information for Chapter 4.....	378
A3.1 Excluded species from phase diagrams and rational.....	378
A3.2 References	378

List of Tables

Table 2.1 Parameters for hydrogeological box model.....	78
Table 3.1 Expected stoichiometric scaling ratios for trace element cross plots.....	133
Table 4.1 Constant used in carbonate system calculations.....	190
Table 4.2 Modern and Archean calcium budget and the time required to establish carbonate buffering.....	191
Table 4.3 The carbon dioxide sequestration potential of the biosphere.....	192
Table A2.1 LA-HR-ICP-MS data for sample WW1-9.....	258
Table A2.2 LA-HR-ICP-MS data for sample WW1-9b.....	264
Table A2.3 LA-HR-ICP-MS data for sample WW1-10.....	276
Table A2.4 Bulk digestion and LA-HR-ICP-MS data for sample DD98-7.....	288
Table A2.5 Bulk digestion and LA-HR-ICP-MS data for sample DD98-12.....	294
Table A2.6 Bulk digestion and LA-HR-ICP-MS data for sample DD98-21a.....	306
Table A2.7 Bulk digestion and LA-HR-ICP-MS data for sample DD98-26.....	318
Table A2.8 Bulk digestion and LA-HR-ICP-MS data for sample DD98-27.....	324
Table A2.9 Bulk digestion and LA-HR-ICP-MS data for sample 090709-4b2.....	330
Table A2.10 Bulk digestion and LA-HR-ICP-MS data for sample 090709-5.....	336
Table A2.11 Bulk digestion and LA-HR-ICP-MS data for sample 090709-2.....	348
Table A2.12 Bulk digestion and LA-HR-ICP-MS data for sample 090710-4.....	360
Table A2.13 Bulk digestion and LA-HR-ICP-MS data for sample 090710-12.....	372
Table A3.1 Activity coefficients for carbonate system calculations.....	385
Table A3.2 Concentrations and activities for phase diagram input components.....	386
Table A3.3 Paleoarchean to Neoproterozoic carbonate succession thickness and associated references.....	387

List of Figures

Figure 1.1	Geochemical models for trace element concentrations through time.....	47
Figure 1.2	Molar nickel to iron ratios in banded iron formations through time.....	48
Figure 1.3	Molar zinc to iron ratios in banded iron formations through time.....	49
Figure 1.4	Molar cobalt to titanium ratios in banded iron formations normalized to evolving continental crust.....	50
Figure 1.5	Chromium enrichments in banded iron formations normalized to evolving continental crust.....	51
Figure 2.1	Schematic diagram of the greenalite depositional model for banded iron formations.....	79
Figure 2.2	Simplified geometry of the Hamersley Basin.....	81
Figure 2.3	Oxidation times for Hamersley Basin banded iron formations returned by the hydrogeological box model.....	82
Figure 3.1	Overview map showing the location of the Nuvvuagittuq Supracrustal Belt, Québec and Hamersley Basin, Western Australia.....	134
Figure 3.2	Example of banded iron formation samples using bulk and <i>in-situ</i> laser ablation techniques.....	135
Figure 3.3	Tukey-Kramer comparison for paired analyses of bulk digestion and laser ablation of hematite grains in banded iron formation samples.....	136
Figure 3.4	Tukey-Kramer comparison for paired analyses of bulk digestion and laser ablation of magnetite grains in banded iron formation samples.....	138
Figure 3.5	Tukey-Kramer comparison for paired laser ablation analyses of hematite and magnetite grains in banded iron formation samples.....	140
Figure 3.6	Inter- and intra-deposit comparison of chromium.....	142
Figure 3.7	Inter- and intra-deposit comparison of cobalt.....	144
Figure 3.8	Inter- and intra-deposit comparison of nickel.....	146
Figure 3.9	Inter- and intra-deposit comparison of copper.....	148
Figure 3.10	Inter- and intra-deposit comparison of zinc.....	150
Figure 3.11	Inter- and intra-deposit comparison of uranium.....	152
Figure 3.12	Inter- and intra-deposit comparison of Y/Ho ratios.....	154
Figure 3.13	Inter- and intra-deposit comparison of cerium anomalies.....	156
Figure 3.14	Inter- and intra-deposit comparison of europium anomalies.....	158
Figure 3.15	PAAS-normalized Ce/Ce*-Pr/Pr* cross plot of solution and laser analyses highlighting true negative Ce/Ce* anomalies.....	160
Figure 3.16	Trace element cross plots and the scaling of trace elements against expected stoichiometries for various exit channels.....	161
Figure 4.1	Paleoarchean to Neoproterozoic carbonate succession thicknesses.....	194
Figure 4.2	pH and calcium concentrations corresponding to carbonate buffered systems over a range of $p\text{CO}_2$	195
Figure 4.3	Iron-pH phase diagrams for Precambrian marine conditions.....	196
Figure 4.4	Iron-CO ₂ phase diagrams for Precambrian marine conditions.....	197
Figure A1.1	Correlation of Transvaal Supergroup and Hamersley Basin Iron Formations, with representative lithofacies from the Kuruman Iron Formation, South Africa.....	256
Figure A1.2	Schematic hydrogeological model for realistic basin parameters.....	257

Chapter 1. Iron Formations as critical Precambrian archives: An introduction¹

1.1 Iron formations

Iron formations (IF) are iron-rich (15-40 wt%) and siliceous (40-60 wt%) sedimentary deposits that precipitated from seawater throughout much of the Archean and Paleoproterozoic (3.75–1.85 Ga) (James, 1954; Trendall, 2002; Klein, 2005). Deposition of IF appears tied to periods of enhanced magmatic and hydrothermal activity (associated with large igneous province emplacement; Isley and Abbot, 1999) that delivered large amounts of ferrous iron to anoxic deep oceans (Bekker et al., 2010; 2014). Low concentrations of Al₂O₃ (<1 wt%) and incompatible elements (Ti, Zr, Th, Hf and Sc <20 ppm) are commonly observed in IF, indicating minimal detrital input during deposition, although this is not universal for all iron formations.

Iron formations may be divided into two petrographic affinities: banded iron formation (BIF) and granular iron formation (GIF). BIF are characterized by distinctive layering of variable thickness, from macrobands (meters in thickness), to the more characteristic mesobands (centimeter-thick units) from which they draw their name, to millimeter and submillimeter microbands (e.g., Trendall and Blockley, 1970; Morris, 1993; Krapež et al., 2003). GIF typically lack banding and consist of granules of chert or other

¹This introduction represents a portion of a review paper, Robbins et al. (2016), published in *Earth-Science Reviews*, and focused on the trace element records recorded by the Precambrian banded iron formation and shale records.

silicates and iron oxides with early diagenetic chert cement filling pore spaces (e.g., Simonson, 1985). BIF dominate the Archean and are more important in terms of total IF tonnage (Bekker et al., 2010). GIF first appear in the rock record at ca. 2.4 Ga (Simonson and Goode, 1989) and are the most common type of iron formation in the Paleoproterozoic, reaching their peak abundance ca. 1.88 Ga. After a 1.88 Ga pulse of IF deposition, which appears to have been globally synchronous (Rasmussen et al., 2012), they effectively disappear in the middle Proterozoic, returning in the Neoproterozoic in association with widespread “Snowball Earth” glaciation (Hoffman et al., 1998). While the Phanerozoic is devoid of the IF resembling those of the Precambrian, the iron oxide-rich sedimentary record continues into the Phanerozoic in the form of ironstones (see Mücke and Farshad, 2005 for review) and exhalative deposits (see Lyons et al., 2006 for review).

Iron formation deposition spans several major redox changes in Earth’s surface composition—from an early anoxic atmosphere to an atmosphere that became at least partially oxygenated (e.g., Klein, 2005; Bekker et al., 2010). Therefore, it is likely that IF formed via different mechanisms throughout the Precambrian. A number of recent reviews detail IF occurrence, mineralogy, mechanisms of formation, depositional environments, and diagenetic history (see Klein, 2005; Bekker et al., 2010, 2014; Posth et al., 2014). For the purpose of this review, the importance of IF is its ability to record marine signatures, and specifically archive trace element concentrations in the Precambrian.

Evidence supporting the idea that IFs record authigenic marine signatures includes marine-like rare earth element and yttrium (REE+Y) patterns and small-scale chemical variations that argue for the preservation of environmental signals (e.g., Bau and Möller, 1993; Bau and Dulski, 1996; Bolhar et al., 2004; Alexander et al., 2008; Pecoits et al.,

2009; Planavsky et al., 2010; Haugaard et al., 2013, 2016). A concern potentially compromising the IF record is the possibility of post-depositional mobilization of trace elements, which can overprint or even eradicate authigenic marine signatures. However, limited post-depositional mobilization or addition of trace elements in IF is indicated by small-scale REE and Fe isotope variations, both within and between Fe-rich mesobands despite experiencing diagenetic and metamorphic conditions up to amphibolite facies (e.g., Bau, 1993; Frost et al., 2007; Whitehouse and Fedo, 2007; Steinhöfel et al., 2010). Trace element compilation efforts for IF have often limited their scope to samples falling at greenschist facies or below in an effort to provide the most robust estimates possible of trace element abundances.

Recently, the use of IF as paleomarine proxies for trace element abundances has been questioned because laboratory studies of Fe(II)-redox driven recrystallization suggest that this process may overprint authigenic trace element records (Friedrich et al., 2011; Friedrich and Catalano, 2012). These studies focused largely on the initial sorption of trace metals and subsequent remobilization that occurs upon further interaction with Fe(II)-rich fluids. They also specifically highlighted the potential for the mobilization of Ni (Friedrich et al., 2011) and Zn (Friedrich and Catalano, 2012). Generally, losses were less than 10% when ferrihydrite doped with Ni or Zn was placed in a Fe(II) solution that contained no Ni or Zn. However, further experimental work (Friedrich et al., 2012) has shown that when impurities of Al, Cr, or Sn are present in the ferrihydrite, Ni and Zn remobilization is attenuated. Such a scenario is likely more comparable to natural iron oxyhydroxides formed in the Precambrian oceans that were the precursors to the minerals presently found in IFs, as they would have incorporated various trace metals and other minor impurities

from the water column. Ultimately, the studies of Frierdich et al. (2011) and Frierdich and Catalano (2012) are based on systems inherently at disequilibrium and that are unlikely to be truly representative of the formation of IF particles in equilibrium with contemporaneous ferruginous seawater. Further, none of these studies have assessed the potential for the mobility of trace elements during later diagenetic mineral phase transitions. In this regard, recent experimental work using diagenetic capsule experiments (Robbins et al., 2015) demonstrated limited mobility for Ni and Zn during simulated diagenetic treatments at high temperature and pressure that capture the transformation from ferrihydrite to hematite. Overall, when all lines of evidence are considered, it is reasonable to conclude that IF do indeed preserve authigenic signatures and thus record the abundances of biologically critical trace elements in ancient oceans with high fidelity.

Recent attempts to connect the record of trace metals in IF to coeval trace element abundances in seawater may be hampered by the empirical sorption models (e.g., linear partitioning, or K_D , models) typically employed to determine metal partitioning between seawater, microbes, mineral colloids, and organic ligands in the water column. These partitioning models are only applicable at the experimental conditions tested and say nothing about the chemical mechanisms of trace metal uptake (Sposito, 1982; Goldberg and Criscenti, 2007). Erel and Stolper (1993), improving on earlier K_D studies such as those of Byrne and Kim (1990) and Koeppenkastrop and De Carlo (1992), proposed a semi-empirical model that linked the binding of marine REE to microbes and particulate matter to their first hydroxide thermodynamic binding constants (e.g., constants for hydrous ferric oxides found in Dzombak and Morel, 1990). Aqueous REE concentrations were successfully modeled by employing REE-carbonate complexation mass action constants.

While admitting that their model could not account for factors including pH and binding site concentrations, Erel and Stolper (1993) found that the model was able to predict REE concentrations in modern seawater and approximate REE patterns observed in Archean BIF.

More recently the surface complexation modeling (SCM) approach, grounded in equilibrium thermodynamics through mass action expressions, has been extended beyond minerals to successfully model trace metal adsorption onto microbial surfaces (Fein et al., 1997, 2005), including marine cyanobacteria (Liu et al., 2015) and anoxygenic photosynthesizers (Martinez et al., 2016). Although data-intensive, the SCM approach allows us to predict the impacts of the aqueous speciation of metals, redox transitions, pH, the precipitation and dissolution of solid phases, competition of multiple metals for specific types of surface binding sites, varying metal-to-sorbent ratios, and ionic strength on the final distribution of trace metals in a system (Davis et al., 1998; Koretsky, 2000)—without conducting additional experiments. For example, SCM studies allow for systematic investigation of the impacts of paleoseawater salinity (Sanford et al., 2013), pH (Pearson and Palmer, 1999; Ohnemueller et al., 2014) and competition on the uptake of trace metals to particles in the photic zone, for instance, Fe-Mn-oxyhydroxides and planktonic microbes. Binding constants from disparate studies in the literature could be combined, unlike in empirical approaches such as the K_D model. Ultimately, the further application of SCM promises to better connect paleoseawater geochemistry and microbiology to trace metals trends observed in the rock record.

A final limitation on the use of the IF record is the lack of direct modern analogues. However, several studies have used Phanerozoic ironstones and hydrothermal exhalites to

extend the record from the Precambrian to the modern (e.g., Konhauser et al., 2009; 2011; 2015; Partin et al., 2013a; Robbins et al., 2013; Swanner et al., 2014). Such hydrothermal deposits provide an opportunity to test experimental and hypothesized partitioning scenarios for trace elements onto IF—but only to a limited extent. As these partitioning scenarios are sensitive to matrix effects, such as different Si concentrations (e.g., Konhauser et al. (2007, 2009) and the presence of additional cations (Jones et al., 2015), they cannot be directly equated. Although the K_D value for P adsorbing to Fe in modern hydrothermal particles (Bjerrum and Canfield, 2002) is very close to the experimentally-derived value for Si-free seawater developed by Konhauser et al. (2007), further refinement of these partitioning scenarios is needed, and SCM may be a useful tool for future work. Additionally, the broad scaling between trace metals and Fe in IF suggest that first order partitioning trends are largely preserved (e.g., Robbins et al., 2013; Konhauser et al., 2015). The observed scaling between Zn and Fe in modern hydrothermal deposits falls just above that for IF Zn/Fe ratios (Robbins et al., 2013). Collectively, these considerations suggest that the use of modern hydrothermal exhalites to extend the IF record is justified.

As IF are likely to retain authigenic, seawater-derived geochemical patterns they are critical archives for Precambrian to Paleoproterozoic ocean chemistry and offer a key window into constraining geochemical changes and biological evolution on the early Earth. Due to their importance as a window into past marine conditions, there are several critical questions regarding the formation and chemistry of these enigmatic deposits, such as (i) what exactly is the primary authigenic phase dictating the precipitation of large superior type iron formations?, (ii) what information can be gleaned from differences in bulk versus *in-situ* mineral phase specific analyses?, and finally, (iii) how does ancient seawater pH

affect our interpretation of the IF record? These questions are critical to our understanding of IFs as archives of ocean and atmospheric chemistry.

1.2 Transition metals and oxidatively mobilized elements, their temporal patterns, and implications for changes in seawater chemistry

As discussed above, IF provide critical constraints on the Fe and Si chemistry of the oceans, as well as the redox state of Archean to Paleoproterozoic seawater. Equally as critical are the records of bioessential and oxidatively mobilized trace elements in IF and how they inform our understanding of biological innovation and changes in Earth's surface environments.

1.2.1 Nickel

Nickel is critical for many prokaryotic metalloenzymes. It is utilized in carbon reduction by both acetogenic and methanogenic bacteria, as well as the cofactors methyl-coenzyme M reductase and acetyl-CoA synthase, both of which are critical for methane production (Hausinger, 1987; Zerkle et al., 2005, and references therein). Furthermore, Ni is used in hydrogenases, carbon monoxide dehydrogenase, and it catalyzes the reduction of CO₂ to CO and the resultant production of acetyl-CoA (e.g., Ragsdale and Kumar, 1996). In non-methanogens, Ni may be used in urease and in a recently evolved superoxide dismutase found in many marine organisms (Frausto da Silva and Williams, 2001; Dupont et al., 2008).

Initial estimates of Ni concentrations in the early ocean were derived from geochemical modeling (Saito et al., 2003) and microbial genomics (Zerkle et al., 2005).

These studies suggested that seawater Ni concentrations were fairly uniform from the Archean through to the modern (Fig. 1.1). The presumed consistency largely stems from Ni behaving conservatively in waters under various redox conditions (Saito et al., 2003). However, a compilation of Ni contents in IF through time (Konhauser et al., 2009) revealed a unidirectional and rapid decrease in Ni just prior to the GOE (Fig. 1.2). This trend remained clear after a near-doubling of the available IF data (Konhauser et al., 2015), suggesting that the observed decline in Ni in IF is robust. Using experimentally derived Ni partitioning coefficients to Si-rich ferrihydrite (in light of assumed elevated Precambrian silica concentrations), it was estimated that paleomarine Ni concentrations dropped by more than half between 2.7 and 2.5 Ga (Fig. 1.2), from close to 400 nM to less than 200 nM. This decline would have strongly impacted methanogenic bacteria, since they are highly dependent on dissolved Ni availability over this range. This decline was attributed to mantle cooling and, with that, the decreasing frequency of Ni-rich ultramafic eruptions. This subsequently limited the amount of Ni-source rocks susceptible to weathering, and perhaps even impacted atmospheric oxygenation by its effect on biological carbon cycling (Konhauser et al., 2009; 2015; see Kasting, 2013 for an alternative view).

Eickhoff et al. (2014) re-examined the partitioning of nickel to both biogenic and abiogenic ferrihydrite in the presence of silica. Although estimates from Eickhoff et al. (2014) are not directly comparable to that of Konhauser et al. (2009) due to differences in their respective experimental approaches, they nonetheless found that when biomass was present, the sorption of Ni onto ferrihydrite decreased, and therefore estimates for the paleomarine Ni concentrations based on IF may be too low. This has led to the suggestion that the collapse of the paleomarine Ni reservoir and the resultant methanogenic famine at

2.7 Ga as described by Konhauser et al. (2009) may have actually occurred closer to the initiation of the GOE shortly before 2.45 Ga. Regardless, changes in the paleomarine Ni reservoir would likely have had profound impacts on the Precambrian biosphere.

Interestingly, the first-order trends in Ni abundances observed in the IF record (Fig. 1.2) are also recorded in sedimentary pyrite. Large et al. (2014) presented a suite of Ni analyses in sedimentary to early diagenetic pyrite that mirrored the observed temporal trend in Ni/Fe ratios observed in IF. Such agreement between two distinct proxy records is encouraging and supports the interpretation that they reflect first-order trends in paleomarine bioavailability. Large et al. (2014) further noted a correlation between Ni and Co in the pyrite record and suggested that this may be tied to the emplacement and subsequent erosion of large igneous provinces. An observation that supports this assertion is the high Ni and Co values observed in pyrites in the Late Permian (Large et al., 2014), in which case the Ni and Co may be associated with the Siberian traps volcanism and Permian mass extinction (Rothman et al., 2014).

Studies of the Permian mass extinction have also invoked links between the temporal evolution of the paleomarine Ni reservoir and its effects on the methanogenic community in efforts to constrain the cause of this event. An expansion of the marine nickel reservoir, coincident with massive eruptions of the Siberian flood basalts around 252.8 Ma, is suggested to have contributed to the severity of the mass extinction (Rothman et al., 2014). Siberian volcanism would have provided a large transient flux of Ni to the oceans and stimulated methane fluxes to the oceans and atmosphere. Those authors found three different lines of proxy evidence for this expansion: (1) an increase in the size of the marine inorganic carbon reservoir and an isotopic signal suggestive of methanogenic activity, (2)

molecular clock analyses indicating the emergence of an efficient acetoclastic methanogenic pathway in *Methanosarcina*, and (3) significantly elevated Ni concentrations in sediments from South China. All three of these signals correlate with the Permian mass extinction and highlight how relatively short-scale perturbations in the bioavailability of trace elements may have potentially affected the biosphere.

Studies in the ferruginous ocean analogue Lake Matano, Indonesia, have shown that green rust may play an important role in scavenging Ni from ferruginous water columns (Zegeye et al. 2012). Further, production of trace hydrogen sulfide through microbial sulfate reduction may play a strong role in governing aqueous Ni concentrations, even under ferruginous conditions (Crowe et al. 2008, Zegeye et al. 2012). In Lake Matano, Ni and Co exhibit divergent behavior implying that different biogeochemical processes govern concentrations of each metal (Crowe et al. 2008).

1.2.2 Zinc

Zinc is amongst the most biologically important trace metals, particularly for eukaryotes, and is a component in a wide variety of metallo-peptides and polymerases (see Lipscomb and Sträter, 1996 for a review on Zn enzymology). Many Zn metalloenzymes are used in processes involving DNA or RNA synthesis (e.g., Lipscomb and Sträter, 1996; Berg and Shi, 1996). In eukaryotes, Zn is also used in Zn-fingers, small protein structural motifs which act as signaling agents in processes centralized in the nucleus and are thought to have emerged relatively late (e.g., Berg and Shi, 1996; Dupont et al., 2006, 2010).

Prior to compilations of Zn data from the sedimentary proxy record, the only estimates for Zn concentrations and bioavailability came from geochemical modeling (e.g.,

Saito et al., 2003) (Fig. 1.1). This modeling work was consistent with the emergence of eukaryotic metalloenzymes and rapid diversification of eukaryotes in the Neoproterozoic following a transition from a widely anoxic ocean with expanded euxinia to a well-oxygenated ocean (Dupont et al., 2010). This view provides a possible explanation for the delay in eukaryotic diversification.

Recently, however, two studies have reevaluated paleomarine concentrations through time, and thereby Zn bioavailability, using the sedimentary rock record. Scott et al. (2013) focused on black shales, building from the observation that Zn/Al ratios in sediments from modern euxinic basins are positively correlated with dissolved Zn concentrations in bottom waters. Scott et al. (2013) found there was no evidence in the Precambrian black shale record to infer a depleted paleomarine Zn reservoir—because the average Zn concentration in Precambrian and Phanerozoic euxinic shales are not significantly different. Accordingly, they suggested that seawater Zn levels remained broadly uniform throughout time at near modern levels and several orders of magnitude above concentrations that would be biolimiting. This finding was bolstered by Robbins et al. (2013) who examined Zn concentrations and Zn/Fe ratios in IF (Fig. 1.3) and found generally constant Zn enrichments through time. When viewed alongside updated geochemical models for Zn speciation and considering hypothesized partitioning scenarios for Zn and Fe co-precipitation, Robbins et al. (2013) estimated a paleomarine Zn reservoir on the order of 10 nM. This value is several orders of magnitude above the $\sim 10^{-13}$ M concentration considered as biolimiting (Brand et al., 1983) and in excellent agreement with the black shale record (Scott et al., 2013). However, Zn displays nutrient-type behavior in modern seawater, and it is possible that Zn drawdown also occurred in ancient

surface waters; sedimentary proxy records are generally considered to reflect the overall size of the paleomarine reservoir without addressing the finer details of its vertical structure.

The updated view of a relatively static paleomarine Zn reservoir (Fig. 1.3) contradicts the findings of earlier geochemical models that linked (1) the low Zn requirements of cyanobacteria to the predicted low levels of total Zn in the Precambrian oceans, and also (2) the proliferation of eukaryotes to an increase in total Zn during the Phanerozoic (e.g., Saito et al., 2003; Dupont et al., 2010). This disparity can be linked to an overestimation of the effects of Zn aqueous complexation by sulfides during the Precambrian by early geochemical models (e.g. Saito et al., 2003). Additionally, this model directly contradicts the behavior of Zn in some modern anoxic aqueous systems. For instance, in some conditions where a strong redoxcline exists, such as in Jellyfish Lake, Palau, total dissolved Zn concentrations increase with depth due to the formation of aqueous sulfide complexes (Landing et al., 1991; Dierssen et al., 2001). Alternatively, Robbins et al. (2013) proposed that an increased proportion of hydrothermal fluxes relative to riverine fluxes and the transport of hydrothermal Fe- and Zn-rich fluids to more distal environments in anoxic Archean and Paleoproterozoic oceans could have helped maintain a large marine Zn reservoir.

This view of severe Zn limitation (e.g., Saito et al., 2003) was also based the assumption that its availability for biological use was limited to free dissolved Zn^{2+} . In the modern oceans, the majority of Zn in surface waters is complexed with organic ligands (90-98%). This organic ligand pool has traditionally been viewed as being a non-bioavailable component of the total Zn pool (Bruland, 1989). This framework was based

on culture work that has either not applied synthetic ligands to culture or introduced EDTA (a strongly binding organic ligand), neither of which are an accurate representative of natural waters. In contrast, it was noted more recently by Lohan et al. (2005) that marine phytoplankton appear to be much more tolerant of low dissolved Zn concentrations than in culture studies. The authors then went on to propose that Zn binding organic ligands may be produced by phytoplankton in order to facilitate biological uptake, and to regulate ambient Zn concentrations. Consistent with this idea is recent culture work after Xu et al. (2012) and Aristilde et al. (2012), where it was demonstrated that weakly binding organic ligands can in fact increase Zn uptake rates in phytoplankton. This work highlights a gap in our understanding of Zn forms available for biological use and complicates predictions on its past bioavailability. As such, debate of Zn bioavailability calls for new methods and data so as to directly test this in future work.

There is also potential for further inferences to be drawn from the stable isotope record of Zn in chemical sediments, such carbonates. A study on a Neoproterozoic (Marinoan) cap carbonate sequence shows variations in $\delta^{66}\text{Zn}$ that are suggested to record an increase in surface runoff and continental weathering coincident with the onset of deglaciation and a subsequent increase in primary productivity caused by development of nutrient-rich surface waters (Kunzmann et al., 2013). A single study on Zn isotopes in IF (Pons et al., 2013) found some of the most enriched $\delta^{66}\text{Zn}$ values between 2.7 Ga and 1.8 Ga. Variations were considered to be rapid and governed by two factors: preferential incorporation of isotopically heavy Zn into carbonates and a significant increase in the amount of marine sediments exposed to weathering around 2.7 Ga coincident as the result of increased continental land mass. These studies highlight the potential of the Zn stable

isotope record for understanding links between trace metal in past environments availability and biological productivity, as well as examining source-sink relationships.

1.2.3 Cobalt

The most recognized biochemical role of cobalt (Co) is its participation as a cofactor in cobalamin (vitamin B₁₂), which is essential for a number of metalloenzymes, including methionine synthase and ribonucleotide reductase (e.g., Marsh, 1999; Frausto da Silva and Williams, 2001). In previous modeling work, researchers have pointed to the antiquity of the cobalamin cofactor, suggesting that its origin somewhere between 3.5 and 2.7 Ga is consistent with the evolution of cyanobacteria in a Co-rich ocean (Saito et al., 2003). Additional biochemical functions of Co exist (Kobayashi and Shimizu 1999), including in cambialistic carbonic anhydrases enzymes (Morel et al., 1994; Roberts et al., 1997), and perhaps more will be discovered with emerging metalloproteomic techniques (e.g., Waldron et al., 2007; Aguirre et al. 2013). Modeling efforts have indicated that seawater Co concentrations could have been relatively high in the Archean, decreased in the Proterozoic, and then further decreased following Neoproterozoic ocean oxygenation (Saito et al., 2003). Despite the predicted decreases in the seawater concentration of Co over time, the biological utilization of Co is suggested to have increased over time, and remains relatively high (David and Alm, 2011; Swanner et al., 2014). This may be related to the occurrence of Co-binding ligands in Co-limited waters, which exerts strong control over the speciation of Co in the modern ocean (Saito and Moffett, 2001; Saito et al., 2005). Indeed, a high degree of Co complexation may favor cyanobacteria over eukaryotic

phytoplankton in modern settings containing picomolar levels of dissolved Co, for example in the Costa Rica upwelling dome (Saito et al. 2005; Ahlgren et al., 2014).

An examination of Co concentrations in IF and pyrite through time suggests an expansion of the paleomarine Co reservoir between 2.8 and 1.8 Ga (Swanner et al., 2014). This conclusion is indicated by a large increase in Co/Ti ratios in IF (Fig. 1.4), euxinic shales, and pyrite relative to the evolving continental crust, with a peak in Co/Ti values observed at ~2.4 Ga. The expansion of the Co reservoir between 2.8 and 1.8 Ga (Fig. 1.4) may be coincident with increased mantle plume activity and associated hydrothermal inputs (Swanner et al., 2014). This expansion is also broadly consistent with an increase in genes that bind Co around this time (David and Alm, 2011). Such conditions simultaneously allow for the establishment of the ferruginous conditions necessary for IF precipitation and an increase in the amount of Co introduced to the ocean. Pervasive anoxic conditions would help keep Co in solution, and as such the residence time of Co would be higher in more anoxic oceans compared to modern, well-oxygenated oceans (c.f., Swanner et al., 2014; also Saito and Moffett, 2002). This is consistent with the relatively high Co concentrations in the anoxic ferruginous waters of Lake Matano compared to its oxic surface waters (Crowe et al. 2008). However, the syngenetic and early diagenetic pyrite record for Co presented by Large et al. (2014) indicates a steadier decline in Co levels from 3 Ga to present. Resolving the discrepancy between the IF and pyrite records would be of great interest and is an area where a more complete black shale record may prove useful in resolving the temporal trends in marine Co from the Archean through to the modern. If the pyrite record for Co proves correct in predicting the overall trajectory, it will be quite

telling, as this would then mirror the general trajectories for Fe and Mn as well, and may offer support for trace element variations as correlative to large igneous province events.

1.2.4 Copper

Copper is used in ‘blue’ copper proteins for electron transfer, energy capture, and in other oxidative enzymes (e.g., Solomon et al., 1996). The emergence of Cu-metalloproteins is thought to have been quite late (Dupont et al., 2010). Similar to Zn, thermodynamic modeling indicates that the seawater Cu reservoir should have reached a low in Proterozoic oceans as the result of expanded water column euxinia (e.g., Frausto da Silva and Williams, 2001; Saito et al., 2003). However, recent examination of authigenic Cu enrichments in BIF and black shales, normalized to detrital input using Ti, are remarkably static throughout the Precambrian (Chi Fru et al., 2016). Despite the static abundance record, there is significant variation in black shale Cu isotope compositions over time that appears to be due to variations in Cu sinks and sources (Chi Fru et al., 2016). The preferential sequestration of ^{65}Cu by iron oxides (e.g., Balistrieri et al., 2008) likely enriched seawater in residual ^{63}Cu , which would have been incorporated into planktonic biomass and ultimately deposited into black shales depleted in ^{65}Cu . After the GOE, oxidative continental weathering of sulfides should have increased the supply of dissolved Cu(II) and delivered more ^{65}Cu -rich runoff to the oceans, while at the same time the isotopically light sink associated with iron oxides waned. This evolution towards heavy $\delta^{65}\text{Cu}$ values coincides with a shift to negative sedimentary $\delta^{56}\text{Fe}$ values and increased marine sulfate after the GOE and is traceable through Phanerozoic black shales to modern marine settings, where marine dissolved and sedimentary $\delta^{65}\text{Cu}$ values are universally positive.

Zerkle et al. (2005) suggested that since the onset of widespread ocean oxygenation in the Neoproterozoic, the biological utilization of Cu enzymes doubled, likely as a result of increased Cu availability. In the modern ocean, Cu-metalloproteins are involved in the first step of nitrification, last step of denitrification, and during ammonia oxidation; the net result is a substantial bacterial Cu requirement (Amin et al., 2013). Low seawater Cu concentrations and bioavailability may also have had significant implications for the Precambrian atmosphere. In this regard, Buick (2007) proposed that in a Cu-limited ocean, denitrification would be incomplete since Cu is an essential component of the enzymes involved in that metabolism. The effect could have been a build-up of N₂O with significant climatic implications because N₂O is a potent greenhouse gas. The results of Chi Fru et al. (2016) would seem to indicate that such a scenario was unlikely, considering the relatively static sedimentary Cu abundance record they present. Additional work is required to understand how Cu abundances and stable isotopes respond to changes in ocean and atmosphere redox – and how the biological history of copper utilization fits into the evolving redox landscape.

1.2.5 Vanadium

Vanadium is also an important bioessential trace element for the early nitrogen cycle. Both Anbar and Knoll (2002) and Zhang et al. (2014) suggested that the V-Fe nitrogenase varieties might have contributed to nitrogen fixation during the Paleoproterozoic, although the V variety is less efficient (Eady, 1996). Correspondingly, Zhang et al. (2014) indicated that low $\delta^{15}\text{N}$ values in Archean cherts may be more consistent with alternative nitrogenases using Fe or V instead of Mo, suggesting a more important role for these

variants in deep time —an interpretation challenged by the recent work of Stüeken et al. (2015). A preliminary trend for V in euxinic black shales through time was presented in Sahoo et al. (2012) (see their figure 3b). It was argued that seawater V concentrations were low in the mid-Proterozoic, and that V enrichments in the Doushantuo Formation (~635-630 Ma) were consistent with a well-oxygenated ocean. Overall, it appears that the black shale record for V mirrors that of Mo, and is relatively consistent with Neoproterozoic enrichments seen in the pyrite record (Large et al., 2014). However, the IF archives have not yet been investigated, and an extensive temporal examination of V in the context of its biological importance is lacking. Further, and perhaps most importantly, the cellular stoichiometry and specific requirements for V remain unclear.

Collectively, the temporal trends of Mo, V, and potentially Cu, suggest a scenario where N-fixing cyanobacteria in the early oceans may have been affected by biolimiting levels of multiple trace metals, especially prior to the GOE. As such, an understanding of Cu and V will be essential in order to obtain a complete picture of the N cycle prior to Neoproterozoic ocean oxygenation. The evolving picture for widespread nitrogen fixation on the early Earth is becoming more sophisticated and complex, and ultimately may have been influenced by the intricate interplay of several key trace metals in the early oceans.

1.2.6 Chromium

Although chromium (Cr) has been identified as a biological component in some higher-level organisms, it is generally regarded as a toxin (Frausto da Silva and Williams, 2001). As such, temporal trends in seawater are unlikely to mirror direct evolutionary controls. Rather, investigations in the sedimentary record have focused on Cr abundances and

isotope compositions for tracking oxygenation as well as the impact of anaerobes in the surface environment. This utility is due to reduced Cr in the form of Cr(III) being effectively immobile at neutral to alkaline pH; Cr becomes mobile when it is oxidized to Cr(VI). Furthermore, Cr is subject to strong stable isotope fractionation during redox reactions, especially reduction (Ellis et al., 2002). As such, variations in Cr abundances and isotopic compositions are likely to represent changes in the redox state of the oceans or atmosphere, as well as associated changes in the mechanisms of Cr mobility and changes in sediment provenance.

Reinhard et al. (2013) investigated Cr and Mo enrichments in anoxic and euxinic shales, coupling these two elemental systems in order to constrain the extent of anoxia versus euxinia in the early oceans. For Cr, there are no significant authigenic enrichments in middle Proterozoic black shales and this was taken to indicate pervasive anoxia. Conversely, Mo is enriched in middle Proterozoic black shales to an intermediate degree relative to Archean and Phanerozoic samples, which indicates the presence of euxinic conditions that were relatively limited on the seafloor—although still far greater than the extents observed today. This distinction is the result of differences in the geochemistry of Cr and Mo. Efficient burial of Cr can occur in sediments deposited under anoxic and ferruginous waters. By contrast, Mo burial, as discussed above, is most efficient in sediments deposited from euxinic waters. Together, these two elements can constrain the relative extent of ferruginous and euxinic conditions. In this regard, Reinhard et al. (2013) estimated at least 30-40% of the middle Proterozoic seafloor was anoxic, and possibly much more, with only 1-10% of the seafloor being euxinic. Large et al. (2014) also investigated Cr and Mo concentrations in sedimentary pyrite and found patterns consistent

with the dominance of anoxic settings in the Proterozoic from 2.15 to 0.7 Ga, with euxinic settings more prevalent between 1.2 and 0.8 Ga. Large et al. (2014) attributed a decrease in Cr concentrations, from the Archean to the Proterozoic, as reflective of a change in source availability. They argued that Cr should be sourced from ultramafic rocks similar to Ni and Co, and that this decrease may reflect a decrease in the abundance of the source (see their Fig. 8c).

Chromium isotope enrichments have also been used to track the oxygenation of the atmosphere and oceans. For instance, small variations in Cr isotope composition in 2.8-2.6 Ga IF were first suggested to document brief pulses in atmospheric oxygen, which mobilized Cr via oxidative weathering and led to Cr sequestration in IF prior to the GOE (Frei et al., 2009). Those authors argued that increases in $\delta^{53}\text{Cr}$ of +0.04 to +0.29‰ in IFs at 2.7, and again at 1.8 Ga, are the direct result of Cr(III) being oxidized to Cr(VI) and that oxidation of Cr must have been catalyzed by oxidized Mn^{2+} in the form of MnO_2 . Subsequently, Konhauser et al. (2011) examined temporal trends in the degree of Cr enrichment in IF and found a peak at 2.48-2.32 Ga (Fig. 1.5). This peak was suggested to indicate the onset of acidic weathering triggered by microaerophilic iron-oxidizing bacteria which accelerated the weathering of pyrite as soon as some atmospheric oxygen became available. Muted $\delta^{53}\text{Cr}$ variations (-0.3 to +0.3‰) at this time were taken as being indicative of Cr cycling in reduced form (Konhauser et al., 2011), in contrast with highly variable values coincident with ocean oxygenation in the Neoproterozoic (up to +4.9‰; Frei et al., 2009).

Chromium isotope data were also acquired from rocks from the Pongola Supergroup, South Africa, in an effort to seek evidence for earlier signs of photosynthetic

oxygen production. Crowe et al. (2013) found that the $\delta^{53}\text{Cr}$ isotope compositions of 2.96 Ga paleosols were fractionated relative to the crustal values, indicating oxidative mobilization of Cr and the presence of low levels of atmospheric oxygen ($\sim 10^{-4}$ PAL; the level required to prevent reduction of Cr[VI] by Fe[II] during transport to the ocean). This conclusion would suggest the presence and activity of oxygenic photosynthesis about ~ 600 million years prior to S-MIF disappearance during the GOE. The idea of early O_2 production is supported by the Mo isotope composition of IF also obtained from within the Pongola Supergroup, where scaling between Mo isotope composition and Mn/Fe ratio indicate the presence of a Mn(IV) oxide exit channel for Mo at that time (Planavsky et al., 2014a). However, it is also plausible that the Cr isotope fractionation observed by Crowe et al. (2013) in the 2.96 Ga paleosols is due to the localized production of oxygen by cyanobacteria within a microbial mat (see Lalonde and Konhauser, 2015). In either case, the sedimentary Cr record, in terms of abundance and especially in isotopic composition, appears to provide important clues regarding oxygen production due to photosynthesis either in the early oceans, or on land, and corresponding oxidative weathering on the early continents. Investigations into the isotopic record of Cr in black shales and IF may continue to be a useful tracer for paleoredox conditions in the Precambrian oceans.

Recently, Planavsky et al. (2014b) presented $\delta^{53}\text{Cr}$ data from Precambrian and Phanerozoic ironstones, as well as Neoproterozoic to Phanerozoic black shales and mudstones. Collectively, this record shows that $\delta^{53}\text{Cr}$ values in Precambrian black shales are similar in composition to crustal Cr until the Neoproterozoic. Beginning approximately 0.8 Ga, relatively large positive $\delta^{53}\text{Cr}$ values are observed in black shales and mudstones, as well as in some Phanerozoic ironstones. Those authors interpreted these trends in $\delta^{53}\text{Cr}$

to suggest that atmospheric oxygen levels were <0.1% PAL (below this level, Cr[III] oxidation is limited by the lack of Mn oxides) prior to the Neoproterozoic. This concentration would have been limiting for metazoans, potentially explaining the delay in their diversification (although see Zhang et al. (2016) for an alternative opinion, as well as a comment on the opposing view by Planavsky et al. (2016)). The capacity of $\delta^{53}\text{Cr}$ from shales and ironstones to resolve changes in oceanic oxygenation state depends on ability to discriminate authigenic from detrital Cr, and this stands as a key challenge and opportunity. Nevertheless, the Cr record links biological and geochemical evolution indirectly via the effect that O_2 has on both.

In an effort to establish a more rigorous calibration of the Cr isotope redox proxy in the modern, Reinhard et al. (2014) examined Cr isotope fractionations in the recent sediments of the Cariaco Basin, Venezuela. A slight increase in $\delta^{53}\text{Cr}$ coupled with elevated Cr enrichments is coincident with the onset of deep-water euxinic conditions in the basin. The authors argued that this observation suggests that such sediments, and their ancient equivalents, can be used to track the Cr isotope composition of the oceans over time—because the $\delta^{53}\text{Cr}$ signature of the overlying water column is approximately recorded by sediments deposited under an anoxic water column. Similar evidence of the reliability of black shales in tracking $\delta^{53}\text{Cr}$ signatures is presented by Gueguen et al. (2016) from the upwelling zone of the Peru Margin, comparable to modern deepwater values. However, Scheiderich et al. (2015) recommended a more cautious approach to Cr isotope proxies based on important variability in Cr concentrations and isotopic compositions in the Arctic ocean and between the Arctic, Atlantic, and Pacific Oceans, emphasizing the need to better understand modern marine Cr cycling.

Most recently, Cole et al. (2016) have expanded the record of black shale $\delta^{53}\text{Cr}$ values throughout Earth history, illustrating a base-level shift at ~ 850 Ma from largely unfractionated $\delta^{53}\text{Cr}$ values similar to the composition of continental crust to highly fractionated $\delta^{53}\text{Cr}$ values. The authors have used this record to suggest a lack of significant terrestrial oxidative weathering of Cr prior to 850 Ma indicative of oxygen levels below $\sim 0.1\%$ PAL (based on the $p\text{O}_2$ estimate from Planavsky et al., 2014b). Again, capacity to constrain authigenic versus detrital Cr is key to these interpretations.

1.2.7 Uranium

The redox-sensitive element uranium (U), though not bioessential, provides constraints on the dynamics of the evolving oxygenation of the Earth. Some bacteria catalyze the reduction of U(VI) to U(IV) in order to obtain energy, including a few dissimilatory Fe(III)- and sulfate-reducing bacteria (e.g., Lovley et al., 1991, Behrends and Van Cappellen, 2005). Microbial U(VI) reduction, in addition to abiotic mechanisms of reduction such as sorption to organic matter or co-precipitation with iron oxides, sequesters marine U into sediments. These processes provide a means to use U concentration in the sedimentary record as a proxy for changes in the oxygen content of the atmosphere-ocean system. In terms of the sedimentary record, U abundances have been investigated in both the IF and black shale records (Partin et al., 2013a,b), while U isotopes have been used in some studies to better illuminate the oxygenation of the oceans (Asael et al., 2013; Kendall et al., 2013, 2015a; Dahl et al., 2014). More recent work has also demonstrated that U isotopes can potentially be used to track the biotic reduction of U(VI), providing the potential for a novel redox biosignature proxy in the rock record (Stylo et al., 2015).

Temporal changes in U abundances in the IF and black shale datasets provide highly complementary records that document the rise and accumulation of oxygen associated with the GOE and yield insights into post-GOE oxygen dynamics (Partin et al., 2013a,b). An increase in U concentration and U/Fe ratios is observed in the IF record around 2.47-2.43 Ga and appears to mark the onset of the GOE—corroborated by a peak in both BIF and black shale U concentrations by 2.32 Ga. Following this initial peak, U and U/Fe ratios in the IF record return to low levels during the late Paleoproterozoic (post 2.05 Ga), until an increase is observed in Neoproterozoic IF and Phanerozoic ironstones (Partin et al., 2013a). In the black shale record, the rise in oxygen associated with the GOE is reflected in a marked increase in U and U/TOC values, followed by a dramatic decrease in the late Paleoproterozoic and a second increase in the latest Neoproterozoic—consistent with pervasive ocean and atmosphere oxygenation. This rise and fall in oxygen levels in the Paleoproterozoic is now the generally accepted paradigm in the evolution of the oxygenation of the Earth’s surface (see Lyons et al., 2014), though the biological implications of these events have only begun to be considered. However, laser ablation analyses of black shale matrices by Large et al. (2014) seem to show an increase in U during the Mesoproterozoic, with a peak between 1.4 to 1.7 Ga (see their 8c). They attribute this rise to enhanced oxidative weathering of U-rich granites. Although, they also show a peak with a similar maximum at 3.1 Ga which is difficult to reconcile with either interpretation of Proterozoic U abundances. Recent work using U-Th-Pb systematics (corrected U concentrations) and $\delta^{56}\text{Fe}$ values from the 3.2 Ga Manzimnyama IF in South Africa are consistent with ambient dissolved oxygen concentrations between 0.4 and 10 μM (Satkoski et al., 2015).

Uranium isotopes have also been used to study the oxygenation of Earth's surface, since U isotope fractionations are linked to changes in the oxidation state of U. Evidence from U isotopes ($\delta^{238}\text{U}$) in the Mt. McRae shale suggest U(IV) oxidation and mobilization as early as 2.5 Ga (Kendall et al., 2013). They attributed $\delta^{238}\text{U}$ values above average upper crustal values that coincide with Mo and Re enrichments (Anbar et al., 2007) to be indicative of the oxidative mobilization of U, possibly within the water column itself.

In the late Paleoproterozoic, coupled U, Mo, and Fe isotope analyses in the ~2.05 Ga Zaonega Formation suggest euxinic depositional conditions—showing values similar to those found in modern euxinic settings (Asael et al. 2013). This low redox state is consistent with a decrease in oxygenation of the atmosphere-ocean system following the GOE, as inferred for the late Paleo- to Mesoproterozoic from the black shale U abundance record (Partin et al., 2013b). Similarly, Kendall et al. (2015a) used coupled U and Mo isotopes from the Ediacaran Doushantuo Formation to examine ocean oxygenation dynamics around the time of metazoan diversification. High $\delta^{238}\text{U}$ values indicate pervasive ocean oxygenation between 560-551 Ma. Collectively, studies such as these have demonstrated the utility in using U, a non-bioessential element, for tracking the redox evolution of the Earth's atmosphere and oceans. This, in turn, has profound effects for the evolution of the biosphere, and perhaps even for tracking the biotic signature of U reduction in the rock record (Stylo et al., 2015).

1.3 Summary

There has been significant progress made in recent years in the examination of IFs as critical archives for the paleomarine availability of transition elements including Ni, Zn,

Cr, and Co, among others and their implications for the evolution of the biosphere and oxidative weathering. Yet questions remain regarding the formation of IFs, the meaning behind their trace element chemistry, and how other aspects of ancient marine chemistry may affect the interpretation of the IF record.

1.3.1 What this thesis entails

The following chapters in this thesis address several critical issues that have arisen regarding the primary mineralogy of IF, including (1) the variability in trace element geochemistry associated with different analytical techniques and how it may affect our interpretation of the IF record, and (2) how poorly constrained aspects of Precambrian marine chemistry affect our understanding of the evolution of transition metals in the ancient oceans.

Chapter 2 addresses recently raised aspects on the primary mineralogy underlying IF deposition, specifically the possibility that greenalite or carbonated green rust mineral phases may play a key role in IF deposition (e.g., Rasmussen et al., 2014, 2015, 2016, 2017; Halevy et al., 2017). Results presented here clearly demonstrate that a ferric, or at least partially-oxidized, iron mineral phase is the precursor phase to IF deposition, and only a very limited role for greenalite is envisioned. This finding is grounded in hydrogeological considerations and is consistent with previous models for IF deposition (e.g., Bekker et al., 2014; Kappler et al., 2005; Konhauser et al., 2017) and a wealth of existing geochemical signatures (e.g., Pecoits et al., 2009; Steinhöfel et al., 2010).

Chapter 3 focuses on interpreting the differences in trace element geochemistry resulting from differential analytical methods being applied to samples from several IF

units from the Archean through to the Paleoproterozoic including: the Nuvvuagittuq Supracrustal Belt, the Marra Mamba Iron Formation, the Dales Gorge and Joffre members of the Brockman Iron Formation, and the Weeli Wolli Formation. Significant differences exist in trace element data generated in three pairwise comparison: (i) bulk geochemical techniques versus the laser ablation of hematite grains, (ii) bulk geochemical techniques versus the laser ablation of magnetite grains, and (iii) the laser ablation of hematite versus magnetite grains. While significant differences exist, it is apparent that the combination of multiple analytical methods is necessary to capture the full range of information preserved in the IF record and moving forward a combination of bulk and *in-situ* techniques represents the best practice for examining the trace element geochemistry of IF.

Chapter 4 examines the implications of two poorly constrained aspects of ancient seawater chemistry, specifically pH estimates and the establishment of a carbonate buffered system, and the implications for existing interpretations of Archean to Paleoproterozoic seawater. Variability in estimates for ancient seawater pH has implications for the speciation of trace metals, and by extension bioavailability, authigenic mineral precipitation, and the reactivity of particle surfaces adsorbing trace elements. Yet, this remains one of the most poorly understood aspects of early marine chemistry. By examining the time necessary to establish carbonate buffering, we can make inferences grounded in thermodynamic calculations, and evaluate these against existing geochemical models for marine pH through time (e.g., Halevy and Bachan, 2017; Krissansen-Totton et al., 2018).

This thesis concludes with an outline of future avenues for research in IF geochemistry and more broadly, assessing the composition and evolution of Precambrian

seawater. These avenues and questions develop as a natural extension of this body of work and provide a strong basis for future research. Some of the critical questions raised include: (i) how can a definitive determination on the depositional mechanism underlying IF deposition be made? (ii) what other biological signals are contained within the IF record and how can they be unlocked with novel isotopic or geochemical tools? and (iii) how can we improve the interpretation of geochemical record for the Archean to Paleoproterozoic oceans? Each of these questions will be outlined and addressed in more detail in the concluding chapter.

1.4 References

- Aguirre, J.D., Clark, H.M., McIlvin, M., Vazquez, C., Palmere, S.L., Grab, D.J., Seshu, J., Hart, P.J., Saito, M., Culotta, V.C., 2013. A manganese-rich environment supports superoxide dismutase activity in a Lyme disease pathogen, *Borrelia burgdorferi*. *Journal of Biological Chemistry* 288, 8468-8478.
- Ahlgren, N.A., Noble, A., Patton, A.P., Roache-Johnson, K., Jackson, L., Robinson, D., McKay, C., Moore, L.R., Saito, M.A., Rocap, G., 2014. The unique trace metal and mixed layer conditions of the Costa Rica upwelling dome support a distinct dense community of *Synechococcus*. *Limnology and Oceanography* 59, 2166-2184.
- Alexander, B., Bau, M., Andersson, P., Dulski, P., 2008. Continentally-derived solutes in shallow Archean seawater: Rare earth element and Nd isotope evidence in iron formation from the 2.9 Ga Pongola Supergroup, South Africa. *Geochimica et Cosmochimica Acta* 72, 378–394.

- Amin, S.A., Moffett, J.W., Martens-Habbena, W., Jacquot, J.E., Han, Y., Devol, A., Ingalls, A.E., Stahl, D.A., Armbrust, E.V., 2013. Copper requirements of the ammonia-oxidizing archaeon *Nitrosopumilus maritimus* SCM1 and implications for nitrification in the marine environment. *Limnology and Oceanography* 58, 2037-2045.
- Anbar, A.D., 2008. Elements and Evolution. *Science* 322, 1481-1483.
- Anbar, A.D., Duan, Y., Lyons, T.W., Arnold, G.L., Kendall, B., Creaser, R.A., Kaufman, A.J., Gordon, G.W., Scott, C., Garvin, J., Buick, R., 2007. A Whiff of Oxygen Before the Great Oxidation Event? *Science* 317, 1903-1906.
- Anbar, A.D., Knoll, A.H., 2002. Proterozoic ocean chemistry and evolution: A bioinorganic bridge? *Science* 297, 1137-1142.
- Aristilde, L., Xu, Y., Morel, F.M.M., 2012. Weak Organic Ligands Enhance Zinc Uptake in Marine Phytoplankton. *Environmental Science & Technology* 46, 5438–5445.
- Asael, D., Tissot, F.L.H., Reinhard, C.T., Rouxel, O., Dauphas, N., Lyons, T.W., Ponzevera, E., Liorzou, C., Chéron, S., 2013. Coupled molybdenum, iron, and uranium stable isotopes as oceanic paleoredox proxies during the Paleoproterozoic Shunga Event. *Chemical Geology* 362, 193-210.
- Bau, M., 1993. Effects of syn- and post-depositional processes on the rare-earth element distribution in Precambrian iron-formations. *European Journal of Mineralogy* 5, 257-267.
- Bau, M., Möller, P., 1993. Rare earth element systematics of the chemically precipitated component in Precambrian iron formations and the evolution of the terrestrial

- atmosphere-hydrosphere-lithosphere system. *Geochimica et Cosmochimica Acta* 57, 2239-2249.
- Bau, M., Dulski, P., 1996. Distribution of yttrium and rare-earth elements in the Penge and Kuruman iron-formations, Transvaal Supergroup, South Africa. *Precambrian Research* 79, 37-55.
- Balistrieri, L.S., Borrok, D., Wanty, R., and Ridley, W., 2008, Fractionation of Cu and Zn isotopes during adsorption onto amorphous Fe(III) oxyhydroxide: Experimental mixing of acid rock drainage and ambient river water. *Geochimica et Cosmochimica Acta* 72, 311–328.
- Behrends, T., Van Cappellen, P., 2005. Competition between enzymatic and abiotic reduction of uranium(VI) under iron reducing conditions. *Chemical Geology* 220, 315-327.
- Bekker, A., Slack, J.F., Planavsky, N., Krapež, B., Hofmann, A., Konhauser, K.O., Rouxel, O.J., 2010. Iron Formation: The Sedimentary Product of a Complex Interplay among Mantle, Tectonic, Oceanic, and Biospheric Processes. *Economic Geology* 105, 467-508.
- Bekker, A., Planavsky, N.J., Krapež, B., Rasmussen, B., Hofmann, A., Slack, J.F., Rouxel, O.J., Konhauser, K.O., 2014. Iron Formations: Their Origins and Implications for Ancient Seawater Chemistry in Holland, H.K., Turekian, K., (eds.) *Treatise on Geochemistry*, 2nd edition, 561-628.
- Berg, J., Shi, Y., 1996. The Galvanization of Biology: A Growing Appreciation for the Roles of Zinc. *Science* 271, 1081-1085.

- Bjerrum, C.J., Canfield, D.E., 2002. Ocean productivity before about 1.9 Gyr ago limited by phosphorus adsorption onto iron oxides. *Nature* 417, 159-162.
- Bolhar, R., Kamber, B.S., Moorbath, S., Fedo, C.M., Whitehouse, M.J., 2004. Characterisation of early Archaean chemical sediments by trace element signatures. *Earth and Planetary Science Letters* 222, 43-60.
- Brand, L.E., Sunda, W.G., Guillard, R.R.L., 1983. Limitation of Marine Phytoplankton Reproductive Rates by Zinc, Manganese, and Iron. *Limnology and Oceanography* 28, 1182-1198.
- Bruland, K.W., 1989. Complexation of Zinc by Natural Organic Ligands in the Central North Pacific. *Limnology and Oceanography* 34, 269-285.
- Buick, R., 2007. Did the Proterozoic 'Canfield Ocean' cause a laughing gas greenhouse? *Geobiology* 5, 97-100.
- Byrne, R. H., Kim K. -H., 1990. Rare earth element scavenging in seawater. *Geochimica et Cosmochimica Acta* 54, 2645-2656.
- Chi-Fru, E., Rodríguez, N.P., Partin, C.A., Lalonde, S.V., Andersson, P., Weiss, D.J., Albani, El, A., Rodushkin, I., Konhauser, K.O., 2016. Cu isotopes in marine black shales record the Great Oxidation Event. *Proceedings of the National Academy of Sciences* 113, 4941-4946.
- Cole, D.B., Reinhard, C.T., Wang, X., Gueguen, B., Halverson, G.P., Gibson, T., Hodgskiss, M.S.W., McKenzie, N.R., Lyons, T.W., Planavsky, N.J., 2016. A shale-hosted Cr isotope record of low atmospheric oxygen during the Proterozoic. *Geology* 44, 555-558.

- Condie, K.C., 1993. Chemical composition and evolution of the upper continental crust: contrasting results from surface samples and shales. *Chemical Geology* 104, 1–37.
- Crowe, S.A., O’Neill, A.H., Katsev, S., Hehanussa, P., Haffner, G.D., Sundby, B., Mucci, A., Fowle, D.A., 2008. The biogeochemistry of tropical lakes: A case study from Lake Matano, Indonesia. *Limnology and Oceanography* 53, 319–331.
- Crowe, S.A., Døssing, L.N., Beukes, N.J., Bau, M., Kruger, S.J., Frei, R., Canfield, D.E., 2013. Atmospheric oxygenation three billion years ago. *Nature* 50, 535-538.
- Dahl, T.W., Boyle, R.A., Canfield, D.E., Connelly, J.N., Gill, B.C., Lenton, T.M., Bizzarro, M., 2014. Uranium isotopes distinguish two geochemically distinct stages during the later Cambrian SPICE event. *Earth and Planetary Science Letters* 401, 313–326.
- David, L.A., Alm, E.J., 2011. Rapid evolutionary innovation during an Archaean genetic expansion. *Nature* 469, 93–96.
- Davis, J. A., Coston, J. A., Kent, D. B., Fuller, C. C., 1998. Application of the surface complexation concept to complex mineral assemblages. *Environmental Science & Technology* 32, 2820-2828.
- Dierssen, H., Balzer, W., Landing, W.M., 2001. Simplified synthesis of an 8-hydroxyquinoline chelating resin and a study of trace metal profiles from Jellyfish Lake, Palau. *Marine Chemistry* 73, 173–192.
- Dupont, C.L., Yang, S., Palenik, B., Bourne, P.E., 2006. Modern proteomes contain putative imprints of ancient shifts in trace metal geochemistry. *Proceedings of the National Academy of Sciences* 103, 17822-17827.

- Dupont, C.L., Neupane, K., Shearer, J., Palenik, B., 2008. Diversity, function and evolution of genes coding for putative Ni-containing superoxide dismutases. *Environmental Microbiology* 10, 1831-1843.
- Dupont, C.L., Butcher, A., Valas, R.E., Bourne, P.E., Caetano-Anollés, G., 2010. History of biological metal utilization inferred through phylogenomic analysis of protein structures. *Proceedings of the National Academy of Sciences* 107, 10567-10572.
- Dzombak, D. A., Morel, F. M. M., 1990. Surface complexation modeling Hydrous ferric oxide. John Wiley and Sons, pp 1-393.
- Eady, R.R., 1996. Structure–Function Relationships of Alternative Nitrogenases. *Chemical Reviews* 96, 3013–3030.
- Eickhoff, M., Obst, M., Schröder, C., Hitchcock, A.P., Tyliszczak, T., Martinez, R.E., Robbins, L.J., Konhauser, K.O., Kappler, A., 2014. Nickel partitioning in biogenic and abiogenic ferrihydrite: The influence of silica and implications for ancient environments. *Geochimica et Cosmochimica Acta* 140, 65-79.
- Ellis, A.S., Johnson, T.M., Bullen, T.D., 2002. Chromium Isotopes and the Fate of Hexavalent Chromium in the Environment. *Science* 295, 2060–2062.
- Erel, Y., Stolper, E.M., 1993. Modeling of rare-earth element partitioning between particles and solution in aquatic environments. *Geochimica et Cosmochimica Acta* 57, 513-518.
- Fein, J. B., Daughney, C. J., Yee, N., Davis, T. A., 1997. A chemical equilibrium model for metal adsorption onto bacterial surfaces. *Geochimica et Cosmochimica Acta* 61, 3319-3328.

- Fein, J. B., Boily, J. –F., Yee, N., Gorman-Lewis, D., Turner, B. F., 2005. Potentiometric titrations of *Bacillus subtilis* cells to low pH and a comparison of modeling approaches. . *Geochimica et Cosmochimica Acta* 69, 1123-1132.
- Frausto da Silva, J.J.R., Williams, R.J., 2001. *The biological chemistry of the elements: The inorganic chemistry of life*. 2nd ed., Oxford University Press, Oxford, United Kingdom. p. 1- 575.
- Frei, R., Gaucher, C., Poulton, S.W., Canfield, D.E., 2009. Fluctuations in Precambrian atmospheric oxygenation recorded by chromium isotopes. *Nature* 461, 250-253.
- Friedrich, A.J., Luo, Y.L., Catalano, J.G., 2011. Trace element cycling through iron oxide minerals during redox driven dynamic recrystallization. *Geology* 39, 1083-1086.
- Friedrich, A.J., Catalano, J.G., 2012. Controls on Fe(II)-Activated Trace Element Release from Goethite and Hematite. *Environmental Science & Technology* 46, 1519-1526.
- Friedrich, A.J., Scherer, M.M., Bachman, J.E., Englehard, M.H., Rapponotti, B.W., Catalano, J.G., 2012. Inhibition of Trace Element Release During Fe(II)-Activated Recrystallization of Al-, Cr-, and Sn-Substituted Goethite and Hematite. *Environmental Science & Technology* 46, 10031-10039.
- Frost, C.D., von Blanckenburg, F., Schoenberg, R., Frost, B.R., Swapp, S.M., 2007. Preservation of Fe isotope heterogeneities during diagenesis and metamorphism of banded iron formation. *Contributions to Mineralogy and Petrology* 153, 211-235.
- Gueguen, B., Reinhard, C.T., Algeo, T.J., Peterson, L.C., Nielsen, S.G., Wang, X., Rowe, H., Planavsky, N.J., 2016. The chromium isotope composition of reducing and oxic marine sediments. *Geochimica et Cosmochimica Acta* 184, 1–19.

- Halevy, I., Bachan, A., 2017. The geologic history of seawater pH. *Science* 355, 1069–1071.
- Haugaard, R., Frei, R., Stendal, H., Konhauser, K., 2013. Petrology and geochemistry of the ~2.9Ga Itilliarsuk banded iron formation and associated supracrustal rocks, West Greenland: Source characteristics and depositional environment. *Precambrian Research* 22, 150–176.
- Haugaard, R., Pecoits, E., Lalonde, S., Rouxel, O., Konhauser, K., 2016. The Joffre banded iron formation, Hamersley Group, Western Australia: Assessing the palaeoenvironment through detailed petrology and chemostratigraphy. *Precambrian Research* 273, 12–37.
- Hausinger, R.P., 1987. Nickel Utilization by Microorganisms. *Microbiological Reviews* 51, 22-42.
- Hoffman, P.F., Kaufman, A.J., Halverson, G.P., Schrag, D.P., 1998. A Neoproterozoic Snowball Earth. *Science* 281, 1342–1346.
- Isley, A.E., Abbott, D.H., 1999. Plume-related mafic volcanism and the deposition of banded iron formation *Journal of Geophysical Research* 104, 15461–15477.
- James, H.L., 1954. Sedimentary facies of iron-formation. *Economic Geology* 49, 235-293.
- Jones, C. Nomosatryo, S., Crowe, S.A., Bjerrum, C.J., Canfield, D.E., 2015. Iron oxides, divalent cations, silica, and the early earth phosphorus crisis. *Geology* 43, 135-138.
- Kappler, A., Pasquero, C., Konhauser, K.O., Newman, D.K., 2005. Deposition of banded iron formations by anoxygenic phototrophic Fe(II)-oxidizing bacteria. *Geology* 33, 865–868.

- Kasting, J.F., 2013. What caused the rise of atmospheric O₂? *Chemical Geology* 362, 13–25.
- Kendall, B., Brennecka, G.A., Weyer, S., Anbar, A.D., 2013. Uranium isotope fractionation suggests oxidative uranium mobilization at 2.50 Ga. *Chemical Geology* 362, 105–114.
- Kendall, B., Komiya, T., Lyons, T.W., Bates, S.M., Gordon, G.W., Romaniello, S.J., Jiang, G., Creaser, R.A., Xiao, S., McFadden, K., Sawaki, Y., Tahata, M., Shu, D., Han, J., Li, Y., Chu, X., Anbar, A.D., 2015a. Uranium and molybdenum isotope evidence for an episode of widespread ocean oxygenation during the late Ediacaran Period. *Geochimica et Cosmochimica Acta* 156, 173-193.
- Klein, C., 2005. Some Precambrian banded iron-formations (BIFs) from around the world: Their age, geologic setting, mineralogy, metamorphism, geochemistry and origin. *American Mineralogist* 90, 1473-1499.
- Kobayashi, M., Shimizu, S., 1999. Cobalt proteins. *European Journal of Biochemistry* 261, 1-9.
- Koeppenkastrop, D., De Carlo, E.H., 1992. Sorption of rare-earth elements from seawater onto synthetic mineral particles: An experimental approach. *Chemical Geology* 95, 251-263.
- Konhauser, K.O., Lalonde S.V., Amskold, L.A., Holland, H.D., 2007. Was There Really an Archean Phosphate Crisis? *Science* 315, 1234.
- Konhauser, K.O., Pecoits, E., Lalonde, S.V., Papineau, D., Nisbet, E.G., Barley, M.E., Arndt, N.T., Zahnle, K., Kamber, B.S., 2009. Oceanic nickel depletion and a methanogen famine before the Great Oxidation Event. *Nature* 458, 750-753.

- Konhauser, K.O., Lalonde, S.V., Planavsky, N.J., Pecoits, E., Lyons, T.W., Mojzsis, S.J., Rouxel, O.J., Barley, M.E., Rosière, C., Fralick, P.W., Kump, L.R., Bekker, A., 2011. Aerobic bacterial pyrite oxidation and acid rock drainage during the Great Oxidation Event. *Nature* 478, 369-373.
- Konhauser, K.O., Robbins, L.J., Pecoits, E., Peacock, C.L., Kappler, A., Lalonde, S.V., 2015. The Archean nickel famine revisited. *Astrobiology* 15, 804-815.
- Konhauser, K.O., Planavsky, N.J., Hardisty, D.S., Robbins, L.J., Warchola, T.J., Haugaard, R., Lalonde, S.V., Partin, C.A., Oonk, P.B.H., Tsikos, H., Lyons, T.W., Bekker, A., Johnson, C.M., 2017. Iron formations: A global record of Neoproterozoic to Palaeoproterozoic environmental history. *Earth-Science Reviews* 172, 140–177.
- Koretsky, C., 2000. The significance of surface complexation reactions in hydrologic systems: a geochemist's perspective. *Journal of Hydrology* 230, 127-171.
- Krapež, B., Barley, M.E., Pickard, A.L., 2003. Hydrothermal and resedimented origins of the precursor sediments to banded iron formation: sedimentological evidence from the Early Palaeoproterozoic Brockman Supersequence of Western Australia. *Sedimentology* 50, 979-1011.
- Krissansen-Totton, J., Arney, G.N., Catling, D.C., 2018. Constraining the climate and ocean pH of the early Earth with a geological carbon cycle model. *Proceedings of the National Academy of Sciences* 252, 201721296–6.
- Kunzmann, M., Halverson, G.P., Sossi, P.A., Raub, T.D., Payne, J.L., Kirby, J., 2013. Zn isotope evidence for immediate resumption of primary productivity after snowball Earth. *Geology* 41, 27-30.

- Lalonde, S.V., Konhauser, K.O., 2015. Benthic perspective on Earth's oldest evidence for oxygenic photosynthesis *Proceedings of the National Academy of Sciences* 112, 995-1000.
- Landing, W.M., Burnett, W.C., Lyons, W.B., Orem, W.H., 1991. Nutrient Cycling and the Biogeochemistry of Manganese, Iron, and Zinc in Jellyfish Lake, Palau. *Limnology and Oceanography* 36, 515–525.
- Large, R.R., Halpin, J.A., Danyushevsky, L.V., Maslennikov, V.V., Bull, S.W., Long, J.A., Gregory, D.D., Lounejeva, E., Lyons, T.W., Sack, P.J., McGoldrick, P.J., Claver, C.R., 2014. Trace element content of sedimentary pyrite as a new proxy for deep-time ocean-atmosphere evolution. *Earth and Planetary Science Letters* 389, 209-220.
- Lipscomb, W.N., Sträter, N., 1996. Recent Advances in Zinc Enzymology. *Chemical Reviews* 96, 2375-2433.
- Liu, Y., Alessi, D.S., Owttrim, G.W., Petrash, D.A., Mloszewska, A.M., Lalonde, S.V., Martinez, R.E., Zhou, Q., Konhauser, K.O., 2015. Cell surface reactivity of *Synechococcus* sp. PCC 7002: Implications for metal sorption from seawater. *Geochimica et Cosmochimica Acta* 169, 30-44.
- Lohan, M.C., Crawford, D.W., Purdie, D.A., Statham, P.J., 2005. Iron and zinc enrichments in the northeastern subarctic Pacific: Ligand production and zinc availability in response to phytoplankton growth. *Limnology and Oceanography* 50, 1427–1437.
- Lovley, D.R., Phillips, E.J.P., Gorby, Y.A., Landa, E.R., 1991. Microbial reduction of uranium. *Nature* 350, 413-416.

- Lyons, T.W., Gellatly, A.M., McGoldrick, P.J., Kah, L.C., 2006. Proterozoic sedimentary exhalative (SEDEX) deposits and links to evolving global ocean chemistry. *In* Kesler, S.E., and Ohmoto, H., eds., *Evolution of Early Earth's Atmosphere, Hydrosphere, and Biosphere—Constraints from Ore Deposits*. Geological Society of America Memoir 198, 169–184.
- Lyons, T.W., Reinhard, C.T., Planavsky, N.J., 2014. The rise of oxygen in Earth's early ocean and atmosphere. *Nature* 506, 307-315.
- Marsh, E.N.G., 1999. Coenzyme B₁₂ (cobalamin)-dependent enzymes. *Essays in Biochemistry* 34, 139-154.
- Martinez, R.E., Konhauser, K.O., Paunova, N., Wu, W., Alessi, D.S., Kappler, A., 2016. Surface reactivity of the anaerobic photoferrotrophic Fe(II)-oxidizing bacterium *Rhodovulum iodosum*: Implications for trace metal budgets in ancient oceans and banded iron formation. *Chemical Geology* 442, 113-120.
- Morel, F.M.M., Reinfelder, J.R., Roberts, S.B., Chamberlain, C.P., Lee, J.G., Yee, D., 1994. Zinc and carbon co-limitation of marine phytoplankton. *Nature* 369, 740-742.
- Morris, R.C., 1993. Genetic modeling for banded iron-formation of the Hamersley Group, Pilbara Craton, Western Australia. *Precambrian Research* 60, 243-286.
- Mücke, A., Farshad, F., 2005. Whole-rock and mineralogical composition of Phanerozoic ooidal ironstones: Comparison and differentiation of types and subtypes. *Ore Geology Reviews* 26, 227–262.
- Ohnemüller, F., Prave, A. R., Fallick, A. E., Kasemann, S. A., 2014. Ocean acidification in the aftermath of the Marinoan glaciation. *Geology* 42, 1103-1106.

- Partin, C.A., Lalonde, S.V., Planavsky, N.J., Bekker, A., Rouxel, O.J., Lyons, T.W., Konhauser, K.O., 2013a. Uranium in iron formations and the rise of atmospheric oxygen. *Chemical Geology* 362, 82-90.
- Partin, C.A., Bekker, A., Planavsky, N.J., Scott, C.T., Gill, B.C., Li, C., Podkovyrov, V., Maslov, A., Konhauser, K.O., Lalonde, S.V., Love, G.D., Poulton, S.W., Lyons, T.W., 2013b. Large-scale fluctuations in Precambrian atmospheric and oceanic oxygen levels from the record of U in shales. *Earth and Planetary Science Letters* 369-370, 284-293.
- Pearson, P. N., Palmer, M. R., 1999. Middle Eocene seawater pH and atmospheric carbon dioxide concentrations. *Science* 284, 1824-1826.
- Pecoits, E., Gingras, M.E., Barley, M.E., Kappler, A., Posth, N.R., Konhauser, K.O., 2009. Petrography and geochemistry of the Dales Gorge banded iron formation: Paragenetic sequence, source and implications for palaeo-ocean chemistry. *Precambrian Research* 172, 163-187.
- Planavsky, N., Bekker, A., Rouxel, O.J., Kamber, B., Hofmann, A., Knudsen, A., Lyons, T.W., 2010. Rare Earth Element and yttrium compositions of Archean and Paleoproterozoic Fe formations revisited: New perspectives on the significance and mechanisms of deposition. *Geochimica et Cosmochimica Acta* 74, 6387–6405.
- Planavsky, N.J., Asael, D., Hofmann, A., Reinhard, C.T., Lalonde, S.V., Knudsen, A., Wang, X., Ossa Ossa, F., Pecoits, E., Smith, A.J.B., Beukes, N.J., Bekker, A., Johnson, T.M., Konhauser, K.O., Lyons, T.W., Rouxel, O.J., 2014a. Evidence for oxygenic photosynthesis half a billion years before the Great Oxidation Event. *Nature Geoscience* 7, 283-286.

- Planavsky, N.J., Reinhard, C.T., Wang, X., Thomson, D., McGoldrick, P., Rainbird, R.H., Johnson, T., Fischer, W.W., Lyons, T.W., 2014b. Low Mid-Proterozoic atmospheric oxygen levels and the delayed rise of animals. *Science* 346, 635-638.
- Planavsky, N.J., Cole, D.B., Reinhard, C.T., Diamond, C., Love, G.D., Luo, G., Zhang, S., Konhauser, K.O., Lyons, T.W., 2016. No evidence for high atmospheric oxygen levels 1,400 million years ago. *Proceedings of the National Academy of Sciences* 113, E2550–E2551.
- Pons, M.L., Fujii, T., Rosing, M., Quitté, G., Télouk, P., Albarède, F., 2013. A Zn isotope perspective on the rise of continents. *Geobiology* 11, 201–214.
- Posth, N.R., Canfield, D.E., Kappler, A., 2014. Biogenic Fe(III) minerals: From formation to diagenesis and preservation in the rock record. *Earth-Science Reviews* 135, 103-121.
- Ragsdale, S.W., Kumar, M., 1996. Nickel-Containing Carbon Monoxide Dehydrogenase/Acetyl-CoA Synthase. *Chemical Reviews* 96, 2515-2539.
- Rasmussen, B., Fletcher, I.R., Bekker, A., Muhling, J.R., Gregory, C.J., Thorne, A.M., 2012. Deposition of 1.88-billion-year-old iron formations as a consequence of rapid crustal growth. *Nature* 484, 498–501.
- Reinhard, C.T., Planavsky, N.J., Robbins, L.J., Partin, C.A., Gill, B.C., Lalonde, S.V., Bekker, A., Konhauser, K.O., Lyons, T.W., 2013. Proterozoic ocean redox and biogeochemical stasis. *Proceedings of the National Academy of Sciences* 110, 5357-5362.

- Reinhard, C.T., Planavsky, N.J., Wang, X., Fischer, W.W., Johnson, T.M., Lyons, T.M., 2014. The isotopic composition of authigenic chromium in anoxic marine sediments: A case study from the Cariaco Basin. *Earth and Planetary Science Letters* 407, 9-18.
- Robbins, L.J., Lalonde, S.V., Saito, M.A., Planavsky, N.J., Mloszewski, A.M., Pecoits, E., Scott, C., Dupont, C.L., Kappler, A., Konhauser, K.O., 2013. Authigenic iron oxide proxies for marine zinc over geological time and implications for eukaryotic metallome evolution. *Geobiology* 11, 295-306.
- Robbins, L.J., Swanner, E.D., Lalonde, S.V., Eickhoff, M., Paranich, M.L., Reinhard, C.T., Peacock, C.L., Kappler, A., Konhauser, K.O., 2015. Limited Zn and Ni mobility during simulated Iron Formation diagenesis. *Chemical Geology* 402, 30-39.
- Robbins, L.J., Lalonde, S.V., Planavsky, N.J., Partin, C.A., Reinhard, C.T., Kendall, B., Scott, C., Hardisty, D.S., Gill, B.C., Alessi, D.S., Dupont, C.L., Saito, M.A., Crowe, S.A., Poulton, S.W., Bekker, A., Lyons, T.W., Konhauser, K.O., 2016. Trace elements at the intersection of marine biological and geochemical evolution. *Earth-Science Reviews* 163, 323–348.
- Roberts, S., Lane, T., Morel, F.M.M., 1997. Carbonic anhydrase in the marine diatom *Thalassiosira weissflogii* (Bacillariophyceae). *Journal of Phycology* 33, 845-850.
- Rothman, D.H., Fournier, G.P., French, K.L., Alm, E.J., Boyle, E.A., Cao, C., Summons, R.E., 2014. Methanogenic burst in the end-Permian carbon cycle. *Proceedings of the National Academy of Sciences* 111, 5462-5467.
- Sahoo, S.K., Planavsky, N.J., Kendall, B., Wang, X., Shi, X., Scott, C., Anbar, A.D., Lyons, T.W., Jiang, G., 2012. Ocean oxygenation in the wake of the Marinoan glaciation. *Nature* 489, 546-549.

- Saito, M.A., Moffett, J.W., 2001. Complexation of cobalt by natural organic ligands in the Sargasso Sea as determined by a new high-sensitivity electrochemical cobalt speciation method suitable for open ocean work. *Marine Chemistry* 75, 49-68.
- Saito, M.A., Sigman, D.M., Morel, F.M.M., 2003. The bioinorganic chemistry of the ancient ocean: the co-evolution of cyanobacterial metal requirements and biogeochemical cycles at the Archean-Proterozoic boundary? *Inorganica Chimica Acta* 356, 308-318.
- Saito, M.A., Rocap, G., Moffett, J.W., 2005. Production of cobalt binding ligands in a *Synechococcus* feature at the Costa Rica upwelling dome. *Limnology and Oceanography* 50, 279-290.
- Sanford, W.E., Doughten, M.W., Coplen, T.B., Hunt, A.G., Bullen, T.D., 2013. Evidence for high salinity of Early Cretaceous sea water from the Chesapeake Bay crater. *Nature* 503, 252-256.
- Satkoski, A.M., Beukes, N.J., Li, W., Beard, B.L., Johnson, C.M., 2015. A redox-stratified ocean 3.2 billion years ago. *Earth and Planetary Science Letters* 430, 43-53.
- Scheiderich, K., Amini, M., Holmden, C., Francois, R., 2015. Global variability of chromium isotopes in seawater demonstrated by Pacific, Atlantic, and Arctic Ocean samples. *Earth and Planetary Science Letters* 423, 87-97.
- Scott, C., Planavsky, N.J., Dupont, C.L., Kendall, B., Gill, B.C., Robbins, L.J., Husband, K.F., Arnold, G.L., Wing, B.A., Poulton, S.W., Bekker, A., Anbar, A.D., Konhauser, K.O., Lyons, T.W., 2013. Bioavailability of zinc in marine systems through time. *Nature Geoscience* 6, 125-128.

- Simonson, B.M., 1985. Sedimentology of cherts in the Early Proterozoic Wishart Formation, Quebec-Newfoundland, Canada. *Sedimentology* 32, 23-40.
- Simonson, B.M., Goode, A.D.T., 1989. First discovery of ferruginous chert arenites in the early Precambrian Hamersley Group of Western Australia. *Geology* 17, 269-272.
- Solomon, E.I., Sundaram, U.M., Machonkin, T.E., 1996. Multicopper oxidases and oxygenases. *Chemical Reviews* 96, 2563-2605.
- Sposito, G., 1982. On the use of the Langmuir equation in the interpretation of “adsorption” phenomena. II. The “two-surface” Langmuir equation. *Soil Science Society of America Journal* 46, 1147-1152.
- Steinboefel, G., von Blanckenburg, F., Horn, I., Konhauser, K.O., Beukes, N.J., Gutzmer, J., 2010. Deciphering formation processes of banded iron formations from the Transvaal and the Hamersley successions by combined Si and Fe isotope analysis using UV femtosecond laser ablation. *Geochimica et Cosmochimica Acta* 74, 2677-2696.
- Stüeken, E.E., Buick, R., Guy, B.M., Koehler, C., 2015. Isotopic evidence for nitrogen fixation by molybdenum-nitrogenase from 3.2 Gyr. *Nature* 520, 666-669.
- Stylo, M., Neubert, N., Wang, Y., Monga, N., Romaniello, S.J., Weyer, S., Bernier-Latmani, R., 2015. Uranium isotopes fingerprint biotic reduction. *Proceedings of the National Academy of Sciences* 112, 5619–5624.
- Swanner, E.D., Planavsky, N.J., Lalonde, S.V., Robbins, L.J., Bekker, A., Rouxel, O.J., Saito, M.A., Kappler, A., Mojzsis, S.J., Konhauser, K.O., 2014. Cobalt and marine redox evolution. *Earth and Planetary Science Letters* 390, 253-263.

- Trendall, A.F., 2002. The significance of iron-formation in the Precambrian stratigraphic record. *Special Publications of the International Association of Sedimentologists* 33, 33-36.
- Trendall, A.F., Blockley, J.G., 1970. The iron formations of the Precambrian Hamersley Group, Western Australia with special reference to the associated crocidolite. *Geological Society of Western Australia Bulletin* 119, 1-366.
- Waldron, K.J., Tottey, S., Yanagisawa, S., Dennison, C., Robinson, N.J., 2007. A Periplasmic Iron-binding Protein Contributes toward Inward Copper Supply. *Journal of Biological Chemistry* 282, 3837-3846.
- Whitehouse, M.J., Fedo, C.M., 2007. Microscale heterogeneity of Fe isotopes in >3.71 Ga banded iron formation from the Isua Greenstone Belt, southwest Greenland. *Geology* 35, 719-722.
- Xu, Y., Shi, D., Aristilde, L., Morel, F., 2012. The effect of pH on the uptake of zinc and cadmium in marine phytoplankton: Possible role of weak complexes. *Limnology and Oceanography* 57, 293-304.
- Zegeye, A., Bonneville, S., Benning, L.G., Sturm, A., Fowle, D.A., Jones, C., Canfield, D.E., Ruby, C., MacLean, L.C., Nomosatryo, S., Crowe, S.A., Poulton, S.W., 2012. Green rust formation controls nutrient availability in a ferruginous water column. *Geology* 40, 599–602.
- Zerle, A.L., House, C.H., Brantley, S.L., 2005. Biogeochemical signatures through time as inferred from whole microbial genomes. *American Journal of Science* 305, 467-502.

Zhang, X., Sigman, D.M., Morel, F.M.M., Kraepiel, A.M.L., 2014. Nitrogen isotope fractionation by alternative nitrogenases and past ocean anoxia. *Proceedings of the National Academy of Sciences* 111, 4782-4787.

Zhang, S., Wang, X., Wang, H., Bjerrum, C.J., Hammarlund, E.U., Costa, M.M., Connelly, J.N., Zhang, B., Su, J., Canfield, D.E., 2016. Sufficient oxygen for animal respiration 1,400 million years ago. . *Proceedings of the National Academy of Sciences* 113, 1731–1736.

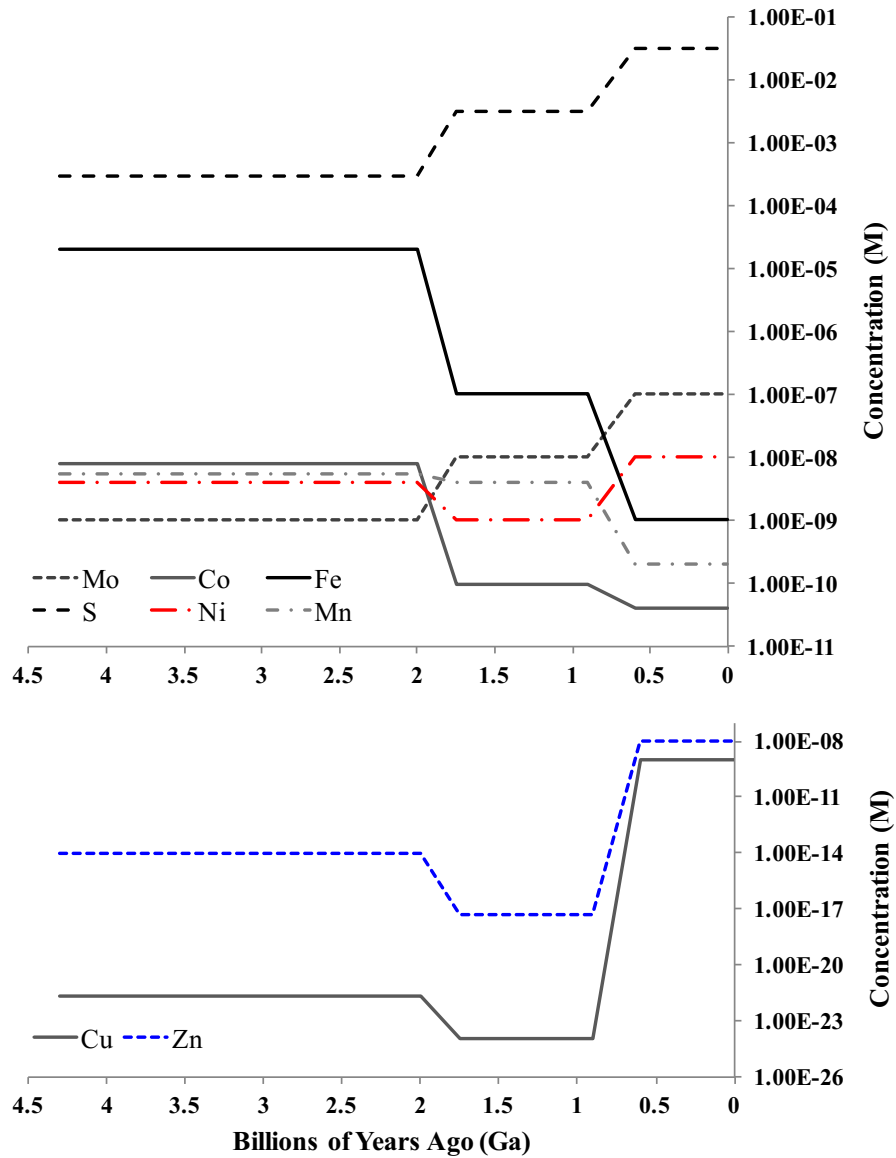


Figure 1.1. Approximate trace element concentrations through time based on previous geochemical modeling and genomic inferences. This traditional view of temporal trace element evolution is largely adapted from the work of Saito et al. (2003), except for molybdenum (Mo) which was based on the ocean box models of Anbar and Knoll (2002) and has been further discussed by Zerkle et al. (2005) and Anbar (2008). Highlighted are nickel (red) and zinc (blue) whose patterns in the rock record diverge greatly from these modeling and genomic suggestions and are discussed in detail below.

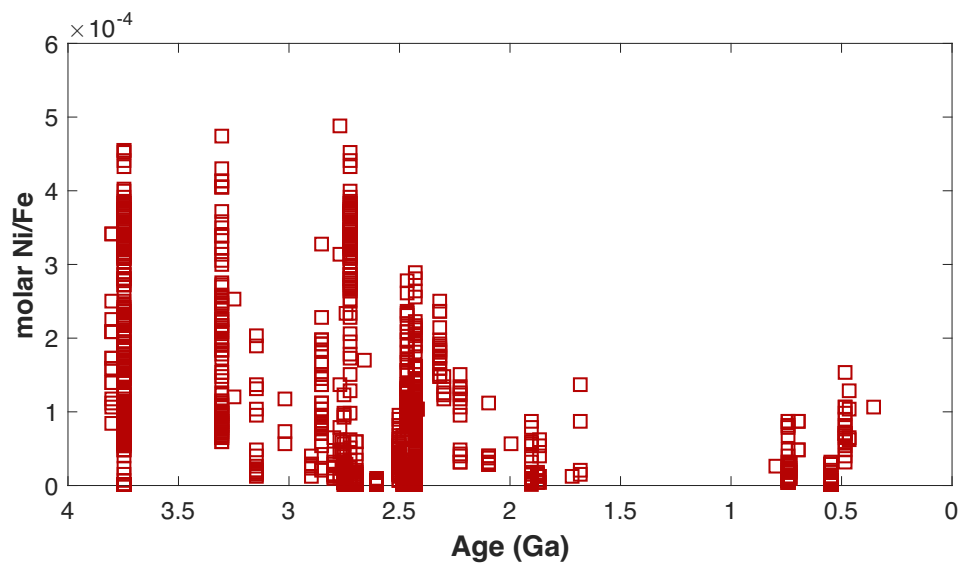


Figure 1.2. Molar Ni to Fe ratios in iron formation through time. This dataset has most recently been updated by Konhauser et al. (2015), who nearly doubled the points available since its initial presentation in Konhauser et al. (2009). A unidirectional decline in molar Ni/Fe is stark and robust. A similar trend is observed in the pyrite record as presented by Large et al. (2014); however, some variability in the Phanerozoic is observed in the pyrite record that is not present in the IF record.

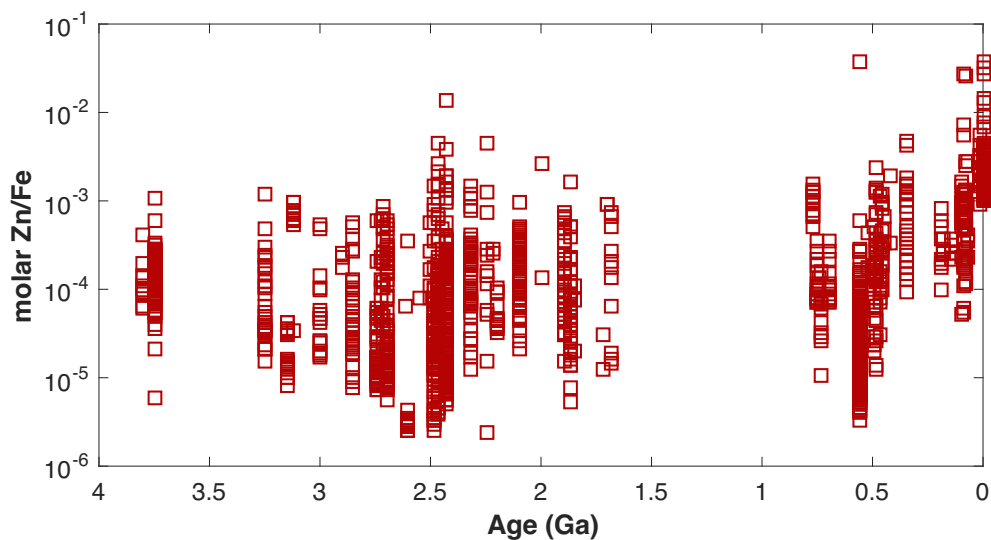


Figure 1.3. Concentrations of Zn in iron formation through time (reproduced from Robbins et al., 2013). This version includes all available IF data and is plotted without the removal of samples indicating detrital contamination (i.e., <1% Al₂O₃ or <0.1% TiO₂). Even when the all samples are included, Zn/Fe ratios in IF tend to fall in a field that spans 2–3 orders of magnitude and is relatively consistent through time. The only notable deviation from this long-term trend is the most modern samples, which may be reflective of local Zn enrichment in near-vent hydrothermal exhalative sediments. See Robbins et al. (2013) for further discussion.

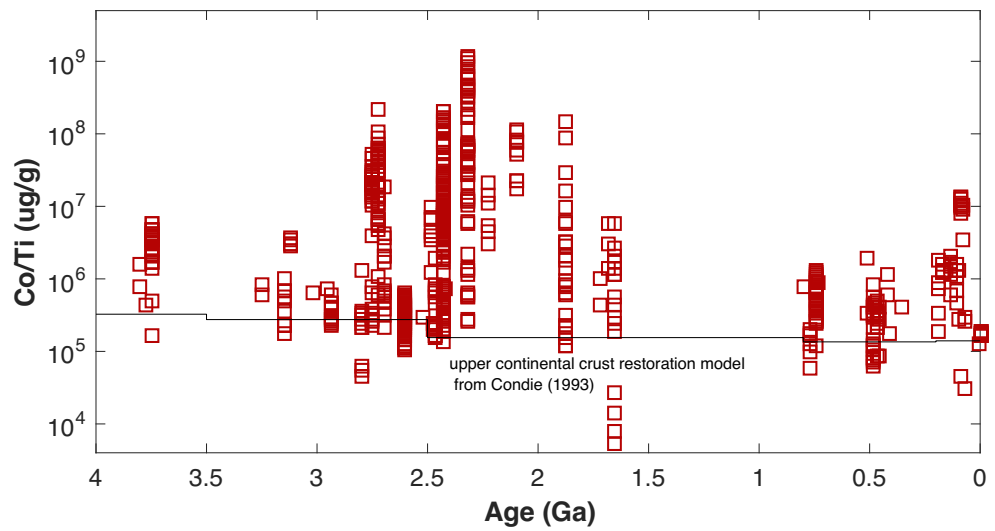


Figure 1.4. Molar cobalt to titanium ratios normalized to evolving continental crust through time. Normalization was performed using the upper continental crust restoration model of Condie (1993). The Co/Ti trend shows an expansion of authigenic Co enrichments in iron formations between ~2.8 and 1.8 Ga. Replotted from Swanner et al. (2014).

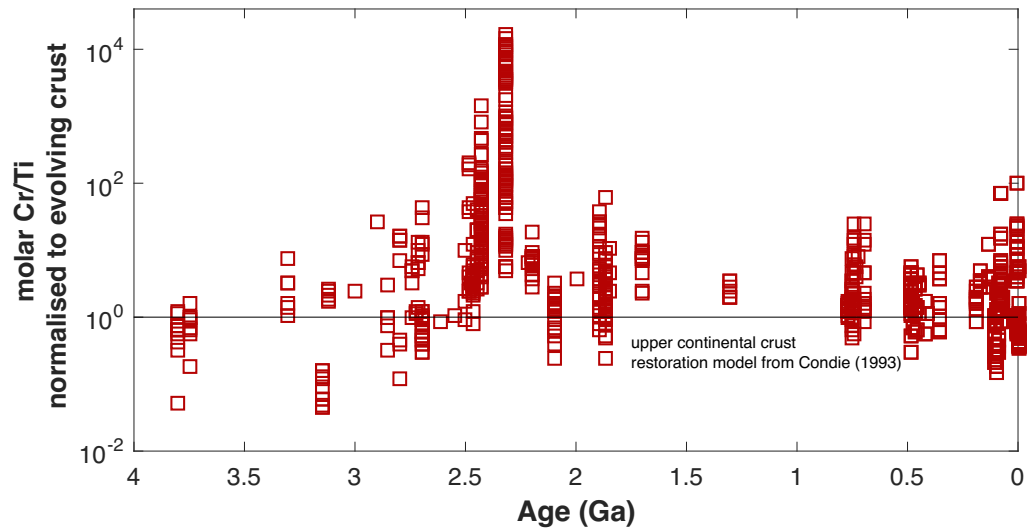


Figure 1.5. Authigenic Cr enrichments in the IF record. Here a peak in molar Cr/Ti ratios is observed at 2.4 Ga and has been interpreted to reflect acid mine drainage caused by massive oxidation of pyrite by aerobic bacteria on land around the time of the GOE. The data, normalized to the upper continental restoration model of Condie (1993), has been replotted from Konhauser et al. (2011).

Chapter 2. Hydrogeological constraints on the post-secondary oxidation of Paleoproterozoic iron formation¹

2.1 Introduction

Amongst the largest IF deposits are those of the Transvaal Supergroup in South Africa (Beukes and Gutzmer, 2008; Bekker et al., 2010, 2014) and the Hamersley Group in Western Australia (e.g., Trendall and Blockley, 1970; Klein, 2005; Bekker et al., 2010, 2014). The 2.48 Ga to 2.43 Ga Transvaal Supergroup in South Africa has an aerial extent of ~110,000 km², a maximum thickness of 950 m, and comprises the Kuruman and Griquatown iron formations, as well as the correlative Penge Iron Formation (e.g., Beukes and Gutzmer, 2008). The Transvaal Supergroup can be correlated with the contemporaneous Hamersley Group in Western Australia (Beukes and Gutzmer, 2008; Appendix Fig. A1.1), which has an aerial extent of over 100,000 km², a thickness of ~2.5 km (e.g., Morris, 1993), and comprises several IF, including the Marra Mamba, Brockman, Weeli Wolli, and Boolgeeda formations, that were deposited between ~2.6 and 2.45 Ga. Peak deposition in terms of tonnage for both the South African and Australian IFs (Isley, 1995; Bekker et al., 2014) closely precedes the onset of the Great Oxidation Event (GOE)

¹ A version of this chapter was submitted as: Robbins, L.J., Funk, S.P., Flynn, S.L., Warchola, T.J., Li, Z., Lalonde, S.V., Rostron, B.J., Smith, A.J.B., Beukes, N.J., Alessi, D.S., and Konhauser K.O., to *Nature Geoscience*.

at ~2.48-2.43 Ga (Konhauser et al., 2011; Gumsley et al., 2017), the time in Earth's history when oxygen first accumulated in the atmosphere (see Farquhar et al., 2011 for review).

The ferric iron in IF is generally considered to have formed by the biological oxidation of dissolved ferrous iron (Fe(II)) in seawater by either oxygen produced by cyanobacteria (e.g., Cloud, 1965) or via anoxygenic photoferrotrophy (Ehrenreich and Widdel, 1994; Konhauser et al., 2002). In either case, the primary minerals deposited would likely have been hydrous ferric oxyhydroxides (HFO), such as ferrihydrite ($\text{Fe}(\text{OH})_3$) (Posth et al., 2013, 2014). The deposition of ferric oxyhydroxides, and their subsequent dehydration to hematite (Fe_2O_3) or reduction to magnetite (Fe_3O_4) and siderite (FeCO_3), is supported by a number of lines of evidence within IF, including mineral textures and petrographic relationships, stable isotopes and rare earth elements (REE) patterns (see Konhauser et al., 2017 for review).

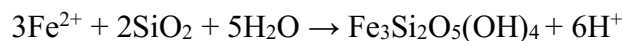
Recently, greenalite ($\text{Fe}_3\text{Si}_2\text{O}_5(\text{OH})_4$), a Fe(II) silicate mineral, has been interpreted in some Transvaal Supergroup and Hamersley Group iron formations as an authigenic water column precipitate that constituted the precursor iron mineral in IF (Fig. 2.1; Rasmussen et al., 2014, 2015, 2016, 2017; Rasmussen and Muhling, 2018; Johnson et al., 2018). If true, this would have significant implications for current models of IF deposition, and more broadly, Archean to Paleoproterozoic seawater chemistry. These implications extend to the trace element archive preserved in IF as it is based on the predictable nature of adsorption reactions occurring at the surface of the authigenic HFO minerals that would have originally precipitated from, and equilibrated with, contemporaneous seawater (e.g., Konhauser et al., 2007, 2009; Planavsky et al., 2010a). Crucially, it implies the lack of a Fe(II) oxidant in seawater at that time, and by extension, a marine photic zone biosphere.

Even for the early Archean, this concept would be difficult to accept given the abundance of carbon-rich sediments, and the difficulty in maintaining an euphotic biosphere based solely on utilization of H₂S or H₂ (see Lyons et al., 2014).

The presence of greenalite in BIF has been long acknowledged (James, 1954; Klein, 2005). James (1954) included greenalite primarily as a component of silicate facies IF and attributes a sedimentary or very early diagenetic origin to this low-grade silicate mineral. Furthermore, James (1954) described minor occurrences of greenalite in the oxide facies IF, characterized dominantly by the oxides, hematite and magnetite. Similarly, French (1973) recognized greenalite as a component of the diagenetic to low-grade metamorphic mineral assemblage of IF. Both James (1954) and French (1973) discuss the uncertainty behind the origin of greenalite, with French (1973) suggesting that it could be the result of precursor Fe-Si gels undergoing diagenesis and low-grade metamorphism rather than a strict water column precipitate. The prevailing paradigm governing IF deposition now attributes IF to the biologic oxidation of Fe²⁺ either through anoxygenic or oxygenic photoferrotrophy and subsequent diagenetic reactions (e.g., Konhauser et al., 2017). The recent description of greenalite nanoparticles, with dusty-hematite oxide coatings by Rasmussen et al. (2014, 2015), however, has led to the resurgence of the notion that greenalite may have played a critical role as a water column precipitate in the formation of

ancient IF, especially with regards to the Paleoproterozoic IFs of the Hamersley Basin and South Africa.

This assertion, that greenalite is an authigenic water column precipitate, would have significant implications for ancient seawater chemistry. The precipitation of greenalite as described in Tosca et al. (2016) can be represented by the equation:



This iteration of the precipitation reaction is a slight variation of that presented in Eugster and Chou (1973) and differs from that for greenalite as a marine clay phase as in Isson and Planavsky (2018). Regardless of the exact parametrization, it is clear that the precipitation of greenalite requires elevated Fe^{2+} as well as SiO_2 , and that a strong pH dependency exists. Given the elevated iron concentrations needed to generate IF (e.g., Morris 1993; Bekker et al., 2010; Konhauser et al., 2017), and silica concentrations that may have approached or reached amorphous silica saturation given the lack of silica secreting organisms prior to the Neoproterozoic (Siever, 1992; Maliva et al., 2005), it seems that authigenic greenalite may be an enticing precursor phase of IF. Indeed, Eugster and Chou (1973) indicate that at Fe^{2+} activities of $\sim 10^{-4}$ (>5ppm) and at low $p\text{CO}_2$ fugacities ($< 10^{-3.5}$) that greenalite should be more insoluble than siderite at circumneutral to mildly alkaline pH, overlapping the stability fields of both aqueous Fe^{2+} and $\text{Fe}(\text{OH})_3$. Despite this, Eugster and Chou (1973) concede that greenalite is unlikely to precipitate barring high levels of supersaturation. Recent solubility experiments by Tosca et al. (2016) reflect the need for this elevated level of supersaturation and demonstrated the relatively rapid precipitation of greenalite at amorphous silica saturation and 1 mM Fe^{2+} (~ 55.85 ppm), in a static pH titrated experiment. Based on those results, Tosca et al. (2016) suggested that

the presence of greenalite, as identified by Rasmussen et al. (2014), could suggest that ancient marine conditions may be characterized by Fe^{2+} concentrations approaching 1 mM or ~55.85 ppm (assuming no activity correction), and a pH of 7.7-8.3. This view, however, is at odds with existing estimates for Paleoproterozoic marine pH of closer to 7.2 (Grotzinger and Kasting, 1993; Blättler et al., 2017; Halevy and Bachan, 2017; Krissansen-Totton et al., 2018; Isson and Planavsky, 2018), as well as suggesting Fe^{2+} concentrations that would likely have been toxic to early cyanobacteria clades (Swanner et al., 2015) and above those suggested to be necessary for IF formation of ~3 ppm based on siderite-calcite equilibrium (Holland, 1984) and genetic modeling of IF formations for the Hamersley Basin (Morris, 1993).

Nonetheless, intrigued by the possibility that greenalite was the precursor IF phase (Fig. 2.1), and that a significant departure in our understanding about Archean-Paleoproterozoic ocean composition is now required, we modelled the feasibility of having secondary, oxygenated fluids oxidize Fe(II) at a basin-sized scale. To do so, we developed a simple hydrogeological box model to test whether the amount of time necessary to post-depositionally oxidize an IF the size of the Hamersley Basin is reasonable or whether IF deposition is more likely the result of HFO precipitation.

2.2 Methods

The proposed mechanism for the oxidation of greenalite in IF and corresponding formation of oxidized mineral phases invoked by Rasmussen et al. (2014) utilizes a hydrogeological model (McLellan et al. 2004) in which meteorically-derived, O_2 -bearing groundwater leads to the dissolution and re-precipitation of the silica layers and concurrent oxidation of the

Fe(II)-rich layers (Fig. 2.1C). In their proposed model, meteoric water infiltrated the Hamersley Basin IF through fractures to a depth of ~2 km at the southern basin margin, with subsequent flow moving laterally along Fe(II)-rich strata to over 10 km in extent. This fluid flow is suggested to have occurred between 2.45 and 2.2 Ga, coincident to the Ophthalmian orogeny (McLellan et al., 2004; Powell et al., 1999).

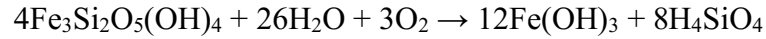
To test the plausibility of meteorically-derived groundwater oxidizing substantial amounts of greenalite in IF on the scale of the Hamersley Basin, we employed a hydrogeological box model to estimate the time necessary to oxidize an equivalent amount of Fe(II) by oxygenated groundwater (Fig. 2.2). Our model seeks to validate that of McLellan et al. (2004), and the ability to extend this model to a basin scale, by employing a series of simulations to test whether the time required to introduce sufficient quantities of dissolved oxygen to oxidize the Fe(II) in the system is reasonable. We employ a simple box model because the first-order groundwater and mass transport conditions approximated by such a model must be plausible in order to justify pursuing a more complex numerical analysis, such as a coupled solute-heat-groundwater flow model. As demonstrated below, a more detailed model was not necessary.

To determine whether a simulation was successful, the calculated time to introduce sufficient quantities of oxygen to oxidize all the Fe in the system had to be equal to, or less than, 250 million years, the length of the Ophthalmian orogeny considered a critical event for the post-depositional oxidation of these IF units (McLellan et al., 2004). Taking a broader view, 2.45 Ga was also used as a secondary cutoff for simulated oxidation times, as this corresponds to the minimum age of the IF and termination of IF sedimentation in the Hamersley Basin. Broadly, to calculate the time necessary to oxidize between 10 to

60% of the 10^{17} kg of iron in the Hamersley Basin, we first calculate the flux of water through the IF for a range of hydraulic gradients, and permeabilities as outlined in Table 2.1. We then calculate the time necessary to introduce a sufficient flux of oxygen necessary to oxidize the requisite amount of iron given a range of dissolved oxygen concentrations (Table 2.1). By varying these four parameters through their respective ranges 3,802,356 permutations are considered in our box model.

Based on the spatial distribution of the formation (McLellan et al. 2004; Powell et al., 1999), we simplified the geometry of the Hamersley Province to be a rectangular prism, with a width of 500 km, a length of 200 km, and total thickness of 2.5 km (Fig. 2.2A; Trendall and Blockley, 1970). Based on the stratigraphy of the Paleoproterozoic Hamersley Basin we conservatively estimated that the iron-rich layers may be represented by a thickness of ~350 m and simplified our box model accordingly (Fig. 2.2B). Assuming a constant density, this resulted in a total tonnage of iron of at least 1×10^{17} kg (Bekker et al., 2014). We assumed that the water flowed into the formation from the southern edge via the major faults within the formation (Fig. 2.2A). Under the idealized conditions for model success, the fault is assumed to be uniform, continuous, and fully penetrating along the southern edge of the formation that delivers a constant flow of water. Flow and transport is assumed to be horizontal and one-dimensional. Furthermore, we assumed the formation was homogeneous and isotropic, with impermeable boundaries on the top, bottom and two side faces (Fig. 2.2B). We assumed an instantaneous reaction whereby 1 mol of O_2 oxidizes 4 mol of Fe. While a number of possible reaction pathways for the oxidation of greenalite by groundwater may exist, we consider the pathway that would produce ferric oxyhydroxides, as this should be the simplest and most likely to occur during early

diagenesis. Critically, in this reaction, each mol of O₂ oxidizes 4 mols of Fe. Any reaction pathways that utilize O₂ less effectively than these, would therefore require a greater flux of O₂ in groundwater to oxidize an equivalent amount of greenalite.



The flow calculations were based on Darcy's Law, equation (1):

$$Q = KA \frac{dh}{dx} \quad (1)$$

where Q is the volumetric flow rate [L³/T], K is the hydraulic conductivity [L/T], A is the cross-sectional area [L²], and dh/dx is the hydraulic gradient [L/L]. The hydraulic gradient for this basin was unknown and thus varied in the simulations, but the lower limit was constrained based on typical topographic gradients found in geological basins, such as the Alberta basin (e.g. Adams et al. 2004) and was varied between 0.001 and 0.1 m/m (Table 2.1). The hydraulic conductivity of the formation was calculated from the permeability of the formation (McLellan et al. 2004) based on the following relationship:

$$K = k \frac{\rho g}{\mu} \quad (2)$$

where k is the permeability [L²], ρ is the density of water (assumed to be 1000 kg/m³), g is the acceleration due to gravity (assumed to be 9.81 m/s²), and μ is the viscosity of water (assumed to be 1 x 10⁻³ Pa s). Permeability was varied between 2x10⁻¹⁶ and 1x10⁻¹² m² (Table 2.1) which represents reasonable subset of the range examined by McLellan et al. (2004).

A key unknown parameter in our calculations was the concentration of dissolved oxygen in the water. Using Henry's Law as a guide, and correcting for the effect of

temperature (Sander, 1999) and the abundance of oxygen in the atmosphere at the time (Lyons et al., 2014), we determined that a realistic range of dissolved oxygen within the water could be between 8 mg/L (modern freshwater exposed to the atmosphere) and 0.00008 mg/L (concentrations in equilibrium with the atmosphere at the GOE) (Table 2.1). The concentration of dissolved oxygen introduced into the formation was assumed to be constant throughout the entire simulation.

Knowing the volumetric flow rate Q into the formation, the mass of Fe in the system, and assuming the concentration of dissolved oxygen, $C_{DO}[\text{M/L}^3]$, we can determine the mass flow rate of oxygen \dot{M} [M/T] by equation (3) and the time t [T] by equation (4) of the reaction by applying the following:

$$\dot{M} = QC_{DO} \quad (3)$$

$$t = \frac{m}{\dot{M}} \quad (4)$$

where m is the mass of oxygen required to oxidize the Fe in the system [M]. Knowing the mass of iron in the system (e.g., Bekker et al., 2014), we calculated the time [t] it required to oxidize that mass [m] using the calculated mass flow rate [\dot{M}] of oxygen. Conservatively, we assumed that only 10% to 60% of the total Fe in the formation needed to be oxidized. This resulted in a total tonnage of iron that ranged from 1×10^{16} to 6×10^{16} kg and represents a fraction of the total mass (1.0×10^{17} kg) of the iron formations within the Hamersley Basin (e.g., Bekker et al., 2014; Konhauser et al., 2017).

2.3 Results

Oxidation time calculations were carried out by varying: the (i) target percentage of iron oxidized, (ii) permeability of the formation, (iii) hydraulic gradient, and (iv) concentration of dissolved oxygen (Table 2.1). A total of 51 different tonnages of Fe, 36 different hydraulic conductivities, 19 different gradients, and 109 different dissolved O₂ concentrations were considered, resulting in a total of 3,802,356 permutations. A permutation was considered successful if the time necessary for the oxidation was less than 250 million years, the length of the Ophthalmian orogeny or taking a broader view, less than the age of the formation ~2.45 Ga. Out of the 3,802,356 simulations run, 40,251 returned oxidation times less than the length of the Ophthalmian orogeny and whose age distributions are provided in Fig. 2.3A, equating to only ~1.06% of the scenarios considered here. Of all model runs only 8.87% returned ages less than the age of the IF themselves, 2.45 Ga.

Of the calculations run, the fastest simulation required only 34.7 million years to oxidize the Fe(II) to Fe(III). However, this specific model run was characterized by the highest permeability, greatest dissolved oxygen concentration, largest topographic gradient, and it required the oxidation of the least iron, only ~10% of the total Fe within the Hamersley Basin. This inherently makes this model run the most favorable, and a fast oxidation time was therefore expected. The ~1.06% of runs that were successful, returning oxidation times less than 250 Ma, share several informative commonalities. All required (i) dissolved O₂ concentrations in excess of 1.2 mg/L (compared to fully oxygenated freshwater which has 8 mg/L O₂), and (ii) permeability greater than 2×10^{-13} m² (compared to approximately 2×10^{-12} m² for sandstone) (Fig. 2.3B), (iii) and a hydraulic gradient

(topographic slope) greater than 0.02 meters/meters. Each of these parameters alone are near the upper end of their ranges (Fig. 2.3B), and the possibility of them co-existing over a 200 km basin scale is remote. Similarly, simulations requiring less than 2.45 Ga to oxidize the iron require high permeability and dissolved O₂ contents (Fig. 2.3B). Based on the results, we argue that the hypothesis that dissolved O₂ introduced into the formation via groundwater flow acting on a basin-scale is highly implausible, requiring fluxes, dissolved O₂ concentrations, and permeability conditions that are unrealistically high. Furthermore, the inclusion of heterogeneities and/or anisotropy within the formation, and/or cross-formational leakage of water into other geological units, would greatly increase the time required to oxidize the formation.

Using the same model and more realistic parameters for a large sedimentary basin, namely: regional permeability = $2 \times 10^{-16} \text{ m}^2$, hydraulic gradient = 0.003, dissolved oxygen = 0.1 mg/L, and for a formation with a total iron tonnage of $\sim 1 \times 10^{17} \text{ kg}$ (Bekker et al., 2014 and references therein), we ran a single simulation for 250 million years to estimate how much Fe(II) could be oxidized and what the oxidized horizontal penetration depth would have to be (Appendix Fig. A1.2). The chosen permeability and hydraulic gradient values are consistent with basin-scale observations from the well characterized Alberta sedimentary basin which is of comparable size (e.g. Adams et al. 2004). This simulation demonstrated that within the allotted 250 million years, $\sim 5.6 \times 10^9 \text{ kg}$ of Fe(II) could be oxidized, equivalent to only a very small fraction (0.0056%) of the total mass of iron formation within the Hamersley Basin. This resulted in a uniform “penetration depth” of 1.08 cm from the fault, along the 500 km southern edge of the basin. While it is known that areas of the basin have been affected by supergene alteration (e.g., Powell et al., 1999;

Taylor et al., 2001), it is likely that these areas represent a unique set of conditions that do not likely apply to a basin spanning 100,000 km².

2.4 Discussion

Although the hydrogeological model of McLellan et al. (2004) might explain the supergene alteration of IF to Fe ore bodies in some small, highly localized areas of the basin (Morris, 1985; Taylor et al., 2001), it is simply not feasible to extrapolate to the entirety of the depositional basin (as implied by Rasmussen et al., 2014) because the extent of alteration evoked in this model is significantly smaller than the areal extent of the Hamersley Basin (nearly 100,000 km²). Moreover, the characteristic products of alteration: microplaty hematite and martite (hematite pseudomorphs that replace magnetite) are far less abundant in IF than in high-grade iron ores (e.g., Haugaard et al., 2016). It is also difficult to envision the origins of a strongly oxygenated groundwater source in the Paleoproterozoic given low levels of atmospheric pO_2 (<0.00001 to <0.1 PAL) during the onset of the GOE (see Lyons et al., 2014). The likelihood for penetration of oxygenated groundwater into fractures, and the translation of these fluids to depth is also unclear. In modern shelf systems, oxygen only penetrates to a depth of a few centimeters in the sediments (Canfield et al., 1993), and both modern marginal marine and groundwater tend to fall towards the reducing field on an Eh-pH discrimination plot (Becking and Kaplan, 1960).

Aside from the hydrogeologic considerations presented here, several conceptual arguments discount the greenalite hypothesis. First, following deposition, sediments would have had to have been decoupled from the photic zone, and any oxygenated surface waters, by the dominantly anoxic water column. A general lack of Ce/Ce* anomalies in IF prior to

1.9 Ga (Planavsky et al., 2010b) indicates that seawater remained dominantly anoxic during the Paleoproterozoic, even following the GOE. In areas of supergene alteration and ore formation, Ce anomalies may develop as the result of alteration within the ore bodies even if the precursor IF lacked true negative Ce anomalies (Smith and Beukes, 2016). Further, if O₂ had reached measurable concentrations at the seafloor, it would almost certainly have been consumed by the heterotrophic respiration of organic matter (settling biomass) - similar to today - and thus it could not have penetrated the sediment pile and led to post-depositional Fe(II)-oxidation.

Second, the Turee Creek Group (2.45-2.22 Ga) was deposited immediately over the Hamersley Group in a conformable succession that records the deposition of ~3.9 km of marine sediments and glacial deposits (Trendall and Blockley, 1970; Trendall, 1979; Van Kranendonk and Mazumder, 2015; Van Kranendonk et al., 2015). Sedimentation of this package would not only have prevented subaerial exposure and the infiltration of meteorically-derived fluids, but the mass of sediment would have contributed to the compaction of the IF sediments hosted in the underlying Hamersley Group. Given the high permeability ($1 \times 10^{-12} \text{ m}^2$) required for the models to return oxidation times <250 Ma (Table 2.1, Fig. 2.3), that are characteristic of unconsolidated fine-grained sands or silt (Freeze and Cherry, 1979; Deming, 2002), the deposition of the Turee Creek Group represents a significant obstacle to maintaining the physical conditions necessary for post-depositional flow of oxygenated groundwater through the sediment pile. Additionally, correlations of the Hamersley Group IF to those of the Transvaal Group IF indicate that these deposits may have originally been deposited within adjacent sub-basins (Beukes and Gutzmer, 2008; see SI discussion). Therefore, given the stratigraphic correlations between these

Paleoproterozoic deposits, any post-depositional alteration would have had to affect both sub-basins in a similar manner over an even larger areal extent than considered in our model.

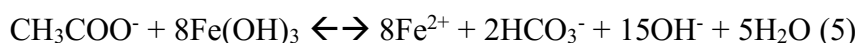
Third, Superior type IF like those of the Hamersley and Transvaal basins have characteristic mm-scale microbands and cm-scale mesobands (Klein, 2005; Bekker et al., 2014; Konhauser et al., 2017). McLennan et al. (2004) proposed that infiltration of the heated, meteoric fluid would have obliterated those layers, increasing the permeability of the IF units and thus facilitating oxidation as well as the emplacement of microplaty hematite. Although a process such as this may be responsible for upgrading initial IF sediments to ore-bodies with much higher levels of iron (Taylor et al., 2001), it is unlikely to apply to formations where mm- and cm-scale Fe- and silica-rich bands are preserved, such as in the Hamersley Group (e.g., Pecoits et al., 2009; Hauggard et al., 2016).

Fourth, the preservation of seawater-like REE+Y patterns suggest that any fluid alteration occurred at lower water to rock ratios (c.f. Bau, 1993), thereby requiring either higher oxygen contents or longer time scales for the post-depositional oxidation of Fe(II) minerals, both of which argue against the rapid post-depositional oxidation of a greenalite precursor phase. In ore bodies, supergene alteration leads to heavy REE depletion, a geochemical characteristic not typical of oxide, carbonate, or silicate facies IF precursors (Smith and Beukes, 2016). Other geochemical indicators such as Fe-isotope heterogeneities would also weigh against the large-scale obliteration of primary mineralogy and suggests at least partial oxidation of Fe(II) in surface waters (Johnson et al., 2008; Steinhofel et al., 2010; Planavsky et al., 2012). Indeed, iron isotope systematics require that at least some of the Fe sedimented during IF deposition was oxidized, and

initially deposited as, at minimum, a mixed-valence phase. Similarly, silicon isotopes suggest that the primary Fe-bearing precipitate was not a Fe(II) phase, but rather a Fe(III)-Si gel (Zheng et al., 2016).

Collectively, the depositional and geochemical considerations presented above point toward a dominantly Fe(III) mineral phase, consistent with ferrihydrite as identified in the thermodynamic models, and a limited role for Fe(II) or mixed valence mineral phases. We suggest an alternative paragenetic sequence for greenalite that simultaneously explains its early origin but decouples its formation from the water column.

The precipitation of primary greenalite requires three key factors: high Fe, high Si, and a mildly alkaline pH. These factors can all be satisfied during early diagenesis within a HFO sediment pile or in amorphous silica deposits that may be precursors to ferruginous cherts. Here, we envision the delivery of Fe(III) and silica to the sediments via the water column Fe-Si shuttle (Fischer and Knoll, 2009). Under such a scenario, a HFO particle with silica adsorbed to the surface sinks to the seafloor and is subjected to DIR within the sediment. This model would produce not only pore-water Fe(II) and Si via DIR, but alkalinity as well, via the reaction:



The bicarbonate generated could be available to form siderite or other carbonates or be effluxed back to the water column. In this manner, DIR could drive greenalite's relatively early production during sediment diagenesis, and if this mechanism was fabric retentive, may explain some of the early formed greenalite described by Rasmussen et al. (2014, 2015, 2016, 2017). Alternatively, a benthic Fe-shuttle (e.g., Severman et al., 2008; Li et al., 2015) may also explain the origins of greenalite, where Fe(II) is liberated from HFO

deposited on the shelf through DIR or reductive dissolution and transported either with groundwater or in the water column to localized environments where greenalite is able to precipitate. Accordingly, we suggest that the presence of greenalite with early formed textures in deeper water IF is an indication of an active Fe-Si shuttle coupled to DIR and formation during the earliest stages of sediment diagenesis-

A second possible origin for greenalite is indicated by the greenalite-rich and chert-poor lithofacies in the shallow-water sections of the Transvaal Supergroup (see SI for discussion). A shallow water origin for greenalite is indicated by increased textural evidence for wave reworking observed in the Westerberg Member (Beukes, 1984), and interbedding with granular iron formation. Evaporation may have led to the supersaturation of Fe(II) in restricted settings, where Si concentrations had been depressed due to chert precipitation in deeper water, thus creating conditions favorable for greenalite precipitation. The greenalite could then be transported into IF depositional basins by currents, thereby decoupling the environment of formation from those that formed the archetypal Hamersley Basin IFs. Critically, whether deposited in more restricted environments prone to evaporation, or in deeper waters via an active Fe-shuttle, it is likely that greenalite is not a precursor mineral phase to archetypal IF.

An emerging possibility is that the generation of greenalite is the result of authigenic clay formation in porewaters that would have buffered marine pH against elevated $p\text{CO}_2$ conditions in the Archean to Paleoproterozoic (Isson and Planavsky, 2018). In this scenario the formation of clay minerals, such as greenalite, consumes bicarbonate, and releases CO_2 to the water column and ultimately to the atmosphere. This simultaneously maintains an ancient ocean with a pH of ~ 7.2 and elevated atmospheric

$p\text{CO}_2$. Critically, under this view the formation of greenalite is decoupled from the precipitation of IF and forms as a diagenetic phase rather than a primary water column precipitate. This means that it cannot be used to directly infer bulk seawater composition as in Tosca et al. (2016).

2.5 Conclusions

Our hydrogeological box model indicates that the primary minerals involved in Paleoproterozoic BIF deposition were necessarily ferric oxyhydroxides, such as ferrihydrite. The large-scale deposition of primarily Fe(II) mineral phases, and their subsequent oxidation by groundwater to the Fe(III) minerals characteristic of IF today, is highly improbable, as the time required to oxidize aerially extensive IF post-depositionally is unreasonable, unless unrealistic parameters are invoked in the box model calculation. Such constraints include, implausibly high dissolved O_2 concentrations, excessive hydraulic gradients for a sedimentary basin, and permeability approaching that characteristics of sandstone. By contrast, the interpretation of a primary ferric oxyhydroxide precursor is consistent with the generally-accepted involvement of either cyanobacteria or anoxygenic photoferrotrophy as a driving mechanism behind IF deposition, as well as the trace element and isotope geochemistry of IF. While the localised precipitation of greenalite cannot be expressly ruled out, results here suggest that the greenalite identified by Rasmussen et al. (2014, 2016, 2017) is more consistent with being an early diagenetic phase, rather than a primary depositional component that necessitates a significant departure from our current understanding of Archean-Paleoproterozoic seawater chemistry.

2.6 References

- Adams, J.J., Rostron, B.J., Mendoza, C.A., 2004. Coupled fluid flow, heat and mass transport, and erosion in the Alberta basin: implications for the origin of the Athabasca oil sands. *Canadian Journal of Earth Sciences* 41, 1077–1095.
- Bau, M., 1993. Effects of syn-and post-depositional processes on the rare-earth element distribution in Precambrian iron-formations. *European Journal of Mineralogy* 5, 257–267.
- Becking, L., Kaplan, I.R., 1960. Limits of the natural environment in terms of pH and oxidation-reduction potentials. *The Journal Of Geology* 68, 243–284.
- Bekker, A., Planavsky, N.J., Krapež, B., Rasmussen, B., Hofmann, A., Slack, J.F., Rouxel, O.J., Konhauser, K.O., 2014. Iron Formations: Their Origins and Implications for Ancient Seawater Chemistry in Holland, H.K., Turekian, K., (eds.) *Treatise on Geochemistry*, 2nd edition, 561-628.
- Bekker, A., Slack, J.F., Planavsky, N., Krapez, B., Hofmann, A., Konhauser, K.O., Rouxel, O.J., 2010. Iron Formation: The Sedimentary Product of a Complex Interplay among Mantle, Tectonic, Oceanic, and Biospheric Processes. *Economic Geology* 105, 467–508.
- Beukes, N.J., Gutzmer, J., 2008. Origin and paleoenvironmental significance of major iron formations at the Archean-Paleoproterozoic boundary. *Society of Economic Geologists Reviews* 15, 5–47.

- Beukes, N., 1984. Sedimentology of the Kuruman and Griquatown iron-formations, Transvaal supergroup, Griqualand West, South Africa. *Precambrian Research* 24, 47–84.
- Blättler, C.L., Kump, L.R., Fischer, W.W., Paris, G., Kasbohm, J.J., Higgins, J.A., 2017. Constraints on ocean carbonate chemistry and pCO₂ in the Archaean and Palaeoproterozoic. *Nature Geoscience* 10, 41–45.
- Canfield, D.E., Jorgensen, B.B., Fossing, H., Glud, R., Gundersen, J., Ramsing, N.B., Thamdrup, B., Hansen, J.W., Nielsen, L.P., Hall, P.O.J., 1993. Pathways of organic carbon oxidation in three continental margin sediments. *Precambrian Res.* 113, 27–40.
- Cloud, P.E., 1965. Significance of the Gunflint (Precambrian) Microflora. *Science* 148, 27–35.
- Deming D (2002) *Introduction to Hydrogeology*. New York, NY, McGraw-Hill, p. 56.
- Ehrenreich, A., Widdel, F., 1994. Anaerobic oxidation of ferrous iron by purple bacteria, a new type of phototrophic metabolism. *Applied and Environmental Microbiology* 60, 4517–4526.
- Eugster, H.P., Chou, I.M., 1973. The depositional environments of Precambrian banded iron-formations. *Economic Geology* 68, 1144–1168.
- Farquhar, J., Zerkle, A.L., Bekker, A., 2011. Geological constraints on the origin of oxygenic photosynthesis. *Photosynth Res* 107, 11–36.
- Fischer, W., Knoll, A.H., 2009. An iron shuttle for deepwater silica in Late Archean and early Paleoproterozoic iron formation. *Geological Society of America Bulletin* 121, 222–235.

- Freeze RA, Cherry JA (1979) *Groundwater*. Englewood Cliffs, NJ, Prentice-Hall, p. 29.
- French, B.M., 1973. Mineral Assemblages in Diagenetic and Low-Grade Metamorphic Iron-Formation. *Economic Geology* 68, 1063–1074.
- Grotzinger, J.P., Kasting, J.F., 1993. New constraints on Precambrian ocean composition. *The Journal Of Geology* 101, 235–243.
- Gumsley, A.P., Chamberlain, K.R., Bleeker, W., Söderlund, U., de Kock, M.O., Larsson, E.R., Bekker, A., 2017. Timing and tempo of the Great Oxidation Event. *Proc. Natl. Acad. Sci.* 114, 1811–1816.
- Halevy, I., Bachan, A., 2017. The geologic history of seawater pH. *Science* 355, 1069–1071.
- Haugaard, R., Pecoits, E., Lalonde, S.V., Rouxel, O.J., Konhauser, K.O., 2016. The Joffre banded iron formation, Hamersley Group, Western Australia: Assessing the palaeoenvironment through detailed petrology and chemostratigraphy. *Precambrian Research* 273, 12–37.
- Isley, A., 1995. Hydrothermal plumes and the delivery of iron to banded iron formation. *The Journal Of Geology* 169–185.
- Isson, T.T., Planavsky, N.J., 2018. Reverse weathering as a long-term stabilizer of marine pH and planetary climate. *Nature* 560, 471–475.
- Johnson, C.M., Beard, B.L., Klein, C., Beukes, N.J., Roden, E.E., 2008. Iron isotopes constrain biologic and abiologic processes in banded iron formation genesis. *Geochimica et Cosmochimica Acta* 72, 151–169.

- Johnson, J.E., Muhling, J.R., Cosmidis, J., Rasmussen, B., Templeton, A.S., 2018. Low-Fe(III) Greenalite Was a Primary Mineral from Neoproterozoic Oceans. *Geophysical Research Letters* 45, 3182-3192.
- Klein, C., 2005. Some Precambrian banded iron-formations (BIFs) from around the world: Their age, geologic setting, mineralogy, metamorphism, geochemistry, and origins. *American Mineralogist* 90, 1473–1499.
- Konhauser, K.O., Hamade, T., Raiswell, R., Morris, R., Ferris, F., Southam, G., Canfield, D., 2002. Could bacteria have formed the Precambrian banded iron formations? *Geology* 30, 1079–1082.
- Konhauser, K.O., Lalonde, S.V., Amskold, L.A., Holland, H., 2007. Was there really an Archean phosphate crisis? *Science* 315, 1234.
- Konhauser, K.O., Pecoits, E., Lalonde, S.V., Papineau, D., Nisbet, E.G., Barley, M.E., Arndt, N.T., Zahnle, K., Kamber, B.S., 2009. Oceanic nickel depletion and a methanogen famine before the Great Oxidation Event. *Nature* 458, 750–753.
- Konhauser, K.O., Lalonde, S.V., Planavsky, N.J., Pecoits, E., Lyons, T.W., Mojzsis, S.J., Rouxel, O.J., Barley, M.E., Rosière, C.A., Fralick, P.W., Kump, L.R., Bekker, A., 2011. Aerobic bacterial pyrite oxidation and acid rock drainage during the Great Oxidation Event. *Nature* 478, 369–373
- Konhauser, K.O., Planavsky, N.J., Hardisty, D.S., Robbins, L.J., Warchola, T.J., Haugaard, R., Lalonde, S.V., Partin, C.A., Oonk, P.B.H., Tsikos, H., Lyons, T.W., Bekker, A., Johnson, C.M., 2017. Iron formations: A global record of Neoproterozoic to Palaeoproterozoic environmental history. *Earth-Science Reviews* 172, 140–177.

- Krissansen-Totton, J., Arney, G.N., Catling, D.C., 2018. Constraining the climate and ocean pH of the early Earth with a geological carbon cycle model. *Proceedings of the National Academy of Sciences* 115, 4105–4110.
- Li, W., Beard, B.L., Johnson, C.M., 2015. Biologically recycled continental iron is a major component in banded iron formations. *Proceedings of the National Academy of Sciences* 112, 8193–8198.
- Lyons, T.W., Reinhard, C.T., Planavsky, N.J., 2014. The rise of oxygen in Earth's early ocean and atmosphere. *Nature* 506, 307–315.
- Maliva, R.G., Knoll, A.H., Simonson, B.M., 2005. Secular change in the Precambrian silica cycle: Insights from chert petrology. *Geological Society of America Bulletin* 117, 835–845.
- McLellan, J.G., Oliver, N.H.S., Schaub, P.M., 2004. Fluid flow in extensional environments; numerical modelling with an application to Hamersley iron ores. *Journal of Structural Geology* 26, 1157–1171.
- Morris, R.C., 1985. Genesis of iron ore in banded iron-formation by supergene and supergene-metamorphic processes – A conceptual model, *Regional Studies and Specific Deposits*. Elsevier. p. 73–235.
- Morris, R.C., 1993. Genetic modelling for banded iron-formation of the Hamersley Group, Pilbara Craton, Western Australia. *Precambrian Research* 60, 243–286.
- Pecoits, E., Gingras, M.K., Barley, M.E., Kappler, A., Posth, N.R., Konhauser, K.O., 2009. Petrography and geochemistry of the Dales Gorge banded iron formation: Paragenetic sequence, source and implications for palaeo-ocean chemistry. *Precambrian Research* 172, 163–187.

- Planavsky, N.J., Rouxel, O.J., Bekker, A., Lalonde, S.V., Konhauser, K.O., Reinhard, C.T., Lyons, T.W., 2010a. The evolution of the marine phosphate reservoir. *Nature* 467, 1088–1090.
- Planavsky, N., Bekker, A., Rouxel, O.J., Kamber, B., Hofmann, A., Knudsen, A., Lyons, T.W., 2010b. Rare Earth Element and yttrium compositions of Archean and Paleoproterozoic Fe formations revisited: New perspectives on the significance and mechanisms of deposition. *Geochimica et Cosmochimica Acta* 74, 6387–6405.
- Planavsky, N., Rouxel, O.J., Bekker, A., Hofmann, A., Little, C.T.S., Lyons, T.W., 2012. Iron isotope composition of some Archean and Proterozoic iron formations. *Geochimica et Cosmochimica Acta* 80, 158–169.
- Posth, N.R., Konhauser, K.O., Kappler, A., 2013. Microbiological processes in banded iron formation deposition. *Sedimentology* 60, 1733–1754.
- Posth, N.R., Canfield, D.E., Kappler, A., 2014. Biogenic Fe(III) minerals: From formation to diagenesis and preservation in the rock record. *Earth-Science Reviews* 135, 103–121.
- Powell, C.M., Oliver, N.H.S., Li, Z.-X., Martin, D.M., Ronaszeki, J., 1999. Synorogenic hydrothermal origin for giant Hamersley iron oxide ore bodies. *Geology* 27, 175–178.
- Rasmussen, B., Krapez, B., Meier, D.B., 2014. Replacement origin for hematite in 2.5 Ga banded iron formation: Evidence for postdepositional oxidation of iron-bearing minerals. *Geological Society of America Bulletin* 126, 438–446.

- Rasmussen, B., Krapež, B., Muhling, J.R., Suvorova, A., 2015. Precipitation of iron silicate nanoparticles in early Precambrian oceans marks Earth's first iron age. *Geology* 43, 303–306.
- Rasmussen, B., Muhling, J.R., Suvorova, A., Krapez, B., 2016. Dust to dust: Evidence for the formation of “primary” hematite dust in banded iron formations via oxidation of iron silicate nanoparticles. *Precambrian Research* 284, 49–63.
- Rasmussen, B., Muhling, J.R., Suvorova, A., Krapez, B., 2017. Greenalite precipitation linked to the deposition of banded iron formations downslope from a late Archean carbonate platform. *Precambrian Research* 290, 49–62.
- Rasmussen, B., Muhling, J.R., 2018. Making magnetite late again: Evidence for widespread magnetite growth by thermal decomposition of siderite in Hamersley banded iron formations. *Precambrian Research* 306, 64–93.
- Sander, R., 1999. Compilation of Henry's law constants for inorganic and organic species of potential importance in environmental chemistry.
- Severmann, S., Lyons, T., Anbar, A.D., McManus, J., Gordon, G., 2008. Modern iron isotope perspective on the benthic iron shuttle and the redox evolution of ancient oceans. *Geology* 36, 487–490.
- Siever, R., 1992. The silica cycle in the Precambrian. *Geochimica et Cosmochimica Acta* 56, 3265–3272.
- Smith, A.J.B., Beukes, N.J., 2016. Paleoproterozoic banded iron formation-hosted high grade hematite iron ore deposits of Transvaal Supergroup, South Africa. *Episodes* 39, 269–16.

- Steinboefel, G., Blanckenburg, F.V., Horn, I., Konhauser, K.O., Beukes, N.J., Gutzmer, J., 2010. Deciphering formation processes of banded iron formations from the Transvaal and the Hamersley successions by combined Si and Fe isotope analysis using UV femtosecond laser ablation. *Geochimica et Cosmochimica Acta* 74, 2677–2696.
- Swanner, E.D., Mloszewska, A.M., Cirpka, O.A., Schoenberg, R., Konhauser, K.O., Kappler, A., 2015. Modulation of oxygen production in Archaean oceans by episodes of Fe (II) toxicity. *Nature Geoscience* 8, 126–130.
- Taylor, D., Dalstra, H., Harding, A., Broadbent, G., Barley, M.E., 2001. Genesis of high-grade hematite orebodies of the Hamersley Province, Western Australia. *Economic Geology* 96, 837–873.
- Trendall A.F., 1979. A revision of the Mount Bruce Supergroup. *Geological Survey of Western Australia Annual Report for 1978*, 63-71.
- Trendall, A.F., Blockley, J.G., 1970. The Iron Formations of The Precambrian Hamersley Group Western Australia With Special Reference to the Associated Crocidolite. *Geological Survey of Western Australia Bulletin* 119, 1–366.
- Van Kranendonk, M.J., Mazumder, R., Precambrian, K.Y., 2015, 2015. Sedimentology of the Paleoproterozoic Kungarra Formation, Turee Creek Group, Western Australia: A conformable record of the transition from early to modern Earth. *Precambrian Res.* 256, 314–343.
- Van Kranendonk, M.J., Mazumder, R., 2015. Two Paleoproterozoic glacio-eustatic cycles in the Turee Creek Group, Western Australia. *Geological Society of America Bulletin* 127, 596–607.

Zheng, X.-Y., Beard, B.L., Reddy, T.R., Roden, E.E., Johnson, C.M., 2016. Abiologic silicon isotope fractionation between aqueous Si and Fe(III)-Si gel in simulated Archean seawater: Implications for Si isotope records in Precambrian sedimentary rocks. *Geochimica et Cosmochimica Acta* 187, 102–122.

Table 2.1: Upper and lower limits for the parameters that varied in the hydrogeology box model simulations; the ranges selected encompass a wide set of possible conditions.

§ from McLellan et al. (2004)

‡ assumed

Parameter	Lower Limit	Upper Limit	Number of steps
Percentage of iron mass (10 ¹⁷ kg) oxidized (%)	10	60	51
Permeability (m ²) §	2 × 10 ⁻¹⁶	1 × 10 ⁻¹²	36
Hydraulic gradient (m/m) ‡	0.001	0.1	19
Dissolved oxygen (mg/L)	0.00008	8	109

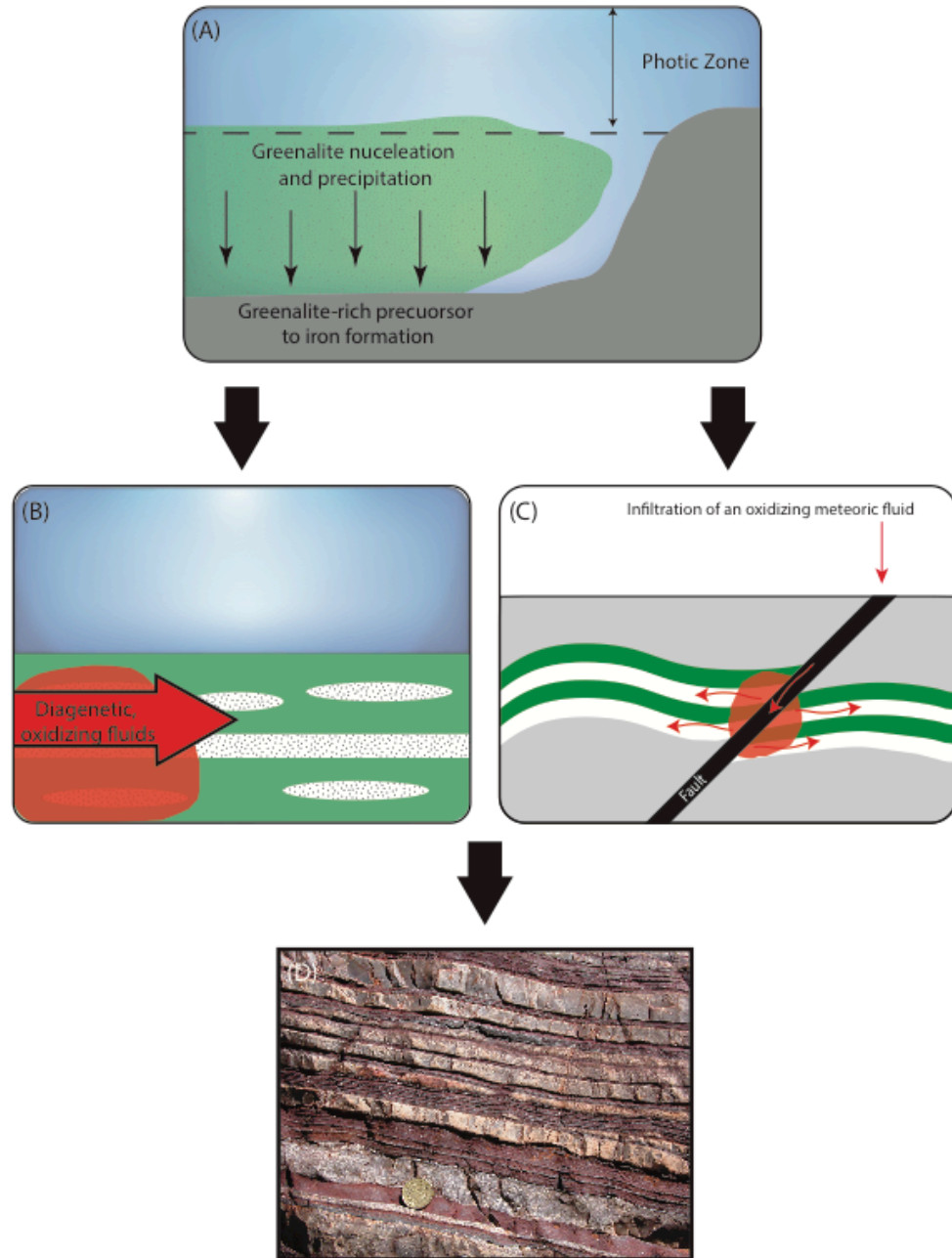
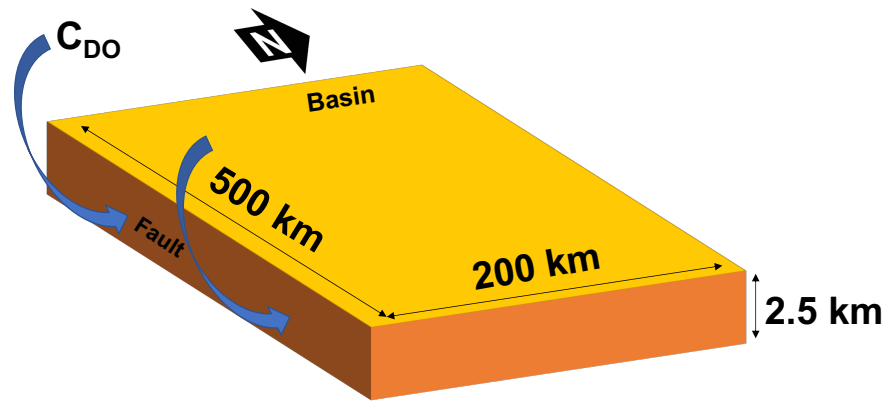


Figure 2.1. Conceptual model for the post-depositional oxidation of greenalite by oxidative groundwater. **(A)** The initial deposition of a greenalite precursor phase to iron formation following Rasmussen et al. (2017) and Johnson et al. (2018), simplified views of post-depositional oxidation pathways including, **(B)** early diagenetic fluids or **(C)** the infiltration of a meteoric oxidizing fluid along the fault and flow parallel to iron-rich layers that

requires the dissolution of chert layers (after McLellan et al., 2004). **(D)** An example of the banding preserved in the Joffre Member of the Brockman Iron Formation, Western Australia. Any post-depositional oxidation must be capable of explaining the preservation of the distinct banding characteristic of banded iron formations.

(A)



(B)

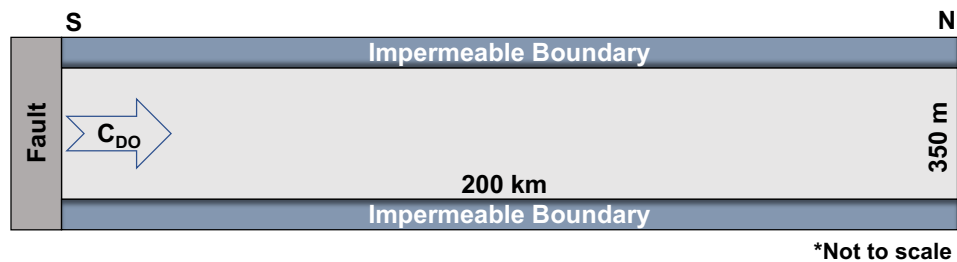
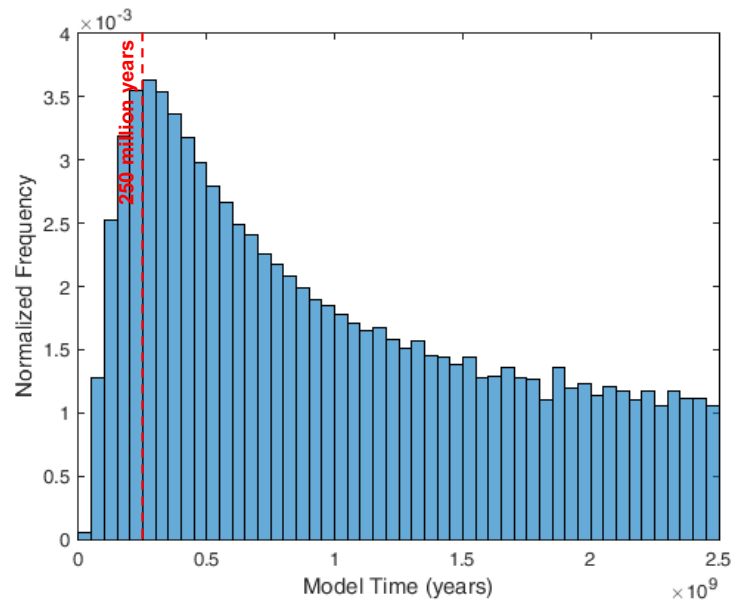


Figure 2.2. (A) Simplified model for the geometry of the Hamersley Basin iron formations. Dimensions and water infiltration along the major axis, mimic the generalized fault distribution and simplified view of the Hamersley Province (Powell et al., 1999; McLellan et al., 2004). (B) Boundary conditions for the hydrogeological box model, that assumes a homogenous, isotropic media with impermeable boundaries on top, bottom, and two lateral faces.

(A)



(B)

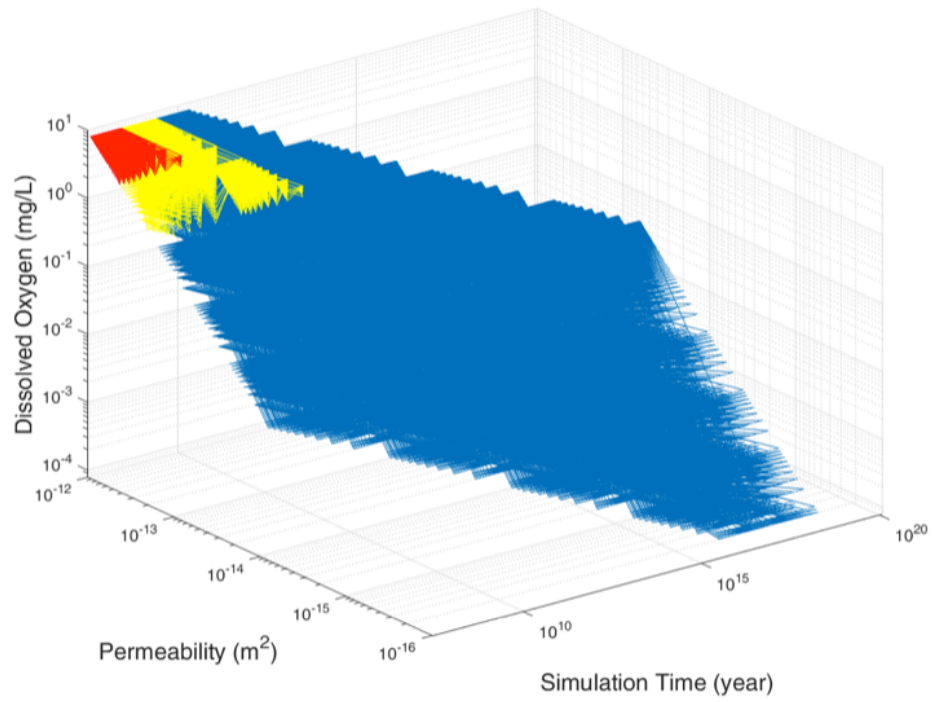


Figure 2.3. (A) The normalized frequency of model times necessary to oxidize the Hamersley Basin iron formations with a meteorically derived oxidizing fluid. Results are a subset of 3,802,356 total model runs, that return times less than 2.45 Ga and represent only 8.87% of all model runs. The red dashed line marks 250 million years, or the approximate length of the Ophthalmian orogeny, considered to be a key event for the post-depositional oxidation (McLellan et al., 2004; Powell et al., 1999); only ~1.06% of model runs require less time than this to oxidize a mass of Fe equivalent to 10 to 60% the mass of the 1×10^{17} kg Hamersley Basin. Over 91% of model runs (not shown) require longer than 2.45 Ga, which corresponds to the termination of deposition of the Hamersley Group and the onset of the Ophthalmian orogeny when the meteoric oxidizing fluid is believed to have infiltrated the basin (McLellan et al., 2004; Powell et al., 1999). **(B)** A three-dimensional view of simulation times required to oxidize 10-60% of iron in the Hamersley Basin. Red indicates simulations that require less than 250 Ma, yellow less than 2.45 Ga, and blue all simulations that require oxidation times longer than the age of the Hamersley Basin iron formations. All successful model runs that take less than 250 Ma require dissolved oxygen concentrations greater than 1.2 mg/L, and regional permeabilities approaching those of sandstones.

Chapter 3. A comparison of bulk versus laser ablation trace element analyses in banded iron formations: Insights into the mechanisms leading to compositional variability¹

3.1 Introduction

Banded iron formations (BIFs) are iron- and silica-rich chemical sediments that precipitated from seawater during the Archean and Paleoproterozoic. Their mineralogy, comprised of hematite, magnetite, chert, siderite, and a variety of accessory Fe silicates, reflects both the primary precursor phases, such as ferrihydrite and amorphous silica, and the cumulative effects of diagenesis to low grade metamorphism (Bekker et al., 2010, 2014; Konhauser et al., 2017). Although their origins are enigmatic, as BIF lacks a true modern analogue in today's oxygenated oceans, these deposits have been demonstrated to be critical archives for early atmosphere and ocean chemistry. Based on the preservation of rare earth element and yttrium (REE+Y) patterns characteristic of seawater, it has been suggested that BIFs record trace element enrichments reflective of marine conditions contemporaneous to their deposition (e.g., Bau and Dulski, 1996; Pecoits et al., 2009; Konhauser et al., 2009; Mloszewska et al., 2012; Robbins et al., 2013, 2016; Haugaard et al., 2016). BIFs have thus been used to track temporal trends in the abundance of biologically critical trace nutrients, including phosphorus (P; Bjerrum and Canfield, 2002;

¹ This chapter has been prepared for submission as: Robbins, L.J., Konhauser, K.O., Warchola, T.J., Homann, M., Thoby, M., Foster, I., Mloszewska, A.M., Alessi, D.S., and Lalonde S.V. A comparison of bulk versus laser ablation trace element analyses in banded iron formations: Insights into the mechanisms leading to compositional variability.

Konhauser et al., 2007; Planavsky et al., 2010a), nickel (Ni; Konhauser et al., 2009, 2015), zinc (Zn; Robbins et al., 2013), cobalt (Co; Swanner et al., 2014), and copper (Cu; Chi Fru et al., 2016). Similarly, redox sensitive trace element abundances in BIF, including chromium (Cr; Konhauser et al., 2011) and uranium (U; Partin et al., 2013a), have provided critical insights on the timing, structure, and tempo of the Great Oxidation Event (GOE), the period in Earth's history 2.45-2.32 Ga when oxygen began to accumulate in the atmosphere (Lyons et al., 2014).

Despite decades of studies on BIFs, several aspects regarding their deposition and trace metal enrichment remain cryptic. Foremost amongst these is the variability in trace element concentrations observed within a given deposit or time period, that in some cases spans several orders of magnitude. For instance, in compilations of Ni/Fe ratios (Konhauser et al., 2009, 2015) the spread in BIF values can exceed two orders of magnitude, especially in samples from before the collapse of the marine Ni reservoir. Similar variability is observed in temporal compilations of Cr, Zn, and Co (Konhauser et al., 2011; Robbins et al., 2013; Swanner et al., 2014, respectively). In the compilation of Zn in BIFs through time (Robbins et al., 2013), samples for a given time period can have Zn/Fe ratios that span almost 4 orders of magnitude. This variability is primarily observed in data generated *in-situ* by laser ablation methods, but it is also observed in bulk digestions analyzed by solution mode mass spectrometry (e.g., Konhauser et al., 2009, 2015; Robbins et al., 2013). While long-term trends in trace metal abundances are likely a reflection of changes in bulk seawater chemistry, the observed spread in trace element values in BIFs has been proposed to reflect periodic drawdown within a depositional basin or the effects of diagenesis and low-grade metamorphism. Yet, the significance of this variability, and the statistical

compatibility of laser ablation vs. bulk rock data, remains a highly under-constrained aspect of BIF geochemistry.

While it has been suggested that the trace metal record of BIF may not faithfully record ancient marine conditions because the rocks were subjected to widespread trace metal remobilization (e.g., Friedrich et al., 2011), simulated diagenetic experiments (Robbins et al., 2015) have instead suggested that transition metals, for instance Zn and Ni, are strongly retained following diagenetic mineral transformations. Similarly, the rare earth elements (REE) are immobile except under water:rock ratios that far exceed those expected during BIF formation or diagenesis (e.g., Bau, 1993). As such, the bulk trace metal record likely does represent the marine conditions contemporaneous to deposition. Despite this, there is an inherent variability in a given formation, the meaning of which remains cryptic. This variability is reflected in both laser-ablation and bulk analysis but is often stronger in data generated by laser ablation. In this work, we examine the systematic differences between BIF data generated by bulk digestions and the laser ablation of hematite and magnetite grains by statistically assessing mean concentrations for similarity between the different methodologies. It may be expected that highly-localized diagenetic effects impart a repartitioning of trace metals during the transformation from the initial precursor ferric oxyhydroxide phase to hematite and/or magnetite. This repartitioning may be manifested in differences in the trace metals concentrations of specific mineral phases. For instance, elevated concentrations may be expected in magnetite which has a higher density of hydroxyl groups and lower disassociation constants than hematite, although hematite has a higher surface area and disassociation constants that are not drastically higher (Cornell and Schwertmann, 2003). Additionally, it is known that several transition metals can be

structurally incorporated into both hematite and magnetite (Robbins et al., 2015 and references therein).

In this study we compare BIF trace element concentration data obtained by bulk digestion and solution-mode analysis versus *in-situ* laser ablation analysis using HR-ICP-MS data from corresponding pairs of BIF slabs and powders spanning six different formations as well as additional bulk rock analyses from the same formations. Samples analyzed include BIF from key examples of Algoma-type and Superior-Type BIF units that vary in depositional setting, age and metamorphic grade. These analyses shed light on the use of bulk versus *in-situ* methods for investigating paleomarine signals recorded in BIFs and inform our framework for interpreting the range in trace element concentrations observed in large temporal records.

3.2 Banded iron formation samples and localities

Samples examined here were previously collected from two distinct BIF-bearing Precambrian sedimentary sequences: the Eoarchean Nuvvuagittuq Supracrustal Belt in Québec (Mloszewska et al., 2012), and the Paleoproterozoic Hamersley Basin in Western Australia (Trendall and Blockley, 1970; Haugaard et al., 2016; Konhauser et al., 2018). The localities and a generalized stratigraphy for the Hamersley Basin are presented in Fig. 3.1. Also included in the dataset is a single sample from the Eoarchean Isua Formation in Greenland that provides another Eoarchean BIF point for comparison.

3.2.1 Nuvvuagittuq Supracrustal Belt

The Nuvvuagittuq Supracrustal Belt (NSB) is located in northwestern Québec, Canada (Fig. 3.1A) on the northern shore of Hudson's Bay, and is amongst the oldest crustal rocks

preserved. Age estimates for the NSB range from 3.75 Ga based on U-Pb zircon dating (Cates and Mjozsis, 2007) to 4.2 Ga based on ^{142}Nd measurements (O'Neil et al., 2008, 2017). The geological context and composition of the NSB has been previously described in detail (e.g., O'Neil et al., 2007, 2008, 2011; Mloszewska et al., 2013) and indicate that not only are these some of the oldest crustal rocks preserved on Earth, but that the chemical sedimentary components likely formed in a marine setting (Mloszewska et al., 2012, 2013). Due to the close association with volcanic rocks, the BIF of the NSB is considered an Algoma-type BIF. Our interest here lies specifically in the BIF sediments preserved within this Archean terrane. Samples analyzed in this study are the same as previously collected and analyzed by Mloszewska et al. (2012). The samples were taken from an exposed BIF unit up to 30 m thick, composed of magnetite and grunerite, and locally rich in quartz (Mloszewska et al., 2012). The NSB BIF offers a rare glimpse into Eoarchean seawater composition (Mloszewska et al., 2012; 2013), as it is the oldest known BIF that records seawater-like signatures. Dodd et al. (2017) reported putative microfossils from the NSB and described them as morphologically similar to iron-oxidizing bacteria. If the biogenicity of these putative fossils can be confirmed, this would make the microfossils of the NSB some of the oldest evidence for life on Earth, underscoring the importance of examining contemporaneous chemical sediments for insight into the depositional paleoenvironment.

3.2.2 Hamersley Basin

The Hamersley Basin is located in Western Australia (Fig. 3.1B) and hosts the archetype BIF succession. The Hamersley Basin succession of BIFs includes the Marra Mamba, Brockman, Weeli Wolli, and Boolgeeda iron formations (Fig. 3.1C). The Brockman Iron Formation can be further subdivided into the Dales Gorge and Joffre members. Spatially,

the Hamersley Group extends for over 100,000 km² and reaches a maximum thickness of up to ~2.5 km (Morris, 1993). Peak iron precipitation in the Hamersley Basin corresponds with the deposition of the Dales Gorge and Joffre Members (Isley, 1995). The tectonic setting, stratigraphy, and geochemistry of the Hamersley Basin BIFs have been previously described in detail (e.g., Trendall and Blockley, 1970; Pecoits et al., 2009, Haugaard et al., 2016) These Superior-type BIF units were deposited on a large continental platform with minimal clastic input. Samples examined here were collected from cores DD98SPG001 (Krapež et al., 2003) and WW1 (Davey 1983, 1992), sampling the Joffre and Dales Gorge Members of the Brockman Iron Formation and the Weeli Wolli Iron Formation, respectively. This large sample set offers the unique opportunity to examine inter- and intra-formation variability in the trace element composition at the bulk and mineral scales of BIF samples from a single basin.

3.3 Methods

3.3.1 Sample preparation

BIF slabs selected for laser ablation high resolution inductively coupled plasma mass spectrometry (LA-HR-ICP-MS) were cut and polished at the European Institute of Marine Studies (IUEM), Université Bretagne Occidentale, in Brest, France. Individual slabs were cut to a size of <5 cm in length and ~2-4 cm in width to ensure an acceptable fit in the laser ablation cell. Samples for bulk rock analyses were cut from the same BIF slabs, then crushed and powdered (Fig. 3.2). All samples were crushed in a tungsten-carbide mill. The mill was rinsed with water, cleaned with ethanol, and then dried with compressed air between each sample and an additional cleaning step described below, to ensure no cross-contamination between samples. Afterwards, samples were powdered in a Retsch RS100

vibratory disc mill using an agate grinding set for ~ 7 minutes. Between BIF samples the entire agate grinding set was cleaned with pure quartz sand for 10 minutes, then rinsed with water, and cleaned with ethanol.

3.3.2 LA-HR-ICP-MS operating conditions and data treatment

Analyses of BIF samples by LA-HR-ICP-MS analysis at IUEM was completed in October and November 2016 using a CopexPro 102 Coherent laser attached in-line to a high-resolution Thermo Element2 sector field mass spectrometer, with an additional session in May 2017. The laser was filled with N₂ gas and operated at a wavelength of 193 nm. The laser ablation cell was flushed with helium gas at 200 ml/min. Tuning of the Element2 was optimized based on observed counts for ⁴³Ca, ¹³⁸La, and the Th to U ratio for multiple ablations of the international glass standard NIST612.

Operating conditions included a 44 µm spot size, 10 J, 10 Hz, and an analysis time of approximately 3 minutes. Each laser ablation data point represents a value obtained by the combined treatment of approximately 50 shots on a single spot in rapid succession at 10 Hz, with the first 10 shots discarded as burn in. Prior to the burn in, the targets were initially ablated with about five shots to clean the surface, and then 30 seconds was allowed for background levels to fall before initiating the burn in and commencing data acquisition.

During analytical sessions, multiple analyses of international standards were used as calibration points and to constrain methodological error. Measurements of the basaltic glasses BCR-2G and BIR-G, as well as NIST certified glass standard NIST 612, were taken at the start and end of each laser session, where each analytical session lasted approximately 45 minutes. During longer sampling sessions, additional BCR and BIR spots were analyzed after every ~15 targets. Analyses of BCR-2G and NIST 612 were used as

calibration points for data treatment while BIR-G was treated as an unknown to estimate precision. Laser ablation data were processed using the SILLS program (Guillong et al., 2008), a free add-in tool operated in MATLAB 2015a. Raw LA-HR-ICP-MS data in counts per second (CPS) was converted into concentrations (ppm) in SILLS based on a calibration from the measurement of BCR-2G and NIST 612 from that corresponding session, while repeated shots of BIR-G across sessions provided estimates of external reproducibility. Concentration data were imported into MATLAB 2017b for further data treatment. Rare earth elements ratios were calculated following the methods of Bau and Dulski (1996) and normalized to the Post Archean Australian Shale (PAAS) shale composite after Taylor and McLennan (1985) and McLennan (1989).

3.3.3 Bulk rock sample digestions and solution mode HR-ICP-MS

After crushing, all weighing and preparation of powdered samples for solution mode ICP-MS was carried out in a class 1000 clean lab at IUEM. Teflon vials were acid washed internally and externally overnight in near-boiling, concentrated nitric acid (HNO₃), rinsed three times with 18.2 MΩ-cm ultrapure water, then dried in a 40°C oven and stored under clean conditions. Crushed and powdered samples were completely digested with a three-step, heated HF-HNO₃-HCl attack. Approximately 50-90 mg of powder was added to an acid cleaned Teflon vial, after which 1.5 mL of 16 M HNO₃ and 1.5 mL of 27 M hydrofluoric acid (HF) were added to the sample. Samples were then capped and left to react overnight at 80°C. Samples were then uncapped and left to evaporate to dryness. In the second step, 3 mL of freshly mixed aqua regia was added to each residue, samples were capped and allowed to react for 6 hours at room temperature to avoid excessive gas buildup.

After 6 hours, caps were removed, and the sample was evaporated overnight at 80°C to dryness. In the final step, 3 mL of 6 M HCl was added to each residue and samples were heated overnight at 80°C. Prior to analysis, 100 µL of each sample was diluted to 5 mL with 2% HNO₃.

Diluted samples were measured in solution mode on a Thermo Element2 HR-ICP-MS at IUEM in Brest, France. Samples were calibrated by multi-element standards at concentrations of 0.5, 5, and 50 ppb that were measured repeatedly throughout the session. Additionally, a 5 ppb In (indium) standard was added to each sample, standard, and rinse, and was used to monitor signal stability and correct for instrumental drift across the session. Each sample and standard were bracketed by a rinse for which data was also acquired to determine the method detection limit. Final concentration data were exported and treated in Matlab 2017b to calculate trace element and REE patterns and ratios, using the methods described above.

3.3.4 Statistical Analysis

To determine whether statistical differences exist between bulk rock solution digests and the laser ablation of hematite and magnetite grains (Fig. 3.2), a one-way ANOVA test was performed across a matrix of 35 elements and 7 common ratios or REY indices for each formation. The results of the one-way ANOVA test were then examined by multiple pair-wise comparison of mean values using the Tukey-Kramer method to control for the increasing false positive error rate that accompanies an increasing number of pair-wise comparisons (Hsu, 1996; Lalonde et al., 2008). This was performed three times, once for i) bulk rock digests and hematite LA-HR-ICP-MS data, for ii) bulk rock digests and

magnetite LA-HR-ICP-MS data, and for iii) hematite and magnetite LA-HR-ICP-MS analyses. In all cases a threshold p -value of <0.05 indicates that the means of the compared analytical techniques are statistically different. Due to some unavailability of data or incompatible mineralogies, for the Weeli Wolli Formation samples, the comparison was solely between hematite and magnetite LA-HR-ICP-MS analyses. For samples from the Dales Gorge and Joffre members, as well as the NSB, all three pairwise comparisons were completed whenever hematite, magnetite and bulk data existed for a given sample. If no magnetite data were present for the considered sample, the Tukey-Kramer test considered only differences in bulk versus hematite LA-HR-ICP-MS analysis. For all analyses that returned abundances less than the detection level, for the purpose of statistical tests, these were treated as “NaN” data within Matlab 2017a, or “not a number” whereby samples are indicated to have no valid concentration data for those points. The only sample not subjected to a pairwise comparison was WW1-9, as only magnetite grains were analyzed.

3.4 Results

3.4.1 Bulk solution versus laser generated averages

The LA-HR-ICP-MS results for fifteen BIF slabs from the NSB and Hamersley Basin, with paired bulk rock data when available, are summarized in Appendix Tables A2.1-13. Tukey-Kramer tests were performed to examine whether statistical differences exist for three independent sets of pairwise comparisons: (i) bulk digestion versus hematite LA-HR-ICP-MS (Fig. 3.3), (ii) bulk digestion versus magnetite LA-HR-ICP-MS (Fig. 3.4), and (iii) hematite versus magnetite LA-HR-ICP-MS generated data (Fig. 3.5). In all cases a p -value <0.05 indicates that there are significant differences in the mean values generated by the compared methodologies. When data were generated by one method but below detection

limits by another (i.e., bulk digestion, but below detection limits for hematite analyzed by LA-HR-ICP-MS), the p-value was set to 0, indicating a significant difference, as one method generated reliable data but the other failed to do so.

Significant differences between mean values generated by hematite LA-HR-ICP-MS and bulk digestion of BIF samples exist for at least one element in 11 out of 12 samples analyzed here, the exception being for sample 090710-2 from the NSB (Fig. 3.3J). When significant differences exist, they tend to be in the lighter elements (Li, B, Ca, Mg) or in the transition metals (e.g., Cr, Cu, Ni, Zn). For several samples (DD98-26, DD9-27), this is the result of several of the transition metals being below detection limits during LA-HR-ICP-MS (Appendix Tables A2.7 & A2.8). Interestingly, despite many individual REE+Y having $p > 0.05$, several of the REE+Y based indices (e.g., Ce/Ce^*_{PAAS} , Eu/Eu^*_{PAAS}) exhibit significant differences when calculated for laser ablation or bulk data, for example in DD98-7 from the Joffre member (Fig. 3.3A).

Similar to the comparison of hematite LA-HR-ICP-MS versus bulk digestion data, magnetite LA-HR-ICP-MS analysis compared to bulk digestion data also has variable instances where significant differences exist between mean values (Fig. 3.4). While samples from the Joffre Member (Fig. 3.4A&B) seem to show a strong correspondence overall between mean magnetite and bulk rock data, mean values of samples from the Dales Gorge Member (Fig. 3.4C) and the NSB (Fig. 3.4D&E) have a higher frequency of elements with significantly different mean values between bulk digestion and magnetite LA-HR-ICP-MS analyses. Part of this may be attributed to low trace element abundances in the magnetite in several of the samples analyzed here (e.g., Appendix Table A2.8).

The final pairwise comparison considered here, hematite versus magnetite LA-HR-ICP-MS data, also highlights a number of samples where mean concentration values differ significantly (Fig. 3.5). These differences are especially pronounced in samples from the NSB (Fig. 3.5F& G), while differences vary from sample to sample in the Weeli Wolli Iron Formation (Fig. 3.5A&B), and the Joffre Member (Fig. 3.5C&D). Some of the significant differences, however, can again be attributed to values in the magnetite or hematite being below detection limits (Appendix Tables A2.7&8).

Overall, it appears that variability in the correspondence of values between compared methodologies is largely dependent on the frequency in which LA-HR-ICP-MS analyses fall below detection limits (e.g., Fig. 3.3D-E, 3.4C, & 3.5E; Appendix Tables A2.7&8). Significant differences, however, vary across the samples and within adjacent samples within a given formation (i.e., WW1-9b versus WW1-10, Fig. 3.5A& B).

3.4.2 Inter-deposit variability

Temporal trends in redox sensitive elements and transition metals including Cr, Co, Ni, Cu, Zn, and U are presented in Figs. 3.6-11, respectively. For Cr (Fig. 3.6A), mean solution values are relatively consistent with the baseline provided by the lone sample from the Isua Formation through the NSB, Dales Gorge, and Joffre samples. Similarly, mean hematite Cr values are low in Dales Gorge samples, close to the baseline of the Isua hematite analyses. However, the NSB show elevated mean Cr values based on hematite and magnetite analyses. The largest spread, however, spanning almost 5 orders of magnitude, is present in the Weeli Wolli LA-HR-ICP-MS data, which also has the highest mean Cr concentrations in magnetite. The Joffre Member and NSB samples show similar mean Cr

values in terms of laser and bulk digestion data, and span approximately four orders of magnitude.

Cobalt (Fig. 3.7A) also shows a wide range in values in both the NSB and Weeli Wolli Iron Formation samples. While the greatest spread is observed in samples from the NSB, mean solution values decrease from the NSB to the Dales Gorge Member, before steadily increasing through the Joffre Member, and reaching high mean laser values in the Weeli Wolli Iron Formation. For the Joffre Member samples, mean Co values for hematite and bulk digestion are quite similar; however, for the NSB samples, the mean laser values, although very similar, are almost four orders of magnitude greater than the mean bulk digestion values (Fig. 3.7A).

Mean nickel concentrations vary less systematically between deposits (Fig. 3.8A) than either Cr or Co. The greatest bulk digestion mean value is observed in the NSB samples, and then falls in the Dales Gorge Member iron formation samples. A slight increase in mean bulk values is observed in the Joffre Member (Fig. 3.8A) but remains about an order of magnitude less than observed in the NSB samples. The greatest spread in values is observed in the laser data from the Weeli Wolli Iron Formation samples, and with the exception of the mean magnetite values from the Weeli Wolli Iron Formation, all mean values fall below those for hematite and magnetite in the NSB. In the formations with the greatest spread and differences in Ni between hematite and magnetite LA-HR-ICP-MS data, namely the Weeli Wolli Iron Formation and the NSB, magnetite is distinctly elevated in Ni (Fig. 3.8A).

Figure 3.9A highlights the temporal pattern in Cu between the formations considered here. Mean values for bulk digestion samples are within about an order of

magnitude of 10 ppm. Samples from the Weeli Wolli Iron Formation and the NSB show a significant spread in values, approaching six orders of magnitude, and in almost all formations, mean Cu values from laser ablation are at least an order of magnitude greater than mean Cu bulk values. Although mean Cu bulk values remain relatively static (Fig. 3.9A) in time, there seems to be a systematic increase in the mean Cu laser ablation values up-sequence in the Hamersley basin from the Dales Gorge Member through to the Weeli Wolli Iron Formation and is readily apparent in the magnetite analyses; this trend is also mirrored in the spread recorded by laser ablation analyses.

Similar to Cu, the mean bulk digestion values for Zn (Fig. 3.10A) show approximately an order of magnitude of variance centered around 10 ppm, with samples from the NSB showing the highest mean Zn bulk values. The greatest spreads are once again observed in samples from the NSB and Weeli Wolli iron formations (Fig. 3.10A). Interestingly, for formations with data for both hematite and magnetite, magnetite grains appear to record a significantly higher mean Zn value, by approximately two orders of magnitude over hematite, within each formation. However, in the Joffre Member, (Fig. 3.10A) there is strong convergence between mean Zn values for bulk, hematite, and magnetite measurements.

As with both Cu and Zn, U (Fig. 3.11A) demonstrates bulk digestion mean values for the NSB, Dales Gorge Member, and Joffre Member samples that cluster within an order of magnitude around 0.1 ppm. For the Dales Gorge and Joffre samples, laser ablation U data corresponds well with the bulk digestion data, however, for the NSB samples, mean hematite and magnetite U concentrations are significantly greater than the bulk digestion mean values. The greatest spread, spanning nearly eight orders of magnitude, is observed

in the Weeli Wolli formation. In almost every formation, laser ablation U concentrations are either equal to or above bulk digestion mean values, and magnetite when present is generally the phase most enriched in U (Fig. 3.11).

Figures 3.12-14 highlight several common REE+Y indices for examining paleomarine seawater conditions. Mean Y/Ho ratios, on a gram-per-gram (g/g) basis, generally show superchondritic values ($Y/Ho > 28$), a classic indication of seawater-like signatures being preserved. The most significant exception to this is the low Y/Ho values observed in magnetite grains within the Weeli Wolli Iron Formation (see section 3.4.3). Cerium anomalies (Ce/Ce^*_{PAAS}) for each of the formations are presented in Fig. 3.13. Generally, mean values for the Ce anomaly are lower (more anomalous) in laser ablation data than in bulk digestion data, suggesting that an oxidative signal may be recorded at the grain scale but diluted or obscured by bulk digestion techniques. However, the laser ablation data also produces some extreme negative anomalies, notably in samples from the Weeli Wolli Iron Formation, that are discussed below in terms of intra-deposit variability. Finally, Eu/Eu^*_{PAAS} anomalies are presented in Fig. 3.14. A clear decreasing trend from the baseline Isua Formation sample through to the Weeli Wolli is evident in both the bulk and laser ablation data (Fig. 3.14A).

3.4.3 Intra-deposit variability

Figures 3.6-11 additionally highlight the intra-deposit variability in trace element abundances by directly comparing the averages of constituent samples alongside the larger formation compilations. Similarly, Figs. 3.12-14, highlight the intra-deposit variability with respect to several common REE+Y ratios. In this manner the consistency in concentrations between multiple samples from a single formation can be evaluated.

Furthermore, instances where a single sample demonstrates an elevated or depleted value and affects the formation average can be highlighted (e.g., Cr in magnetite grains from sample WW1-9, Fig. 3.6B).

3.4.3.1 Weeli Wolli Iron Formation

Consistently high trace element concentrations in magnetite from WW1-9 tend to drive the formation average for individual elements quite high (Fig. 3.6B-11B), highlighting the ability for a single sample where trace elements may be elevated to skew mean formation values. Overall, the mean values for hematite in WW1-9b and WW1-10 are more consistent with each other and the bulk rock values. Despite some low concentrations in magnetite from WW1-10 (e.g., Cr; Fig. 3.6B), the overall formation mean is skewed by the elevated concentrations in WW1-9 (Fig. 3.6B). Similarly, WW1-9 shows markedly depressed Y/Ho ratios (Fig. 3.12B) and Ce/Ce*_{PAAS} values (Fig. 3.13B), and accounts for some of the extreme negative spread observed in these ratios, while WW1-9b and WW1-10 are quite consistent in these ratios. Despite this spread in Y/Ho and Ce/Ce*_{PAAS}, mean Eu/Eu*_{PAAS} (Fig. 3.14B) values in all Weeli Wolli Iron Formation samples analyzed here are markedly similar.

3.4.3.2 Joffre Member, Brockman Iron Formation

With respect to several indicators examined here, including Co, Zn, U, and Y/Ho (Figs. 3.7C, 3.10C, 3.11C, & 3.12C, respectively), the different datasets from the Joffre Member of the Brockman Iron Formation show some of the most consistent mean values within the formation's larger sample set. For instance, bulk rock and laser-based mean values cluster relatively tightly for Zn (Fig. 3.10C) and U (Fig. 3.11C) in Joffre Member samples, although DD98-12 is slightly lower in U than DD98-7 and DD98-21a.

Chromium, Ni, and Cu show the most intra-formation variability, with a greater spread in sample DD98-21a that approaches three orders of magnitude for these elements. Indeed, sample DD98-21a pulls mean formation values for hematite and magnetite to significantly higher levels when viewing the formation as a whole. While Y/Ho ratios (Fig. 3.12C) are quite consistent across all samples, in both bulk and laser ablation data, Ce/Ce*_{PAAS} and Eu/Eu*_{PAAS} show some interesting differences (Figs. 3.13C & 3.14C, respectively). In terms of Ce/Ce*_{PAAS} values, while samples show similar bulk digestion and laser ablation data, it is evident that mean laser ablation values are systematically lower, indicating that there may be true negative Ce anomalies preserved at the grain scale that are otherwise cryptic in bulk rock data. Similarly, Eu/Eu*_{PAAS} averages for bulk digestions cluster around 1.9-2, while laser generated averages are much lower, clustering around 1.45. Overall, however, the three constituent samples for the Joffre Member show Ce- and Eu-anomalies that are comparable between samples for any given analytical method.

3.4.3.3 Dales Gorge Member, Brockman Iron Formation

The Dales Gorge Member of the Brockman Iron Formation is represented by two paired powder-slab samples, DD98-26 and DD98-27. Overall, DD98-26 and DD98-27 correspond well in trace element abundances, often within one to two orders of magnitude of one another with respect to both mean bulk digestion and laser ablation values. When present, magnetite is the more enriched mineral phase (e.g., Cu, Zn, and U; Figs. 3.9D-11D, respectively). Yttrium-holmium ratios (Fig. 3.12D) have mean bulk digestion and laser ablation values that cluster around 40, with a similar spread, but with lower Y/Ho ratios in DD98-26 and slightly elevated ratios in DD98-27. Both Ce/Ce*_{PAAS} and

Eu/Eu*_{PAAS} exhibit similar behavior in the Dales Gorge Member samples (Figs. 3.13D & 3.14D). Interestingly though, it appears that in terms of Y/Ho, Ce/Ce*_{PAAS}, and Eu/Eu*_{PAAS}, magnetite grains record lower values than the hematite in samples DD98-27 and DD98-26; an observation that runs counter to the trends observed for Cu, Zn, and U.

3.4.3.4 Nuvvuagittuq Supracrustal Belt

The NSB is represented by five samples 090709-4b2, 090709-5, 090710-2, 090710-4, and 090710-12. Magnetite grains were analyzed in both 090709-5 and 090710-2. Typically, magnetite grains in 090710-2 have elevated trace element abundances (e.g., Cr, Co, Ni, Zn, U; Figs. 3.6E-3.8E, 3.10E, & 3.11E, respectively), but Cu is notably absent (Fig. 3.9E). Conversely, 090709-5 has magnetites that are largely devoid of other trace metals but has Cu present at levels close to bulk digestion, but well below mean hematite values (Fig. 3.9E). Most NSB samples generally show a similar level of spread, with the exception of 090709-4b2, which often has the lowest trace element values and tightest spread in values.

Similar to Joffre Member samples, the Y/Ho ratios of NSB samples (Fig. 3.12E) have superchondritic bulk digestion values that are above mean hematite laser ablation values. A notable exception to this is magnetite in 090710-2, which has an average Y/Ho ratio above that of the bulk digestions. A similar observation is apparent in Eu/Eu*_{PAAS} values for NSB samples, where the highest mean value is recorded by in magnetite of 090710-2 (Fig. 3.14E). Finally, it is remarkable that the range in Ce/Ce*_{PAAS} values recorded by laser ablation data fall below 0.95; in all samples, most mean hematite and magnetite values fall below the mean bulk digestion for Ce/Ce*_{PAAS}, with the lowest mean values recorded in magnetites of 090710-2, but the lowest overall values in 090710-4.

3.4.4 Trace metal systematics

Two distinct methods of examining trace element systematics were considered here: the classic PAAS-normalized cross plot of Ce/Ce^*_{PAAS} and Pr/Pr^*_{PAAS} (Bau and Dulski, 1996; Fig. 3.15), and the scaling between example sets of trace metals (Fig. 3.16). The sets of trace metals in Fig. 3.16 were selected to determine what, if any, information could be determined based on the mechanism underlying either BIF deposition, their trace element source or the mechanism of sequestration. In a PAAS-normalized Ce/Ce^* - Pr/Pr^* cross plot, true negative Ce anomalies are distinguished from potential false negative anomalies that might arise in Ce/Ce^* from the positive seawater La anomaly; true negative Ce anomalies will be accompanied by a positive Pr/Pr^* anomaly. It is clear that the majority of bulk samples fall in the field where no true negative Ce anomalies are indicated (Fig. 3.15). A handful of samples, however, that were analyzed by LA-HR-ICP-MS from the NSB, Joffre, and Weeli Wolli iron formations, fall in the lower right-hand field, where true negative Ce- anomalies are indicated. These are discussed in more detail below.

Figure 3.16 examines the scaling of four selected pairs of trace elements (i) Cr and Ni, (ii) Cr and Mo, (iii) Mo and Zn, and (iv) Ni and Zn. In all cases, these elements show strong linear co-variation. Overlain on the plots are the expected scaling relationships between the elements based on different adsorptive or sequestration mechanisms. Encouragingly, most of these elemental cross plots correspond to a least one of the expected scaling stoichiometries. These correlations and their implications are discussed in detail in section 3.5.3.

3.5 Discussion

3.5.1 Statistical reproducibility of bulk versus laser generated trace element concentrations

Tukey-Kramer tests (Figs. 3.3-3.5) indicate that the reproducibility of bulk digestion trace element geochemistry by LA-HR-ICP-MS analysis of the same sample is a complex and dynamic issue. For some samples, values seem to agree quite well, with p-values dominantly greater than 0.05 (e.g., Figs. 3.3C,H, 3.4B, & 3.5D), which indicates a strong comparability between the two approaches. Conversely, for a number of samples, p-values less than 0.05 indicated statistically significant differences between the two methods for a large number of elements (e.g., Figs., 3.4C-E, 3.5B, F, & G). Critically, these differences exist in each of the pairwise comparisons considered here: (i) bulk digestion versus laser ablation of hematite grains, (ii) bulk digestion versus laser ablation of magnetite grains, and (iii) laser ablation of hematite versus magnetite grains. The p-values of the pairwise comparisons appear to be unrelated to the age of samples, or Algoma- versus Superior-type BIF, with samples from both the Hamersley Basin and the NSB showing examples of elements for which methodologies dominantly agree or are significantly different. This suggests that the observed differences are not necessarily a function of age, increasing metamorphism, or depositional setting, as represented by the consideration of these two disparate BIF deposits. Furthermore, the p-values do not scale with either the ratio of number of laser shots to number of solution analyses, crustal abundance of the elements, or the detection limits for LA-HR-ICP-MS (data not shown). Some of the difference between methodologies can certainly be ascribed to differences between analytical sessions in instrumental sensitivity and stability during laser ablation. For instance, samples DD98-26 (Fig. 3.3D; Appendix Table A2.7) and DD98-27 (Fig. 3.3E, 3.4C, & 3.5E) were run on days when poor sensitivity during laser ablation sessions resulted in unresolvable

concentrations for transition metals in the majority of laser shots. As a result, a p-value of 0 was assigned to these samples for many of the transition metals, in contrast bulk digestions were able to produce transition metal concentrations, but the laser data were below detection limits.

An interesting observation is that in several instances, while the majority of REE+Y concentrations may be indistinguishable across the pairwise comparisons, some of their respective indices (Y/Ho, Ce/Ce*_{PAAS}, Eu/Eu*_{PAAS}, Σ REE) may vary significantly with p-values falling below the 0.05 threshold (e.g., Figs. 3.3A, 3.4A, & 3.5E). This suggests that when considering elemental ratios and indices, although individual elements may be similar in a pairwise comparison, cumulative differences may drive ratios and indices to statistically different values. Generally, however, when the pairwise comparisons of REE+Y values returns p-values >0.05, indices also show a high level of agreement (e.g., Figs. 3.3C, G,H, & J, Fig. 3.4B, Figs. 3.5A & D). Finally, when a critical REE+Y element used in the calculation falls below the threshold for being significantly different, the corresponding ratio in which it is used also generally falls below the 0.05 threshold. For instance, as seen in Fig. 3.3I, Sm is the lone REE that is significantly different when analyzed by bulk digestion of hematite versus LA-HR-ICP-MS in sample 090710-4 from the NSB. As Sm is used in the calculation of the Eu-anomaly ($Eu/Eu^*_{PAAS} = Eu_{PAAS} / (0.67Sm + 0.33Tb)_{PAAS}$; Bau and Dulski, 1996), the significant difference in the constituent element manifests in significantly different values of the anomaly.

When plotting the laser ablation data and the bulk digestion data simultaneously (Figs. 3.6-11), bulk digestion means values typically fall either within or below the range

of laser ablation data, demonstrating that the laser generated data captures a much larger range in concentrations than bulk digestions. This observation may be attributable to one of several factors. First, the analysis of specific mineral phases, here hematite and magnetite, generates concentrations in excess of bulk digestion data as concentrations are not diluted by trace element poor mineral phases, such as chert. Second, within individual samples, variability is frequently observed when hematite or magnetite is the most trace element-enriched phase. For instance, in samples from the Weeli Wolli Formation, magnetite in WW1-9 is significantly enriched in trace metals (Figs. 3.6-11B), but in the other two Weeli Wolli Formation samples WW1-9b and WW1-10, hematite is the more trace metal-rich phase. Similarly, in the Joffre Formation (Figs. 3.6-11C), mean magnetite values typically fall close to, or below, mean hematite values, and in several instances (e.g., Cr, Co; Figs. 3.6C & 3.7C) fall below bulk concentrations as well. Conversely, when above detection limits in Dales Gorge Member and NSB samples (Figs. 3.6-11D&E), magnetite appears to be among the more enriched phase in terms of trace element concentrations. This may be the result of diagenetic repartitioning of trace metals on a highly localized scale, which results in mineral specific analyses exceeding the bulk digestion estimates for concentration.

3.5.2 The origin of variability within the trace metal record

There is significant variability with regards to trace metal concentrations in BIF, even within a given sample (Figs. 3.6-12). This is apparent in laser ablation analyses, and as such cannot be solely attributed to analytical effects. Instead, the spread observed in this case might be attributed to one of two possible causes: (i) localized diagenetic effects

concentrating trace metals in specific phases, or (ii) transient environmental signals that occur on short timescales.

With regards to the first possibility, given that a few millimetres of BIF can represent the accumulation of precursor sediments that occurred over decades to hundreds of years (e.g., Morris, 1993; Konhauser et al., 2002) a sample that is several centimetres in length could, therefore, potentially represent tens to hundreds of thousands of years. While a bulk sample necessarily homogenizes geochemical signals in a cm-scale sample, and that differences in BIF deposits separated by millions of years may reflect true first-order trends in evolving marine chemistry, it is entirely possible that the spread in laser ablation within a given cm-scale sample captures transient signals that record events or changes in geochemical inputs that occur on much shorter timescales. This would be manifested in adjacent or closely spaced laser-ablation samples that have highly disparate concentrations, as seen in many of the samples here (Figs. 3.6-12). In this light, differences may be attributable to short term fluctuations in local sources or weathering inputs over timescales of thousands to 100's of thousands of years and may be viewed as analogous to variations in environmental signals detected on coarser scales within the Boolgeeda Iron Formation, where multiple cycles are captured over ~70 m of BIF (Warchola et al., 2018).

Second, it may be anticipated that magnetite has a higher affinity for trace metals due to elevated hydroxyl group concentrations and lower disassociation constants for surface functional groups (Cornell and Schwertmann, 2003). However, the diagenetic repartitioning may rely on localized conditions, such as the relative abundance between magnetite and hematite, or the pH during diagenesis for instance. This possibility is highlighted by several cases where hematite and magnetite averages differ, and magnetite

is the enriched phase (e.g., Zn or U in DD98-27, Fig. 3.10&11). These possibilities are discussed in detail below.

3.5.2.1 An environmental signal

Due to their importance as metalloenzyme reaction centers and cofactors, there has been a great deal of interest in reconstructing the availability of transition metals in the ocean through time (e.g., Anbar and Knoll, 2002; Dupont et al., 2010; Robbins et al., 2016). Some of the transition metals investigated here, including Ni, Zn, Co, and Cu, are critical for a number of prokaryotic and eukaryotic enzymes, and the BIF record has been instrumental in reconstructing their respective marine reservoir size and the evolution of their respective abundances through geological time (e.g., Chi Fru et al., 2016; Konhauser et al., 2009, 2015; Robbins et al., 2013, 2016; Swanner et al., 2014). Previous investigations of chemical sedimentary and organic-rich siliciclastic records (namely BIFs and black shales) indicated relatively static marine abundances for both Cu and Zn through much of the Archean and Proterozoic (Chi Fru et al., 2016; Robbins et al., 2013; Scott et al., 2013). The deposit comparisons presented here offer only a narrow interval of the temporal trends for Cu and Zn (Fig. 3.9A & 3.10A). However, similar to these compilations, the spread in values from both laser ablation and bulk digestion techniques are similar, showing an approximately one order of magnitude variance. This observation lends support to the hypothesis that the concentrations of these transition metals may be buffered by organic ligands (see Robbins et al., 2013), or were characterized by relatively long residence times.

Cobalt (Fig. 3.7A) and Ni (Fig. 3.8A) show slightly more variation with respect to mean formation values. For instance, Co appears to be relatively enriched in the ≥ 3.75 Ga NSB BIF, it peaks in the Dales Gorge and Joffre members of the Brockman Iron Formation, and

then declines in the Weeli Wolli Iron Formation. Peak average Co in the Dales Gorge and Joffre members is consistent with a broader temporal compilation presented by Swanner et al. (2014), who identify increased Co concentrations in Superior-type BIF and ironstones beginning around 2.5 Ga and peaking in the ~2.3 Ga Timeball Hill Formation. The spike in Co concentrations reflected in higher mean values for bulk rock digests (Fig. 3.7A) would be consistent with a mafic volcanic supply, linked, in turn, to large igneous provinces developing during mantle plume events (Barley et al., 1997; Isley, 1995). The order of magnitude declines in average bulk Ni concentrations observed (Fig. 3.8A) between BIF samples from the NSB and Hamersley Basin is consistent with previous studies on BIFs that show a decline in Ni abundances during the Archean; (Konhauser et al., 2009; 2015). Although Weeli Wolli samples show elevated average Ni concentrations in magnetite (Fig. 3.8A & B), these are predominantly due to the elevated concentration observed in magnetite from WW1-9 and may be the result of localized diagenetic repartitioning or an anomalous input flux of Ni during the deposition of the Weeli Wolli Iron Formation; in either case, it is not representative of the long-term trends recorded by BIFs (Konhauser et al., 2009; 2015).

The concentrations of redox sensitive elements (RSE), such as Cr, U, Mo, and V, from BIFs and black shales have similarly been used to track the evolution of Earth's surface redox conditions (e.g., Konhauser et al., 2011; Partin et al., 2013a,b; Sahoo et al., 2012; Scott et al., 2008). Two significant increases in RSE are recorded within the sedimentary record: one coincident with the GOE and a second in the Neoproterozoic at about 850 Ma. While the formations examined here all pre-date the GOE, the youngest of them, the Dales Gorge and Joffre members of the Brockman, and the Weeli Wolli iron formation, were

deposited during the onset or immediate lead up to the GOE. While mean formation values remain relatively static across all formations here with respect to RSE and show variance of approximately an order of magnitude around their mean values, maximum values recorded by hematite and magnetite tend to increase as formations become younger (Fig. 3.6A & 3.11A). This is especially true for U (Fig. 3.11A), which likely indicates increasing levels of oxidative weathering in the run-up to the GOE, a signal that appears best reflected by maximum values in laser generated data. The increased concentrations of both Cr and U in laser data observed here (Fig. 3.6A & 3.11A) is consistent with elevated levels observed in broad compilations for these RSE in BIFs immediately before the GOE (Konhauser et al., 2011; Partin et al., 2013a).

Rare earth element signals captured here by both bulk digestion and laser ablation techniques include super chondritic Y/Ho ratios (Fig. 3.12), variable Ce anomalies (Figs. 3.13 & 3.15), and positive Eu-anomalies decline in progressively younger formations (Fig. 3.14). Perhaps more interesting though, with respect to the REE, is the presence of negative Ce anomalies revealed by LA-HR-ICP-MS analyses, that are otherwise obscured in bulk digest data (Figs. 3.13 & 3.15). While negative Ce anomalies are indicative of the presence of oxygen in the water column (e.g., Bau and Dulski, 1996; Bolhar et al., 2004), they are typically absent in BIFs predating the GOE (Planavsky et al., 2010b). This observation has previously been used to argue for the prevalence of an anoxic, ferruginous water column during the Archean. However, their absence in BIFs predating the GOE may also be attributable to the dilution of Ce/Ce^*_{PAAS} anomalies that were generated in the upper water column and subsequently recycled by Ce(IV) reduction below a chemocline (c.f., De Carlo and Green, 2002). In our study, the presence of putative negative Ce anomalies identified

here by laser ablation in the Eoarchean to Paleoproterozoic BIFs (Fig. 3.15) is inconsistent with previous data (e.g., Bau and Dulski, 1996; Planavsky et al. (2010b)) indicating that negative Ce anomalies indeed existed before the GOE, which, in turn, suggests the presence of oxygen in the oceans. Not surprisingly, evidence for an early appearance of oxygenic photosynthesis has grown in recent years, and now includes signs of oxidative cycling of Cr at 3.7 Ga and U at 3.2 Ga, (Frei et al. (2016) and Satkoski et al. (2015), respectively), negatively fractionated $\delta^{98}\text{Mo}$ that correlate with Fe/Mn ratios in the 2.95 Ga Sinqeni Formation, Pongola Supergroup (Planavsky et al., 2014), and Fe and S isotope data indicating oxygen production in surface waters of the 2.97 Ga Chobeni Formation, also from the Pongola Supergroup (Eickmann et al., 2018). The negative Ce anomalies identified here by laser ablation (Fig. 3.15) suggest that the search for early signs of oxygenic photosynthesis may benefit from the small-scale, high spatial resolution approach offered by *in situ* analytical techniques such as LA-HR-ICP-MS. Further micro-scale analysis is warranted for formations that have previously shown a lack of negative Ce anomalies in bulk digestions, especially considering the uncertainty associated with differing estimates for the origins of the appearance of oxygenic photosynthesis using genetic approaches (e.g., Shih et al., 2016; Ward et al., 2016, Mangnabosco et al., 2018) and those of geochemical indicators (e.g., Planavsky et al., 2014; Satkoski et al., 2015).

The iron in BIFs is generally considered to have been sourced from hydrothermal activity, then upwelled onto the shelf where it was ultimately deposited (e.g., Holland, 1973, 1978; Bekker et al., 2014; Konhauser et al., 2017). In this regard, the peak in BIF deposition at ~ 2.45 Ga (Isley, 1995; Klein, 2005) seemingly coincides with the emplacement of large igneous provinces and enhanced mantle plume activity. Since the

iron is sourced from hydrothermal processes, the secular decline observed in Eu anomalies preserved in BIFs through time (see Fig. 5 in Konhauser et al., 2017) has traditionally been interpreted to represent a waning hydrothermal flux (e.g., Derry and Jacobsen, 1990; Bau and Möller, 1993, Viehmann et al., 2015). While not as stark of a trend as that presented in Konhauser et al. (2017), the Eu-anomalies presented here (Fig. 3.14) show a progressive decline with increasingly younger formations, re-enforcing the idea that high temperature hydrothermal inputs to BIF depositional settings declined progressively into the earliest Paleoproterozoic.

Estimates for BIF depositional rates are uncertain and range in values from a few hundred years to tens of thousands of years per meter of compacted BIF, equating to an accumulation of <1mm/year (Morris, 1993; Konhauser et al., 2002, Bekker et al., 2014). When considering consolidation rates on top of these estimates, it is more than likely that a few mm's of BIF represent a depositional period spanning decades, if not hundreds of years. Accordingly, it may be expected that during deposition, currents and nutrient fluxes in the depositional basin changed. A recent study by Warchola et al. (*in review*) highlights this possibility. Through the examination of a high-resolution chemostratigraphic profile of the Boolgeeda Iron Formation, the terminal deposit in the Hamersley Basin, the authors identify a pseudo-sinusoidal shift in trace and REE+Y abundances linked to shifting detrital input, attributable to transgressive and regressive events over the course of a signal BIF unit being deposited. As such, some of the variability observed in the trace element concentrations within a BIF deposit are likely a function of localized environmental signals, detectable via high resolution chemostratigraphy but that are masked by the overall

first-order trends observed in large temporal compilations (e.g., Konhauser et al., 2009, 2015; Robbins et al., 2013).

Despite a number of instances where bulk and laser data differ significantly for a given sample (Figs. 3.3-3.5), it is encouraging that the patterns observed in our sample set coincide well with previously identified temporal trends in trace nutrients, RSE, and REE+Y anomalies such as $\text{Eu}/\text{Eu}^*_{\text{PAAS}}$. This suggests that while both bulk digestion and laser ablation data are capable of reproducing paleomarine seawater trends in trace element concentrations, that laser ablation analyses may provide a more detailed picture of the environmental signal capture by within a single BIF deposit.

3.5.2.2 Trace element removal pathways

The scaling between selected transition metals was examined for the correspondence to the expected stoichiometric ratios of proposed exit fluxes for trace elements in BIFs (Fig. 3.12). We examined scaling to assess whether transition metal systematics can shed additional light on the mechanisms behind trace element sequestration, the dominant controls on BIF deposition, and how different mechanisms of deposition may have lead to variations in trace metal concentrations in BIFs. Konhauser et al. (2018) argued that the trace element stoichiometry of the Dales Gorge Member closely relates to the cellular stoichiometry of anoxygenic phototrophs and thus indicates a role for these bacteria in BIF deposition. Commonly envisioned sequestration mechanisms for trace elements to BIF include the contribution of detrital material, the adsorption of trace elements to hydrous ferric oxides (e.g., Dzombak and Morel, 1990; Bjerrum and Canfield, 2002, Konhauser et al., 2009), and the association of trace elements with biomass (Konhauser et al., 2002, 2018; Li et al., 2011; Martinez et al., 2016). Overlain on cross-plots of transition metals are scaling ratios

(Table 3.1) that can be expected for several possible vectors that may have sequestered trace elements into BIFs. These scaling ratios were derived from elemental ratios of upper continental crust (Condie, 1993; Rudnick and Gao, 2014), the relative strength of adsorption constants of trace elements to hydrous ferric oxides (Dzombak and Morel, 1990), ratios present in modern seawater (Bruland et al., 2014), and, where possible, stoichiometric ratios characteristic of biomass of the marine photoferrotroph *Rhodovulum iodosum* (Konhauser et al., 2018). The scaling expected due to adsorption to hydrous ferric oxides is represented by the ratio of the site-1 binding constants of Dzombak and Morel (1990) for the respective trace metals.

Curiously, the expected stoichiometric ratios for these exit pathways (Table 3.1) seem to correlate well with transition metal scaling preserved within BIFs by both bulk digest and laser data (Fig. 3.16). Laser and bulk solution data both show a near-linear scaling between transition metals essential for biological functions and those that are mobilized by oxidative weathering (Cr vs. Ni, Mo vs. Zn; Figs. 3.16 A & C, respectively). A clear correspondence is observable between all transition metals and expected detrital, seawater, and phototroph stoichiometries. Further, in most cases, there is also a strong adherence to scaling predicted by ratios of adsorption constants for hydrous ferric oxides as measured by Dzombak and Morel (1990). Figure 3.16B highlights the scaling of Cr relative to Mo, elements that can form oxyanions in solution. Interestingly, most samples fall either on or immediately below the scaling expected based on the ratio of adsorption constants for Mo and Cr oxyanions to hydrous ferric oxides (Dzombak and Morel, 1990). This may indicate these elements were mobilized by oxidative weathering before being adsorbed as oxidized species. This is further supported by a large deviation from the

Cr³⁺/MoO₄²⁻ scaling lines, but the strong adherence to the CrO₄²⁻/MoO₄²⁻ adsorption constant ratio.

As the majority of stoichiometries for exit fluxes are quite convergent (Fig. 3.16A & D), it is unlikely that in most cases the sequestration mechanism can be delineated using the transition metal systematics of two selected trace elements. As such a holistic approach that considers multiple trace metals simultaneously, such as that employed by Konhauser et al. (2018), is required to elucidate further information on BIF depositional mechanisms. However, it is quite interesting that both Mo relative to Zn, and Ni relative to Zn, plot closely to the anoxygenic photoferrotroph line derived from the stoichiometries characteristic of *Rhodovulum iodolum* biomass (Konhauser et al., 2018), as one would expect if anoxygenic phototrophs played a large role in BIF deposition.

3.5.2.3 Diagenesis

Effectively all minerals found in present day BIFs are the result of diagenesis and metamorphism following deposition of the initial iron precursors (Klein, 2005; Bekker et al., 2014; Konhauser et al., 2017). Accordingly, a critical aspect of exploiting the BIF record is understanding the fate of trace elements during burial and how the trace element distribution in various mineral phases may be a function of the diagenetic and/or metamorphic repartitioning. The current mineralogy of BIFs, namely hematite, magnetite, chert, siderite, and a variety of accessory Fe silicates, reflects both the primary precursor phases and the cumulative effects of diagenesis to low grade metamorphism (Klein, 2005). It is probable that the hematite forms through the dehydration and thermal maturation of a precursor phase such as ferrihydrite (e.g., Ahn and Buseck, 1990; Sun et al., 2015), while magnetite and siderite are likely the products of Fe(III) reduction coupled to the oxidation

of organic carbon (e.g., Konhauser et al., 2005; Johnson et al., 2008). Consistent with this view, experimental diagenetic incubations of a simple admixture of ferrihydrite and glucose (as a proxy for organic carbon) at 170°C and 1.2 kbar, conditions considered to be representative for recrystallization from ferrihydrite to hematite in the Penge Iron Formation, South Africa (e.g., Miyano and Klein, 1984), have been shown to reproduce a mineralogy characteristic of modern-day BIF (e.g., Posth et al., 2013; Köhler et al., 2013). Recent thermochemical Fe(III) reduction experiments (Halama et al., 2016), however, complicate this view as no magnetite was observed when biomass was incubated with either ferrihydrite, goethite, or hematite at 170°C and 1.2 kbar. This suggests that more recalcitrant forms of biomass adsorbed to the mineral surface may insulate against mineral transformations, or that short term experiments are insufficient for recreating the diagenetic reactions that produce the characteristic stable mineral phases when a more recalcitrant organic carbon source is provided. What is certain is that the modern mineralogy of BIFs reflects burial diagenesis and metamorphism.

Banded iron formations of various ages have been shown to retain seawater-like REE+Y patterns despite undergoing a range of metamorphic conditions up to, and including, amphibolite facies metamorphism (Bau, 1993; Bau and Dulski, 1996; Bohlar et al., 2004; Pecoits et al., 2009; Mloszewska et al., 2012; Haugaard et al., 2016), indicating that an authigenic marine signal is retained even after diagenesis and metamorphism. Additionally, experimental incubations of ferrihydrite doped with Zn and Ni designed to capture the transition of precursor hydrous ferric oxides to hematite and more crystalline Fe phases have shown that transition metals may be retained by the resultant mineral phases following BIF diagenesis (Robbins et al., 2015), although the distribution amongst specific

mineral phases was not examined. The localized mobilization of trace elements during diagenesis and metamorphism can never be expressly ruled out, and likely occurs at very fine spatial scales. For instance, Alibert (2016) demonstrated that the concentration of REE+Y in certain minerals, namely apatite and ankerite, reflects diagenetic processes in BIFs, while hematite and magnetite tend to show REE+Y patterns reflective of porewater adsorption processes. Despite this repartitioning, Alibert (2016) demonstrate that diagenetic to metamorphic minerals – e.g., apatite, hematite, siderite – may retain seawater-like REE+Y patterns but differ with respect to concentration. Accordingly, the analysis of either trace element rich or poor mineral phases by LA-HR-ICP-MS will induce a greater spread in concentration within a given BIF sample than would otherwise be observed in bulk digests of the same sample.

3.5.3 Implications for the interpretation of environmental signal in banded iron formations

The observed spread in trace element concentrations, and trace element to iron ratios, in temporal records (Konhauser et al., 2009; 2015; Robbins et al., 2013, 2016; Partin et al., 2013a; Swanner et al., 2014) is likely due in part to heterogeneity at the mineral and hand-sample scale, but also in part to temporal changes in the concentration of trace elements in seawater. It is worth noting that there are several instances where trace element concentrations fluctuate relative to stratigraphically adjacent samples, and while this fluctuation may be present, even if slightly attenuated in mean bulk values, it also bears out in the respective hematite and/or magnetite mean values. Examples can be seen in Figs. 3.8F, 3.9C, 3.10E, & 3.11C. In Fig. 3.8E, the bulk value of sample 090710-2 is slightly elevated over the neighboring samples and coincides with an increase in Ni in magnetite

grains within this sample, while the hematite averages and range are similar to the adjacent samples. Similarly, an increase in Cu concentration in two samples from the Joffre Member, DD98-7 and DD98-12 (Fig. 3.9C), are reflected both in bulk digest and laser ablation generated data. This also bears out for several samples with respect to U in the Joffre Member and NSB BIF samples (Fig. 3.11C & E), where changes in bulk mean values are reflected by increases or decreases in mineral specific averages between adjacent samples. This would suggest that the observed range in trace metal concentrations from within a given formation may itself be a reflection of subtle, more nuanced chemostratigraphic changes during the deposition of a given formation, that may be obscured in large compilations where the emphasis is on longer term, more dramatic first-order shifts in trace metal availability (e.g., Robbins et al., 2016).

While bulk digests likely offer a more conservative reflection of seawater composition, they may be ill-suited for capturing the true temporal variation in trace element enrichments within a given deposit, as some geochemical signals present at the mineral scale may be diluted or entirely cryptic. For instance, negative Ce anomalies are captured in laser ablation data from several formations, including the ≥ 3.75 Ga NSB, Joffre Member, and Weeli Wolli Iron Formation, while bulk rock data show muted or absent anomalies (Fig. 3.15). True negative Ce anomalies are observed in laser data from the NSB BIF, (Fig. 3.15), which might be indicative of localized oxygen production at low levels during the deposition of NSB sediments. Alternatively, the negative Ce-anomaly observed in the NSB could be due to recent oxidative weathering of samples exposed at or close to the surface, or the partitioning of REE+Y during metamorphism of this unit. In order to resolve these possibilities, either a detailed comparison between hand samples collected at

the surface and fresh drill core would be required, or the Ce-anomaly could be directly dated using the La-Ce geochronometer (Köhler et al., in prep) Similarly, the exclusive consideration of bulk digestion data may dilute certain geochemical signals. The spike in BIF Cr concentrations identified by Konhauser et al. (2011) and attributed to the aerobic oxidation of pyrite on land and subsequent transport of Cr to BIF depositional basins is observable in bulk digest data, but even more pronounced in Cr records generated by LA-HR-ICP-MS (see their Fig. 1). Examples such as these suggest that when evaluating temporal records of BIF composition, an approach that utilizes a combination of laser and bulk digestion data is necessary to capture the range and variation of trace element concentrations within a given deposit and when comparing BIFs through time.

3.5.4 A suggested methodology for future studies

It is clear that some differences in average values may be attributed to analytical methods (Figs. 3.3-5), and that some geochemical signals such as (e.g., Ce/Ce*_{PAAS}; Fig. 3.15) may be diluted by bulk digestions. Accordingly, future studies focused on BIF chemostratigraphy should employ the following recommendations:

(i) When investigating long term temporal trends, a mixture of bulk and laser ablation analyses should be used along with a statistical approach to analyzing the time series. Such a statistical approach may include time binning analyses and then examining differences between temporal averages and their respective two-sigma standard deviations. Methods such as these have recently been used to examine P in shales (e.g., Reinhard et al., 2017) as well as Zn/Fe ratios in carbonates (Liu et al., 2016). This approach could be complimented with a random bootstrap resampling of the data in order to statistically assess the validity of the time bin averages (e.g., Reinhard et al., 2017). This would have the added

benefit of effectively minimizing the impact of extraneous sample values generated by laser ablation when examining long-term temporal trends by placing emphasis on changes in average formation values.

(ii) When investigating signals that are prone to dilution and that are likely to be masked by bulk digestions (e.g., Ce/Ce^*_{PAAAS}), high-resolution *in-situ* techniques, such as LA-HR-ICP-MS should be employed, as the likelihood of detection by bulk digestion alone is unlikely. Yet, caution must be taken as it has recently been demonstrated that negative Ce/Ce^*_{PAAAS} anomalies in outcrop samples may be the result of recent oxidative weathering (Köhler et al., *in review*). Accordingly, any negative Ce/Ce^*_{PAAAS} values identified by LA-HR-ICP-MS, especially in outcrop samples such as those of the NSB, would need to be verified by additional geochemical investigations or the identification of other unambiguous oxidative signals in pristine drill core. Additionally, LA-HR-ICP-MS is critical for capturing the full range of trace element values recorded in BIF, and it is important to still visualize the range of values recorded as changes in maximum values may still reflect events with an environmental significance (e.g., Cr, Konhauser et al., 2011).

3.6 Conclusions

Although BIFs are critical archives for understanding the trace element and redox evolution of seawater, the variance of trace element concentrations and trace element to iron ratios within a given deposit, and the comparability of laser ablation to bulk rock digestion data has remained enigmatic. Intra-formational comparisons of bulk digestion versus LA-HR-ICP-MS data reveal that some of the variation observed within a given BIF deposit is derived from heterogeneity at the micro-scale, as one may well expect. Mean formation

values for bulk versus laser ablation data, however, can differ significantly for a given BIF sample, but are typically within an order of magnitude of each other. This suggests an overall fidelity of the BIF record in capturing authigenic seawater signatures at a variety of scales, but also an inherent need to examine both bulk digestion and laser ablation data to capture the full range of information recorded in the elemental composition of BIFs. As variability is generally less for solution mode analyses of bulk samples, these samples likely provide more conservative estimates for ancient seawater but, as a result, may dilute or obscure geochemical signals that can be detected using a higher-resolution *in situ* technique such as LA-HR-ICP-MS. For instance, we found previously undocumented negative Ce anomalies in Archean to Paleoproterozoic BIFs at the grain scale that are cryptic at the bulk-rock scale. These negative Ce anomalies, generally considered indicative of oxygen at the time of formation, have been identified in BIF samples from the ≥ 3.75 Ga NSB. Whether these are the result of an ancient oxygenic phototrophic metabolism or the result of more recent outcrop weathering remains a critical question for future research. The results presented here highlight the advantage of a combined approach utilizing both bulk and LA-HR-ICP-MS geochemical analyses of BIFs to assess the trace element and redox evolution of ancient seawater. While no single cause for the variability can be unambiguously identified, variation in trace element concentrations within a given formation are likely the combination of subtle shifts in environmental controls, vectors delivering the trace elements to the BIFs, and localized diagenetic to metamorphic effects. Nonetheless, the BIF record captures first-order trends in trace element abundances consistent with other marine chemical sedimentary records (e.g., black shales, pyrites),

supporting the assertion that these are archiving changes in Precambrian seawater composition.

3.7 References

- Ahn, J.H., Buseck, P.R., 1990. Hematite nanospheres of possible colloidal origin from a Precambrian banded iron formation. *Science* 250, 111–113.
- Alibert, C., 2016. Rare earth elements in Hamersley BIF minerals. *Geochimica et Cosmochimica Acta* 184, 311–328.
- Anbar, A.D., Knoll, A.H., 2002. Proterozoic ocean chemistry and evolution: A bioinorganic bridge? *Science* 297, 1137–1142.
- Barley, M.E., Pickard, A., Sylvester, P., 1997. Emplacement of a large igneous province as a possible cause of banded iron formation 2.45 billion years ago. *Nature* 385, 55–58.
- Bau, M., 1993. Effects of syn-and post-depositional processes on the rare-earth element distribution in Precambrian iron-formations. *European Journal of Mineralogy* 5, 257–267.
- Bau, M., Möller, P., 1993. Rare earth element systematics of the chemically precipitated component in Early Precambrian iron formations and the evolution of the terrestrial atmosphere-hydrosphere-lithosphere system. *Geochimica et Cosmochimica Acta* 57, 2239–2249.
- Bau, M., Dulski, P., 1996. Distribution of yttrium and rare-earth elements in the Penge and Kuruman iron-formations, Transvaal Supergroup, South Africa. *Precambrian Research* 79, 37–55.

- Bekker, A., Slack, J.F., Planavsky, N., Krapez, B., Hofmann, A., Konhauser, K.O., Rouxel, O.J., 2010. Iron Formation: The Sedimentary Product of a Complex Interplay among Mantle, Tectonic, Oceanic, and Biospheric Processes. *Economic Geology* 105, 467–508.
- Bekker, A., Planavsky, N., Krapez, B., Rasmussen, B., Hofmann, A., Slack, J., Rouxel, O.J., Konhauser, K.O., 2014. Iron formations: their origins and implications for ancient seawater chemistry, in: Holland, H.D., Turekian, K. (Eds.), *Treatise on Geochemistry*. *Treatise on Geochemistry*. Second edition, Elsevier Ltd., pp. 561–628.
- Bjerrum, C.J., Canfield, D.E., 2002. Ocean productivity before about 1.9 Gyr ago limited by phosphorus adsorption onto iron oxides. *Geology* 417, 159–162.
- Bolhar, R., Kamber, B., Moorbath, S., Fedo, C., Whitehouse, M., 2004. Characterisation of early Archaean chemical sediments by trace element signatures. *Earth and Planetary Science Letters* 222, 43–60.
- Bruland, K.W., Middag, R., Lohan, M.C., 2014. Controls of Trace Metals in Seawater, in: Holland, H.D., Turekian, K. (Eds.), *Treatise on Geochemistry*. Second edition. Elsevier Ltd., Vol. 8. pp. 19–51.
- Cates, N., Mojzsis, S., 2007. Pre-3750 Ma supracrustal rocks from the Nuvvuagittuq supracrustal belt, northern Québec. *Earth and Planetary Science Letters* 255, 9–21.
- Chi Fru, E., Rodríguez, N.P., Partin, C.A., Lalonde, S.V., Andersson, P.S., Weiss, D.J., Albani, El, A., Rodushkin, I., Konhauser, K.O., 2016. Cu isotopes in marine black

- shales record the Great Oxidation Event. *Proceedings of the National Academy of Sciences* 113, 4941–4946.
- Condie, K.C., 1993. Chemical composition and evolution of the upper continental crust: contrasting results from surface samples and shales. *Chemical Geology* 104, 1–37.
- Cornell, R.M., Schwertmann, U., 2003. *The Iron Oxides*, Second. ed. Wiley-VCH Verlag GmbH & Co. pp. 1-664.
- Davy, R., 1983. Chapter 8 Part A. A Contribution on the Chemical Composition of Precambrian Iron-Formations, in: Trendall, A.F., Morris, R.C. (Eds.), *Iron-Formation Facts and Problems, Developments in Precambrian Geology*. Elsevier, pp. 325–343.
- Davy, R., 1992. Mineralogy and chemical composition of a core from the Weeli Wolli Formation in the Hamersley Basin (No. Record 1991/6). Geological Survey of Western Australia, Perth. pp. 1-103.
- De Carlo, E.H., Green, W.J., 2002. Rare earth elements in the water column of Lake Vanda, McMurdo Dry Valleys, Antarctica. *Geochimica et Cosmochimica Acta* 66, 1323–1333.
- Derry, L., Jacobsen, S., 1990. The chemical evolution of Precambrian seawater: Evidence from REEs in banded iron formations. *Geochimica et Cosmochimica Acta* 54, 2965–2977.
- Dodd, M.S., Papineau, D., Grenne, T., Slack, J.F., Rittner, M., Pirajno, F., O’Neil, J., Little, C.T.S., 2017. Evidence for early life in Earth’s oldest hydrothermal vent precipitates. *Nature* 543, 60–64.

- Dupont, C.L., Butcher, A., Valas, R.E., Bourne, P.E., Caetano-Anollés, G., 2010. History of biological metal utilization inferred through phylogenomic analysis of protein structures. *Proceedings of the National Academy of Sciences* 107, 10567–10572.
- Dzombak, D.A., Morel, F.M.M., 1990. *Surface Complexation Modeling*. Wiley-Interscience. pp. 1-393.
- Eickmann B., Hofmann A., Wille M., Bui T. H., Wing B. A., Schoenberg R, 2018, Isotopic evidence for oxygenated Mesoarchaeon shallow oceans. *Nature Geoscience* 11, 133–138.
- Frei, R., Crowe, S.A., Bau, M., Polat, A., Fowle, D.A., 2016. Oxidative elemental cycling under the low O₂ Eoarchean atmosphere. *Scientific Reports* 6, 21058.
- Friedrich, A.J., Luo, Y., Catalano, J.G., 2011. Trace element cycling through iron oxide minerals during redox-driven dynamic recrystallization. *Geology* 39, 1083–1086.
- Guillong, M., Meier, D.L., Allan, M.M., Heinrich, C.A., Yardley, B.W.D., 2008. SILLS: A MATLAB-based program for the reduction of laser ablation ICP-MS data of homogeneous materials and inclusions. *Mineralogical Association of Canada Short Course 40*, Vancouver, B.C., p. 328-333.
- Halama, M., Swanner, E.D., Konhauser, K.O., Kappler, A., 2016. Evaluation of siderite and magnetite formation in BIFs by pressure–temperature experiments of Fe(III) minerals and microbial biomass. *Earth and Planetary Science Letters* 450, 243–253.
- Haugaard, R., Pecoits, E., Lalonde, S.V., Rouxel, O.J., Konhauser, K.O., 2016. The Joffre banded iron formation, Hamersley Group, Western Australia: Assessing the

- palaeoenvironment through detailed petrology and chemostratigraphy. *Precambrian Research* 273, 12–37.
- Holland, H., 1973. The Oceans: A Possible Source of Iron in Iron-Formations. *Economic Geology* 68, 1169–1172.
- Holland, H.D., 1978. *The Chemistry of the Atmosphere and Oceans*. Wiley, New York, pp. 1–369.
- Hsu J. C. (1996) *Multiple Comparisons. Theory and Methods*. Chapman and Hall, London, England.
- Isley, A., 1995. Hydrothermal plumes and the delivery of iron to banded iron formation. *The Journal Of Geology* 169–185.
- Johnson, C.M., Beard, B.L., Klein, C., Beukes, N., Roden, E., 2008. Iron isotopes constrain biologic and abiologic processes in banded iron formation genesis. *Geochimica et Cosmochimica Acta* 72, 151–169.
- Klein, C., 2005. Some Precambrian banded iron-formations (BIFs) from around the world: Their age, geologic setting, mineralogy, metamorphism, geochemistry, and origins. *American Mineralogist* 90, 1473–1499.
- Köhler, I., Konhauser, K.O., Papineau, D., Bekker, A., Kappler, A., 2013. Biological carbon precursor to diagenetic siderite with spherical structures in iron formations. *Nature Communications* 4, 1741–7.
- Köhler, I., Bonnand, P., Boyet, M., Heubeck, C., Homann, M., Nonotte, P., Konhauser, K.O., Lalonde, S.V., *in prep*, Post-depositional REE mobility in a Paleoproterozoic iron formation revealed by La-Ce geochronology: A cautionary tale for signals of ancient oxygenation. *Earth and Planetary Science Letters*.

- Konhauser, K.O., Hamade, T., Raiswell, R., Morris, R., Ferris, F., Southam, G., Canfield, D., 2002. Could bacteria have formed the Precambrian banded iron formations? *Geology* 30, 1079–1082.
- Konhauser, K.O., Newman, D., Kappler, A., 2005. The potential significance of microbial Fe (III) reduction during deposition of Precambrian banded iron formations. *Geobiology* 3, 167–177.
- Konhauser, K.O., Lalonde, S.V., Amskold, L.A., Holland, H., 2007. Was there really an Archean phosphate crisis? *Science* 315, 1234.
- Konhauser, K.O., Pecoits, E., Lalonde, S.V., Papineau, D., Nisbet, E.G., Barley, M.E., Arndt, N.T., Zahnle, K., Kamber, B.S., 2009. Oceanic nickel depletion and a methanogen famine before the Great Oxidation Event. *Nature* 458, 750–753.
- Konhauser, K.O., Lalonde, S.V., Planavsky, N.J., Pecoits, E., Lyons, T.W., Mojzsis, S.J., Rouxel, O.J., Barley, M.E., Rosière, C.A., Fralick, P.W., Kump, L.R., Bekker, A., 2011. Aerobic bacterial pyrite oxidation and acid rock drainage during the Great Oxidation Event. *Nature* 478, 369–373.
- Konhauser, K.O., Robbins, L.J., Pecoits, E., Peacock, C., Kappler, A., Lalonde, S.V., 2015. The Archean Nickel Famine Revisited. *Nature* 521, 804–815.
- Konhauser, K.O., Planavsky, N.J., Hardisty, D.S., Robbins, L.J., Warchola, T.J., Haugaard, R., Lalonde, S.V., Partin, C.A., Oonk, P.B.H., Tsikos, H., Lyons, T.W., Bekker, A., Johnson, C.M., 2017. Iron formations: A global record of Neoproterozoic to Palaeoproterozoic environmental history. *Earth-Science Reviews* 172, 140–177.
- Konhauser, K.O., Robbins, L.J., Alessi, D.S., Flynn, S.L., Gingras, M.K., Martinez, R.E., Kappler, A., Swanner, E.D., Li, Y.-L., Crowe, S.A., Planavsky, N.J., Reinhard,

- C.T., Lalonde, S.V., 2018. Phytoplankton contributions to the trace-element composition of Precambrian banded iron formations. *Geological Society of America Bulletin*, 130, 941-951.
- Krapez, B., Barley, M.E., Pickard, A.L., 2003. Hydrothermal and resedimented origins of the precursor sediments to banded iron formation: sedimentological evidence from the Early Palaeoproterozoic Brockman Supersequence of Western Australia. *Sedimentology* 50, 979–1011.
- Lalonde, S.V., Smith, D., Owttrim, G., Konhauser, K.O., 2008. Acid-base properties of cyanobacterial surfaces. II: Silica as a chemical stressor influencing cell surface reactivity. *Geochimica et Cosmochimica Acta* 72, 1269–1280.
- Li, Y.L., Konhauser, K.O., Cole, D.R., Phelps, T.J., 2011. Mineral ecophysiological data provide growing evidence for microbial activity in banded-iron formations. *Geology* 39, 707–710.
- Liu, X.M., Kah, L.C., Knoll, A.H., Cui, H., Kaufman, A.J., Shahar, A., Hazen, R.M., 2016. Tracing Earth's O₂ evolution using Zn/Fe ratios in marine carbonates. *Geochemical Perspectives Letters* 2, 24–34.
- Lyons, T.W., Reinhard, C.T., Planavsky, N.J., 2014. The rise of oxygen in Earth's early ocean and atmosphere. *Nature* 506, 307–315.
- Magnabosco, C., Moore, K.R., Wolfe, J.M., Fournier, G.P., 2018. Dating phototropic microbial lineages with reticulate gene histories. *Geobiology* 16, 179-189.
- Martinez, R.E., Konhauser, K.O., Paunova, N., Wu, W., Alessi, D.S., Kappler, A., 2016. Surface reactivity of the anaerobic phototrophic Fe (II)-oxidizing bacterium

- Rhodovulum iodolum: Implications for trace metal budgets in ancient oceans and banded iron formations. *Chemical Geology* 442, 113–120.
- McLennan, S., 1989. Rare Earth Elements in Sedimentary Rocks: Influence of Provenance and Sedimentary Processes, in: Lipin, B.R., McKay, G.A. (Eds.) *Geochemistry and mineralogy of rare earth elements. Reviews in Mineralogy and Geochemistry* 21, 169–200.
- Miyano, T., Klein, C., 1984. Evaluation of the stability relations of amphibole asbestos in metamorphosed iron formations. *Mineral Geology* 33, 213–222.
- Mloszewska, A., Pecoits, E., Cates, N., Mojzsis, S.J., O'Neil, J., Robbins, L.J., Konhauser, K.O., 2012. The composition of Earth's oldest iron formations: The Nuvvuagittuq Supracrustal Belt (Québec, Canada). *Earth and Planetary Science Letters* 317-318, 331–342.
- Mloszewska, A.M., Mojzsis, S.J., Pecoits, E., Papineau, D., Dauphas, N., Konhauser, K.O., 2013. Chemical sedimentary protoliths in the >3.75Ga Nuvvuagittuq Supracrustal Belt (Québec, Canada). *Gondwana Research* 23, 574–594.
- Morris, R., 1993. Genetic modelling for banded iron-formation of the Hamersley Group, Pilbara Craton, Western Australia. *Precambrian Research* 60, 243–286.
- O'Neil, J., Maurice, C., Stevenson, R.K., Larocque, J., Cloquet, C., David, J., Francis, D., 2007. The Geology of the 3.8 Ga Nuvvuagittuq (Porpoise Cove) Greenstone Belt, Northeastern Superior Province, Canada. *Developments in Precambrian Geology* 15, 219–250.
- O'Neil, J., Carlson, R., Francis, D., Stevenson, R., 2008. Neodymium-142 evidence for Hadean mafic crust. *Science* 321, 1828–1831.

- O'Neil, J., Francis, D., Carlson, R.W., 2011. Implications of the Nuvvuagittuq Greenstone Belt for the Formation of Earth's Early Crust. *Journal of Physical Chemistry* 52, 985–1009.
- O'Neil, J., Carlson, R.W., 2017. Building Archean cratons from Hadean mafic crust. *Science* 355, 1199–1202.
- Partin, C.A., Lalonde, S.V., Planavsky, N.J., Bekker, A., Rouxel, O.J., Lyons, T.W., Konhauser, K.O., 2013a. Uranium in iron formations and the rise of atmospheric oxygen. *Chemical Geology* 362, 82–90.
- Partin, C.A., Bekker, A., Planavsky, N.J., Scott, C.T., Gill, B.C., Li, C., Podkovyrov, V., Maslov, A., Konhauser, K.O., Lalonde, S.V., Love, G.D., Poulton, S.W., Lyons, T.W., 2013b. Large-scale fluctuations in Precambrian atmospheric and oceanic oxygen levels from the record of U in shales. *Earth and Planetary Science Letters* 369-370, 284–293.
- Pecoits, E., Gingras, M.K., Barley, M.E., Kappler, A., Posth, N.R., Konhauser, K.O., 2009. Petrography and geochemistry of the Dales Gorge banded iron formation: Paragenetic sequence, source and implications for palaeo-ocean chemistry. *Precambrian Research* 172, 163–187.
- Planavsky, N.J., Rouxel, O.J., Bekker, A., Lalonde, S.V., Konhauser, K.O., Reinhard, C.T., Lyons, T.W., 2010a. The evolution of the marine phosphate reservoir. *Nature* 467, 1088–1090.
- Planavsky, N., Bekker, A., Rouxel, O.J., Kamber, B., Hofmann, A., Knudsen, A., Lyons, T.W., 2010b. Rare Earth Element and yttrium compositions of Archean and Paleoproterozoic Fe formations revisited: New perspectives on the significance

and mechanisms of deposition. *Geochimica et Cosmochimica Acta* 74, 6387–6405.

Planavsky, N.J., Asael, D., Hofmann, A., Reinhard, C.T., Lalonde, S.V., Knudsen, A., Wang, X., Ossa Ossa, F., Pecoits, E., Smith, A.J.B., Beukes, N.J., Bekker, A., Johnson, T.M., Konhauser, K.O., Lyons, T.W., Rouxel, O.J., 2014. Evidence for oxygenic photosynthesis half a billion years before the Great Oxidation Event. *Nature Geoscience* 7, 283–286.

Posth, N.R., Köhler, I., D Swanner, E., Schröder, C., Wellmann, E., Binder, B., Konhauser, K.O., Neumann, U., Berthold, C., Nowak, M., Kappler, A., 2013. Simulating Precambrian banded iron formation diagenesis. *Chemical Geology* 362, 66–73.

Reinhard, C.T., Planavsky, N.J., Gill, B.C., Ozaki, K., Robbins, L.J., Lyons, T.W., Fischer, W.W., Wang, C., Cole, D.B., Konhauser, K.O., 2017. Evolution of the global phosphorus cycle. *Nature* 541, 386–389.

Robbins, L.J., Lalonde, S.V., Saito, M.A., Planavsky, N.J., Mloszewska, A.M., Pecoits, E., Scott, C., Dupont, C.L., Kappler, A., Konhauser, K.O., 2013. Authigenic iron oxide proxies for marine zinc over geological time and implications for eukaryotic metallome evolution. *Geobiology* 11, 295–306.

Robbins, L.J., Swanner, E.D., Lalonde, S.V., Eickhoff, M., Paranich, M.L., Reinhard, C.T., Peacock, C.L., Kappler, A., Konhauser, K.O., 2015. Limited Zn and Ni mobility during simulated iron formation diagenesis. *Chemical Geology* 402, 30–39.

Robbins, L.J., Lalonde, S.V., Planavsky, N.J., Partin, C.A., Reinhard, C.T., Kendall, B., Scott, C., Hardisty, D.S., Gill, B.C., Alessi, D.S., Dupont, C.L., Saito, M.A., Crowe, S.A., Poulton, S.W., Bekker, A., Lyons, T.W., Konhauser, K.O., 2016.

- Trace elements at the intersection of marine biological and geochemical evolution. *Earth-Science Reviews* 163, 323–348.
- Rudnick, R.L., Gao, S., 2014. Composition of the Continental Crust, in: Holland, H.D., Turekian, K. (Eds.), *Treatise on Geochemistry*. Second edition. Elsevier Ltd., Vol. 4. pp. 1–51.
- Sahoo, S.K., Planavsky, N.J., Kendall, B., Wang, X., Shi, X., Scott, C., Anbar, A.D., Lyons, T.W., Jiang, G., 2012. Ocean oxygenation in the wake of the Marinoan glaciation. *Nature* 488, 546–549.
- Satkoski, A.M., Beukes, N.J., Li, W., Beard, B.L., Johnson, C.M., 2015. A redox-stratified ocean 3.2 billion years ago. *Earth and Planetary Science Letters* 430, 43–53.
- Scott, C., Lyons, T.W., Bekker, A., Shen, Y., Poulton, S.W., Chu, X., Anbar, A.D., 2008. Tracing the stepwise oxygenation of the Proterozoic ocean. *Nature* 452, 456–459.
- Scott, C., Planavsky, N.J., Dupont, C.L., Kendall, B., Gill, B.C., Robbins, L.J., Husband, K.F., Arnold, G.L., Wing, B.A., Poulton, S.W., Bekker, A., Anbar, A.D., Konhauser, K.O., Lyons, T.W., 2013. Bioavailability of zinc in marine systems through time. *Nature Geoscience* 6, 125–128.
- Shih, P.M., Hemp, J., Ward, L.M., Matzke, N.J., Fischer, W.W., 2016. Crown group Oxyphotobacteria postdate the rise of oxygen. *Geobiology* 15, 19–29.
- Sun, S., Konhauser, K.O., Kappler, A., Li, Y.-L., 2015. Primary hematite in Neoproterozoic to Paleoproterozoic oceans. *Geological Society of America Bulletin* 127, 850–861.
- Swanner, E.D., Planavsky, N.J., Lalonde, S.V., Robbins, L.J., Bekker, A., Rouxel, O.J., Saito, M.A., Kappler, A., Mojzsis, S.J., Konhauser, K.O., 2014. Cobalt and marine redox evolution. *Earth and Planetary Science Letters* 390, 253–263.

- Taylor, S.R. & McLennan, S.M. 1985. The Continental Crust: its Composition and Evolution - An Examination of the Geochemical Record Preserved in Sedimentary Rocks. Blackwell Scientific Publications, Oxford. pp 1-312.
- Trendall, A.F., Blockley, J.G., 1970. The Iron Formations of The Precambrian Hamersley Group Western Australia With Special Reference to the Associated Crocidolite. Geological Survey of Western Australia Bulletin 119, 1–366.
- Viehmann, S., Bau, M., Hoffmann, J.E., Münker, C., 2015. Geochemistry of the Krivoy Rog Banded Iron Formation, Ukraine, and the impact of peak episodes of increased global magmatic activity on the trace element composition of Precambrian seawater. *Precambrian Research* 270, 165–180.
- Warchola, T., Lalonde, S.V., Pecoits, E., Gunten, K.V., Robbins, L.J., Alessi, D.S., Philippot, P., Konhauser, K.O., 2018. Petrology and Geochemistry of the Boolgeeda Iron Formation, Hamersley Basin, Western Australia. *Precambrian Research* 316, 155–173.
- Ward, L.M., Kirschvink, J.L., Fischer, W.W., 2016. Timescales of Oxygenation Following the Evolution of Oxygenic Photosynthesis. *Origins of Life and Evolution of Biospheres* 46, 51–65.

Table 3.1. Expected stoichiometric scaling for possible exit pathways for trace elements to banded iron formations.

Ratio	Detrital - low*	Detrital - high*	Photoferrotrophs**	Seawater***	Adsorption Constants (K ₁ /K ₁)****
Ni/Zn	0.343	2.448	0.103	0.718	0.240
Mo/Zn	0.016	-	0.001	15.300	3.24x10 ⁸
Cr/Ni	1.744	1.913	-	0.443	48.978
Cr/Mo	40.000	260.000	-	0.021	3.63x10 ⁻⁸
Chromate/Zn	-	-	-	-	7.24x10 ⁹
Chromate/Ni	-	-	-	-	3.02x10 ¹⁰
Chromate/Mo	-	-	-	-	22.387

*Values represent the widest possible range from the combination of Condie (1993) Rudnick and Gao (2014).

**Photoferrotroph values from Konhauser et al. (2018)

***Values from Bruland et al. (2014)

****Based on log K values for site 1 in Dzombak and Morel (1990)

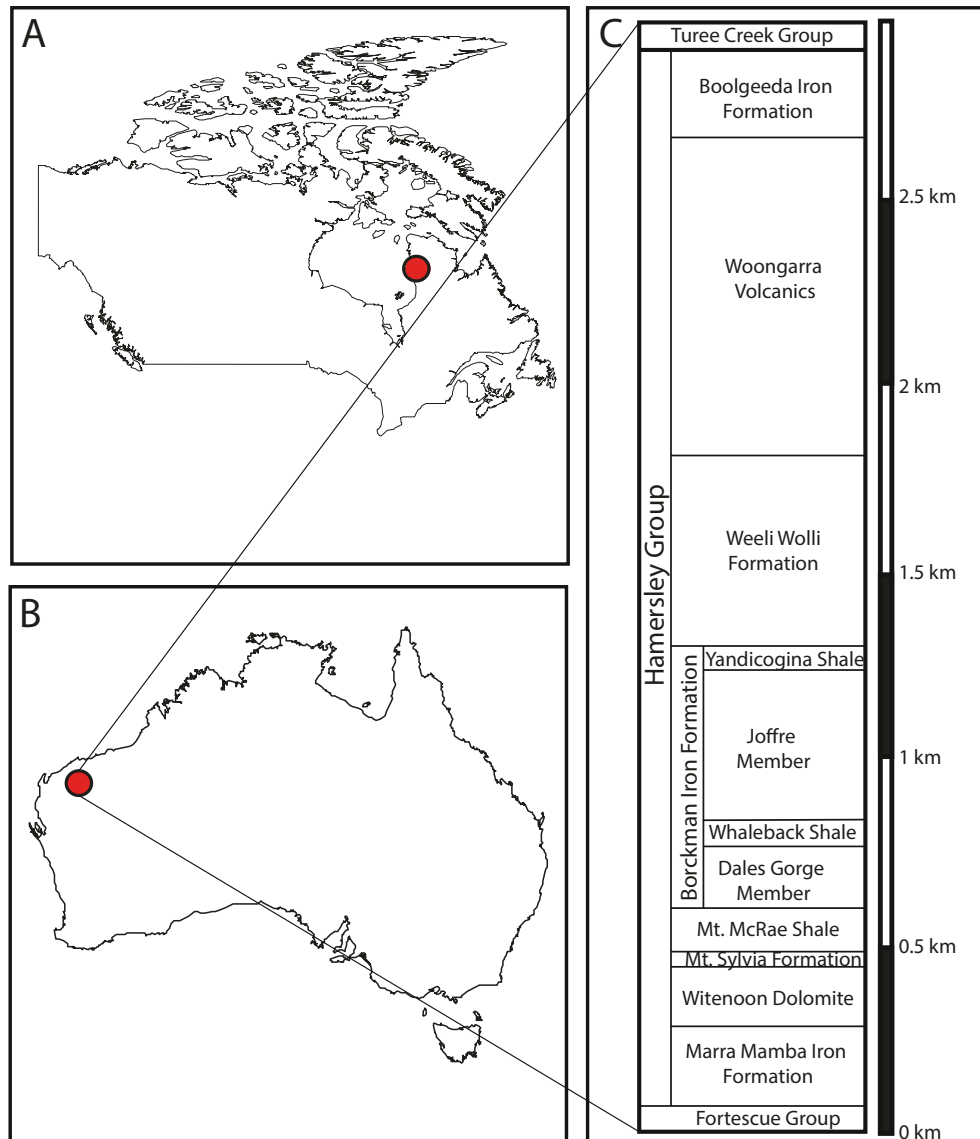


Figure 3.1. Schematic diagram showing the locations of (A) the Nuvvuagittuq Supracrustal belt in northwestern Québec, Canada, and (B) the Hamersley Basin in northwestern Australia. (C) The composite stratigraphic column of the Hamersley Basin, showing the stratigraphic position of the banded iron formations analyzed here (adapted from Pecoits et al., 2009).

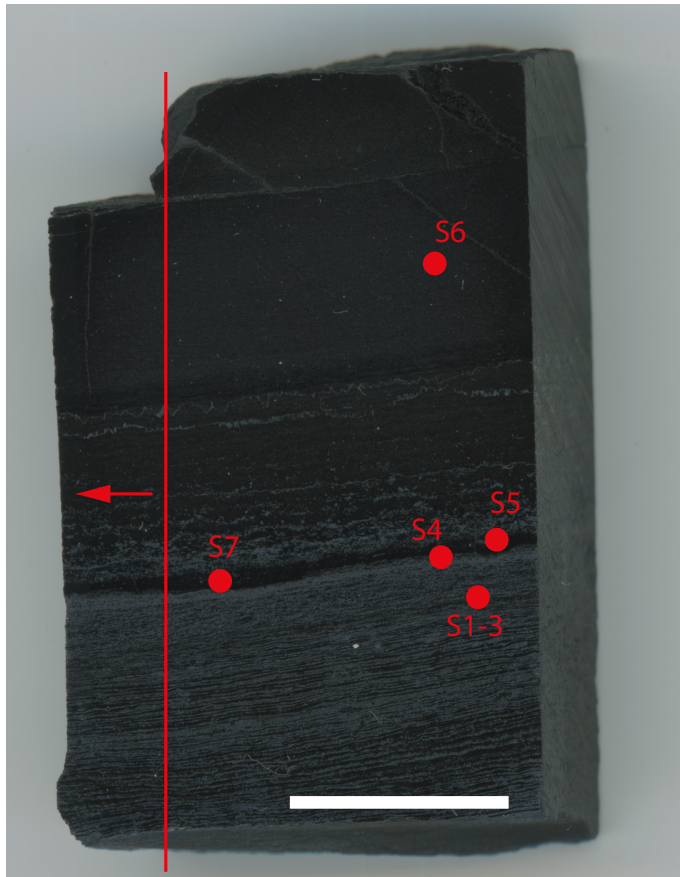


Figure 3.2. Example of a BIF slab sampled for bulk digestion HR-ICP-MS and LA-HR-ICP-MS, in this case sample DD98-7 (Joffre Member, Brockman Iron Formation). After polishing, the portion of the sample to the left of the red line was removed, crushed, and powdered for bulk digestion analysis as described in the methods. The sample to the right of the red line was analyzed by LA-HR-ICP-MS. Each spot (1-7) corresponds to three separate laser ablation shots, 44 μm in diameter, into either hematite or magnetite grains. The averaged laser data is then compared to bulk digestion values to determine if a statistical correspondence exists. In some samples, individual laser shots were more widely distributed, but an effort was made to ensure laser shots were distributed throughout the sample. White bar is 1 cm.

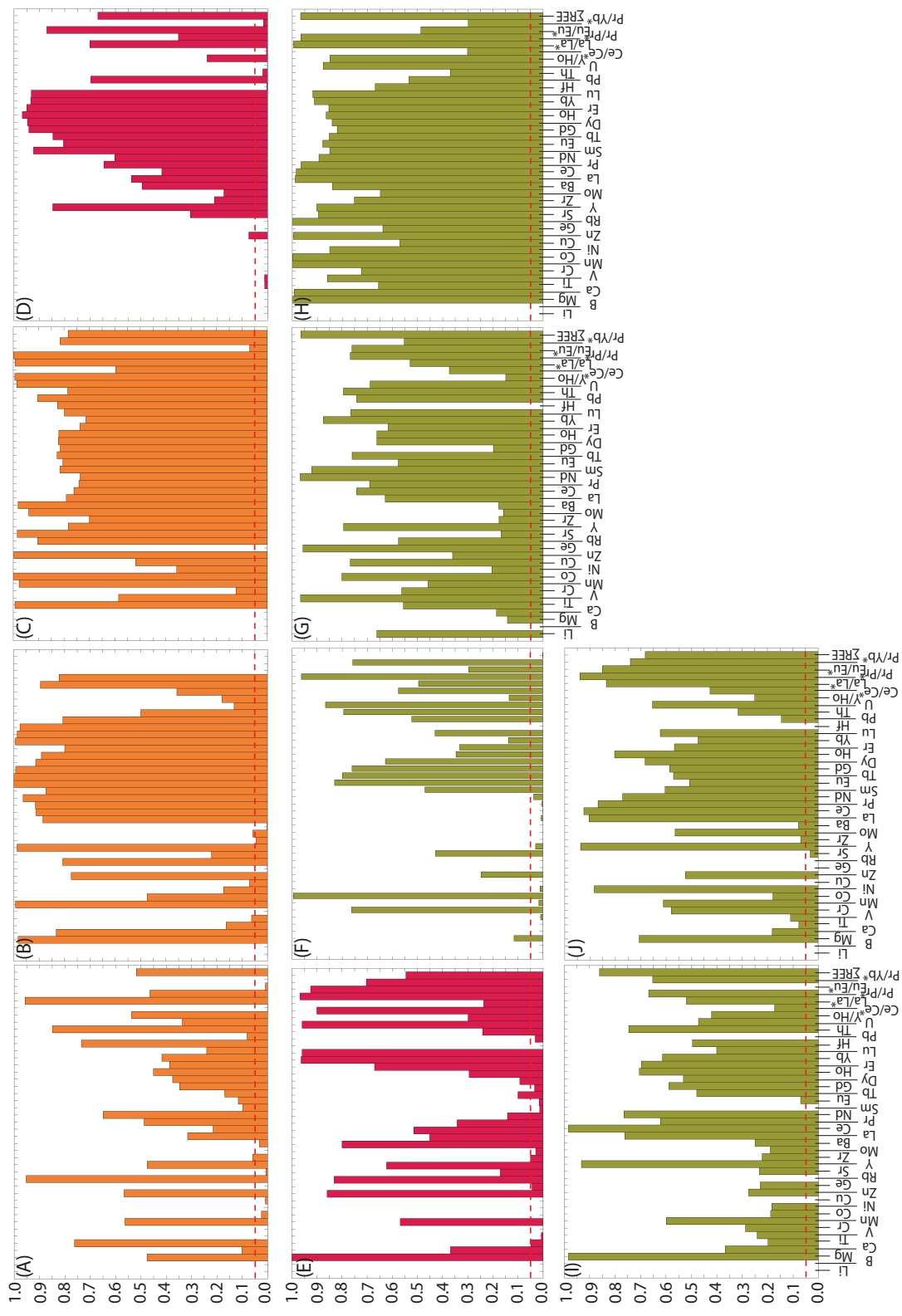


Figure 3.3. Tukey-Kramer results indicating the degree of comparability between bulk digestion generated data and hematite LA-HR-ICP-MS for samples (A) DD98-7, (B) DD98-12, and (C) DD98-21a from the Joffre Member of the Brockman Iron Formation (orange), (D) DD98-26 and (E) DD98-27 from the Dales Gorge Member of the Brockman Iron Formation (red), (F) 090709-4b2, (G) 090709-5, (H) 090710-2, (I) 090710-4, and (J) 090710-12 from the Nuvvuagittuq Supracrustal Belt (green). A p-value greater than 0.05, above the red dashed threshold line, indicates that the average values produced by the compared methodologies are not significantly different.

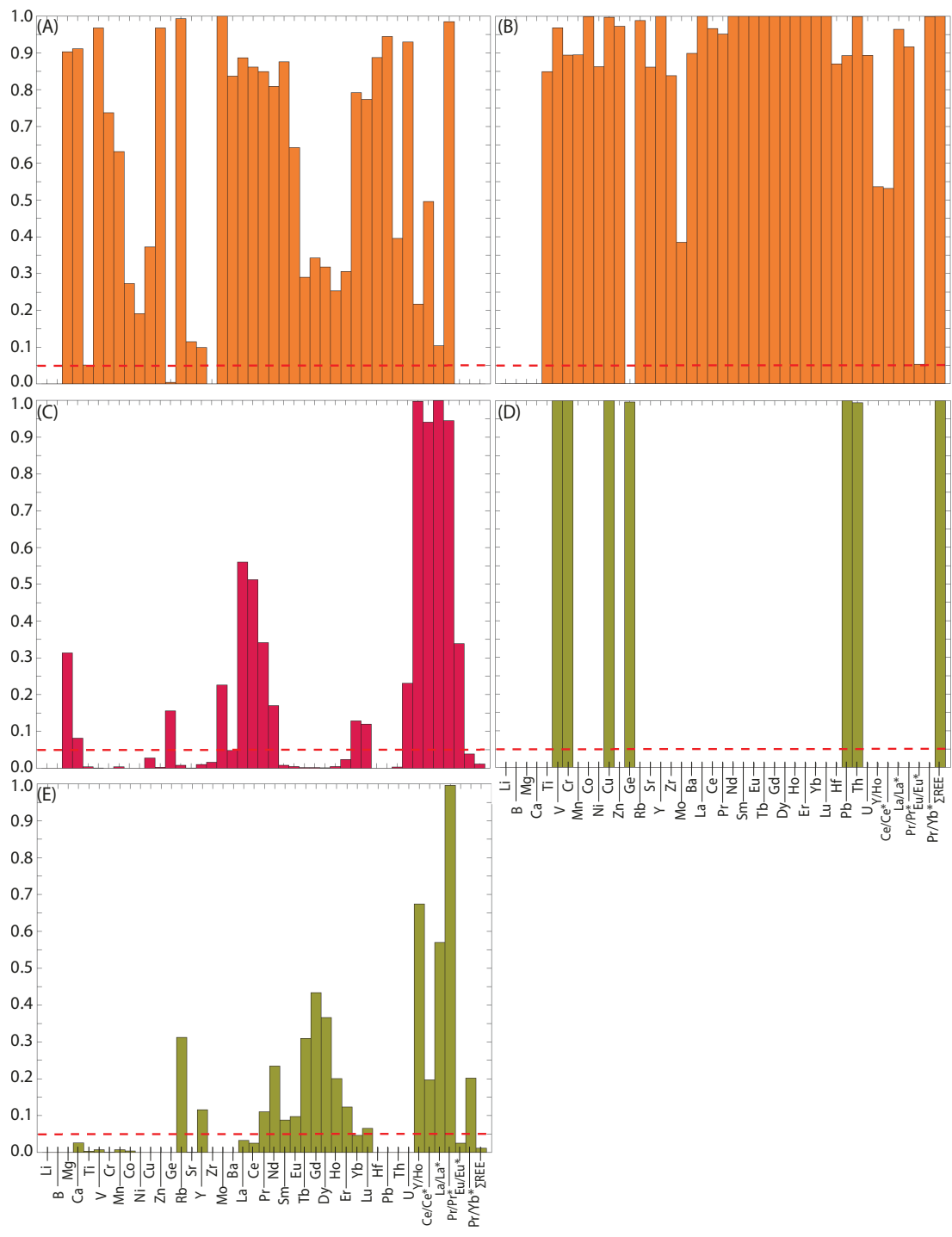


Figure 3.4. Tukey-Kramer results indicating significant differences between bulk digestion data and magnetite LA-HR-ICP-MS analyses for samples (A) DD98-12 and (B) DD98-21a from the Joffre Member of the Brockman Iron Formation (orange), (C) DD98-27 from the Dales Gorge Member of the Brockman Iron Formation (red), and (D) 090709-5 and (E) 090710-2 from the Nuvvuagittuq Supracrustal Belt (green). A p-value greater than 0.05, above the black dashed threshold line, indicates that the average values produced by the compared methodologies are not significantly different. Colours as in previous figure.

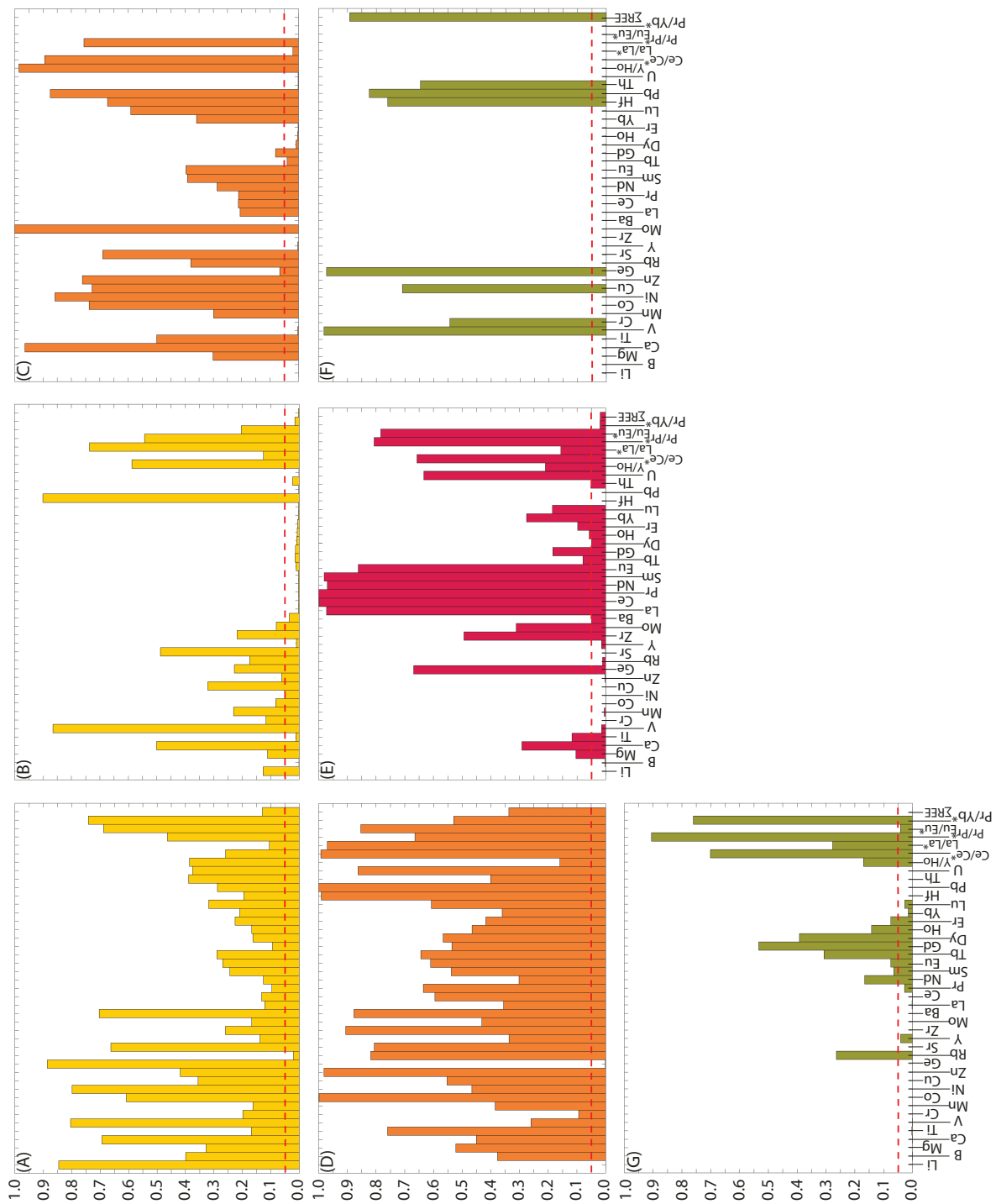


Figure 3.5. Tukey-Kramer results indicating significant differences between hematite and magnetite LA-HR-ICP-MS analyses for samples (A) WW1-9b and (B) WW1-10 from the Weeli Wolli Iron Formation (yellow), (C) DD98-12 and (D) DD98-21a from the Joffre Member of the Brockman Iron Formation (orange), (E) DD98-27 from the Dales Gorge Member of the Brockman Iron Formation (red), and (F) 090709-5 and (G) 090710-2 from the Nuvvuagittuq Supracrustal Belt (green). A p-value greater than 0.05, above the black dashed threshold line, indicates that the average values produced by the compared methodologies are not significantly different.

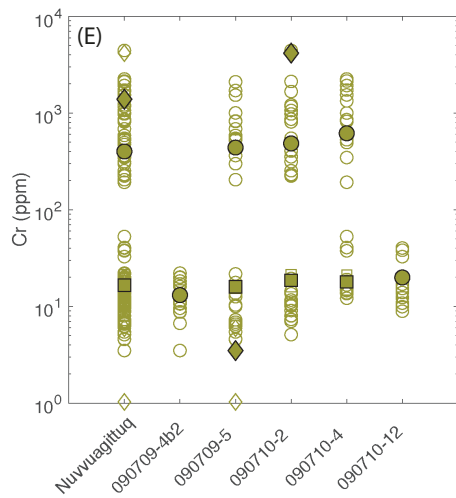
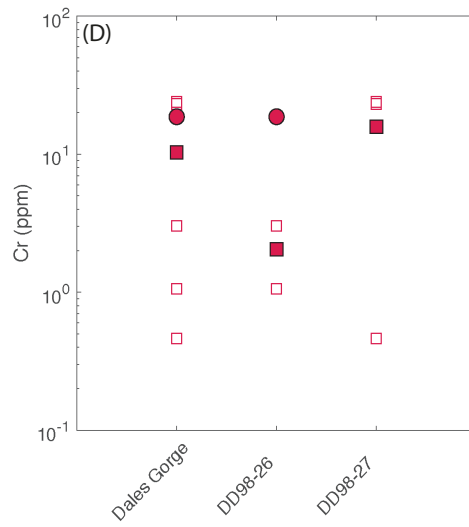
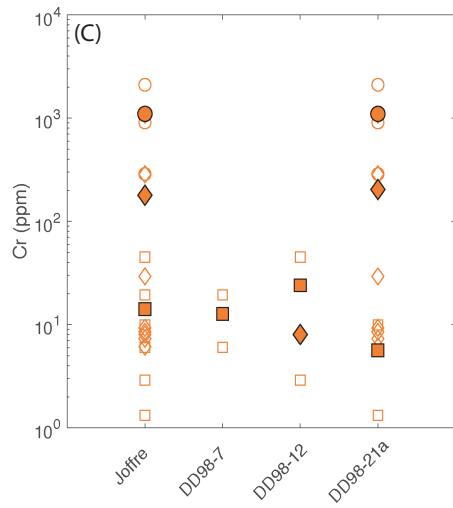
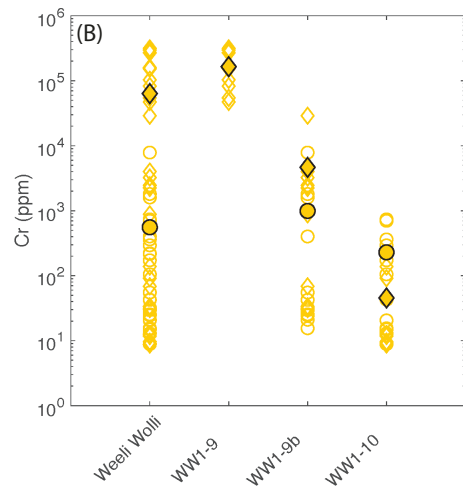
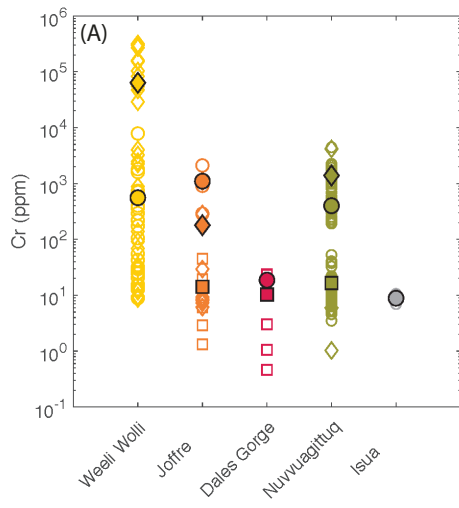


Figure 3.6. Inter-deposit comparison for chromium (A), and intra-deposit comparisons showing the formation cumulative formation data and that of constituent samples for the Weeli Wolli Iron Formation (B), Joffre Member (C) and Dales Gorge Member (D) of the Brockman Iron Formation, and the BIF of the Nuvvuagittuq Supracrustal Belt (E). Open circles represent hematite LA-HR-ICP-MS data, open diamonds represent magnetite LA-HR-ICP-MS data, and open squares represent bulk digestion data. Filled symbols represent the mean values of the respective methodologies. Colours as in Figure 3.5. Note differences in scale.

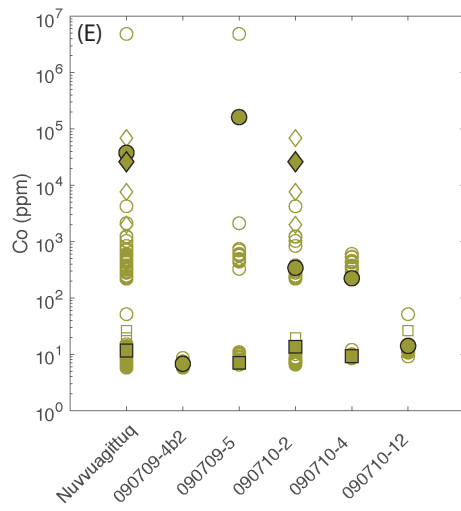
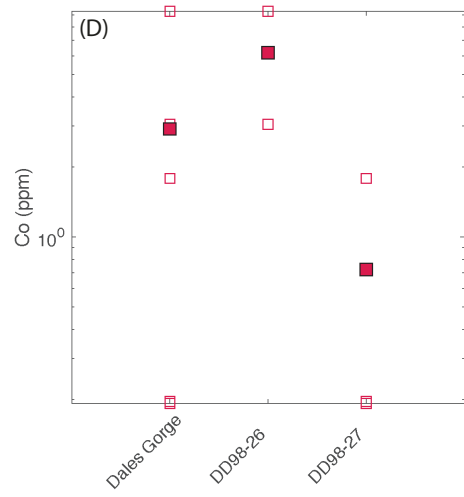
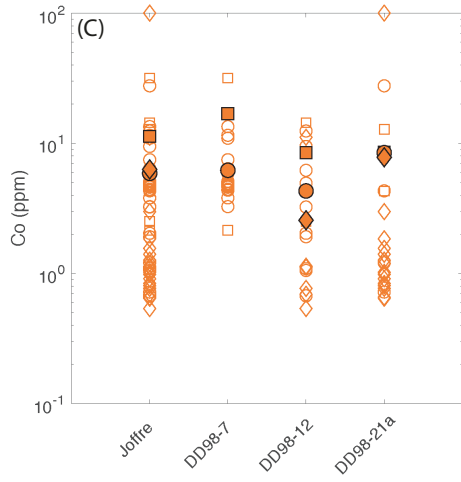
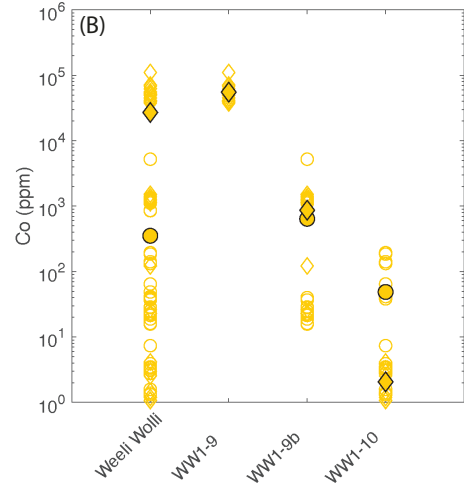
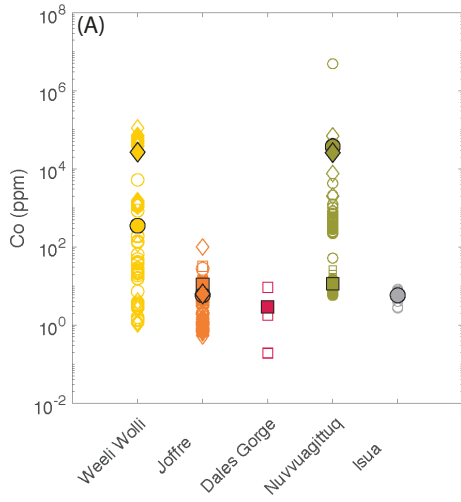


Figure 3.7. Inter-deposit comparison for cobalt (A), and intra-deposit comparisons showing the formation cumulative formation data and that of constituent samples for the Weeli Wolli Iron Formation (B), Joffre Member (C) and Dales Gorge Member (D) of the Brockman Iron Formation, and the BIF of the Nuvvuagittuq Supracrustal Belt (E). Symbols as described in Figure 3.6, colours as in Figure 3.5. Note differences in scale.

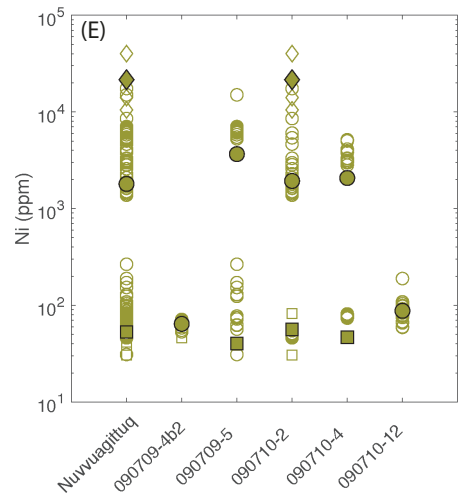
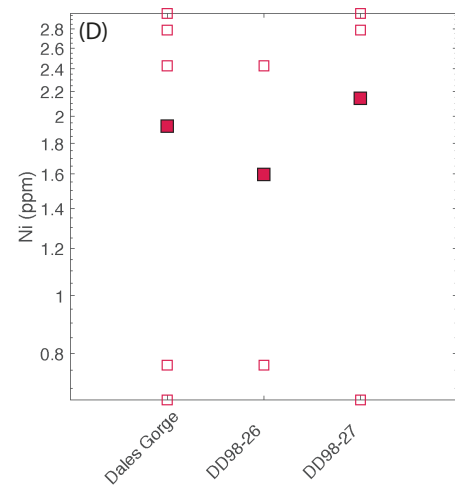
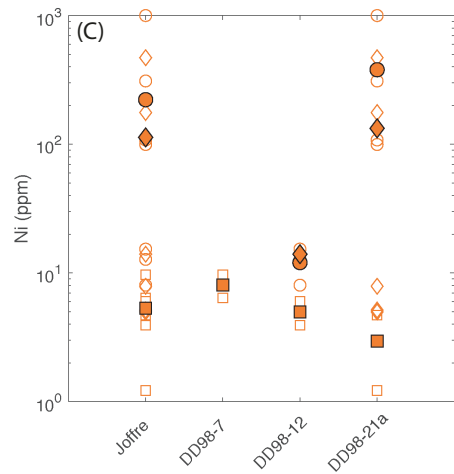
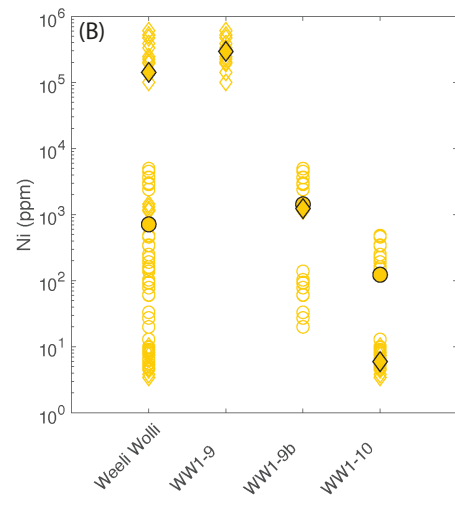
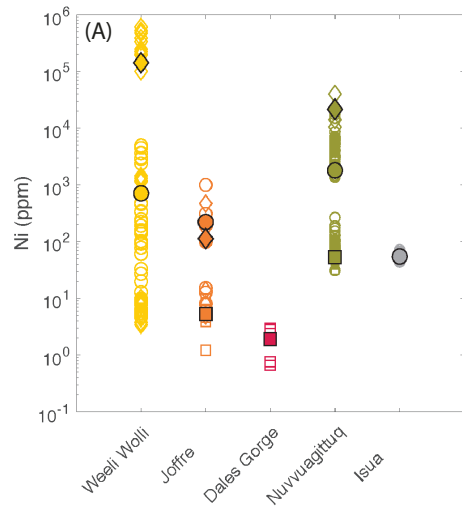


Figure 3.8. Inter-deposit comparison for nickel (A), and intra-deposit comparisons showing the formation cumulative formation data and that of constituent samples for the Weeli Wolli Iron Formation (B), Joffre Member (C) and Dales Gorge Member (D) of the Brockman Iron Formation, and the BIF of the Nuvvuagittuq Supracrustal Belt (E). Symbols as described in Figure 3.6, colours as in Figure 3.5. Note differences in scale.

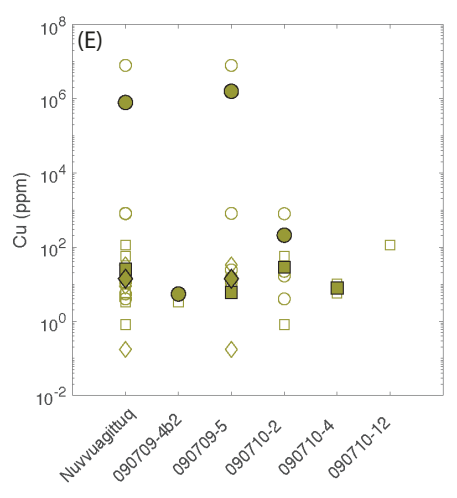
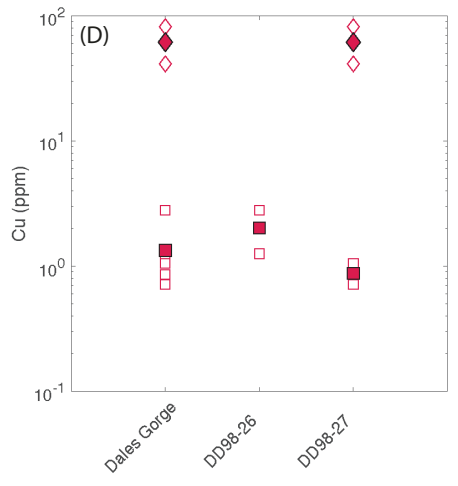
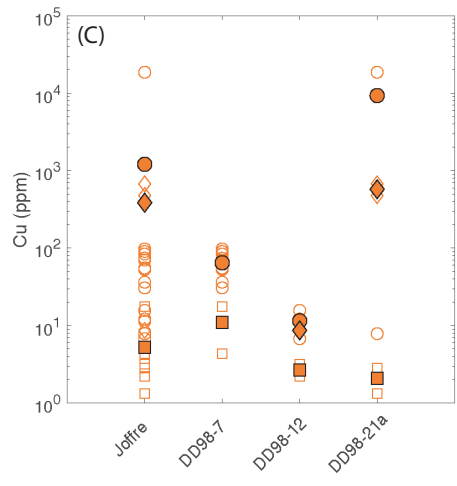
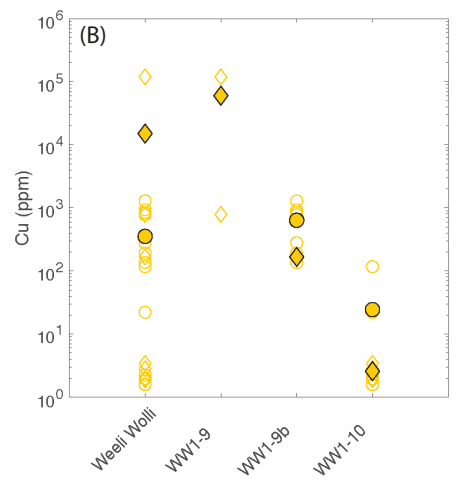
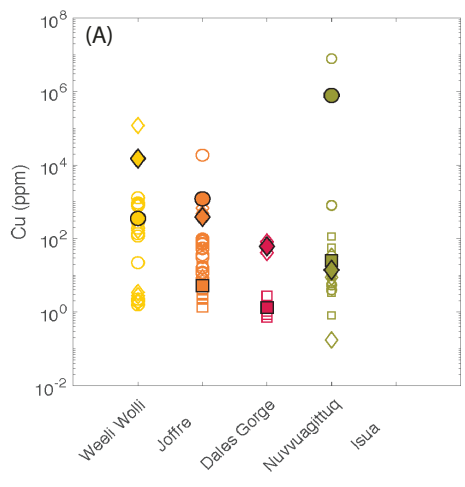


Figure 3.9. Inter-deposit comparison for copper (A), and intra-deposit comparisons showing the formation cumulative formation data and that of constituent samples for the Weeli Wolli Iron Formation (B), Joffre Member (C) and Dales Gorge Member (D) of the Brockman Iron Formation, and the BIF of the Nuvvuagittuq Supracrustal Belt (E). Symbols as described in Figure 3.6, colours as in Figure 3.5. Note differences in scale.

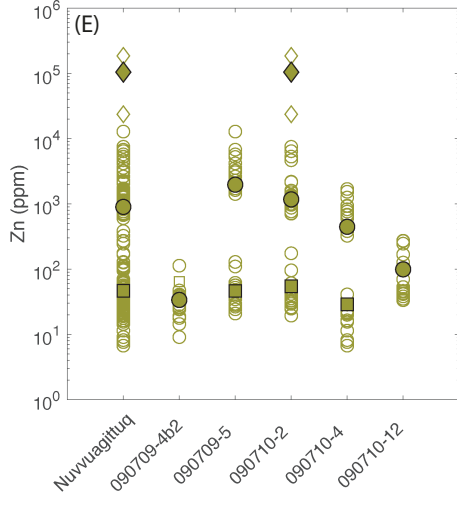
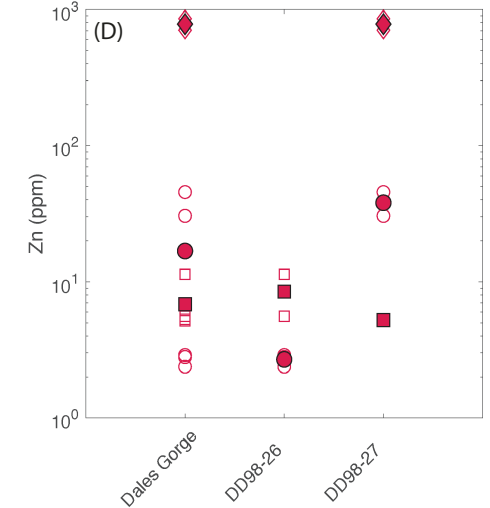
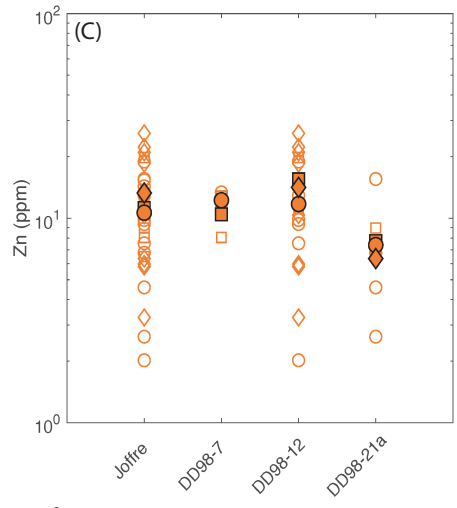
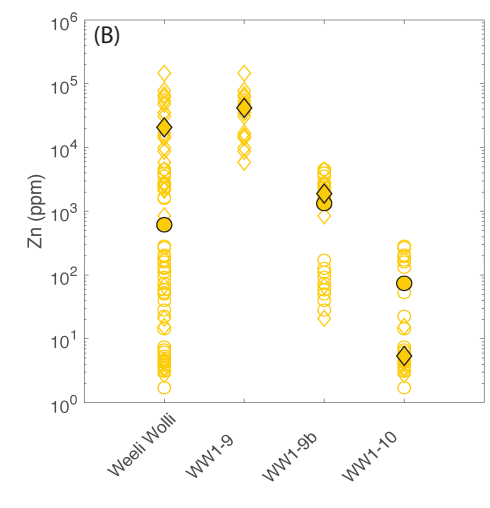
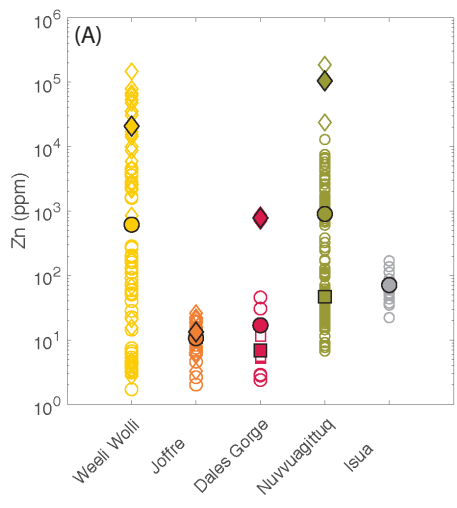


Figure 3.10. Inter-deposit comparison for zinc (A), and intra-deposit comparisons showing the formation cumulative formation data and that of constituent samples for the Weeli Wolli Iron Formation (B), Joffre Member (C) and Dales Gorge Member (D) of the Brockman Iron Formation, and the BIF of the Nuvvuagittuq Supracrustal Belt (E). Symbols as described in Figure 3.6, colours as in Figure 3.5. Note differences in scale.

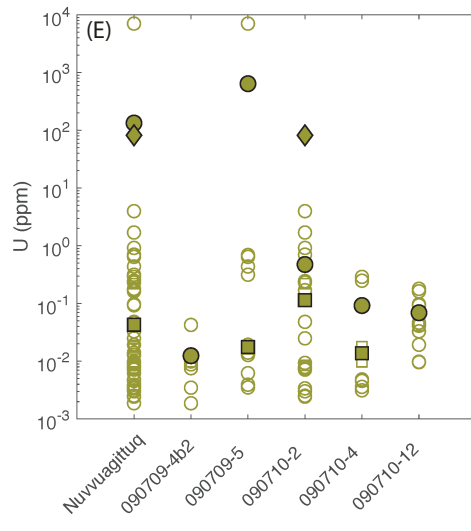
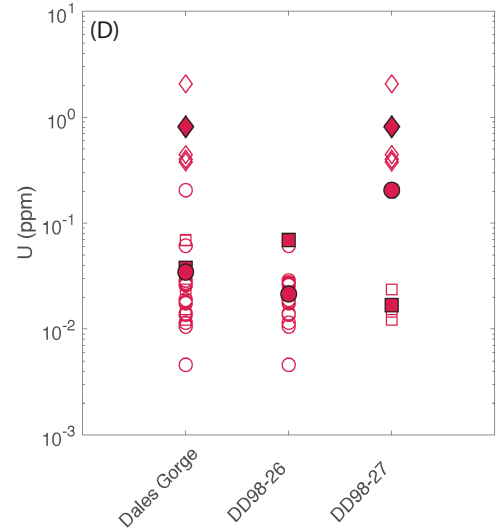
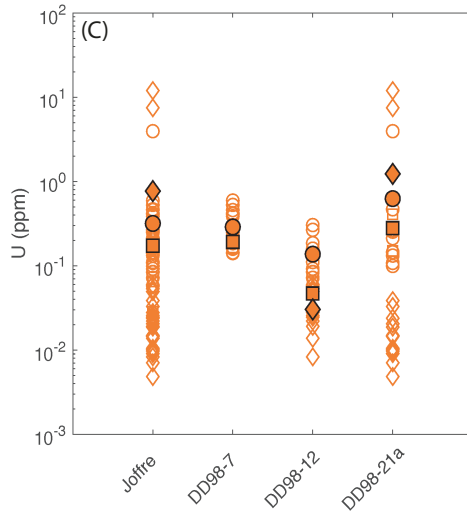
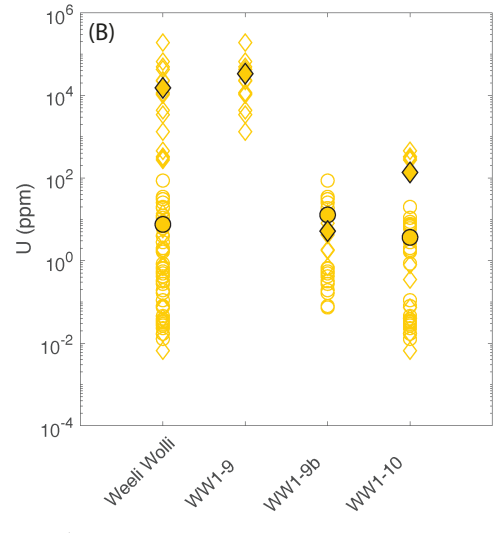
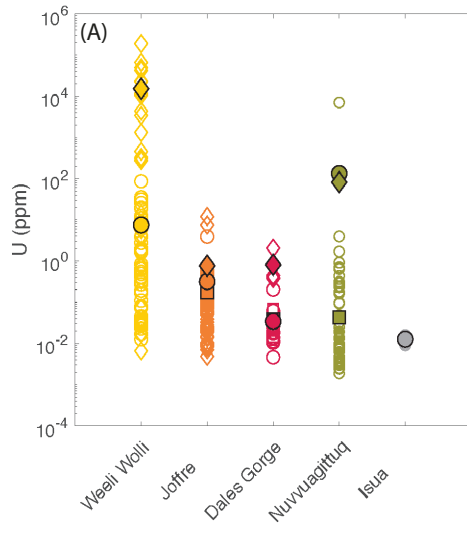


Figure 3.11. Inter-deposit comparison for uranium (A), and intra-deposit comparisons showing the formation cumulative formation data and that of constituent samples for the Weeli Wolli Iron Formation (B), Joffre Member (C) and Dales Gorge Member (D) of the Brockman Iron Formation, and the BIF of the Nuvvuagittuq Supracrustal Belt (E). Symbols as described in Figure 3.6, colours as in Figure 3.5. Note differences in scale.

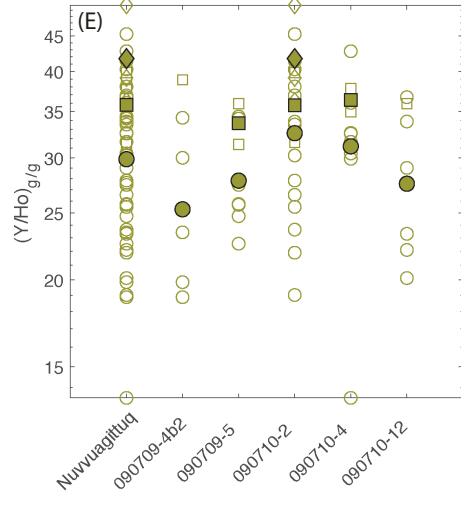
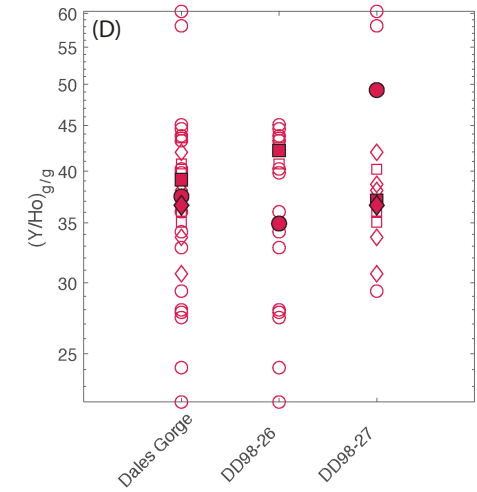
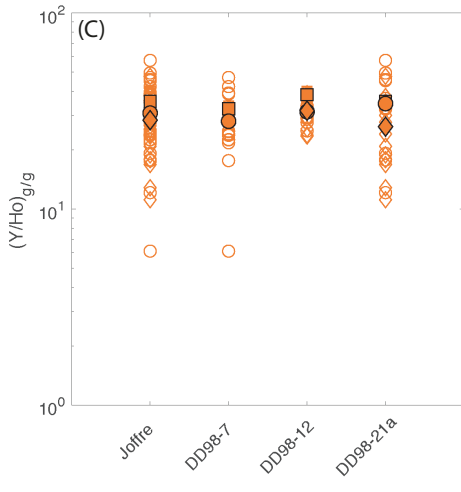
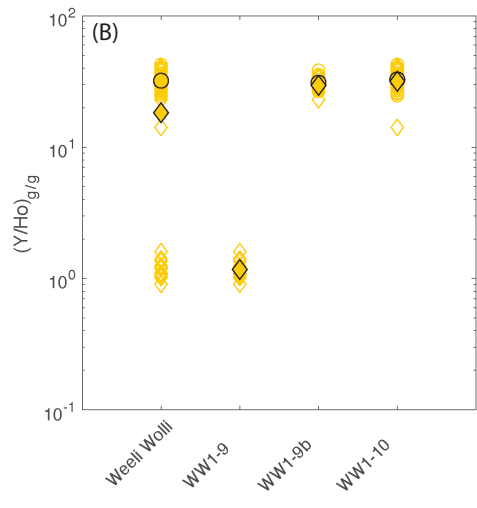
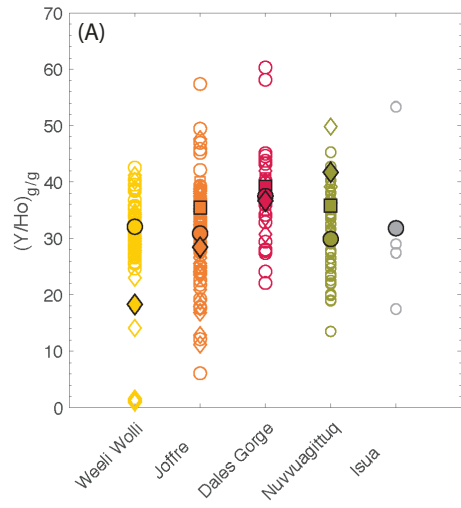


Figure 3.12. Inter-deposit comparison for Y/Ho ratios (g/g) (A), and intra-deposit comparisons showing the cumulative formation data and that of constituent samples for the Weeli Wolli Iron Formation (B), Joffre Member (C) and Dales Gorge Member (D) of the Brockman Iron Formation, and the BIF of the Nuvvuagittuq Supracrustal Belt (E). Symbols as described in Figure 3.6, colours as in Figure 3.5. Note differences in scale.

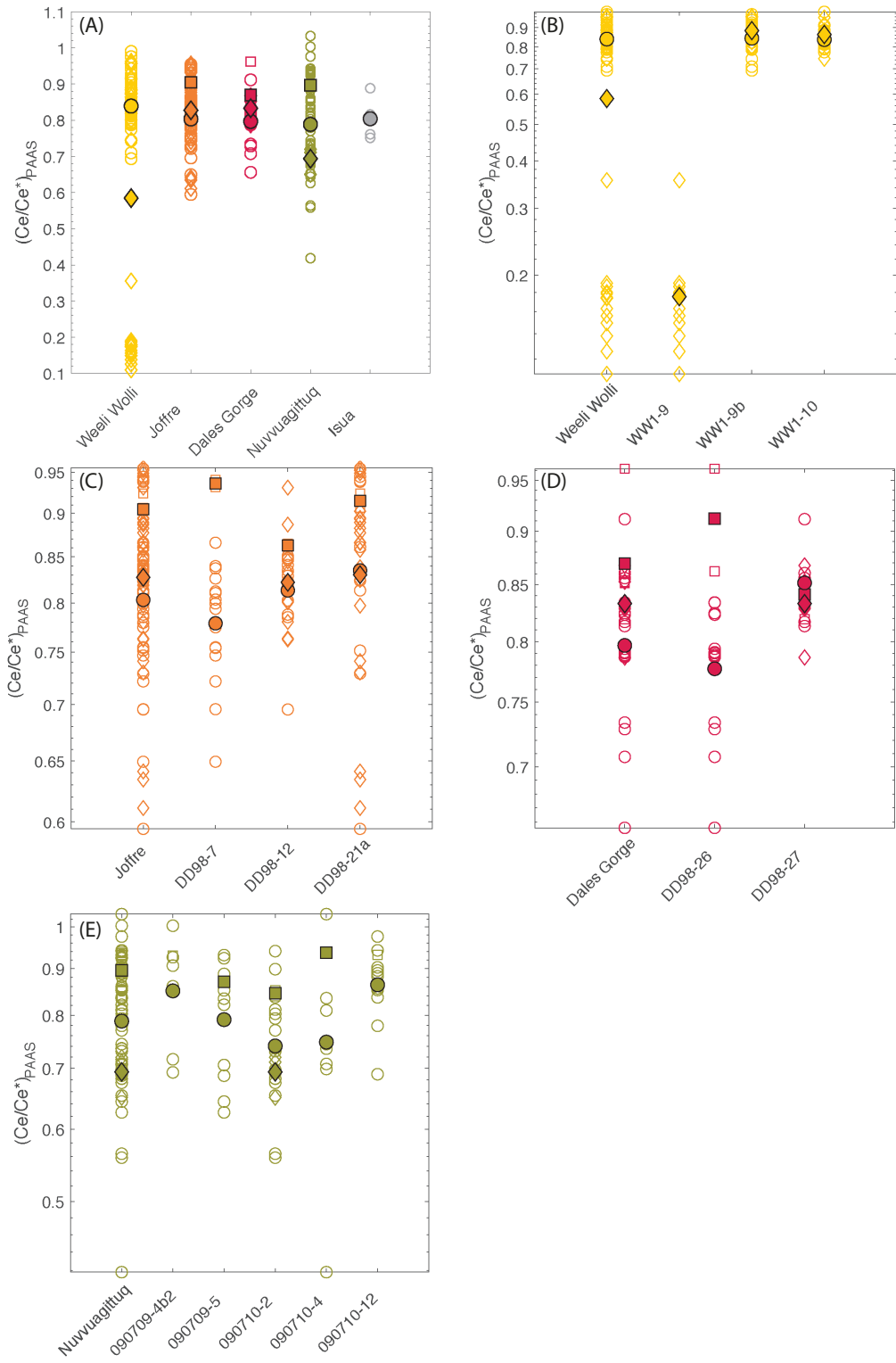


Figure 3.13. Inter-deposit comparison for Ce/Ce^*_{PAAS} calculated after Bau and Dulski (1996) (A), and intra-deposit comparisons showing the cumulative formation data and that of constituent samples for the Weeli Wolli Iron Formation (B), Joffre Member (C) and Dales Gorge Member (D) of the Brockman Iron Formation, and the BIF of the Nuvvuagittuq Supracrustal Belt (E). Symbols as described in Figure 3.6, colours as in Figure 3.5. PAAS normalization after Taylor and McLennan (1985). Note differences in scale.

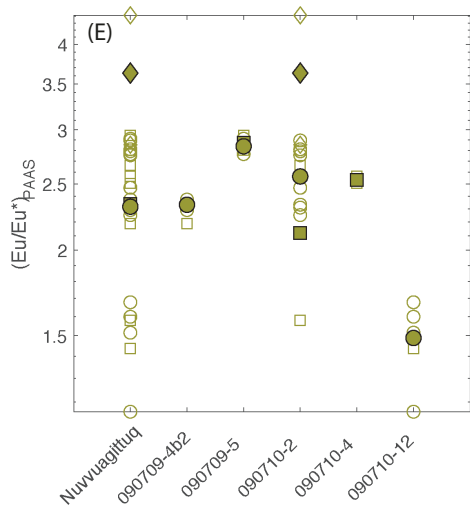
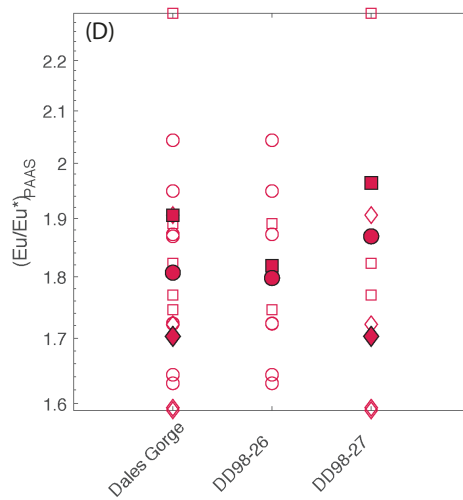
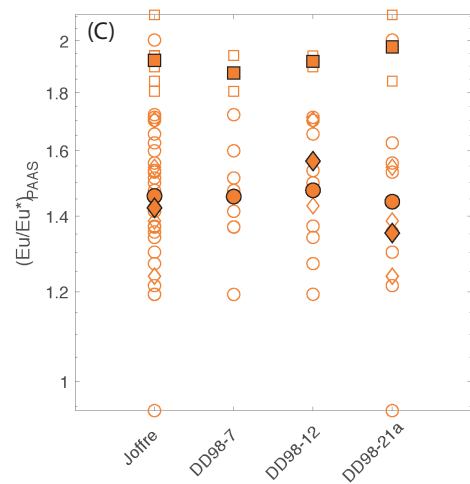
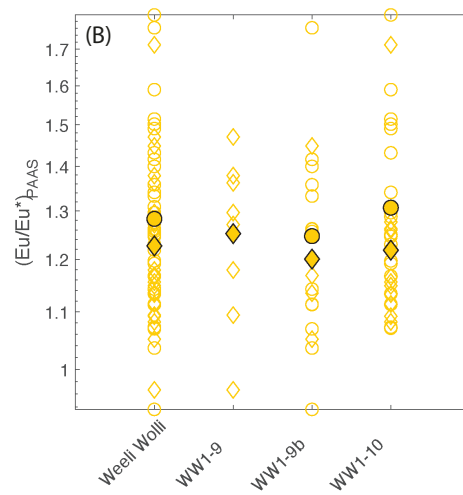
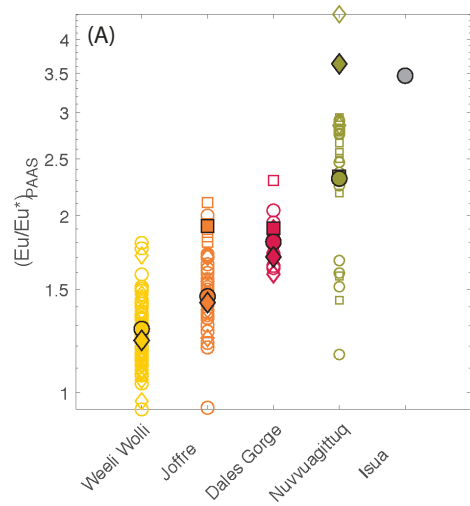


Figure 3.14. Inter-deposit comparison for $\text{Eu}/\text{Eu}^*_{\text{PAAS}}$ calculated after Bau and Dulski (1996) (A), and intra-deposit comparisons showing the cumulative formation data and that of constituent samples for the Weeli Wolli Iron Formation (B), Joffre Member (C) and Dales Gorge Member (D) of the Brockman Iron Formation, and the BIF of the Nuvvuagittuq Supracrustal Belt (E). Symbols as described in Figure 3.6, colours as in Figure 3.5. PAAS normalization after Taylor and McLennan (1985). Note differences in scale.

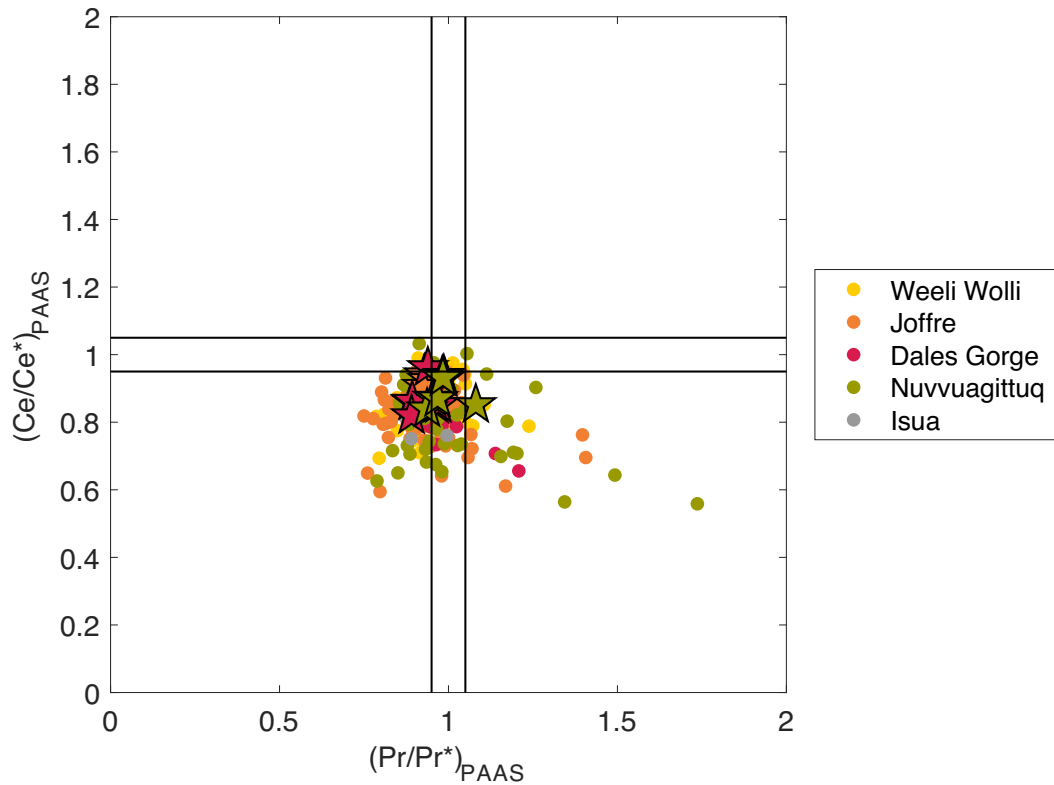


Figure 3.15. Cross-plot of Pr/Pr* versus Ce/Ce* normalized to PAAS after Bau and Dulski (1996). True shale-normalized negative Ce/Ce* fall in the lower right-hand quadrant of the diagram and are present for data generated by LA-HR-ICP-MS. Yet, bulk samples show no resolvable negative Ce anomalies, suggesting that bulk chemical digestions tend to dilute geochemical signals that are otherwise resolvable at the grain scale. Colours indicate their respective formations, consistent with previous figures. Stars indicate bulk digestions and circles laser generated data. Colours as in Figure 3.5.

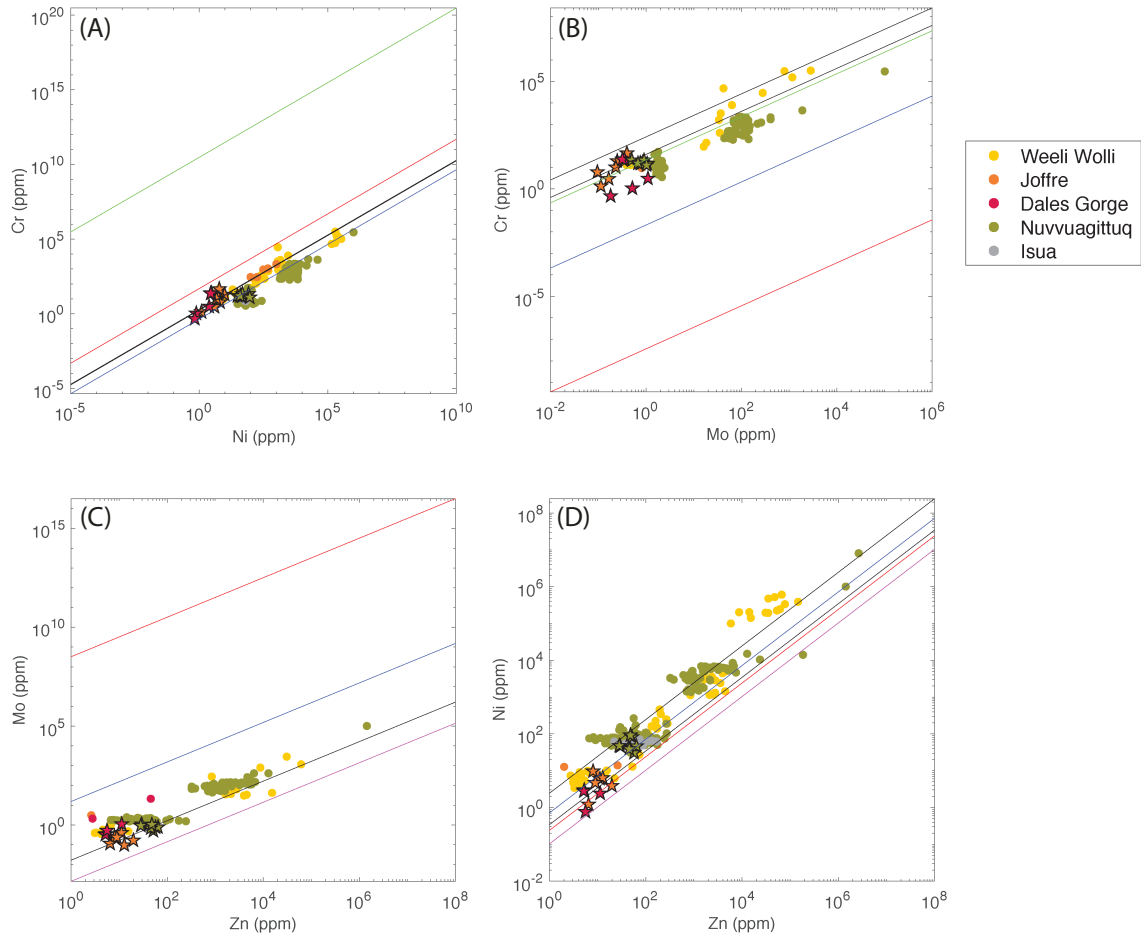


Figure 3.16. Scaling of transition metals (A) Cr vs. Ni, (B) Cr vs. Mo, (C) Mo vs. Zn, and (D) Ni vs. Zn. All transition metals pairs examined here show relatively strong linear scaling. Overlain are expected scaling factors based on the ratios of transition metals in modern seawater (blue; Bruland et al., 2014), the first binding constants for strong sites on hydrous ferric oxides (red; Dzombak and Morel, 1990), the possible range of upper continental crust (black; Condie, 1993; Rudnick and Gao, 2014), and biomass of the marine photoferrotroph *Rhodovulum iodosum* (magenta; Konhauser et al., 2018). For (B), the green line represents the expected scaling for Cr and Zn given the binding constants for chromate and Zn, while the red line is trivalent Cr to Zn (Dzombak and Morel, 1990). Stars

represent bulk solution data, while circles represent *in-situ* LA-HR-ICP-MS analyses.

Colours as in Figure 3.5.

Chapter 4. New considerations on Precambrian paleomarine pH conditions: carbonate buffering and thermodynamic calculations¹

4.1 Introduction

The chemistry of Archean to Paleoproterozoic seawater is intimately coupled to the co-evolution of life and the Earth's surface systems. Considerable progress has been made in evaluating the global reservoir size for several biologically critical trace elements (i.e. Co, Ni, and Zn) and temporal variations in their abundances and redox chemistry (e.g., Konhauser et al., 2007, 2009, 2015; Robbins et al., 2013, 2016; Scott et al., 2008, 2013; Swanner et al., 2014). However, definitive constraints on marine pH remain elusive despite the fact that it is a critical aspect not only for the reconstruction of trace metal abundances from the chemical sedimentary archives but also because it exerted a fundamental control over the speciation and complexation of soluble trace elements, the surface reactivity of suspended particles such as the iron oxyhydroxides that contributed to banded iron formation (e.g., Konhauser et al., 2007, 2009) and microbial biomass (e.g., Liu et al., 2015; Martinez et al., 2016; Konhauser et al., 2018), and as a solubility control on authigenic mineral precipitation (e.g., Tosca et al., 2016). More definitive constraints on pH are also required to calibrate atmospheric composition and climate models, especially for model

¹ This chapter has been prepared for submission as: Robbins, L.J., Lalonde, S.V., Flynn, S.L., Alessi, D.S., and Konhauser, K.O. New considerations on paleomarine pH conditions: carbonate buffering and thermodynamic calculations.

components such as $p\text{CO}_2$ and $p\text{CH}_4$, the former of which is directly coupled to marine pH over geological timescales (e.g., Pavlov et al., 2001; Olson et al., 2016).

An obstacle to reconstructing marine pH conditions in the Archean is a lack of direct geochemical proxies, requiring the use of chemical speciation models to estimate paleomarine chemistry. Previous geochemical models developed to explore the pH of the transition from the Archean to the Proterozoic ocean relied on estimates of $p\text{CO}_2$ and the oceanic Ca^{2+} reservoir. For instance, Grotzinger and Kasting (1993) modeled marine pH assuming Ca^{2+} concentrations of 3-9 mM based on Holland's (1984) proposed siderite-calcium equilibrium. This hypothesized system resulted in a predicted pH range of 5.7 to 8.3. Similarly, Hardie (2003) assumed a neutral to mildly alkaline pH while extrapolating variations in the Ca/Mg ratio based on changes in flux ratios of mid-ocean ridge hydrothermal fluids and river water, from the Late Archean through to Neoproterozoic, assuming an excess of Ca^{2+} relative to bicarbonate due to acid rain producing an abundance of aqueous Ca^{2+} species. More recent efforts have employed charge and mass balance constraints (Halevy and Bachan, 2017), using the $\delta^{44/40}\text{Ca}$ isotopic measurements of Precambrian carbonates (Blättler et al., 2017), or coupling climate and ocean chemistry models that incorporate weathering and seafloor buffering (Krissansen-Totton et al., 2018). Collectively, these three studies identify a secular trend in pH from ~ 6.5 in the Archean to 8.2 in the modern oceans.

Despite advances in reconstructing aspects of ancient marine chemistry gained from examining the chemical sedimentary record a number of fundamental questions remain largely unanswered. Foremost amongst these is what was the pH of the ancient oceans and how can this be assessed more directly through rock record observations or

geochemical measurements? While Cenozoic marine pH can be reconstructed through the measurement of boron isotopes (e.g., Foster and Rae, 2016), methods aside from geochemical modelling for examining pH in the Precambrian, remain elusive. Constraining pH in the ancient ocean has direct bearing on a number of outstanding questions, including what were the primary precipitates that characterized authigenic marine precipitation in the Archean to Paleoproterozoic ocean? and what atmospheric composition mitigated the paradox of the faint young Sun? Knowing the composition of the primary precipitates has significant implications for both marine chemistry and depositional models for unique chemical sediments such as banded iron formations (see Chapter 2). Previously suggested phases include a variety of carbonates (calcite, aragonite; Hardie, 2003), ferric oxyhydroxides (Chapter 2; Konhauser et al., 2002, 2005, 2017; Bekker et al., 2010), and ferrous silicates, such as greenalite (James, 1954; Rasmussen et al., 2014, 2015). Similarly, constraining the pH of the ancient ocean has direct bearing on the atmospheric $p\text{CO}_2$ and how climate on the ancient Earth was regulated (e.g., Isson and Planavsky, 2018).

Building on recent geochemical models, we seek to investigate the time necessary to establish a carbonate buffered ocean. First, we interrogate the Archean to Paleoproterozoic rock record for evidence of carbonate precipitation, in order to assess whether first-order trends in carbonate deposition through time that may reflect fundamental Earth system changes are present. Then, using a set of equations that represent the key chemical reactions governing carbonate speciation in seawater, we predict the Ca^{2+} concentrations necessary to establish a carbonate buffered ocean across varied $p\text{CO}_2$ and given a diverse set of possible carbonate saturation states. These Ca^{2+} concentrations are then combined with annual Ca^{2+} flux estimates (Wolery and Sleep 1976; Schmitt et al.,

2003; Farkaš et al., 2007) which allow us to extrapolate the time necessary to establish a carbonate buffered ocean. Finally, we consider thermodynamic phase diagrams that predict the primary precipitates in paleomarine systems and evaluate the predicted aqueous and mineral species over a range of possible pH conditions and their compatibility with the Archean to Paleoproterozoic rock record and existing pH estimates.

4.2 Methods

To investigate first-order trends in carbonate deposition from the Archean to the Paleoproterozoic, we compiled a brief literature survey of deposit thicknesses from several well characterized sedimentary basins (Fig. 4.1). These were globally distributed and include deposits located in Australia, South Africa, and Canada. Deposit thicknesses were plotted as a function of age, and the modern Grand Bahamas bank thickness was used as a point of comparison.

For all geochemical calculations, activity corrections were performed using the Truesdell-Jones equation at an ionic strength of 0.7 (Langmuir, 1997), the exception being for the activity coefficients for H_2CO_3 and SiO_2 , which were calculated using the Setchenow equation (Langmuir, 1997) that is suitable for calculating activity coefficients of uncharged aqueous species at high ionic strength.

4.2.1 Ca^{2+} concentration calculation

A relatively simple set of equations that govern the carbonate system and calcite precipitation (equations 1-6) are defined as follows:

$$K_{CO_2} = \alpha_{H_2CO_3} / pCO_2 \quad (1)$$

$$K_1 = (\alpha_{HCO_3^-} \cdot \alpha_{H^+}) / \alpha_{H_2CO_3} \quad (2)$$

$$K_2 = (\alpha_{CO_3^{2-}} \cdot \alpha_{H^+}) / \alpha_{HCO_3^-} \quad (3)$$

$$K_{sp} \cdot \Omega = \alpha_{Ca^{2+}} \cdot \alpha_{CO_3^{2-}} \quad (4)$$

$$K_w = \alpha_{H^+} \cdot \alpha_{OH^-} \quad (5)$$

$$\alpha_{H^+} + 2 \cdot \alpha_{Ca^{2+}} = \alpha_{HCO_3^-} + 2 \cdot \alpha_{CO_3^{2-}} + \alpha_{OH^-} \quad (6)$$

where K_{CO_2} , K_1 , and K_2 are the mass action constants governing the dissolution of $CO_{2(g)}$ into water and the first and second dissociation constants for carbonic acid, and are equal to $10^{-1.47}$, $10^{-6.35}$, $10^{-10.33}$, respectively. The aqueous geochemical components of these equations include protons (H^+), carbonic acid (H_2CO_3), bicarbonate (HCO_3^-), carbonate (CO_3^{2-}) and calcium (Ca^{2+}), and are treated in terms of activity of the respective species (α_x). The α_x of each species is the apparent concentration corrected for ionic strength. Equations 1-5 can then be combined and rearranged such that each variable in equation 6 can be presented as a function of the related terms H^+ and pCO_2 . This leads to the generation of equations 7-10:

$$\alpha_{H^+} = ((a \cdot (pCO_2)^2) + (b \cdot pCO_2))^{1/3} \quad (7)$$

$$pH = -\log(\alpha_{H^+}) \quad (8)$$

$$\alpha_{Ca^{2+}} = (c \cdot (\alpha_{H^+})^2) / pCO_2 \quad (9)$$

$$[Ca^{2+}] = \alpha_{Ca^{2+}} / \gamma_{Ca^{2+}} \quad (10)$$

where the empirical constants a and b are derived using the empirical constants and saturation states for each case considered here and simplifying equation 6 with each variable being placed in terms of α_{H^+} and the equation simplified as a function of $p\text{CO}_2$. Similarly, the constant c is derived by replacing the carbonate term in equation 4 with carbonate as a function of $p\text{CO}_2$ and H^+ . The constants a, b, and c are summarized in Table 4.1. A summary of the activity coefficients used in the carbonate system is shown in Appendix Table A3.1.

Equation 4 governs calcite precipitation (eq. 4), and its precipitation is defined as a function of the solubility product (K_{sp}) and degree of supersaturation (Ω). The corresponding pH and Ca^{2+} concentrations necessary to achieve a carbonate buffered system are then calculated for the same range of $p\text{CO}_2$ based on equations 7-10 (Fig. 4.2). Calculations were performed for three separate scenarios governing calcite precipitation: (i) $K_{\text{sp}}=10^{-8.48}$ and $\Omega=1$; (ii) $K_{\text{sp}}=10^{-8.48}$ and $\Omega=6$; and (iii) $K_{\text{sp}}=10^{-6}$ and $\Omega=1$. While a K_{sp} of $10^{-8.48}$ represents the K_{sp} for calcite formation at standard temperature and pressure conditions, 10^{-6} is the solubility product employed by Grotzinger and Kasting (1993) and is derived from the observed solubility of calcite and aragonite in modern oceans (Broecker and Peng, 1972; Walker, 1983).

4.2.2 Calcium fluxes and timing necessary to develop carbonate buffering

Using previously published values for Ca^{2+} fluxes (Wolery and Sleep 1976; Schmitt et al., 2003; Farkaš et al., 2007), we examine Ca^{2+} riverine and hydrothermal inputs for both modern and Archean systems (Table 4.2). For the Archean scenario, we assume that hydrothermal fluxes were four times greater than in the modern due to increased

hydrothermal activity in the ancient ocean, and that there was effectively no riverine input due to minimal continental emergence before ~ 3.0 Ga (e.g., Flament, 2013; Dhumie et al., 2013), although the initial production of continental crust began much earlier (Wilde et al., 2001). For the modern scenario, we fix riverine and hydrothermal Ca^{2+} fluxes at levels reported for the modern oceans where carbonate buffering is evidently active (i.e., mean concentration $10.3 \text{ mmol kg}^{-1}$; Bruland et al., 2014). Using these input fluxes, and assuming a lack of carbonate precipitation or other significant Ca^{2+} sinks before ~ 3.0 Ga, effectively removing any Ca^{2+} exit fluxes, we calculate the minimum amount of time necessary to establish sufficient Ca^{2+} concentrations for carbonate buffering for the broadest range of Ca^{2+} concentrations derived from the range of $p\text{CO}_2$ and K_{sp} conditions examined here.

4.2.3 Thermodynamic phase diagrams

As a complement to the Ca^{2+} concentration calculations presented above, we provide a set of thermodynamic phase diagrams that assess the potential primary phases in Archean to Paleoproterozoic seawater over a range of Fe and pH/ $p\text{CO}_2$ conditions. This allows for an assessment for compatibility with the Archean rock record with model derived estimates for ancient seawater pH.

The default thermodynamic database in Geochemist's Workbench (thermos.mod) was amended to include various amorphous green rust phases, including carbonated green rust (Halevy et al., 2017), as well as chloride, hydroxide, and sulfate green rusts (Rickard and Luther III, 2007). The mass action constant (K) value for greenalite saturation was updated to 27.70 for 25°C , reflecting the recent solubility experiments of Tosca et al. (2016). Input values are summarized in Appendix Table A3.2. Models were run twice, once

under an anoxygenic atmosphere and once in equilibrium with a weakly oxic atmosphere ($fO_{2(g)}$ of 10^{-7}). The weakly oxic atmosphere was intentionally set to below the threshold of 10^{-5} atm needed to maintain the mass-independent fractionation of sulfur isotopes prior to the GOE (Farquhar et al., 2011; Lyons et al., 2014).

Phase predominance diagrams were produced in Geochemists' Workbench Act2 to visualize the thermodynamically favorable primary mineral phases in $\log a_{Fe^{2+}}-pH$ and $\log a_{Fe^{2+}}-fpCO_2$ space for a range of pH and pCO_2 conditions. For simplicity, in the $\log a_{Fe^{2+}}-pH$ diagrams fCO_2 was set at a conservative $10^{-2.1}$. This value is an independent estimate for the terminal Archean based on Paleoproterozoic paleosols (Sheldon, 2006) and is towards the lower end of the spectrum for pCO_2 estimates prior to 3.0 Ga (Krissansen-Totton et al., 2018). The system was carbonate buffered by fixing the ratio of HCO_3^- to Ca^{2+} at 2:1. This represents the probable upper limit for most of Earth's history (Halevy and Bachan, 2017), while calcium to alkalinity ratios (Ca/ALK) indicate calcite saturation. The buffering was accomplished by allowing the solution activity of Ca^{2+} to purely be a function of HCO_3^- concentration. The only exception to this was for the $\log a_{Fe^{2+}}-pCO_2$ model where HCO_3^- was fixed relative to Ca^{2+} activity. To limit the possible mineral phases to those likely to precipitate authigenically (e.g., green rust phases, ferrihydrite, siderite, and greenalite), we purposefully excluded crystalline, igneous, or metamorphic mineral phases (e.g., minnesotaite, hedenbergite, $FeO_{(c)}$, hematite) whose precipitation are not kinetically realistic. A list of excluded phases is provided in the Appendix 3.

4.3 Results and discussion

4.3.1 Carbonate thickness in the Archean and Paleoproterozoic

From the Archean to the start of the Paleoproterozoic there is a significant increase in the thickness of carbonate platform deposits (Fig. 4.1), from a few 10's of meters (e.g., the Onverwacht Group, South Africa and the Pilbara Craton, Australia; Appendix Table A3.3) to several thousand meters (e.g., the Campbellrand Supergroup, South Africa); for comparison, Phanerozoic deposits in the Bahamas can attain thicknesses >5000 m (e.g., Jansa, 1981). Although the record may have an inherent preservation bias due to the ease with which carbonates can be chemically weathered, several key observations may be gleaned from Fig. 4.1. First, there is strong evidence for a distinct increase in carbonate deposit thickness between 3.5 and 2.9 Ga, with deposits reaching several hundred meters thick by 2.9 Ga (e.g., Steep Rock Formation, northeastern Canada) (Riding, 2014). After 2.5 Ga, carbonate deposits such as the Campbellrand-Malmani platform effectively reach the same thickness (>1 km) as is typical of Phanerozoic carbonate platforms. The rise in the sedimentary record of thick carbonate deposits from 3.5 to 2.9 Ga therefore raises the question of whether this is a function of (i) a preservational bias towards carbonate lithologies in the Archean rock record, (ii) seawater was more acidic in the early Archean, (iii) there initially existed a limited planktonic biosphere capable of driving carbonate precipitation, (iv) there initially existed Ca^{2+} limitation, or (v) some combination of the above factors. In any event, by ~2.9 Ga the thickness of preserved carbonate platforms increases dramatically (Fig. 4.1), suggesting whatever limitation was imposed on the formation of early Archean carbonate deposits was alleviated. One of the more intriguing possibilities is the potential that Ca^{2+} concentrations limited both carbonate precipitation and the establishment of carbonate buffering.

4.3.2 pH, Ca²⁺, and pCO₂

In the coupled pH-Ca²⁺-pCO₂ calculations explored here, there is a direct scaling between pCO₂ and both pH and Ca²⁺ concentration required for a carbonate buffered system. This is consistent with previous geochemical models (Grotzinger and Kasting, 1993) and as expected for a generalized carbonate buffered system (e.g., Konhauser, 2007). While pH shows a linear decline with increasing log pCO₂ (Fig. 4.2A), Ca²⁺ concentrations show a non-linear relationship (Fig. 4.2B) that is accentuated when the requisite K_{sp} to generate calcite precipitation is set to elevated values (i.e., K_{sp}=10⁻⁶ after Grotzinger and Kasting, 1993). This relationship is clear for all three K_{sp} and saturation state scenarios considered here. For the first case explored (K_{sp}=10^{-8.48} and Ω=1), pH is predicted to fall in the range of 6.26-8.26 as pCO₂ is varied from 10^{-0.5} to 10^{-3.5} atm and corresponds to Ca²⁺ concentrations of 17.57 to 1.76 mM, respectively. Similarly, the second case examined (K_{sp}=10^{-8.48}, Ω=6) suggests that pH varies between 6.52 and 8.52, with Ca²⁺ concentrations corresponding to a range between 31.92 to 3.20 mM as pCO₂ is systematically increased. Both of these scenarios return reasonable and relatively consistent results that fall within the ranges predicted by previous geochemical models (Grotzinger and Kasting, 1993; Blättler et al., 2017; Tosca et al., 2016; Halevy and Bachan, 2017; Krissansen-Totton et al., 2018). In the third scenario considered, we test the carbonate buffering model of Grotzinger and Kasting (1993) (K_{sp}=10⁻⁶, Ω=1), and the results of those calculations predict pH ranging from 7.09 to 9.09, with corresponding Ca²⁺ concentrations of 117.86 mM and 11.8 mM (Fig. 4.2). While this model scenario falls outside the range of several previous models

(Blättler et al., 2017, Krissansen-Totton et al., 2018), it falls within the window of uncertainty of Halevy and Bachan (2017).

All three scenarios are consistent with recent pH estimates of 7.7-8.3 for the Archean derived from greenalite solubility experiments (Tosca et al., 2016), but for scenarios 1 and 2, this represents the upper limit predicted based on low $p\text{CO}_2$ conditions. As scenarios 1 and 2 are more consistent with a variety of previous modeling efforts, especially the recent coupled carbon and ocean geochemistry model of Krissansen-Totton et al. (2018), we consider them to be a more realistic assessment of the Ca^{2+} levels necessary to establish carbonate buffering as a function of $p\text{CO}_2$. In all cases modeled here, the calcium to alkalinity ratio ($\text{Ca}/\text{ALK} = \text{Ca}/[\text{HCO}_3^- + 2\text{CO}_3^{2-}]$) was >0.75 , consistent with Blättler et al. (2017) who reported $\delta^{44/40}\text{Ca}$ values from carbonates that necessitate $\text{Ca}/\text{ALK} >0.75$ by at least 2.7 Ga. The pH range predicted by scenarios 1 and 2 is also consistent with the recent model of Krissansen-Totton et al. (2018), which suggests pH at 4.0 Ga is between 6.2-7.2. Although Krissansen-Totton et al. (2018), discuss the possibility that pH was buffered by seafloor silicate weathering, the early establishment of a carbonate buffered ocean may also account for the buffered nature of their system as well.

Overall, Ca^{2+} concentrations necessary to establish buffering are on the order of ~1.8-118 mM range (Fig. 4.2B), depending on the K_{sp} , saturation state and $p\text{CO}_2$ conditions. Encouragingly, the upper end of this range, 118 mM, falls below estimates of 500 mM Ca^{2+} based on 3.5 Ga fluid inclusions (Foriel et al., 2004) that form the basis for the maximum Ca^{2+} concentrations used in Krissansen-Totton et al. (2018). These calculations demonstrate that at Ca^{2+} concentrations within an order of magnitude of modern oceans (mean concentration $10.3 \text{ mmol kg}^{-1}$; Bruland et al., 2014), pH buffering

by carbonate minerals should be readily established for a range of $p\text{CO}_2$ conditions. Under such conditions, driving pH below 6 should be difficult, unless acidic inputs were dramatically higher and capable of overwhelming the early Earth ocean's carbonate buffering through the complete dissolution of primitive carbonate platforms. Mechanisms capable of overwhelming early carbonate buffering may include increased acidic hydrothermal input (e.g., Douville et al., 2002) or elevated acid deposition prior to 3.5 Ga via SO_2 volcanic degassing in association with possible continental emergence (Gaillard et al., 2011).

4.3.3 Ca^{2+} fluxes and establishment of carbonate buffering

Hardie (2003) examined shifts in the Ca/Mg ratios from 2.8 Ga to present, assuming a circumneutral pH based on the balance of a representative mid-ocean ridge hydrothermal brine and average river water, and generated estimates of seawater Ca^{2+} ranging from ~12 to 28 mM. While his oldest estimates post-date the rise in carbonate platform thickness (Fig. 4.1), they offer a glimpse at what expected Ca^{2+} concentrations may have been in the Archean. Similarly, Jones et al. (2015) modeled the evolution of Ca^{2+} from 3.5 Ga to present, accounting for changes in continental emergence and seafloor spreading rates, and determined that there has been an almost secular decline in Ca^{2+} concentrations from ~42 to ~10 mM. It is important to note, however, that both the Hardie (2003) and Jones et al. (2015) models are based on riverine fluxes, that in turn, rely on continental production rather than emergence. However, in Table 4.2 we estimate Ca^{2+} fluxes for pre-3.0 Ga oceans, assuming a lack of emerged continents, and thereby no continental riverine flux of Ca^{2+} , as well as a modern estimate which includes continental and hydrothermal fluxes.

Based on this, and the maximum potential range of Ca^{2+} concentrations required to generate carbonate platforms which are predicted to be $\sim 1.76\text{-}118 \text{ mM Ca}^{2+}$, we calculate that it would take between 0.15-10.25 Ma to build up sufficient Ca^{2+} concentrations to establish carbonate buffering. The rapid rate at which carbonate buffering can be established through the build-up of Ca^{2+} , despite the lack of emerged continents in the Archean, is consistent with the integrative geochemical and global ocean chemistry models that suggest marine $\text{pH} > 6.2$ after 4.0 Ga (Krissansen-Totton et al., 2018) and the establishment of elevated Ca/ALK ratios before at least 2.7 Ga (Blättler et al., 2017).

4.3.4 Phase diagram pH implications and primary marine precipitates

Thermodynamic phase diagrams are used to assess the favorable authigenic phase that contributed to banded iron formation (BIF) deposition, following the approach of Halevy et al. (2017). Amorphous ferric oxyhydroxides, the precursor to BIF (e.g., Bekker et al., 2014; Konhauser et al., 2017), imply paleomarine pH conditions in excess of 4.5 (the pH for ferric iron formation; e.g., Langmuir, 1997): if pH were below 4.5, both ferrous and ferric iron would be soluble in seawater, thus preventing the precipitation of the ferric oxyhydroxides that formed BIF. As a complement to the carbonate buffering calculations presented above, we provide a set of thermodynamic phase diagrams that assess the potential primary phases in Archean to Paleoproterozoic seawater over a range of Fe and pH/pCO_2 conditions. This allows for an assessment for compatibility with the Archean rock record with model derived estimates for ancient seawater pH and provides further insights into the potential for the early establishment of carbonate buffering.

Phase diagrams of two critical geochemical fields were produced: $\log a_{\text{Fe}^{2+}}\text{-pH}$ space, and $\log a_{\text{Fe}^{2+}}\text{-}f\text{CO}_2$. For every model, the solution was set to be at equilibrium with $f\text{CO}_2$ as a gaseous component in the presence or absence of minor $f\text{O}_{2(\text{g})}$. Figure 4.3 illustrates the predicted aqueous and mineral phases that are dominant in $\log a_{\text{Fe}^{2+}}\text{-pH}$ space, when $\text{O}_{2(\text{g})}$ is both excluded (panel A) and included (panel B) at a nominal fugacity of 10^{-7} , or approximately $10^{-6.3}$ x PAL (present atmospheric levels). In the absence of atmospheric $\text{O}_{2(\text{g})}$ and from pH 5.2 to 10, siderite is predicted to be the dominant Fe(II) mineral phase provided Fe^{2+} activity is greater than 10^{-7} (Fig. 4.3A). By contrast, greenalite is only predicted to form at pH conditions >10 , and when Fe^{2+} activities are higher than 10^{-7} ; greenalite can form at lower Fe^{2+} activities but with a corresponding shift in pH to even more alkaline conditions. When oxygen is included, ferrihydrite becomes the prevalent mineral phase under a wide range of pH conditions (Fig. 4.3B), provided sufficient levels of Fe(II) exist. In the absence of sufficient Fe(II) to form ferrihydrite, aqueous Fe(III) species are dominant (Fig. 4.3). These findings support previous results (e.g., Tosca et al., 2016) that demonstrate the authigenic water column precipitation of greenalite would require 1 mM dissolved Fe(II) and relatively alkaline seawater (pH 7.7-8.3) to prevent the formation of siderite. By extension, this suggests that greenalite would be indicative of low $f\text{CO}_2$ conditions. Both of these requirements, 1 mM Fe(II) and low $f\text{CO}_2$, are at odds with previous estimates for the Archean and Paleoproterozoic. For instance, previous predictions for marine Fe(II) concentrations range from 0.05 mM (based on coupled calcite and siderite solubility estimates; Holland, 1984) to 0.5 mM (based on the mass balance of Fe required to deposit the Hamersley banded iron formations; Morris, 1993). Additionally,

the suggestion of relatively high ocean pH contradicts previous estimates for mildly acidic to circumneutral pH conditions, as discussed above.

Similar results are indicated by phase diagrams for $\log a_{\text{Fe}^{2+}}-f\text{CO}_2$ space. In the absence of $\text{O}_{2(\text{g})}$, greenalite is dominant at $f\text{CO}_2$ conditions below $\sim 10^{-4}$, a value less than even modern atmospheric levels of $10^{-3.5}$ (Fig. 4.3A). At higher, more realistic Archean to Paleoproterozoic $f\text{CO}_2$ conditions, siderite is the dominant mineral phase. When aqueous Fe(II) concentrations are insufficient for siderite to form, the system is predicted to be controlled by either the aqueous phases of $\text{FeCO}_{3(\text{aq})}$ or $\text{Fe}^{2+}_{(\text{aq})}$, depending on the fugacity of $\text{CO}_{2(\text{g})}$. As with the $\log a_{\text{Fe}^{2+}}-\text{pH}$ phase diagrams in Fig. 4.3B, when oxygen is included, ferrihydrite becomes the dominant precipitated phase over a broad range of conditions. The prevalence of siderite and ferrihydrite being stable over a range of $p\text{CO}_2/\text{pH}$ conditions is consistent with carbonate buffered Archean to Paleoproterozoic oceans, characterized by BIF and carbonate precipitation. Furthermore, the basin-scale deposition of greenalite is considered highly unlikely due to the difficulties in oxidizing extensive ferrous silicate deposits post-depositionally (Robbins et al., *in review*). Collectively, these considerations point to pH conditions below $\sim 8-10$ that would be necessary for the widespread precipitation of greenalite. While thermodynamic phase diagrams are not a definitive mechanism for identifying the primary phases that led to the deposition of chemical sediments, they do highlight the need for understanding both the kinetic controls and the consequences of an operative oxidative mechanism in assessing the primary phase of Archean to Paleoproterozoic marine chemical sediments and their relationship to pH and $p\text{CO}_2$ conditions.

4.3.5 The biosphere as a driver of carbonate precipitation

The deposition of thick carbonate successions is driven by the metabolic activity of planktonic communities within the photic zone and microbial mats, and has been since the Archean (e.g., Riding, 2000; Riding et al., 2014). Grotzinger and James (2000) have also highlighted the presence of Archean carbonates that formed either abiotically or biotically as laterally extensive sea-floor encrustations, reaching thicknesses of several meters, and the conspicuous decrease in these seafloor carbonate precipitates from the Archean through to the Mesoproterozoic. The precipitation of herringbone calcite in the Archean as a seafloor carbonate has been attributed to the precipitation of carbonate phases under anaerobic conditions and the inhibition of calcite precipitation by Mn^{2+} and Fe^{2+} (Sumner and Grotzinger, 1996). Similarly, it has been suggested that the carbonatization of plagioclase or mafic seafloor may have been a substantial sink for CO_2 in the Archean oceans, removing the equivalent of up to 3.8×10^{13} mol C/year, and generating calcite or ankerite as an alteration phase (Nakamura and Kato, 2004). While this process may be a legitimate removal pathway for CO_2 it is not a significant flux of Ca^{2+} to seawater (Nakamura and Kato, 2004) and is, therefore, unlikely to contribute significantly to reaching the Ca^{2+} concentrations necessary to establish carbonate buffering. Furthermore, although carbonatization may sequester CO_2 in the seafloor, it has recently been suggested that reverse weathering and the authigenic formation of clays in marine porewaters may release CO_2 back into the water column, and ultimately the atmosphere, acting to regulate pH and pCO_2 prior to the initiation of biological silica precipitation (Isson and Planavsky, 2018).

Given the short time necessary to establish carbonate buffering calculated above (Table 4.2), it is possible that the lack of thick carbonate succession before 2.9 Ga is a

function of limited planktonic activity rather than pH or Ca^{2+} concentrations. If early planktonic communities were nutrient limited, they may not have been capable of driving the precipitation of large amounts of calcite. In a given year, the ability of the biosphere to draw down $p\text{CO}_2$ and alter marine pH is relatively low (Table 4.3), at most increasing pH by 0.69. This relies on low atmospheric $p\text{CO}_2$ and no recycling or respiration of the removed carbon. When 95% is recycled by aerobic respiration this would result in a maximum change in pH of only 0.01. The extrapolation of a biospheric effect on millennial or longer timescales, however, remains uncertain, as calculations on those timescales are likely reliant on a well constrained understanding of external, non-biological $p\text{CO}_2$ fluxes and they remain difficult to extrapolate. For instance, at low atmospheric $p\text{CO}_2$, such an extrapolation could remove all CO_2 from the atmosphere, implying a balance that relies heavily on recycling and external forcing.

An additional mechanism of generating alkalinity occurs during burial, i.e., diagenesis. With the burial of organic carbon, anaerobic respiration, such as bacterial Fe(III) reduction or sulfate reduction, releases bicarbonate into the pore water system. Increased alkalinity can cause the equilibrium ion activity product for calcium carbonate to be exceeded, leading to the precipitation of early diagenetic carbonate minerals that are relatively stable once formed and not subject to rapid recycling by redox reactions in the same way as sulphides and oxides (Irwin et al., 1977). Such processes become most predominant within the sulphate reduction zone, because that metabolic process increases alkalinity.

Irrespective of whether alkalinity was generated within the water column or sediment pile, it remains a distinct possibility that the rise in carbonate platform thickness

around 2.9 Ga (Fig. 4.1) represents a fundamental shift in the activity of the biosphere and the initial triggering of biogenic carbonate precipitation on a large scale. Given this possibility, the early establishment of a carbonate buffered ocean may have been insufficient to drive the production of large carbonate platforms, despite establishing a favourable, circumneutral marine pH.

4.6 Conclusions

Constraints on the pH of the Precambrian ocean have primarily come from geochemical models, many of which suggest the establishment of a carbonate or otherwise buffered ocean by at least 2.7 Ga. In this work, our use of simple flux calculations indicates that a sufficient Ca^{2+} concentration should build up in the Archean to Paleoproterozoic ocean within 0.15-10.1 Ma, invoking solely hydrothermal Ca^{2+} fluxes. This suggests that the establishment of a carbonate buffered ocean should have occurred earlier in Earth's history and would have been followed by a temporal increase in pH from ~6 to 8 over the course of the Precambrian and Phanerozoic that is tied to the secular decrease in $p\text{CO}_2$ (e.g., Kirssansen-Totton et al., 2018). Critically, this suggests a lower bound on marine pH of ~6.26, given the sufficient Ca^{2+} fluxes predicted here. Yet, there exists a clear disconnect between the establishment of carbonate buffering and the record of carbonate deposits in the Archean sedimentary record. This disconnect may be attributed to a preservational bias or limited biosphere activity, rather than a depressed ocean pH.

Thermodynamic phase diagrams indicate broad fields in pH or $p\text{CO}_2$ space for which several potential precursor phases to Archean or Paleoproterozoic chemical sediments are predicted to be stable. The dominant mineral phase, identified here as either

siderite or ferrihydrite, is highly dependent on oxygen abundance. Accordingly, insights into paleomarine pH conditions based on the identification of purported primary minerals such as greenalite or siderite should be taken cautiously.

Many of the recent geochemical models that have advanced our understanding of secular trends in marine pH (Halevy and Bachan, 2017; Kirssansen-Totton et al., 2018) rely on input parameters including charge balances based on previous estimates for geochemical component inputs ($p\text{CO}_2$, Ca^{2+} , Mg^{2+} , Cl^- , Fe^{2+} , etc.), models of seafloor spreading, continental emergence, independent estimates for $p\text{CO}_2$, and a wide range in estimates for outgassing. Collectively, these input variables contribute to the uncertainty in model derived estimates for pH, and without new or improved constraints on the input variables, decreasing uncertainty in paleomarine pH in deep time will rely on dynamic geochemical models of increasing complexity that seek to minimize the propagation of errors associated with input variables. Both of these factors highlight the necessity for the development of a calibrated rock-record based proxy for examining Precambrian pH, which would allow for more direct constraints to be placed on the secular evolution of marine pH and, in turn allow back calibration of model inputs such as $p\text{CO}_2$ or outgassing that currently have wide ranges of permissible values within model runs.

4.7 References

Bekker, A., Planavsky, N.J., Krapež, B., Rasmussen, B., Hofmann, A., Slack, J.F., Rouxel, O.J., Konhauser, K.O., 2014. Iron Formations: Their Origins and Implications for Ancient Seawater Chemistry in Holland, H.K., Turekian, K., (eds.) *Treatise on Geochemistry*, 2nd edition, 561-628.

- Bekker, A., Slack, J., Planavsky, N., Krapez, B., Hofmann, A., Konhauser, K.O., Rouxel, O.J., 2010. Iron Formation: The Sedimentary Product of a Complex Interplay among Mantle, Tectonic, Oceanic, and Biospheric Processes. *Economic Geology* 105, 467–508.
- Blättler, C.L., Kump, L.R., Fischer, W.W., Paris, G., Kasbohm, J.J., Higgins, J.A., 2017. Constraints on ocean carbonate chemistry and pCO₂ in the Archaean and Palaeoproterozoic. *Nature Geoscience* 10, 41–45.
- Broecker, W.S., Peng, T.H., 1982. *Tracers in the Sea*. Lamont-Doherty Geological Observatory, Palisades, New York. pp. 1-690.
- Bruland, K.W., Middag, R., Lohan, M.C., 2014. Controls of Trace Metals in Seawater, in: Holland, H.D., Turekian, K. (Eds.), *Treatise on Geochemistry*. Second edition. Elsevier Ltd., Vol. 8. pp. 19–51.
- Dhuime, B., Wuestefeld, A., Hawkesworth, C.J., 2015. Emergence of modern continental crust about 3 billion years ago. *Nature Geoscience* 8, 552–555.
- Douville, E., Charlou, J., Oelkers, E., Bienvenu, P., 2002. The rainbow vent fluids (36°14'N, MAR): the influence of ultramafic rocks and phase separation on trace metal content in Mid-Atlantic Ridge hydrothermal fluids. *Chemical Geology* 184, 37–48.
- Farkaš, J., Buhl, D., Blenkinsop, J., Veizer, J., 2007. Evolution of the oceanic calcium cycle during the late Mesozoic: Evidence from $\delta^{44/40}\text{Ca}$ of marine skeletal carbonates. *Earth and Planetary Science Letters* 253, 96–111.

- Farquhar, J., Zerkle, A.L., Bekker, A., 2011. Geological constraints on the origin of oxygenic photosynthesis. *Photosynth Res* 107, 11–36.
- Flament, N., Coltice, N., Rey, P.F., 2013. The evolution of the $^{87}\text{Sr}/^{86}\text{Sr}$ of marine carbonates does not constrain continental growth. *Precambrian Research* 229, 177–188.
- Foriel, J., Philippot, P., Rey, P., Somogyi, A., Banks, D., Ménez, B., 2004. Biological control of Cl/Br and low sulfate concentration in a 3.5-Gyr-old seawater from North Pole, Western Australia. *Earth and Planetary Science Letters* 228, 451–463.
- Foster, G.L., Rae, J.W.B., 2016. Reconstructing Ocean pH with Boron Isotopes in Foraminifera. *Annual Review of Earth and Planetary Sciences* 44, 207–237.
- Gaillard, F., Scaillet, B., Arndt, N.T., 2015. Atmospheric oxygenation caused by a change in volcanic degassing pressure. *Nature* 478, 229–232.
- Grotzinger, J.P., Kasting, J.F., 1993. New constraints on Precambrian ocean composition. *The Journal Of Geology* 101, 235–243.
- Grotzinger, J.P., James, N.P., 2000. Precambrian carbonates: evolution of understanding, in: Grotzinger, J.P., James, N.P. (Eds.), *Carbonate Sedimentation and Diagenesis in the Evolving Precambrian World*. SEPM (Society for Sedimentary Geology), pp. 3–20.
- Halevy, I., Bachan, A., 2017. The geologic history of seawater pH. *Science* 355, 1069–1071.

- Halevy, I., Alesker, M., Schuster, E.M., Popovitz-Biro, R., Feldman, Y., 2017. A key role for green rust in the Precambrian oceans and the genesis of iron formations. *Nature Geoscience* 10, 135–139.
- Hardie, L.A., 2003. Secular variations in Precambrian seawater chemistry and the timing of Precambrian aragonite seas and calcite seas. *Geology* 31, 785–788.
- Holland, H.D., 1984, Oxygen in the Precambrian Atmosphere: Evidence from Marine Environments, *in* The chemical evolution of the atmosphere and oceans, Princeton University Press, Princeton, NJ, p. 337–440.
- Irwin, H., Curtis, C., Coleman, M., 1977. Isotopic evidence for source of diagenetic carbonates formed during burial of organic-rich sediments. *Nature* 269, 209–213.
- Isson, T.T., Planavsky, N.J., 2018. Reverse weathering as a long-term stabilizer of marine pH and planetary climate. *Nature* 560, 471–475.
- James, H., 1954. Sedimentary facies of iron-formation. *Economic Geology* 49, 235–293.
- Jansa, L.F., n.d. Mesozoic carbonate platforms and banks of the eastern North American margin. *Marine Geology* 44, 97–117.
- Jones, C., Nomosatryo, S., Crowe, S.A., Bjerrum, C.J., Canfield, D.E., 2015. Iron oxides, divalent cations, silica, and the early earth phosphorus crisis. *Geology* 43, 135–138.
- Konhauser, K.O., 2007, Introduction to Geomicrobiology: Blackwell Science Ltd., Malden, MA, USA. pp. 1-425.

- Konhauser, K.O., Hamade, T., Raiswell, R., Morris, R., Ferris, F., Southam, G., Canfield, D., 2002. Could bacteria have formed the Precambrian banded iron formations? *Geology* 30, 1079–1082.
- Konhauser, K.O., Newman, D., Kappler, A., 2005. The potential significance of microbial Fe (III) reduction during deposition of Precambrian banded iron formations. *Geobiology* 3, 167–177.
- Konhauser, K.O., Lalonde, S.V., Amskold, L.A., Holland, H., 2007. Was there really an Archean phosphate crisis? *Science* 315, 1234.
- Konhauser, K.O., Pecoits, E., Lalonde, S.V., Papineau, D., Nisbet, E.G., Barley, M.E., Arndt, N.T., Zahnle, K., Kamber, B.S., 2009. Oceanic nickel depletion and a methanogen famine before the Great Oxidation Event. *Nature* 458, 750–753.
- Konhauser, K.O., Planavsky, N.J., Hardisty, D.S., Robbins, L.J., Warchola, T.J., Haugaard, R., Lalonde, S.V., Partin, C.A., Oonk, P.B.H., Tsikos, H., Lyons, T.W., Bekker, A., Johnson, C.M., 2017. Iron formations: A global record of Neoproterozoic to Palaeoproterozoic environmental history. *Earth-Sci. Rev.* 172, 140–177.
- Konhauser, K.O., Robbins, L.J., Alessi, D.S., Flynn, S.L., Gingras, M.K., Martinez, R.E., Kappler, A., Swanner, E.D., Li, Y.-L., Crowe, S.A., Planavsky, N.J., Reinhard, C.T., Lalonde, S.V., 2018. Phytoplankton contributions to the trace-element composition of Precambrian banded iron formations. *Geological Society of America Bulletin* 130, 941–951.

- Krissansen-Totton, J., Arney, G.N., Catling, D.C., 2018. Constraining the climate and ocean pH of the early Earth with a geological carbon cycle model. *Proceedings of the National Academy of Sciences* 252, 201721296–6.
- Langmuir D (1997) *Aqueous Environmental Geochemistry*: Prentice Hall, Upper Saddle River, New Jersey, pp. 1-600.
- Liu, Y., Alessi, D.S., Owtrim, G.W., Petrash, D.A., 2015. Cell surface reactivity of *Synechococcus* sp. PCC 7002: Implications for metal sorption from seawater. *Geochimica et Cosmochimica Acta* 169, 30–44.
- Lyons, T.W., Reinhard, C.T., Planavsky, N.J., 2014. The rise of oxygen in Earth's early ocean and atmosphere. *Nature* 506, 307–315.
- Martinez, R.E., Konhauser, K.O., Paunova, N., Wu, W., Alessi, D.S., Kappler, A., 2016. Surface reactivity of the anaerobic phototrophic Fe (II)-oxidizing bacterium *Rhodovulum iodolum*: Implications for trace metal budgets in ancient oceans and banded iron formations. *Chemical Geology* 442, 113–120.
- Morris, R., 1993. Genetic modelling for banded iron-formation of the Hamersley Group, Pilbara Craton, Western Australia. *Precambrian Research* 60, 243–286.
- Nakamura, K., Kato, Y., 2004. Carbonatization of oceanic crust by the seafloor hydrothermal activity and its significance as a CO₂ sink in the Early Archean. *Geochimica et Cosmochimica Acta* 68, 4595–4618.

- Olson, S.L., Reinhard, C.T., Lyons, T.W., 2016. Limited role for methane in the mid-Proterozoic greenhouse. *Proceedings of the National Academy of Sciences* 113, 11447–11452.
- Pavlov, A.A., Kasting, J.F., Eigenbrode, J.L., Freeman, K.H., 2001. Organic haze in Earth's early atmosphere: Source of low-¹³C Late Archean kerogens? *Geology* 29, 1003–1006.
- Rasmussen, B., Krapez, B., Meier, D.B., 2014. Replacement origin for hematite in 2.5 Ga banded iron formation: Evidence for postdepositional oxidation of iron-bearing minerals. *Geological Society of America Bulletin* 126, 438–446.
- Rasmussen, B., Krapež, B., Muhling, J.R., Suvorova, A., 2015. Precipitation of iron silicate nanoparticles in early Precambrian oceans marks Earth's first iron age. *Geology* 43, 303–306.
- Rickard, D., Luther, G.W., III, 2007. Chemistry of Iron Sulfides. *Chemical Reviews* 107, 514–562.
- Riding, R., 2000. Microbial carbonates: the geological record of calcified bacterial-algal mats and biofilms. *Sedimentology* 47, 179–214.
- Riding, R., Fralick, P., Liang, L., 2014. Identification of an Archean marine oxygen oasis. *Precambrian Research* 251, 232–237.
- Robbins, L.J., Lalonde, S.V., Saito, M.A., Planavsky, N.J., Mloszewska, A.M., Pecoits, E., Scott, C., Dupont, C.L., Kappler, A., Konhauser, K.O., 2013. Authigenic iron oxide

proxies for marine zinc over geological time and implications for eukaryotic metallome evolution. *Geobiology* 11, 295–306.

Robbins, L.J., Lalonde, S.V., Planavsky, N.J., Partin, C.A., Reinhard, C.T., Kendall, B., Scott, C., Hardisty, D.S., Gill, B.C., Alessi, D.S., Dupont, C.L., Saito, M.A., Crowe, S.A., Poulton, S.W., Bekker, A., Lyons, T.W., Konhauser, K.O., 2016. Trace elements at the intersection of marine biological and geochemical evolution. *Earth-Science Reviews* 163, 323–348.

Schmitt, A.-D., Chabaux, F., Stille, P., 2003. The calcium riverine and hydrothermal isotopic fluxes and the oceanic calcium mass balance. *Earth and Planetary Science Letters* 213, 503–518.

Scott, C., Lyons, T.W., Bekker, A., Shen, Y., Poulton, S.W., Chu, X., Anbar, A.D., 2008. Tracing the stepwise oxygenation of the Proterozoic ocean. *Nature* 452, 456–459.

Scott, C., Planavsky, N.J., Dupont, C.L., Kendall, B., Gill, B.C., Robbins, L.J., Husband, K.F., Arnold, G.L., Wing, B.A., Poulton, S.W., Bekker, A., Anbar, A.D., Konhauser, K.O., Lyons, T.W., 2013. Bioavailability of zinc in marine systems through time. *Nature Geoscience* 6, 125–128.

Sheldon, N.D., 2006. Precambrian paleosols and atmospheric CO₂ levels. *Precambrian Research* 147, 148–155.

Sumner, D.Y., Grotzinger, J.P., 1996. Herringbone calcite: petrography and environmental significance. *Journal of Sedimentary Research* 66, 419–429.

- Swanner, E.D., Planavsky, N.J., Lalonde, S.V., Robbins, L.J., Bekker, A., Rouxel, O.J., Saito, M.A., Kappler, A., Mojzsis, S.J., Konhauser, K.O., 2014. Cobalt and marine redox evolution. *Earth and Planetary Science Letters* 390, 253–263.
- Tosca, N.J., Guggenheim, S., Pufahl, P.K., 2016. An authigenic origin for Precambrian greenalite: Implications for iron formation and the chemistry of ancient seawater. *Geological Society of America Bulletin* 128, 511–530.
- Walker, J.C.G., 1983. Possible limits on the composition of the Archaean ocean. *Astrobiology* 302, 518–520.
- Wilde, S.A., Valley, J.W., Peck, W.H., Graham, C.M., 2001. Evidence from detrital zircons for the existence of continental crust and oceans on the Earth 4.4 Gyr ago. *Astrobiology* 409, 175–178.
- Wolery, T.J., Sleep, N.H., 1976. Hydrothermal Circulation and Geochemical Flux at Mid-Ocean Ridges. *The Journal Of Geology* 84, 249–275.

Table 4.1. Constants used in the calculation of minimum Ca^{2+} concentrations (equations 1-10).

$\log K_{\text{CO}_2}$	$\log K_1$	$\log K_2$	$\log K_{\text{sp}}$	Ω	$\log a$	$\log b$	$\log c$
-1.47	-6.35	-10.33	-8.48	1	-17.79	-23.97	9.67
-1.47	-6.35	-10.33	-8.48	6	-18.57	-24.75	10.45
-1.47	-6.35	-10.33	-6	1	-20.27	-26.45	12.15

Table 4.2. Modern and Archean Ca²⁺ riverine and hydrothermal input fluxes, and the time necessary to establish sufficient Ca²⁺ concentrations to achieve carbonate buffering.

	Archean (>3 Ga)	Modern
Range in Riverine Flux (T mol yr ⁻¹) ^a	-	2.13-12
Range in Hydrothermal Flux (T mol yr ⁻¹) ^a	13.5-19.2	3.37-4.8
Riverine Flux (T mol yr ⁻¹)	0	12
Hydrothermal Flux (T mol yr ⁻¹)	16.35	4.1
[Ca ²⁺] required (mM) - high side ^b	117.86	117.86
Ca ²⁺ required (mol) - high side ^b	1.65E+20	1.65E+20
Time to accumulate Ca ²⁺ (Ma) - high side ^b	10.09	10.25
[Ca ²⁺] required (mM) - low side ^c	1.76	1.76
Ca ²⁺ required (mol) - low side ^c	2.46E+18	2.46E+18
Time to accumulate Ca ²⁺ (Ma) - low side ^c	0.15	0.15
^a References: Wolery and Sleep (1976); Schmitt et al. (2003); Farkaš et al. (2007) ^b High side based on Ca ²⁺ concentrations for K _{sp} =10 ⁻⁶ , Ω=1, and pCO ₂ = 10 ^{-0.5} atm ^c Low side based on Ca ²⁺ concentrations for K _{sp} =10 ⁻⁶ , Ω=1, and pCO ₂ = 10 ^{-3.5} atm		

Table 4.3. CO₂ sequestration potential for the biosphere under ideal conditions and the ability to perturbate marine pH under idealized conditions and when 95% of biomass is recycled.

	$p\text{CO}_2$ (atm)	$\log p\text{CO}_2$		Units
Mass of atmosphere			5.14E+18	kg
Mass of CO ₂ in atmosphere modern			2.99E+15	kg
Mass of CO ₂ in atmosphere modern			2.99E+21	mg
ppm CO ₂ in atmosphere modern (by mass)			582.00	ppm
Moles CO ₂ in atmosphere modern	0.000316	-3.5	6.79E+16	mol
Moles CO ₂ in atmosphere 10X modern	0.003162	-2.5	6.79E+17	mol
Moles CO ₂ in atmosphere 100x modern	0.031623	-1.5	6.79E+18	mol
Moles CO ₂ in atmosphere 1000x modern	0.316228	-0.5	6.79E+19	mol
Volume of photic zone (510.1 million km ² surface area)			5.101E+16	m ³
Cell concentrations			1.00E+06	cells/mL
Cell concentrations			1.00E+12	cells/m ³
# of cells in photic zone			5.10E+28	cells
3 day cellular turnover (total cells)			6.17E+30	cells per year
CO ₂ sequestration per cell			1.00E-14	mol C/cell
CO ₂ sequestration potential per year.			6.17E+16	mol C
pH sensitivity			-0.667	pH/log atm
1X (delta log $p\text{CO}_2$ delata pH)		-1.04	0.69	pH
10X (delta log $p\text{CO}_2$ delata pH)		-0.04	0.03	pH
100X (delata log $p\text{CO}_2$, delta pH)		0.00	0.003	pH
1000X (delata log $p\text{CO}_2$, delta pH)		0.00	0.0003	pH
<u>If 95% of C recycled:</u>				
Moles CO ₂ in atmosphere modern	0.000316	-3.5	6.79E+16	mol
Moles CO ₂ in atmosphere 10X modern	0.003162	-2.5	6.79E+17	mol
Moles CO ₂ in atmosphere 100x modern	0.031623	-1.5	6.79E+18	mol
Moles CO ₂ in atmosphere 1000x modern	0.316228	-0.5	6.79E+19	mol
Volume of photic zone (510.1 million km ² surface area)			5.101E+16	m ³
Cell concentrations			1.00E+06	cells/mL
Cell concentrations			1.00E+12	cells/m ³
# of cells in photic zone			5.10E+28	cells
Cellular turnover (total cells)			6.17E+30	cells per year
CO ₂ sequestration per cell			1.00E-14	mol C/cell
CO ₂ sequestration potential per year.			3.09E+15	mol C

sensitivity			-0.667	pH/log atm
1X (delta log $p\text{CO}_2$ delata pH)		-0.02	0.01	pH
10X (delta log $p\text{CO}_2$ delata pH)		-0.002	0.001	pH
100X (delata log $p\text{CO}_2$, delta pH)		-0.0002	0.0001	pH
1000X (delata log $p\text{CO}_2$, delta pH)		-0.00002	0.00001	pH

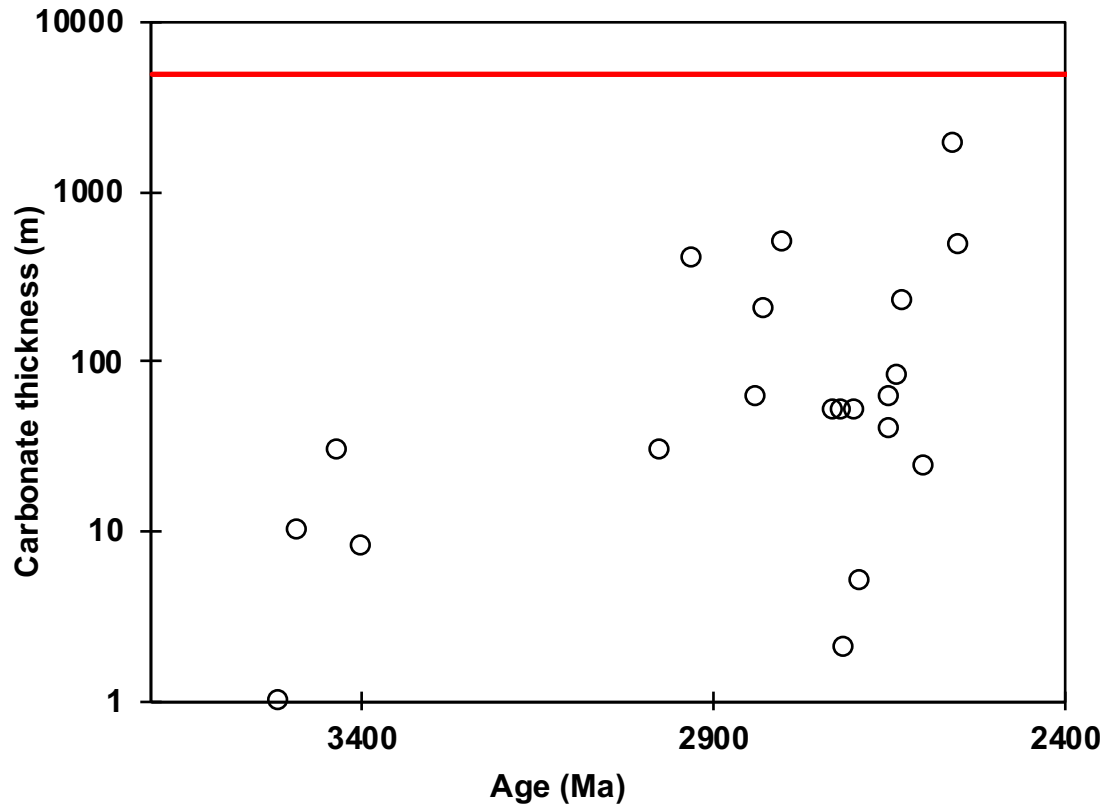


Figure 4.1. The thickness of carbonate successions in the Paleoarchean to Neoproterozoic. By 2.5 Ga, at the Archean to Paleoproterozoic boundary, carbonate successions begin to attain thicknesses of several thousand meters. The red line references the Great Bahamas Bank (> 5000 m; Jansa, 1981). In the Archean, however, there appears to be a secular trend with regards to increasing carbonate thickness. The black arrow indicates that Paleoproterozoic to modern carbonate successions reach maximum thicknesses greater consistent with observation from the modern Bahamas (See Appendix Table A3.1 for data and associated references).

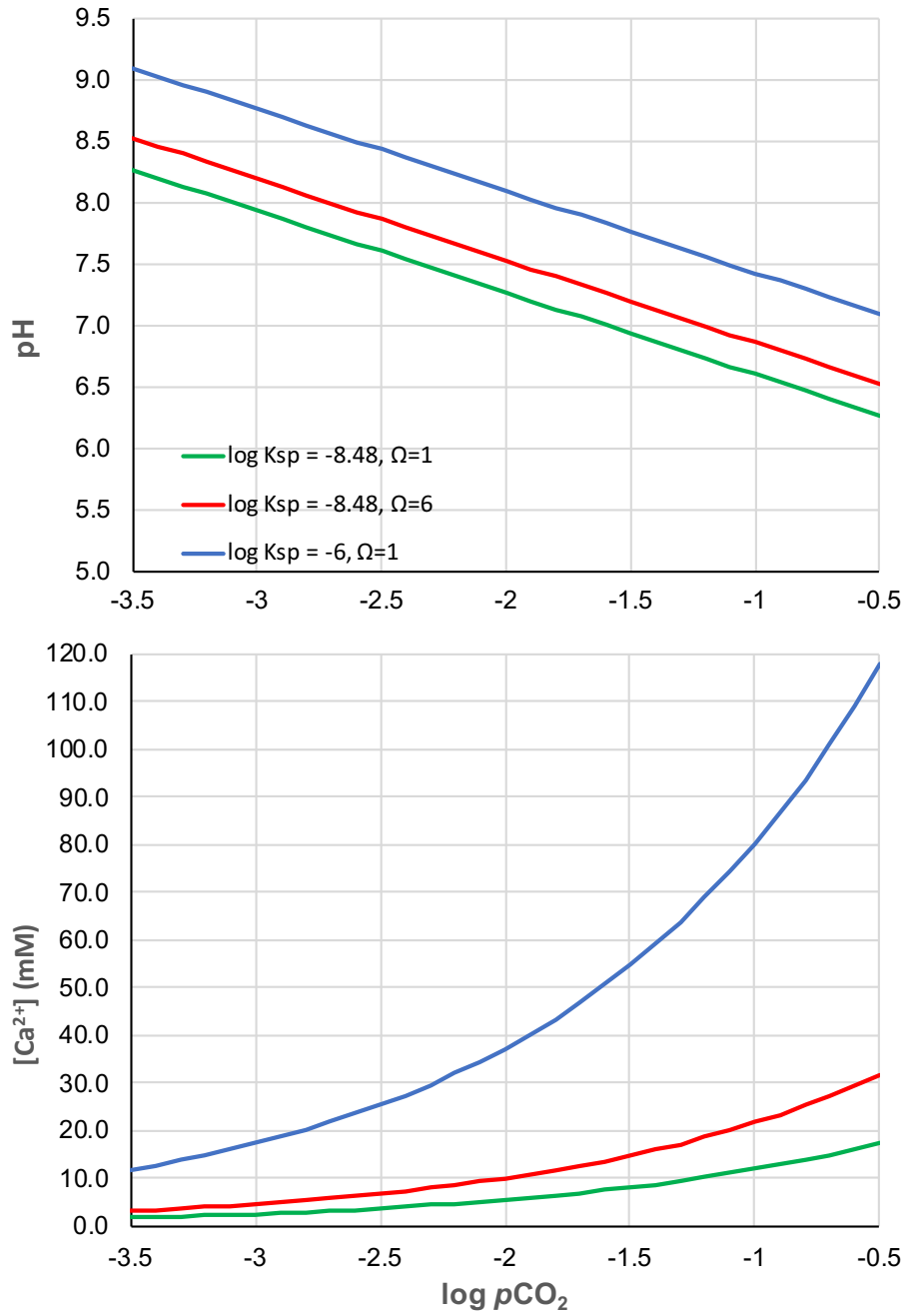


Figure 4.2. (A) The pH in a carbonate buffered system and (B) the Ca^{2+} concentration necessary to establish carbonate buffering over increasing $p\text{CO}_2$ conditions.

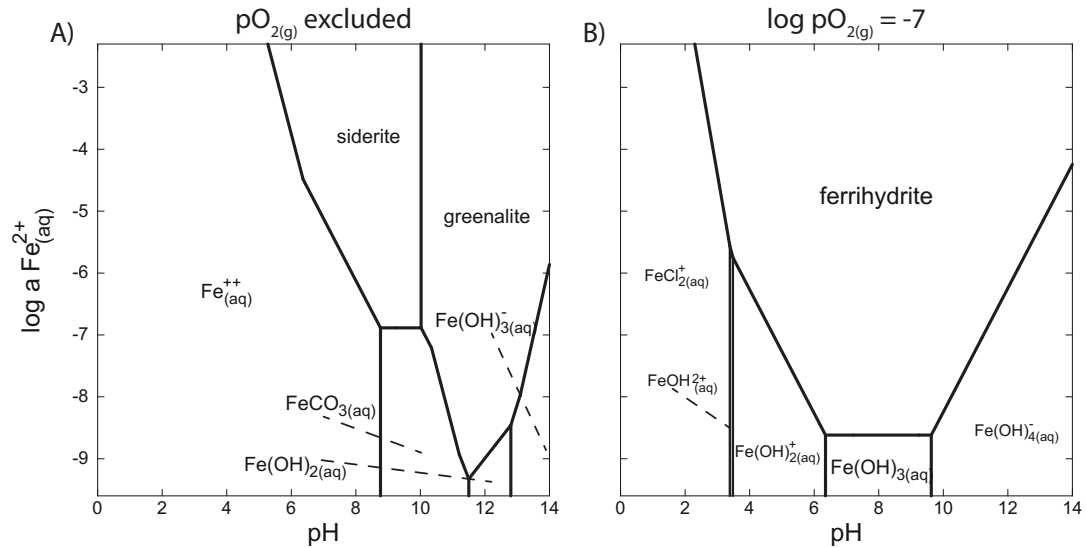


Figure 4.3. Phase diagrams for $\alpha_{\text{Fe}^{2+}}$ -pH space, at a fixed $p\text{CO}_2$ fugacity of $10^{-2.1}$ atm (see methods for discussion), when oxygen is excluded from the model (A) or added at a nominal fugacity below those necessary to maintain S-MIF (10^{-7} atm). Phase diagrams show a large region for aqueous Fe^{2+} under conditions considered here and a likelihood of siderite being the dominant Fe(II) mineral phase when oxygen is excluded. When oxygen is included the model, ferrihydrite becomes the dominant mineral phase over a wide range of conditions, suggesting that even under weakly oxidizing systems ferrihydrite should be thermodynamically favorable precipitate.

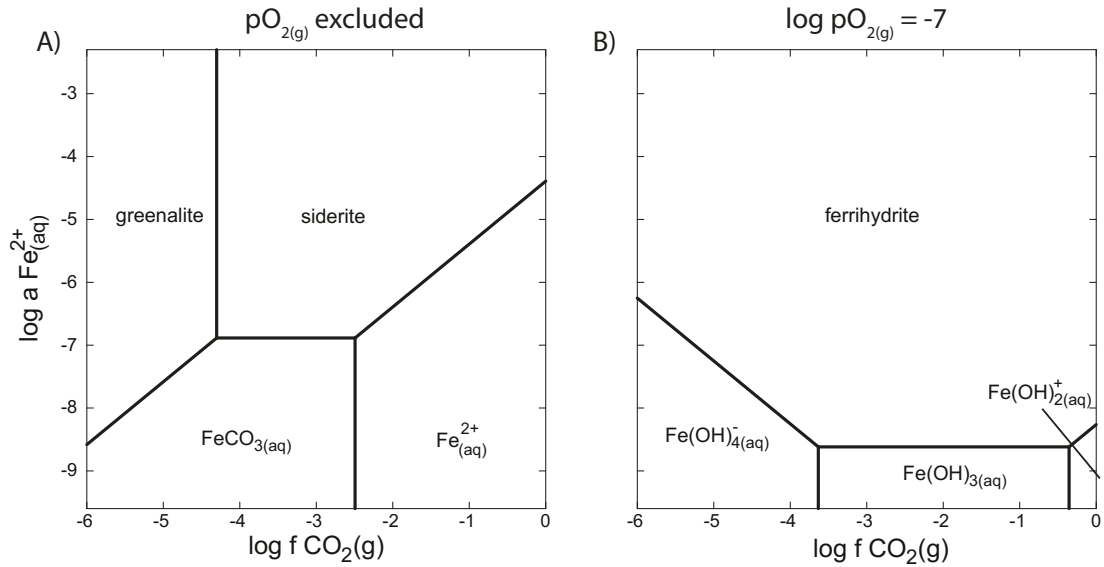


Figure 4.4. Phase diagrams for $\alpha_{\text{Fe}^{2+}}/f\text{CO}_2(\text{g})$ space when oxygen is excluded from the model (A) or included at a nominal fugacity, below atmospheric levels necessary to maintain S-MIF (10^{-7} atm). At low $f\text{CO}_2(\text{g})$ conditions, below that of even the modern atmosphere ($\sim 10^{-3.5}$), greenalite is the dominant mineral phase, while at higher $f\text{CO}_2(\text{g})$ conditions, siderite becomes thermodynamically favorable. When oxygen is included (B) it is apparent that ferrihydrite once again dominates the system.

Chapter 5. Conclusions

Banded iron formations (BIF) are a crucial chemical sedimentary archive because they are one of the few avenues available for examining the linkages between the evolution of marine geochemistry and life in the Archean and Paleoproterozoic oceans. The origin and initial composition of BIF remains a matter of ongoing debate (e.g., Rasmussen et al., 2017; Johnson et al., 2018, Chapter 2) despite more than a century of research (e.g., Lieth, 1903; Gruner, 1922). Critical insights into the oxygenation of Earth's atmosphere and the links between evolving marine geochemistry and life have been garnered from studies that focused primarily on the chemical composition of globally distributed BIF deposits (see Konhauser et al. (2017) and Robbins et al. (2016) for extensive reviews). While considerable progress has been made, there are still many unanswered questions regarding BIF deposition and the information held within the chemical records that these deposits contain. The work in this thesis offers new approaches to assessing the primary composition of BIF, including a statistical comparison between BIF data generated using varied analytical approaches, and the origin of variability with respect to trace element concentrations within the record. This thesis also provides new insights on Precambrian geochemical parameters that remain uncertain, such as paleomarine pH, that may influence how the BIF record is interpreted. The thesis concludes by offering several suggested avenues through which BIF deposits may further improve our understanding of how life and the Earth co-evolved during the Archean and Paleoproterozoic.

5.1 The iron formation record and its interpretation

Extensive investigations into the BIF record have led to critical insights into the secular evolution of Earth's atmosphere from dominantly anoxic to the oxygenated state that we experience today (Konhauser et al., 2017). Similarly, compilations of bioessential trace elements in BIF have resulted in a number of insights into the evolution of Archean to Paleoproterozoic seawater and their relationship to the trajectory of biological evolution (as reviewed in Chapter 1, Robbins et al., 2016). Investigations into the trace element concentrations in BIF have indicated a unidirectional decline in Ni concentrations around 2.7 Ga that could have imparted an environmental pressure on methanogenic communities, leading to their marginalization in the lead up to the Great Oxidation Event (GOE; Konhauser et al., 2009, 2015; Robbins et al., 2016). This may have allowed emergent cyanobacterial clades to expand into new niches, contributing to the initial rise of oxygen in the atmosphere. Similarly, a spike in Cr concentrations in BIF at 2.48 Ga may indicate the advent of aerobic pyrite oxidation on land, and the resulting solubilization and mobilization of substantial amounts of oxidized Cr for the first time in Earth's history (Konhauser et al., 2011). Perturbations such as these in the trace metal record of BIF provide evidence for key events and transitions in the Archean and Paleoproterozoic that have had a profound impact on the evolution of Earth's coupled ocean-atmosphere-biosphere system. Conversely, records of trace metals in BIF that are static over geologic time, such as for Zn (Robbins et al., 2013) and Cu (Chi Fru et al., 2016), may be indicative of systems buffered against changes in bulk ocean chemistry due to complexation of trace elements by organic ligands. This view is consistent with observations from modern oceans, where more than 97% of all Zn and Cu are organically complexed by strong metal-specific ligands (e.g., Vraspir and Butler, 2009; Bruland et al., 2014). The timing of the

origin of these strong organic ligands and their implications for paleomarine geochemistry remains uncertain.

The ability to use the BIF record for studies such as these is fundamentally based on the ability of reactive precursor mineral phases, namely iron oxyhydroxides (e.g., ferrihydrite) or microbial biomass (e.g., anoxygenic photoferrotrophs) to adsorb and sequester trace metals from the water column during their deposition (e.g., Trivedi and Axe, 2001; Bjerrum and Canfield, 2002; Konhauser et al., 2007, 2009; Robbins et al., 2013; Martinez et al., 2016; Konhauser et al., 2018). Empirical models used to determine the adsorption of trace metals from seawater are inherently dependent on the experimental conditions under which they are conducted, and remain the subject of debate (e.g., Bjerrum and Canfield, 2002; Konhauser et al., 2007; Jones et al., 2015). At the same time, the interpretation of the BIF record remains fundamentally dependent on understanding the reactivity of iron oxyhydroxides and biomass as a precursor phase.

The classic model of BIF deposition remains widely accepted (Bekker et al., 2014; Konhauser et al., 2017), wherein ferrous iron is oxidized by either free oxygen produced by cyanobacteria (e.g., Cloud, 1965) or anoxygenic photoferrotrophs (e.g., Kappler et al., 2005). However, an alternative hypothesis has emerged, which has radically different implications for the chemistry of ancient seawater. Based on the observation of greenalite, a ferrous silicate, in petrographic thin sections, several studies (e.g., Rasmussen et al., 2017; Johnson et al., 2018) suggest that BIF were largely deposited as ferrous silicate muds then oxidized post-depositionally by groundwater flow. This greenalite challenges the use of the BIF record as an archive of seawater; if correct, this hypothesis would require an extensive reassessment of the record.

To address this issue, in Chapter 2 it was demonstrated using a hydrogeological box model, approximating the archetypal 2.6-2.45 Ga Hamersley Group BIF, that the post-depositional oxidization of BIF on a basin-scale by ground water flow is unrealistic. Nearly 4 million model runs demonstrate that while it is theoretically possible to oxidize a large amount of ferrous iron within a BIF, the geological constraints necessary to generate a reasonable oxidation time (oxygen concentration in ground water, hydraulic gradient, and permeability) are untenable on a basin scale or for a lithology consistent with BIF. This effectively excludes the possibility that most BIFs were deposited as greenalite and subsequently oxidized. This leaves intact the conclusion that the precursor phase for the iron-rich layers in BIF must have been a ferric oxyhydroxide, a phase favourable for the removal of trace metals from the water column.

A troubling aspect of the BIF trace metal record has been the observed spread in trace metal concentrations within a given formation or ‘time bin’ that can exceed two orders of magnitude (e.g., Robbins et al., 2013). While several possibilities exist (see section 5.3 Future Work), at least some of the spread can be attributed to artifacts of variable analytical approaches. In Chapter 3, a statistical assessment of BIF trace element data generated by *in-situ* Laser Ablation High Resolution Inductively Coupled Plasma Mass Spectrometry (LA-HR-ICP-MS) of mineral-specific phases versus bulk digestion solution High Resolution Inductively Coupled Plasma Mass Spectrometry (HR-ICP-MS) analysis was presented. The use of these two methodologies can account for a significant portion of the observed spread, as LA-HR-ICP-MS analysis has a tendency to sample locally concentrated regions that may be masked by bulk digestion methods. These hot spots recorded by the iron mineral phases are diluted by the inclusion of trace element poor

phases, such as chert, during bulk digestions. Encouragingly, Chapter 3 of this thesis demonstrates that for a number of trace elements in multiple BIF formations, from the Eoarchean Nuvvuagittuq Supracrustal Belt to the Paleoproterozoic Hamersley Basin, average trace element abundances produced by bulk digestions and LA-HR-ICP-MS are statistically indistinguishable at the 95% confidence level. This suggests that both methodologies can be used to reliably recreate paleomarine trends in BIF geochemistry. Several instances, however, are identified where important environmental signals that may be obscured in bulk digestions but may be detected using LA-HR-ICP-MS, for instance the presence of localized Ce-anomalies. These instances highlight the need for a combination of bulk and LA-ICP-MS analyses when examining BIF for ancient environmental signals. Collectively, these two chapters provide new insights into the debate regarding the deposition of BIF and their reliability as a proxy record for the early oceans, and that the reactivity of iron oxyhydroxides towards trace metals in the early oceans can be used as a reliable model for reconstructing trends in ancient seawater composition.

Despite the progress made in reconstructing ancient seawater chemistry using the chemical sedimentary record, including BIF (e.g., Robbins et al., 2016), several aspects of Archean to Paleoproterozoic seawater chemistry remain uncertain. In Chapter 4, the time necessary to establish carbonate buffering and its implications for the pH of ancient seawater was investigated. It was determined that carbonate buffering in the oceans could have been established in approximately 0.1 to 10 million years. This suggests that pH would likely have been between 6.2-8.5 throughout the majority of Earth's history – a finding consistent with a number of recent geochemical models exploring marine pH from the Archean through to the modern (e.g., Halevy and Bachan, 2017; and Krissansen-Totton

et al., 2018). While this is an important finding, large uncertainties remain, up to a pH unit, in estimates of the pH of early oceans (e.g., Krissansen-Totton et al., 2018). This uncertainty may propagate into considerable uncertainty of pH dependent processes operative in the ancient oceans, such as authigenic mineral precipitation (e.g., Tosca et al., 2016; Halevy et al., 2017), the adsorption of trace metal to reactive particle phases (e.g., Konhauser et al., 2007, 2018; Martinez et al., 2016), and the aqueous complexation of trace elements.

5.2 Future work

Banded iron formations remain one of the few windows through which paleomarine geochemistry can be reconstructed, and they provide context to the links between geochemical and biological evolution. Despite recent debates as to their origin (e.g., Rasmussen et al., 2017; Johnson et al., 2018), advances presented in this reinforce the traditional model that invokes the formation of BIF due to the precipitation of ferric oxyhydroxide precursor minerals. As the traditional model does not invoke the secondary oxidation by large quantities of groundwater, the results further support the continued use of BIF as a key proxy for reconstructing the chemistry of the ancient and the linked atmosphere-hydrosphere-biosphere system. This work has also elucidated a number of future research questions, which are outlined briefly below:

(1) How can a definitive determination on the depositional mechanism underlying BIF deposition be made? This may include such questions as:

- (i) Which paragenetic pathways best explain the minor occurrences of greenalite in BIF identified by Rasmussen et al. (2017), assuming that the initial phase was ferric oxyhydroxide?
 - (ii) How can more detailed petrographic and sequence stratigraphic studies of archetypal BIF successions, including the Hamersley Basin in Western Australia, as well as its stratigraphic equivalent, the Transvaal Supergroup in South Africa, shed light on the distinct depositional requirements for greenalite-rich successions versus the more typical microbands that characterize BIF?
 - (iii) While we are unable to distinguish between the oxidative mechanisms of UV light, free oxygen, or anoxygenic photoferrotrophy (e.g., Nie et al., 2017) using iron isotopes in the iron bearing phases of BIF, what if anything, do iron isotope measurements in greenalite reveal? Are these measurements consistent with isotopic signatures for hydrothermal imprinting, dissimilatory iron reduction, or other processes?
- (2) What other biological signals are contained within the BIF record, and how can they be unlocked with novel isotopic or geochemical tools?
- (i) With the advent of non-traditional stable metal isotopes, there is a vast potential for examining the potential for nutrient-like behaviour in trace elements in high resolution chemostratigraphic profiles of BIF successions. Which environmental or biological signals can be unlocked by applying non-

traditional stable metal isotopes (e.g., Zn, Ni, and Cr) to high resolution chemostratigraphic studies of BIF?

- (ii) What controls the reliability of transition metal signals as recorded by iron specific mineral phases and their relationship to bulk digestion generated values. For instance, are there petrographic indicators that can point towards phases more likely to preserve a conservative signal similar to bulk values, versus locally enriched concentrations typical of some LA-HR-ICP-MS analyses? Are the extreme values themselves a primary feature, or at least a remnant thereof, as has been the traditional interpretation, or are they the result of preferential partitioning during BIF diagenesis and low-grade metamorphism?
- (ii) How can we more directly assess, or even measure, the pH of the ancient oceans, and by extension the $p\text{CO}_2$ conditions of the early atmosphere, via the BIF record? This record may have key implications for estimating the productivity of the early biosphere as well as the activity of early metabolisms (i.e., methanogens) as revealed through calibrated global climate models (e.g., Olson et al., 2016). A promising avenue may be the application of boron isotopes on iron oxides and coeval manganese oxides, as the coupled measurement is not only pH dependent but does not require any *ad hoc* knowledge of the boron isotopic composition of seawater (e.g., Lemarchand et al., 2007).

(3) How can we improve the interpretation of geochemical records for the Archean to Paleoproterozoic oceans?

(i) One of the largest uncertainties with regards to paleomarine trace metal geochemistry is the potential for their complexation with dissolved organic ligands. In modern marine systems, in excess of 97% of trace metals such as Zn, Cu, and Fe may be organically complexed by strong organic ligands (e.g., Vraspir and Butler, 2009; Bruland et al., 2014). There are some indications in the BIF record that this may have been the case for extended periods in Earth's history (e.g., Robbins et al., 2013; Chi Fru et al., 2016). The implications for the ancient oceans and BIF deposition remains largely unexplored. If several trace metal reservoirs are indeed ligand buffered, how does this affect our understanding of trace element bioavailability? Are ligands produced to sequester sparingly available bioessential trace metals as in modern oceans, or are they produced to combat toxic levels of these same, or different, metals? How does the rise in iron specific ligands, namely siderophores (e.g., Vraspir and Butler, 2009), relate to the timing of the GOE and the termination of BIF deposition?

(ii) Surface complexation modeling (SCM) is a methodology for exploring the adsorption of chemical constituents to particle surfaces. It is a more robust and flexible approach than simple empirical models (see discussion in Robbins et al., 2016) and can be readily adapted to changes in system geochemical conditions (pH, ionic strength, reactive particle surfaces, constituent concentrations, etc.). The application of SCM could provide a greatly improved

way to assess BIF trace element records that remain in question due to a current dependence on empirical adsorption models (e.g., Bjerrum and Canfield, 2002; Konhauser et al., 2007; Jones et al., 2015). SCM can easily be tested for a wide variety of input conditions and are thoroughly grounded in the underlying chemical thermodynamics. The question arises, how can SCM coupled to BIF trace element records improve our understanding of paleoseawater composition, trace metal availability, and the reactivity of ancient particle phases? Along these lines, it may be possible that BIF record be used to unlock estimates for Archean to Paleoproterozoic seawater pH. Trace element adsorption to ferric oxyhydroxide minerals is a pH dependent process (e.g., Trivedi and Axe, 2001; Konhauser et al., 2007, 2009). Given the wealth of trace element data collected from the BIF record, it may be possible to develop a SCM coupled to a Monte Carlo simulation that utilizes trace element-to-iron ratios in the BIF record and independently derived estimates for trace element concentrations to determine marine pH through time. This would provide a new and novel method for constraining paleomarine pH that is not dependent on *ad hoc* assumptions regarding the partial pressure of carbon dioxide in the atmosphere.

In summary, BIF are, and remain, a critical proxy record for the exploration of ancient ocean chemistry. Novel work presented in this thesis has reinforced their origin as a biologically driven ferric oxyhydroxide deposit, as well as the reliability of this proxy method for examining trends in ancient seawater chemistry through the implementation of

several analytical approaches. Furthermore, considerations regarding important variables underlying the application of the BIF record, such as pH in the ancient oceans and the establishment of carbonate buffering, have been discussed. As a consequence of this work, a number of outstanding questions that highlight the continued potential of the BIF chemical sedimentary record to provide crucial insights into Archean to Paleoproterozoic ocean chemistry, and more broadly, environmental conditions have been highlighted, laying the framework for several promising future research directions.

5.3 References

- Bekker, A., Planavsky, N.J., Kraepz, B., Rasmussen, B., Hofmann, A., Slack, J.F., Rouxel, O.J., Konhauser, K.O., 2014. Iron Formations: Their Origins and Implications for Ancient Seawater Chemistry, in: Holland, H.D., Turekian, K. (Eds.), *Treatise on Geochemistry*, 2nd edition, vol. 9. Elsevier, pp. 561–628.
- Bjerrum, C.J., Canfield, D.E., 2002. Ocean productivity before about 1.9 Gyr ago limited by phosphorus adsorption onto iron oxides. *Nature* 417, 159–162.
- Bruland, K.W., Middag, R., Lohan, M.C., 2014. Controls of Trace Metals in Seawater, in: Holland, H.D., Turekian, K. (Eds.), *Treatise on Geochemistry*, 2nd edition, vol. 8. Elsevier Ltd., pp. 19–51.
- Chi Fru, E., Rodríguez, N.P., Partin, C.A., Lalonde, S.V., Andersson, P.S., Weiss, D.J., Albani, El, A., Rodushkin, I., Konhauser, K.O., 2016. Cu isotopes in marine black shales record the Great Oxidation Event. *Proceedings of the National Academy of Sciences* 113, 4941–4946.
- Cloud, P.E., 1965. Significance of the Gunflint (Precambrian) Microflora. *Science* 148, 27–35.

- Gruner, J.W., 1922. The origin of sedimentary iron-formations: the Biwabik Formation of the Mesabi Range. *Economic Geology* 22, 407–460.
- Halevy, I., Bachan, A., 2017. The geologic history of seawater pH. *Science* 355, 1069–1071.
- Halevy, I., Alesker, M., Schuster, E.M., Popovitz-Biro, R., Feldman, Y., 2017. A key role for green rust in the Precambrian oceans and the genesis of iron formations. *Nature* 10, 135–139.
- Johnson, J.E., Muhling, J.R., Cosmidis, J., Rasmussen, B., Templeton, A.S., 2018. Low-Fe(III) Greenalite Was a Primary Mineral from Neoproterozoic Oceans. *Geophysical Research Letters* 45, 3182-3192.
- Jones, C., Nomosatryo, S., Crowe, S.A., Bjerrum, C.J., Canfield, D.E., 2015. Iron oxides, divalent cations, silica, and the early earth phosphorus crisis. *Geology* 43, 135–138.
- Kappler, A., Pasquero, C., Konhauser, K.O., Newman, D., 2005. Deposition of banded iron formations by anoxygenic phototrophic Fe (II)-oxidizing bacteria. *Geology* 33, 865–868.
- Konhauser, K.O., Lalonde, S.V., Amskold, L.A., Holland, H., 2007. Was there really an Archean phosphate crisis? *Science* 315, 1234.
- Konhauser, K.O., Pecoits, E., Lalonde, S.V., Papineau, D., Nisbet, E.G., Barley, M.E., Arndt, N.T., Zahnle, K., Kamber, B.S., 2009. Oceanic nickel depletion and a methanogen famine before the Great Oxidation Event. *Nature* 458, 750–753.
- Konhauser, K.O., Lalonde, S.V., Planavsky, N.J., Pecoits, E., Lyons, T.W., Mojzsis, S.J., Rouxel, O.J., Barley, M.E., Rosière, C.A., Fralick, P.W., Kump, L.R., Bekker, A.,

2011. Aerobic bacterial pyrite oxidation and acid rock drainage during the Great Oxidation Event. *Nature* 478, 369–373.
- Konhauser, K.O., Robbins, L.J., Pecoits, E., Peacock, C., Kappler, A., Lalonde, S.V., 2015. The Archean Nickel Famine Revisited. *Astrobiology* 15, 804–815.
- Konhauser, K.O., Planavsky, N.J., Hardisty, D.S., Robbins, L.J., Warchola, T.J., Haugaard, R., Lalonde, S.V., Partin, C.A., Oonk, P.B.H., Tsikos, H., Lyons, T.W., Bekker, A., Johnson, C.M., 2017. Iron formations: A global record of Neoproterozoic to Palaeoproterozoic environmental history. *Earth-Science Reviews* 172, 140–177.
- Konhauser, K.O., Robbins, L.J., Alessi, D.S., Flynn, S.L., Gingras, M.K., Martinez, R.E., Kappler, A., Swanner, E.D., Li, Y.-L., Crowe, S.A., Planavsky, N.J., Reinhard, C.T., Lalonde, S.V., 2018. Phytoplankton contributions to the trace-element composition of Precambrian banded iron formations. *Geological Society of America Bulletin* 130, 941-951.
- Krissansen-Totton, J., Arney, G.N., Catling, D.C., 2018. Constraining the climate and ocean pH of the early Earth with a geological carbon cycle model. *Proceedings of the National Academy of Sciences* 252, 201721296–6.
- Leith, C.K., 1903. The Mesabi iron-bearing district of Minnesota. In: *Monographs*. 43. United States Geological Survey, pp. 1–324.
- Lemarchand, E., Schott, J., Gaillardet, J.R.M., 2007. How surface complexes impact boron isotope fractionation: Evidence from Fe and Mn oxides sorption experiments. *Earth and Planetary Science Letters* 260, 277–296.
- Martinez, R.E., Konhauser, K.O., Paunova, N., Wu, W., Alessi, D.S., Kappler, A., 2016. Surface reactivity of the anaerobic phototrophic Fe (II)-oxidizing bacterium

- Rhodovulum iodosum*: Implications for trace metal budgets in ancient oceans and banded iron formations. *Chemical Geology* 442, 113–120.
- Nie, N.X., Dauphas, N., Greenwood, R.C., 2017. Iron and oxygen isotope fractionation during iron UV photo-oxidation: Implications for early Earth and Mars. *Earth and Planetary Science Letters* 458, 179–191.
- Olson, S.L., Reinhard, C.T., Lyons, T.W., 2016. Limited role for methane in the mid-Proterozoic greenhouse. *Proceedings of the National Academy of Sciences* 113, 11447–11452.
- Rasmussen, B., Muhling, J.R., Suvorova, A., Krapež, B., 2017. Greenalite precipitation linked to the deposition of banded iron formations downslope from a late Archean carbonate platform. *Precambrian Research* 290, 49–62.
- Robbins, L.J., Lalonde, S.V., Saito, M.A., Planavsky, N.J., Mloszewska, A.M., Pecoits, E., Scott, C., Dupont, C.L., Kappler, A., Konhauser, K.O., 2013. Authigenic iron oxide proxies for marine zinc over geological time and implications for eukaryotic metallome evolution. *Geobiology* 11, 295–306.
- Robbins, L.J., Lalonde, S.V., Planavsky, N.J., Partin, C.A., Reinhard, C.T., Kendall, B., Scott, C., Hardisty, D.S., Gill, B.C., Alessi, D.S., Dupont, C.L., Saito, M.A., Crowe, S.A., Poulton, S.W., Bekker, A., Lyons, T.W., Konhauser, K.O., 2016. Trace elements at the intersection of marine biological and geochemical evolution. *Earth-Science Reviews* 163, 323–348.
- Tosca, N.J., Guggenheim, S., Pufahl, P.K., 2016. An authigenic origin for Precambrian greenalite: Implications for iron formation and the chemistry of ancient seawater. *Geological Society of America Bulletin* 128, 511–530.

- Trivedi, P., Axe, L., 2001. Ni and Zn sorption to amorphous versus crystalline iron oxides: macroscopic studies. *Journal of Colloid and Interface Science* 244, 221–229.
- Vraspir, J.M., Butler, A., 2009. Chemistry of marine ligands and siderophores. *Annual Review of Marine Science* 1, 43–63.

Bibliography

- Abell, P.I., McClory, J., Martin, A., Nisbet, E.G., Kyser, T.K., 1985. Petrography and stable isotope ratios from Archaean stromatolites, Mushandike Formation, Zimbabwe. *Precambrian Research* 27, 385–398.
- Adams, J.J., Rostron, B.J., Mendoza, C.A., 2004. Coupled fluid flow, heat and mass transport, and erosion in the Alberta basin: implications for the origin of the Athabasca oil sands. *Canadian Journal of Earth Sciences* 41, 1077–1095.
- Aguirre, J.D., Clark, H.M., McIlvin, M., Vazquez, C., Palmere, S.L., Grab, D.J., Seshu, J., Hart, P.J., Saito, M., Culotta, V.C., 2013. A manganese-rich environment supports superoxide dismutase activity in a Lyme disease pathogen, *Borrelia burgdorferi*. *Journal of Biological Chemistry* 288, 8468-8478.
- Ahlgren, N.A., Noble, A., Patton, A.P., Roache-Johnson, K., Jackson, L., Robinson, D., McKay, C., Moore, L.R., Saito, M.A., Rocap, G., 2014. The unique trace metal and mixed layer conditions of the Costa Rica upwelling dome support a distinct dense community of *Synechococcus*. *Limnology and Oceanography* 59, 2166-2184.
- Ahn, J.H., Buseck, P.R., 1990. Hematite nanospheres of possible colloidal origin from a Precambrian banded iron formation. *Science* 250, 111–113.
- Alexander, B., Bau, M., Andersson, P., Dulski, P., 2008. Continentally-derived solutes in shallow Archean seawater: Rare earth element and Nd isotope evidence in iron formation from the 2.9 Ga Pongola Supergroup, South Africa. *Geochimica et Cosmochimica Acta* 72, 378–394.

- Alibert, C., 2016. Rare earth elements in Hamersley BIF minerals. *Geochimica et Cosmochimica Acta* 184, 311–328.
- Amin, S.A., Moffett, J.W., Martens-Habben, W., Jacquot, J.E., Han, Y., Devol, A., Ingalls, A.E., Stahl, D.A., Armbrust, E.V., 2013. Copper requirements of the ammonia-oxidizing archaeon *Nitrosopumilus maritimus* SCM1 and implications for nitrification in the marine environment. *Limnology and Oceanography* 58, 2037-2045.
- Anbar, A.D., 2008. Elements and Evolution. *Science* 322, 1481-1483.
- Anbar, A.D., Duan, Y., Lyons, T.W., Arnold, G.L., Kendall, B., Creaser, R.A., Kaufman, A.J., Gordon, G.W., Scott, C., Garvin, J., Buick, R., 2007. A Whiff of Oxygen Before the Great Oxidation Event? *Science* 317, 1903-1906.
- Anbar, A.D., Knoll, A.H., 2002. Proterozoic ocean chemistry and evolution: A bioinorganic bridge? *Science* 297, 1137-1142.
- Aristilde, L., Xu, Y., Morel, F.M.M., 2012. Weak Organic Ligands Enhance Zinc Uptake in Marine Phytoplankton. *Environmental Science & Technology* 46, 5438–5445.
- Asael, D., Tissot, F.L.H., Reinhard, C.T., Rouxel, O., Dauphas, N., Lyons, T.W., Ponzevera, E., Liorzou, C., Chéron, S., 2013. Coupled molybdenum, iron, and uranium stable isotopes as oceanic paleoredox proxies during the Paleoproterozoic Shunga Event. *Chemical Geology* 362, 193-210.
- Awramik, S.M., Buchheim, H.P., 2009. A giant, Late Archean lake system: The Meentheena Member (Tumbiana Formation; Fortescue Group), Western Australia. *Precambrian Research* 174, 215–240.

- Balistrieri, L.S., Borrok, D., Wanty, R., and Ridley, W., 2008, Fractionation of Cu and Zn isotopes during adsorption onto amorphous Fe(III) oxyhydroxide: Experimental mixing of acid rock drainage and ambient river water. *Geochimica et Cosmochimica Acta* 72, 311–328.
- Barley, M.E., Pickard, A., Sylvester, P., 1997. Emplacement of a large igneous province as a possible cause of banded iron formation 2.45 billion years ago. *Nature* 385, 55–58.
- Bau, M., 1993. Effects of syn- and post-depositional processes on the rare-earth element distribution in Precambrian iron-formations. *European Journal of Mineralogy* 5, 257-267.
- Bau, M., Möller, P., 1993. Rare earth element systematics of the chemically precipitated component in Precambrian iron formations and the evolution of the terrestrial atmosphere-hydrosphere-lithosphere system. *Geochimica et Cosmochimica Acta* 57, 2239-2249.
- Bau, M., Dulski, P., 1996. Distribution of yttrium and rare-earth elements in the Penge and Kuruman iron-formations, Transvaal Supergroup, South Africa. *Precambrian Research* 79, 37-55.
- Becking, L., Kaplan, I.R., 1960. Limits of the natural environment in terms of pH and oxidation-reduction potentials. *The Journal Of Geology* 68, 243–284.
- Behrends, T., Van Cappellen, P., 2005. Competition between enzymatic and abiotic reduction of uranium(VI) under iron reducing conditions. *Chemical Geology* 220, 315-327.

- Bekker, A., Slack, J.F., Planavsky, N., Krapež, B., Hofmann, A., Konhauser, K.O., Rouxel, O.J., 2010. Iron Formation: The Sedimentary Product of a Complex Interplay among Mantle, Tectonic, Oceanic, and Biospheric Processes. *Economic Geology* 105, 467-508.
- Bekker, A., Planavsky, N.J., Krapež, B., Rasmussen, B., Hofmann, A., Slack, J.F., Rouxel, O.J., Konhauser, K.O., 2014. Iron Formations: Their Origins and Implications for Ancient Seawater Chemistry in Holland, H.K., Turekian, K., (eds.) *Treatise on Geochemistry*, 2nd edition, 561-628.
- Berg, J., Shi, Y., 1996. The Galvanization of Biology: A Growing Appreciation for the Roles of Zinc. *Science* 271, 1081-1085.
- Beukes, N.J., 1980. Lithofacies and stratigraphy of the Kuruman and Griquatown iron-formations, Northern Cape Province, South Africa. *Transactions of the Geological Society of South Africa*. 83, 69-86.
- Beukes, N.J., 1984. Sedimentology of the Kuruman and Griquatown iron-formations, Transvaal supergroup, Griqualand West, South Africa. *Precambrian Research* 24, 47-84.
- Beukes, N.J., Gutzmer, J., 2008. Origin and paleoenvironmental significance of major iron formations at the Archean-Paleoproterozoic boundary. *Society of Economic Geologists Reviews* 15, 5-47.
- Bjerrum, C.J., Canfield, D.E., 2002. Ocean productivity before about 1.9 Gyr ago limited by phosphorus adsorption onto iron oxides. *Nature* 417, 159-162.

- Blättler, C.L., Kump, L.R., Fischer, W.W., Paris, G., Kasbohm, J.J., Higgins, J.A., 2017. Constraints on ocean carbonate chemistry and pCO₂ in the Archaean and Palaeoproterozoic. *Nature Geoscience* 10, 41–45.
- Bolhar, R., Van Kranendonk, M.J., 2007. A non-marine depositional setting for the northern Fortescue Group, Pilbara Craton, inferred from trace element geochemistry of stromatolitic carbonates. *Precambrian Research* 155, 229–250.
- Bolhar, R., Hofmann, A., Woodhead, J., Hergt, J., Dirks, P., 2002. Pb- and Nd-isotope systematics of stromatolitic limestones from the 2.7 Ga Ngezi Group of the Belingwe Greenstone Belt: constraints on timing of deposition and provenance. *Precambrian Research* 114, 277–294.
- Bolhar, R., Kamber, B.S., Moorbath, S., Fedo, C.M., Whitehouse, M.J., 2004. Characterisation of early Archaean chemical sediments by trace element signatures. *Earth and Planetary Science Letters* 222, 43-60.
- Brand, L.E., Sunda, W.G., Guillard, R.R.L., 1983. Limitation of Marine Phytoplankton Reproductive Rates by Zinc, Manganese, and Iron. *Limnology and Oceanography* 28, 1182-1198.
- Broecker, W.S., Peng, T.H., 1982. *Tracers in the Sea*. Lamont-Doherty Geological Observatory, Palisades, New York. pp. 1-690.
- Bruland, K.W., 1989. Complexation of Zinc by Natural Organic Ligands in the Central North Pacific. *Limnology and Oceanography* 34, 269-285.
- Bruland, K.W., Middag, R., Lohan, M.C., 2014. Controls of Trace Metals in Seawater, in: Holland, H.D., Turekian, K. (Eds.), *Treatise on Geochemistry*. Second edition. Elsevier Ltd., Vol. 8. pp. 19–51.

- Buck, S.G., 1980. Stromatolite and ooid deposits within the fluvial and lacustrine sediments of the Precambrian Ventersdorp Supergroup of South Africa. *Precambrian Research* 12, 311–330.
- Buick, R., 2007. Did the Proterozoic ‘Canfield Ocean’ cause a laughing gas greenhouse? *Geobiology* 5, 97-100.
- Byrne, R. H., Kim K. –H., 1990. Rare earth element scavenging in seawater. *Geochimica et Cosmochimica Acta* 54, 2645-2656.
- Canfield, D.E., Jorgensen, B.B., Fossing, H., Glud, R., Gundersen, J., Ramsing, N.B., Thamdrup, B., Hansen, J.W., Nielsen, L.P., Hall, P.O.J., 1993. Pathways of organic carbon oxidation in three continental margin sediments. *Precambrian Res.* 113, 27–40.
- Cates, N., Mojzsis, S., 2007. Pre-3750 Ma supracrustal rocks from the Nuvvuagittuq supracrustal belt, northern Québec. *Earth and Planetary Science Letters* 255, 9–21.
- Cheney, E.S., 1996. Sequence stratigraphy and plate tectonic significance of the Transvaal succession of southern Africa and its equivalent in Western Australia. *Precambrian Research* 79, 3-24.
- Chi Fru, E., Rodríguez, N.P., Partin, C.A., Lalonde, S.V., Andersson, P., Weiss, D.J., Albani, El, A., Rodushkin, I., Konhauser, K.O., 2016. Cu isotopes in marine black shales record the Great Oxidation Event. *Proceedings of the National Academy of Sciences* 113, 4941-4946.
- Cloud, P.E., 1965. Significance of the Gunflint (Precambrian) Microflora. *Science* 148, 27–35.

- Cole, D.B., Reinhard, C.T., Wang, X., Gueguen, B., Halverson, G.P., Gibson, T., Hodgskiss, M.S.W., McKenzie, N.R., Lyons, T.W., Planavsky, N.J., 2016. A shale-hosted Cr isotope record of low atmospheric oxygen during the Proterozoic. *Geology* 44, 555–558.
- Condie, K.C., 1993. Chemical composition and evolution of the upper continental crust: contrasting results from surface samples and shales. *Chemical Geology* 104, 1–37.
- Corfu, F., Wallace, H., 1986. U–Pb zircon ages for magmatism in the Red Lake greenstone belt, northwestern Ontario. *Canadian Journal of Earth Sciences* 23, 27–42.
- Cornell, R.M., Schwertmann, U., 2003. *The Iron Oxides*, Second. ed. Wiley-VCH Verlag GmbH & Co. pp. 1-664.
- Crowe, S.A., O'Neill, A.H., Katsev, S., Hehanussa, P., Haffner, G.D., Sundby, B., Mucci, A., Fowle, D.A., 2008. The biogeochemistry of tropical lakes: A case study from Lake Matano, Indonesia. *Limnology and Oceanography* 53, 319–331.
- Crowe, S.A., Døssing, L.N., Beukes, N.J., Bau, M., Kruger, S.J., Frei, R., Canfield, D.E., 2013. Atmospheric oxygenation three billion years ago. *Nature* 50, 535–538.
- Crowe, S.A., Paris, G., Katsev, S., Jones, C., Kim, S.-T., Zerkle, A.L., Nomosatryo, S., Fowle, D.A., Adkins, J.F., Sessions, A.L., Farquhar, J., Canfield, D.E., 2014. Sulfate was a trace constituent of Archean seawater. *Science* 346, 735–739.
- Dahl, T.W., Boyle, R.A., Canfield, D.E., Connelly, J.N., Gill, B.C., Lenton, T.M., Bizzarro, M., 2014. Uranium isotopes distinguish two geochemically distinct stages during the later Cambrian SPICE event. *Earth and Planetary Science Letters* 401, 313–326.
- David, L.A., Alm, E.J., 2011. Rapid evolutionary innovation during an Archaean genetic expansion. *Nature* 469, 93–96.

- Davis, J. A., Coston, J. A., Kent, D. B., Fuller, C. C., 1998. Application of the surface complexation concept to complex mineral assemblages. *Environmental Science & Technology* 32, 2820-2828.
- Davy, R., 1983. Chapter 8 Part A. A Contribution on the Chemical Composition of Precambrian Iron-Formations, in: Trendall, A.F., Morris, R.C. (Eds.), *Iron-Formation Facts and Problems, Developments in Precambrian Geology*. Elsevier, pp. 325–343.
- Davy, R., 1992. Mineralogy and chemical composition of a core from the Weeli Wolli Formation in the Hamersley Basin (No. Record 1991/6). Geological Survey of Western Australia, Perth. pp. 1-103.
- De Carlo, E.H., Green, W.J., 2002. Rare earth elements in the water column of Lake Vanda, McMurdo Dry Valleys, Antarctica. *Geochimica et Cosmochimica Acta* 66, 1323–1333.
- Deming D (2002) *Introduction to Hydrogeology*. New York, NY, McGraw-Hill, p. 56.
- Derry, L., Jacobsen, S., 1990. The chemical evolution of Precambrian seawater: Evidence from REEs in banded iron formations. *Geochimica et Cosmochimica Acta* 54, 2965–2977.
- Devaney, J.R., 2001. Sedimentology and Volcanology of Selected Tectonized Stratigraphic Units, Southern Birch–Uchi Greenstone Belt, Uchi Subprovince (No. 6031). Ontario Geological Survey Open File Report. p. 1-47.
- Dhuime, B., Wuestefeld, A., Hawkesworth, C.J., 2015. Emergence of modern continental crust about 3 billion years ago. *Nature Geoscience* 8, 552–555.

- Dierssen, H., Balzer, W., Landing, W.M., 2001. Simplified synthesis of an 8-hydroxyquinoline chelating resin and a study of trace metal profiles from Jellyfish Lake, Palau. *Marine Chemistry* 73, 173–192.
- Dodd, M.S., Papineau, D., Grenne, T., Slack, J.F., Rittner, M., Pirajno, F., O’Neil, J., Little, C.T.S., 2017. Evidence for early life in Earth’s oldest hydrothermal vent precipitates. *Nature* 543, 60–64.
- Douville, E., Charlou, J., Oelkers, E., Bienvenu, P., 2002. The rainbow vent fluids (36°14’N, MAR): the influence of ultramafic rocks and phase separation on trace metal content in Mid-Atlantic Ridge hydrothermal fluids. *Chemical Geology* 184, 37–48.
- Dupont, C.L., Yang, S., Palenik, B., Bourne, P.E., 2006. Modern proteomes contain putative imprints of ancient shifts in trace metal geochemistry. *Proceedings of the National Academy of Sciences* 103, 17822-17827.
- Dupont, C.L., Neupane, K., Shearer, J., Palenik, B., 2008. Diversity, function and evolution of genes coding for putative Ni-containing superoxide dismutases. *Environmental Microbiology* 10, 1831-1843.
- Dupont, C.L., Butcher, A., Valas, R.E., Bourne, P.E., Caetano-Anollés, G., 2010. History of biological metal utilization inferred through phylogenomic analysis of protein structures. *Proceedings of the National Academy of Sciences* 107, 10567-10572.
- Dzombak, D. A., Morel, F. M. M., 1990. Surface complexation modeling Hydrous ferric oxide. John Wiley and Sons, pp 1-393.
- Eady, R.R., 1996. Structure–Function Relationships of Alternative Nitrogenases. *Chemical Reviews* 96, 3013–3030.

- Ehrenreich, A., Widdel, F., 1994. Anaerobic oxidation of ferrous iron by purple bacteria, a new type of phototrophic metabolism. *Applied and Environmental Microbiology* 60, 4517–4526.
- Eickhoff, M., Obst, M., Schröder, C., Hitchcock, A.P., Tyliczszak, T., Martinez, R.E., Robbins, L.J., Konhauser, K.O., Kappler, A., 2014. Nickel partitioning in biogenic and abiogenic ferrihydrite: The influence of silica and implications for ancient environments. *Geochimica et Cosmochimica Acta* 140, 65-79.
- Eickmann B., Hofmann A., Wille M., Bui T. H., Wing B. A., Schoenberg R, 2018, Isotopic evidence for oxygenated Mesoarchaeon shallow oceans. *Nature Geoscience* 11, 133–138.
- Ellis, A.S., Johnson, T.M., Bullen, T.D., 2002. Chromium Isotopes and the Fate of Hexavalent Chromium in the Environment. *Science* 295, 2060–2062.
- Erel, Y., Stolper, E.M., 1993. Modeling of rare-earth element partitioning between particles and solution in aquatic environments. *Geochimica et Cosmochimica Acta* 57, 513-518.
- Eugster, H.P., Chou, I.M., 1973. The depositional environments of Precambrian banded iron-formations. *Economic Geology* 68, 1144–1168.
- Farkaš, J., Buhl, D., Blenkinsop, J., Veizer, J., 2007. Evolution of the oceanic calcium cycle during the late Mesozoic: Evidence from $\delta^{44/40}\text{Ca}$ of marine skeletal carbonates. *Earth and Planetary Science Letters* 253, 96–111.
- Farquhar, J., Zerkle, A.L., Bekker, A., 2011. Geological constraints on the origin of oxygenic photosynthesis. *Photosynth Res* 107, 11–36.

- Fein, J. B., Daughney, C. J., Yee, N., Davis, T. A., 1997. A chemical equilibrium model for metal adsorption onto bacterial surfaces. *Geochimica et Cosmochimica Acta* 61, 3319-3328.
- Fein, J. B., Boily, J. -F., Yee, N., Gorman-Lewis, D., Turner, B. F., 2005. Potentiometric titrations of *Bacillus subtilis* cells to low pH and a comparison of modeling approaches. *Geochimica et Cosmochimica Acta* 69, 1123-1132.
- Fischer, W., Knoll, A.H., 2009. An iron shuttle for deepwater silica in Late Archean and early Paleoproterozoic iron formation. *Geological Society of America Bulletin* 121, 222–235.
- Flament, N., Coltice, N., Rey, P.F., 2013. The evolution of the $^{87}\text{Sr}/^{86}\text{Sr}$ of marine carbonates does not constrain continental growth. *Precambrian Research* 229, 177–188.
- Foriel, J., Philippot, P., Rey, P., Somogyi, A., Banks, D., Ménez, B., 2004. Biological control of Cl/Br and low sulfate concentration in a 3.5-Gyr-old seawater from North Pole, Western Australia. *Earth and Planetary Science Letters* 228, 451–463.
- Fralick, P., Hollings, P., King, D., 2008. Stratigraphy, geochemistry, and depositional environments of Mesoarchean sedimentary units in western Superior Province: Implications for generation of early crust, in: Condie, K.C., Pease, V. (Eds.), *When Did Plate Tectonics Begin on Planet Earth*. Special Paper 440: *When Did Plate Tectonics Begin on Planet Earth?* pp. 77–96.
- Green, M.G., 2001, Early Archaean crustal evolution: evidence from ~3.5 billion year old greenstone successions in the Pilgangoora Belt, Pilbara Craton, Australia: 277 p.

- Frausto da Silva, J.J.R., Williams, R.J., 2001. *The biological chemistry of the elements: The inorganic chemistry of life*. 2nd ed., Oxford University Press, Oxford, United Kingdom. p. 1- 575.
- Frei, R., Gaucher, C., Poulton, S.W., Canfield, D.E., 2009. Fluctuations in Precambrian atmospheric oxygenation recorded by chromium isotopes. *Nature* 461, 250-253.
- Frei, R., Crowe, S.A., Bau, M., Polat, A., Fowle, D.A., 2016. Oxidative elemental cycling under the low O₂ Eoarchean atmosphere. *Scientific Reports* 6, 21058.
- Freeze RA, Cherry JA (1979) *Groundwater*. Englewood Cliffs, NJ, Prentice-Hall, p. 29.
- French, B.M., 1973. Mineral Assemblages in Diagenetic and Low-Grade Metamorphic Iron-Formation. *Economic Geology* 68, 1063–1074.
- Friedrich, A.J., Luo, Y.L., Catalano, J.G., 2011. Trace element cycling through iron oxide minerals during redox driven dynamic recrystallization. *Geology* 39, 1083-1086.
- Friedrich, A.J., Catalano, J.G., 2012. Controls on Fe(II)-Activated Trace Element Release from Goethite and Hematite. *Environmental Science & Technology* 46, 1519-1526.
- Friedrich, A.J., Scherer, M.M., Bachman, J.E., Englehard, M.H., Rapponotti, B.W., Catalano, J.G., 2012. Inhibition of Trace Element Release During Fe(II)-Activated Recrystallization of Al-, Cr-, and Sn-Substituted Goethite and Hematite. *Environmental Science & Technology* 46, 10031-10039.
- Foster, G.L., Rae, J.W.B., 2016. Reconstructing Ocean pH with Boron Isotopes in Foraminifera. *Annual Review of Earth and Planetary Sciences* 44, 207–237.
- Frost, C.D., von Blanckenburg, F., Schoenberg, R., Frost, B.R., Swapp, S.M., 2007. Preservation of Fe isotope heterogeneities during diagenesis and metamorphism of banded iron formation. *Contributions to Mineralogy and Petrology* 153, 211-235.

- Gaillard, F., Scaillet, B., Arndt, N.T., 2015. Atmospheric oxygenation caused by a change in volcanic degassing pressure. *Nature* 478, 229–232.
- Grotzinger, J.P., Kasting, J.F., 1993. New constraints on Precambrian ocean composition. *The Journal Of Geology* 101, 235–243.
- Grotzinger, J.P., James, N.P., 2000. Precambrian carbonates: evolution of understanding, in: Grotzinger, J.P., James, N.P. (Eds.), *Carbonate Sedimentation and Diagenesis in the Evolving Precambrian World*. SEPM (Society for Sedimentary Geology), pp. 3–20.
- Gruner, J.W., 1922. The origin of sedimentary iron-formations: the Biwabik Formation of the Mesabi Range. *Economic Geology* 22, 407–460.
- Gueguen, B., Reinhard, C.T., Algeo, T.J., Peterson, L.C., Nielsen, S.G., Wang, X., Rowe, H., Planavsky, N.J., 2016. The chromium isotope composition of reducing and oxic marine sediments. *Geochimica et Cosmochimica Acta* 184, 1–19.
- Guillong, M., Meier, D.L., Allan, M.M., Heinrich, C.A., Yardley, B.W.D., 2008. SILLS: A MATLAB-based program for the reduction of laser ablation ICP-MS data of homogeneous materials and inclusions. *Mineralogical Association of Canada Short Course 40*, Vancouver, B.C., p. 328-333.
- Gumsley, A.P., Chamberlain, K.R., Bleeker, W., Söderlund, U., de Kock, M.O., Larsson, E.R., Bekker, A., 2017. Timing and tempo of the Great Oxidation Event. *Proc. Natl. Acad. Sci.* 114, 1811–1816.
- Halevy, I., Bachan, A., 2017. The geologic history of seawater pH. *Science* 355, 1069–1071.

- Halevy, I., Alesker, M., Schuster, E.M., Popovitz-Biro, R., Feldman, Y., 2017. A key role for green rust in the Precambrian oceans and the genesis of iron formations. *Nature* 10, 135–139.
- Halama, M., Swanner, E.D., Konhauser, K.O., Kappler, A., 2016. Evaluation of siderite and magnetite formation in BIFs by pressure–temperature experiments of Fe(III) minerals and microbial biomass. *Earth and Planetary Science Letters* 450, 243–253.
- Harnmeijer, J., 2010. Squeezing blood from a stone: Inferences into the life and depositional environments of the Early Archaean. PhD Thesis, University of Washington. p. 1-609.
- Hardie, L.A., 2003. Secular variations in Precambrian seawater chemistry and the timing of Precambrian aragonite seas and calcite seas. *Geology* 31, 785–788.
- Haugaard, R., Frei, R., Stendal, H., Konhauser, K., 2013. Petrology and geochemistry of the ~2.9Ga Itilliarsuk banded iron formation and associated supracrustal rocks, West Greenland: Source characteristics and depositional environment. *Precambrian Research* 22, 150–176.
- Haugaard, R., Pecoits, E., Lalonde, S., Rouxel, O., Konhauser, K., 2016. The Joffre banded iron formation, Hamersley Group, Western Australia: Assessing the palaeoenvironment through detailed petrology and chemostratigraphy. *Precambrian Research* 273, 12–37.
- Hausinger, R.P., 1987. Nickel Utilization by Microorganisms. *Microbiological Reviews* 51, 22-42.

- Hegner, E., Kröner, A., Hunt, P., 1994. A precise U-Pb zircon age for the Archaean Pongola Supergroup volcanics in Swaziland. *Journal of African Earth Sciences* 18, 339–341.
- Henderson, J.B., 1975. Archean Stromatolites in the Northern Slave Province, Northwest Territories, Canada. *Canadian Journal of Earth Sciences* 12, 1619–1630.
- Hofmann, A., Dirks, P.H.G.M., Jelsma, H.A., 2004. Shallowing-Upward Carbonate Cycles in the Belingwe Greenstone Belt, Zimbabwe: A Record of Archean Sea-Level Oscillations. *Journal of Sedimentary Research* 74, 64–81.
- Hoffman, P.F., Kaufman, A.J., Halverson, G.P., Schrag, D.P., 1998. A Neoproterozoic Snowball Earth. *Science* 281, 1342–1346.
- Holland, H., 1973. The Oceans: A Possible Source of Iron in Iron-Formations. *Economic Geology* 68, 1169–1172.
- Holland, H.D., 1978. *The Chemistry of the Atmosphere and Oceans*. Wiley, New York, pp. 1–369.
- Holland, H.D., 1984, Oxygen in the Precambrian Atmosphere: Evidence from Marine Environments, *in* *The chemical evolution of the atmosphere and oceans*, Princeton University Press, Princeton, NJ, p. 337–440.
- Hsu J. C. (1996) *Multiple Comparisons. Theory and Methods*. Chapman and Hall, London, England.
- Irwin, H., Curtis, C., Coleman, M., 1977. Isotopic evidence for source of diagenetic carbonates formed during burial of organic-rich sediments. *Nature* 269, 209–213.
- Isley, A., 1995. Hydrothermal plumes and the delivery of iron to banded iron formation. *The Journal Of Geology* 169–185.

- Isley, A.E., Abbott, D.H., 1999. Plume-related mafic volcanism and the deposition of banded iron formation *Journal of Geophysical Research* 104, 15461–15477.
- Isson, T.T., Planavsky, N.J., 2018. Reverse weathering as a long-term stabilizer of marine pH and planetary climate. *Nature* 560, 471–475.
- James, H.L., 1954. Sedimentary facies of iron-formation. *Economic Geology* 49, 235-293.
- Jansa, L.F., n.d. Mesozoic carbonate platforms and banks of the eastern North American margin. *Marine Geology* 44, 97–117.
- Johnson, C.M., Beard, B.L., Klein, C., Beukes, N.J., Roden, E.E., 2008. Iron isotopes constrain biologic and abiologic processes in banded iron formation genesis. *Geochimica et Cosmochimica Acta* 72, 151–169.
- Johnson, J.E., Muhling, J.R., Cosmidis, J., Rasmussen, B., Templeton, A.S., 2018. Low-Fe(III) Greenalite Was a Primary Mineral from Neoproterozoic Oceans. *Geophysical Research Letters* 45, 3182-3192.
- Jones, C., Nomosatryo, S., Crowe, S.A., Bjerrum, C.J., Canfield, D.E., 2015. Iron oxides, divalent cations, silica, and the early earth phosphorus crisis. *Geology* 43, 135-138.
- Kamber, B.S., Bolhar, R., Webb, G.E., 2004. Geochemistry of late Archaean stromatolites from Zimbabwe: evidence for microbial life in restricted epicontinental seas. *Precambrian Research* 132, 379–399.
- Kappler, A., Pasquero, C., Konhauser, K.O., Newman, D.K., 2005. Deposition of banded iron formations by anoxygenic phototrophic Fe(II)-oxidizing bacteria. *Geology* 33, 865–868.
- Kasting, J.F., 2013. What caused the rise of atmospheric O₂? *Chemical Geology* 362, 13–25.

- Kendall, B., Brennecka, G.A., Weyer, S., Anbar, A.D., 2013. Uranium isotope fractionation suggests oxidative uranium mobilization at 2.50 Ga. *Chemical Geology* 362, 105–114.
- Kendall, B., Komiya, T., Lyons, T.W., Bates, S.M., Gordon, G.W., Romaniello, S.J., Jiang, G., Creaser, R.A., Xiao, S., McFadden, K., Sawaki, Y., Tahata, M., Shu, D., Han, J., Li, Y., Chu, X., Anbar, A.D., 2015a. Uranium and molybdenum isotope evidence for an episode of widespread ocean oxygenation during the late Ediacaran Period. *Geochimica et Cosmochimica Acta* 156, 173-193.
- Klein, C., 2005. Some Precambrian banded iron-formations (BIFs) from around the world: Their age, geologic setting, mineralogy, metamorphism, geochemistry and origin. *American Mineralogist* 90, 1473-1499.
- Klein, C., Beukes, N.J., 1989. Geochemistry and sedimentology of a facies transition from limestone to iron-formation in the early Proterozoic Transvaal Supergroup, South Africa. *Economic Geology* 84, 1733–1774.
- Kobayashi, M., Shimizu, S., 1999. Cobalt proteins. *European Journal of Biochemistry* 261, 1-9.
- Koeppenkastrop, D., De Carlo, E.H., 1992. Sorption of rare-earth elements from seawater onto synthetic mineral particles: An experimental approach. *Chemical Geology* 95, 251-263.
- Köhler, I., Konhauser, K.O., Papineau, D., Bekker, A., Kappler, A., 2013. Biological carbon precursor to diagenetic siderite with spherical structures in iron formations. *Nature Communications* 4, 1741–7.

- Köhler, I., Bonnand, P., Boyet, M., Heubeck, C., Homann, M., Nonotte, P., Konhauser, K.O., Lalonde, S.V., *in review*, Post-depositional REE mobility in a Paleoproterozoic iron formation revealed by La-Ce geochronology: A cautionary tale for signals of ancient oxygenation. *Earth and Planetary Science Letters*.
- Konhauser, K.O., 2007, *Introduction to Geomicrobiology*: Blackwell Science Ltd., Malden, MA, USA. pp. 1-425.
- Konhauser, K.O., Hamade, T., Raiswell, R., Morris, R., Ferris, F., Southam, G., Canfield, D., 2002. Could bacteria have formed the Precambrian banded iron formations? *Geology* 30, 1079–1082.
- Konhauser, K.O., Newman, D., Kappler, A., 2005. The potential significance of microbial Fe (III) reduction during deposition of Precambrian banded iron formations. *Geobiology* 3, 167–177.
- Konhauser, K.O., Lalonde S.V., Amskold, L.A., Holland, H.D., 2007. Was There Really an Archean Phosphate Crisis? *Science* 315, 1234.
- Konhauser, K.O., Pecoits, E., Lalonde, S.V., Papineau, D., Nisbet, E.G., Barley, M.E., Arndt, N.T., Zahnle, K., Kamber, B.S., 2009. Oceanic nickel depletion and a methanogen famine before the Great Oxidation Event. *Nature* 458, 750-753.
- Konhauser, K.O., Lalonde, S.V., Planavsky, N.J., Pecoits, E., Lyons, T.W., Mojzsis, S.J., Rouxel, O.J., Barley, M.E., Rosière, C., Fralick, P.W., Kump, L.R., Bekker, A., 2011. Aerobic bacterial pyrite oxidation and acid rock drainage during the Great Oxidation Event. *Nature* 478, 369-373.
- Konhauser, K.O., Robbins, L.J., Pecoits, E., Peacock, C.L., Kappler, A., Lalonde, S.V., 2015. The Archean nickel famine revisited. *Astrobiology* 15, 804-815.

- Konhauser, K.O., Planavsky, N.J., Hardisty, D.S., Robbins, L.J., Warchola, T.J., Haugaard, R., Lalonde, S.V., Partin, C.A., Oonk, P.B.H., Tsikos, H., Lyons, T.W., Bekker, A., Johnson, C.M., 2017. Iron formations: A global record of Neoproterozoic to Palaeoproterozoic environmental history. *Earth-Science Reviews* 172, 140–177.
- Konhauser, K.O., Robbins, L.J., Alessi, D.S., Flynn, S.L., Gingras, M.K., Martinez, R.E., Kappler, A., Swanner, E.D., Li, Y.-L., Crowe, S.A., Planavsky, N.J., Reinhard, C.T., Lalonde, S.V., 2018. Phytoplankton contributions to the trace-element composition of Precambrian banded iron formations. *Geological Society of America Bulletin*, 130, 941-951.
- Koretsky, C., 2000. The significance of surface complexation reactions in hydrologic systems: a geochemist's perspective. *Journal of Hydrology* 230, 127-171.
- Krapež, B., Barley, M.E., Pickard, A.L., 2003. Hydrothermal and re-sedimented origins of the precursor sediments to banded iron formation: sedimentological evidence from the Early Palaeoproterozoic Brockman Supersequence of Western Australia. *Sedimentology* 50, 979-1011.
- Krissansen-Totton, J., Arney, G.N., Catling, D.C., 2018. Constraining the climate and ocean pH of the early Earth with a geological carbon cycle model. *Proceedings of the National Academy of Sciences* 252, 201721296–6.
- Kunzmann, M., Halverson, G.P., Sossi, P.A., Raub, T.D., Payne, J.L., Kirby, J., 2013. Zn isotope evidence for immediate resumption of primary productivity after snowball Earth. *Geology* 41, 27-30.

- Lalonde, S.V., Konhauser, K.O., 2015. Benthic perspective on Earth's oldest evidence for oxygenic photosynthesis *Proceedings of the National Academy of Sciences* 112, 995-1000.
- Lalonde, S.V., Smith, D., Owttrim, G., Konhauser, K.O., 2008. Acid-base properties of cyanobacterial surfaces. II: Silica as a chemical stressor influencing cell surface reactivity. *Geochimica et Cosmochimica Acta* 72, 1269–1280.
- Lambert, M.B., 1998. Stromatolites of the late Archean Back River stratovolcano, Slave structural province, Northwest Territories, Canada. *Canadian Journal of Earth Sciences* 35, 290–301.
- Landing, W.M., Burnett, W.C., Lyons, W.B., Orem, W.H., 1991. Nutrient Cycling and the Biogeochemistry of Manganese, Iron, and Zinc in Jellyfish Lake, Palau. *Limnology and Oceanography* 36, 515–525.
- Langmuir D (1997) *Aqueous Environmental Geochemistry*: Prentice Hall, Upper Saddle River, New Jersey, pp. 1-600.
- Large, R.R., Halpin, J.A., Danyushevsky, L.V., Maslennikov, V.V., Bull, S.W., Long, J.A., Gregory, D.D., Lounejeva, E., Lyons, T.W., Sack, P.J., McGoldrick, P.J., Claver, C.R., 2014. Trace element content of sedimentary pyrite as a new proxy for deep-time ocean-atmosphere evolution. *Earth and Planetary Science Letters* 389, 209-220.
- Leith, C.K., 1903. The Mesabi iron-bearing district of Minnesota. In: *Monographs*. 43. United States Geological Survey, pp. 1–324.
- Lemarchand, E., Schott, J., Gaillardet, J.R.M., 2007. How surface complexes impact boron isotope fractionation: Evidence from Fe and Mn oxides sorption experiments. *Earth and Planetary Science Letters* 260, 277–296.

- Li, W., Beard, B.L., Johnson, C.M., 2015. Biologically recycled continental iron is a major component in banded iron formations. *Proceedings of the National Academy of Sciences* 112, 8193–8198.
- Li, Y.L., Konhauser, K.O., Cole, D.R., Phelps, T.J., 2011. Mineral ecophysiological data provide growing evidence for microbial activity in banded-iron formations. *Geology* 39, 707–710.
- Liu, Y., Alessi, D.S., Owttrim, G.W., Petrash, D.A., 2015. Cell surface reactivity of *Synechococcus* sp. PCC 7002: Implications for metal sorption from seawater. *Geochimica et Cosmochimica Acta* 169, 30–44.
- Liu, X.M., Kah, L.C., Knoll, A.H., Cui, H., Kaufman, A.J., Shahar, A., Hazen, R.M., 2016. Tracing Earth's O₂ evolution using Zn/Fe ratios in marine carbonates. *Geochemical Perspectives Letters* 2, 24–34.
- Lipscomb, W.N., Sträter, N., 1996. Recent Advances in Zinc Enzymology. *Chemical Reviews* 96, 2375-2433.
- Liu, Y., Alessi, D.S., Owttrim, G.W., Petrash, D.A., Mloszewska, A.M., Lalonde, S.V., Martinez, R.E., Zhou, Q., Konhauser, K.O., 2015. Cell surface reactivity of *Synechococcus* sp. PCC 7002: Implications for metal sorption from seawater. *Geochimica et Cosmochimica Acta* 169, 30-44.
- Lohan, M.C., Crawford, D.W., Purdie, D.A., Statham, P.J., 2005. Iron and zinc enrichments in the northeastern subarctic Pacific: Ligand production and zinc availability in response to phytoplankton growth. *Limnology and Oceanography* 50, 1427–1437.

- Lovley, D.R., Phillips, E.J.P., Gorby, Y.A., Landa, E.R., 1991. Microbial reduction of uranium. *Nature* 350, 413-416.
- Lowe, D.R., L. P. Knauth, 1977. Sedimentology of the Onverwacht Group (3.4 Billion Years), Transvaal, South Africa, and Its Bearing on the Characteristics and Evolution of the Early Earth. *The Journal Of Geology* 85, 699–723.
- Lowe, D.R., Byerly, G.R., 2007, An Overview of the Geology of the Barberton Greenstone Belt and Vicinity: Implications for Early Crustal Development, *in* Van Kranendonk, M.J., Smithies, R.H., and Bennett, V.C. eds., *Earth's Oldest Rocks, Developments in Precambrian Geology*, Elsevier, p. 481–526.
- Lyons, T.W., Gellatly, A.M., McGoldrick, P.J., Kah, L.C., 2006. Proterozoic sedimentary exhalative (SEDEX) deposits and links to evolving global ocean chemistry. *In* Kesler, S.E., and Ohmoto, H., eds., *Evolution of Early Earth's Atmosphere, Hydrosphere, and Biosphere—Constraints from Ore Deposits*. Geological Society of America Memoir 198, 169–184.
- Lyons, T.W., Reinhard, C.T., Planavsky, N.J., 2014. The rise of oxygen in Earth's early ocean and atmosphere. *Nature* 506, 307-315.
- Magnabosco, C., Moore, K.R., Wolfe, J.M., Fournier, G.P., 2018. Dating phototropic microbial lineages with reticulate gene histories. *Geobiology* 16, 179-189.
- Maliva, R.G., Knoll, A.H., Simonson, B.M., 2005. Secular change in the Precambrian silica cycle: Insights from chert petrology. *Geological Society of America Bulletin* 117, 835–845.
- Marsh, E.N.G., 1999. Coenzyme B₁₂ (cobalamin)-dependent enzymes. *Essays in Biochemistry* 34, 139-154.

- Martin, A., Nisbet, E.G., Bickle, M.J., 1980. Archaean stromatolites of the Belingwe Greenstone Belt, Zimbabwe (Rhodesia). *Precambrian Research* 13, 337–362.
- Martinez, R.E., Konhauser, K.O., Paunova, N., Wu, W., Alessi, D.S., Kappler, A., 2016. Surface reactivity of the anaerobic photoferrotrophic Fe(II)-oxidizing bacterium *Rhodovulum iodosum*: Implications for trace metal budgets in ancient oceans and banded iron formation. *Chemical Geology* 442, 113-120.
- Mason, T.R., Brunn, Von, V., 1977. 3-Gyr-old stromatolites from South Africa. *Nature* 266, 47–49.
- McLellan, J.G., Oliver, N.H.S., Schaub, P.M., 2004. Fluid flow in extensional environments; numerical modelling with an application to Hamersley iron ores. *Journal of Structural Geology* 26, 1157–1171.
- McLennan, S., 1989. Rare Earth Elements in Sedimentary Rocks: Influence of Provenance and Sedimentary Processes, in: Lipin, B.R., McKay, G.A. (Eds.) *Geochemistry and mineralogy of rare earth elements. Reviews in Mineralogy and Geochemistry* 21, 169–200.
- Miyano, T., Klein, C., 1984. Evaluation of the stability relations of amphibole asbestos in metamorphosed iron formations. *Mineral Geology* 33, 213–222.
- Mloszewska, A., Pecoits, E., Cates, N., Mojzsis, S.J., O'Neil, J., Robbins, L.J., Konhauser, K.O., 2012. The composition of Earth's oldest iron formations: The Nuvvuagittuq Supracrustal Belt (Québec, Canada). *Earth and Planetary Science Letters* 317-318, 331–34

- Mloszewska, A.M., Mojzsis, S.J., Pecoits, E., Papineau, D., Dauphas, N., Konhauser, K.O., 2013. Chemical sedimentary protoliths in the >3.75Ga Nuvvuagittuq Supracrustal Belt (Québec, Canada). *Gondwana Research* 23, 574–594.
- Morel, F.M.M., Reinfelder, J.R., Roberts, S.B., Chamberlain, C.P., Lee, J.G., Yee, D., 1994. Zinc and carbon co-limitation of marine phytoplankton. *Nature* 369, 740-742.
- Morris, R.C., 1985. Genesis of iron ore in banded iron-formation by supergene and supergene-metamorphic processes – A conceptual model, *Regional Studies and Specific Deposits*. Elsevier. p. 73–235.
- Morris, R.C., 1993. Genetic modeling for banded iron-formation of the Hamersley Group, Pilbara Craton, Western Australia. *Precambrian Research* 60, 243-286.
- Mücke, A., Farshad, F., 2005. Whole-rock and mineralogical composition of Phanerozoic ooidal ironstones: Comparison and differentiation of types and subtypes. *Ore Geology Reviews* 26, 227–262.
- Murphy, M.A., Sumner, D.Y., 2008. Tube structures of probable microbial origin in the Neoproterozoic Carawine Dolomite, Hamersley Basin, Western Australia. *Geobiology* 6, 83–93.
- Nakamura, K., Kato, Y., 2004. Carbonatization of oceanic crust by the seafloor hydrothermal activity and its significance as a CO₂ sink in the Early Archean. *Geochimica et Cosmochimica Acta* 68, 4595–4618.
- Nie, N.X., Dauphas, N., Greenwood, R.C., 2017. Iron and oxygen isotope fractionation during iron UV photo-oxidation: Implications for early Earth and Mars. *Earth and Planetary Science Letters* 458, 179–191.

- O'Neil, J., Maurice, C., Stevenson, R.K., Larocque, J., Cloquet, C., David, J., Francis, D., 2007. The Geology of the 3.8 Ga Nuvvuagittuq (Porpoise Cove) Greenstone Belt, Northeastern Superior Province, Canada. *Developments in Precambrian Geology* 15, 219–250.
- O'Neil, J., Carlson, R., Francis, D., Stevenson, R., 2008. Neodymium-142 evidence for Hadean mafic crust. *Science* 321, 1828–1831.
- O'Neil, J., Francis, D., Carlson, R.W., 2011. Implications of the Nuvvuagittuq Greenstone Belt for the Formation of Earth's Early Crust. *Journal of Physical Chemistry* 52, 985–1009.
- O'Neil, J., Carlson, R.W., 2017. Building Archean cratons from Hadean mafic crust. *Science* 355, 1199–1202.
- Ohnemüller, F., Prave, A. R., Fallick, A. E., Kasemann, S. A., 2014. Ocean acidification in the aftermath of the Marinoan glaciation. *Geology* 42, 1103-1106.
- Olson, S.L., Reinhard, C.T., Lyons, T.W., 2016. Limited role for methane in the mid-Proterozoic greenhouse. *Proceedings of the National Academy of Sciences* 113, 11447–11452.
- Partin, C.A., Lalonde, S.V., Planavsky, N.J., Bekker, A., Rouxel, O.J., Lyons, T.W., Konhauser, K.O., 2013a. Uranium in iron formations and the rise of atmospheric oxygen. *Chemical Geology* 362, 82-90.
- Partin, C.A., Bekker, A., Planavsky, N.J., Scott, C.T., Gill, B.C., Li, C., Podkovyrov, V., Maslov, A., Konhauser, K.O., Lalonde, S.V., Love, G.D., Poulton, S.W., Lyons, T.W., 2013b. Large-scale fluctuations in Precambrian atmospheric and oceanic

- oxygen levels from the record of U in shales. *Earth and Planetary Science Letters* 369-370, 284-293.
- Pavlov, A.A., Kasting, J.F., Eigenbrode, J.L., Freeman, K.H., 2001. Organic haze in Earth's early atmosphere: Source of low-¹³C Late Archean kerogens? *Geology* 29, 1003–1006.
- Pearson, P. N., Palmer, M. R., 1999. Middle Eocene seawater pH and atmospheric carbon dioxide concentrations. *Science* 284, 1824-1826.
- Pecoits, E., Gingras, M.E., Barley, M.E., Kappler, A., Posth, N.R., Konhauser, K.O., 2009. Petrography and geochemistry of the Dales Gorge banded iron formation: Paragenetic sequence, source and implications for palaeo-ocean chemistry. *Precambrian Research* 172, 163-187.
- Planavsky, N.J., Rouxel, O.J., Bekker, A., Lalonde, S.V., Konhauser, K.O., Reinhard, C.T., Lyons, T.W., 2010a. The evolution of the marine phosphate reservoir. *Nature* 467, 1088–1090.
- Planavsky, N., Bekker, A., Rouxel, O.J., Kamber, B., Hofmann, A., Knudsen, A., Lyons, T.W., 2010b. Rare Earth Element and yttrium compositions of Archean and Paleoproterozoic Fe formations revisited: New perspectives on the significance and mechanisms of deposition. *Geochimica et Cosmochimica Acta* 74, 6387–6405.
- Planavsky, N., Rouxel, O.J., Bekker, A., Hofmann, A., Little, C.T.S., Lyons, T.W., 2012. Iron isotope composition of some Archean and Proterozoic iron formations. *Geochimica et Cosmochimica Acta* 80, 158–169.
- Planavsky, N.J., Asael, D., Hofmann, A., Reinhard, C.T., Lalonde, S.V., Knudsen, A., Wang, X., Ossa Ossa, F., Pecoits, E., Smith, A.J.B., Beukes, N.J., Bekker, A.,

- Johnson, T.M., Konhauser, K.O., Lyons, T.W., Rouxel, O.J., 2014a. Evidence for oxygenic photosynthesis half a billion years before the Great Oxidation Event. *Nature Geoscience* 7, 283-286.
- Planavsky, N.J., Reinhard, C.T., Wang, X., Thomson, D., McGoldrick, P., Rainbird, R.H., Johnson, T., Fischer, W.W., Lyons, T.W., 2014b. Low Mid-Proterozoic atmospheric oxygen levels and the delayed rise of animals. *Science* 346, 635-638.
- Planavsky, N.J., Cole, D.B., Reinhard, C.T., Diamond, C., Love, G.D., Luo, G., Zhang, S., Konhauser, K.O., Lyons, T.W., 2016. No evidence for high atmospheric oxygen levels 1,400 million years ago. *Proceedings of the National Academy of Sciences* 113, E2550–E2551.
- Pons, M.L., Fujii, T., Rosing, M., Quitté, G., Télouk, P., Albarède, F., 2013. A Zn isotope perspective on the rise of continents. *Geobiology* 11, 201–214.
- Posth, N.R., Konhauser, K.O., Kappler, A., 2013. Microbiological processes in banded iron formation deposition. *Sedimentology* 60, 1733–1754.
- Posth, N.R., Canfield, D.E., Kappler, A., 2014. Biogenic Fe(III) minerals: From formation to diagenesis and preservation in the rock record. *Earth-Science Reviews* 135, 103-121.
- Powell, C.M., Oliver, N.H.S., Li, Z.-X., Martin, D.M., Ronaszeki, J., 1999. Synorogenic hydrothermal origin for giant Hamersley iron oxide ore bodies. *Geology* 27, 175–178.
- Ragsdale, S.W., Kumar, M., 1996. Nickel-Containing Carbon Monoxide Dehydrogenase/Acetyl-CoA Synthase. *Chemical Reviews* 96, 2515-2539.

- Rasmussen, B., Fletcher, I.R., Bekker, A., Muhling, J.R., Gregory, C.J., Thorne, A.M., 2012. Deposition of 1.88-billion-year-old iron formations as a consequence of rapid crustal growth. *Nature* 484, 498–501.
- Rasmussen, B., Krapez, B., Meier, D.B., 2014. Replacement origin for hematite in 2.5 Ga banded iron formation: Evidence for postdepositional oxidation of iron-bearing minerals. *Geological Society of America Bulletin* 126, 438–446.
- Rasmussen, B., Krapež, B., Muhling, J.R., Suvorova, A., 2015. Precipitation of iron silicate nanoparticles in early Precambrian oceans marks Earth's first iron age. *Geology* 43, 303–306.
- Rasmussen, B., Muhling, J.R., Suvorova, A., Krapez, B., 2016. Dust to dust: Evidence for the formation of “primary” hematite dust in banded iron formations via oxidation of iron silicate nanoparticles. *Precambrian Research* 284, 49–63.
- Rasmussen, B., Muhling, J.R., Suvorova, A., Krapez, B., 2017. Greenalite precipitation linked to the deposition of banded iron formations downslope from a late Archean carbonate platform. *Precambrian Research* 290, 49–62.
- Rasmussen, B., Muhling, J.R., 2018. Making magnetite late again: Evidence for widespread magnetite growth by thermal decomposition of siderite in Hamersley banded iron formations. *Precambrian Research* 306, 64–93.
- Reinhard, C.T., Planavksy, N.J., Robbins, L.J., Partin, C.A., Gill, B.C., Lalonde, S.V., Bekker, A., Konhauser, K.O., Lyons, T.W., 2013. Proterozoic ocean redox and biogeochemical stasis. *Proceedings of the National Academy of Sciences* 110, 5357–5362.

- Reinhard, C.T., Planavsky, N.J., Wang, X., Fischer, W.W., Johnson, T.M., Lyons, T.M.,
2014. The isotopic composition of authigenic chromium in anoxic marine sediments:
A case study from the Cariaco Basin. *Earth and Planetary Science Letters* 407, 9-18.
- Reinhard, C.T., Planavsky, N.J., Gill, B.C., Ozaki, K., Robbins, L.J., Lyons, T.W., Fischer,
W.W., Wang, C., Cole, D.B., Konhauser, K.O., 2017. Evolution of the global
phosphorus cycle. *Nature* 541, 386–389.
- Rickard, D., Luther, G.W., III, 2007. Chemistry of Iron Sulfides. *Chemical Reviews* 107,
514–562.
- Riding, R., 2000. Microbial carbonates: the geological record of calcified bacterial-algal
mats and biofilms. *Sedimentology* 47, 179–214.
- Riding, R., Fralick, P., Liang, L., 2014. Identification of an Archean marine oxygen oasis.
Precambrian Research 251, 232–237.
- Robbins, L.J., Lalonde, S.V., Saito, M.A., Planavsky, N.J., Mloszewska, A.M., Pecoits, E.,
Scott, C., Dupont, C.L., Kappler, A., Konhauser, K.O., 2013. Authigenic iron oxide
proxies for marine zinc over geological time and implications for eukaryotic
metallome evolution. *Geobiology* 11, 295-306.
- Robbins, L.J., Swanner, E.D., Lalonde, S.V., Eickhoff, M., Paranich, M.L., Reinhard, C.T.,
Peacock, C.L., Kappler, A., Konhauser, K.O., 2015. Limited Zn and Ni mobility
during simulated Iron Formation diagenesis. *Chemical Geology* 402, 30-39.
- Robbins, L.J., Lalonde, S.V., Planavsky, N.J., Partin, C.A., Reinhard, C.T., Kendall, B.,
Scott, C., Hardisty, D.S., Gill, B.C., Alessi, D.S., Dupont, C.L., Saito, M.A., Crowe,
S.A., Poulton, S.W., Bekker, A., Lyons, T.W., Konhauser, K.O., 2016. Trace

- elements at the intersection of marine biological and geochemical evolution. *Earth-Science Reviews* 163, 323–348.
- Roberts, S., Lane, T., Morel, F.M.M., 1997. Carbonic anhydrase in the marine diatom *Thalassiosira weissflogii* (Bacillariophyceae). *Journal of Phycology* 33, 845-850.
- Rothman, D.H., Fournier, G.P., French, K.L., Alm, E.J., Boyle, E.A., Cao, C., Summons, R.E., 2014. Methanogenic burst in the end-Permian carbon cycle. *Proceedings of the National Academy of Sciences* 111, 5462-5467.
- Rudnick, R.L., Gao, S., 2014. Composition of the Continental Crust, in: Holland, H.D., Turekian, K. (Eds.), *Treatise on Geochemistry*. Second edition. Elsevier Ltd., Vol. 4. pp. 1–51.
- Russell, J., Chadwick, B., Rao, B.K., Vasudev, V.N., 1996. Whole-rock Pb/Pb isotopic ages of Late Archaean limestones, Karnataka, India. *Precambrian Research* 78, 261–272.
- Sagan, C., Mullen, G., 1972. Earth and Mars: Evolution of Atmospheres and Surface Temperatures. *Science* 177, 52–56.
- Sahoo, S.K., Planavsky, N.J., Kendall, B., Wang, X., Shi, X., Scott, C., Anbar, A.D., Lyons, T.W., Jiang, G., 2012. Ocean oxygenation in the wake of the Marinoan glaciation. *Nature* 489, 546-549.
- Sahoo, S.K., Planavsky, N.J., Kendall, B., Wang, X., Shi, X., Scott, C., Anbar, A.D., Lyons, T.W., Jiang, G., 2012. Ocean oxygenation in the wake of the Marinoan glaciation. *Nature* 488, 546–549.

- Saito, M.A., Moffett, J.W., 2001. Complexation of cobalt by natural organic ligands in the Sargasso Sea as determined by a new high-sensitivity electrochemical cobalt speciation method suitable for open ocean work. *Marine Chemistry* 75, 49-68.
- Saito, M.A., Sigman, D.M., Morel, F.M.M., 2003. The bioinorganic chemistry of the ancient ocean: the co-evolution of cyanobacterial metal requirements and biogeochemical cycles at the Archean-Proterozoic boundary? *Inorganica Chimica Acta* 356, 308-318.
- Saito, M.A., Rocap, G., Moffett, J.W., 2005. Production of cobalt binding ligands in a *Synechococcus* feature at the Costa Rica upwelling dome. *Limnology and Oceanography* 50, 279-290.
- Sander, R., 1999. Compilation of Henry's law constants for inorganic and organic species of potential importance in environmental chemistry.
- Sanford, W.E., Doughten, M.W., Coplen, T.B., Hunt, A.G., Bullen, T.D., 2013. Evidence for high salinity of Early Cretaceous sea water from the Chesapeake Bay crater. *Nature* 503, 252-256.
- Satkoski, A.M., Beukes, N.J., Li, W., Beard, B.L., Johnson, C.M., 2015. A redox-stratified ocean 3.2 billion years ago. *Earth and Planetary Science Letters* 430, 43-53.
- Scheiderich, K., Amini, M., Holmden, C., Francois, R., 2015. Global variability of chromium isotopes in seawater demonstrated by Pacific, Atlantic, and Arctic Ocean samples. *Earth and Planetary Science Letters* 423, 87-97.
- Schmitt, A.-D., Chabaux, F., Stille, P., 2003. The calcium riverine and hydrothermal isotopic fluxes and the oceanic calcium mass balance. *Earth and Planetary Science Letters* 213, 503-518.

- Schopf, J., 2006. Fossil evidence of Archaean life. *Philosophical Transactions of the Royal Society B: Biological Sciences* 361, 869–885.
- Schröder, S., Beukes, N.J., Sumner, D.Y., 2009. Microbialite–sediment interactions on the slope of the Campbellrand carbonate platform (Neoproterozoic, South Africa). *Precambrian Research* 169, 68–79.
- Scott, C., Lyons, T.W., Bekker, A., Shen, Y., Poulton, S.W., Chu, X., Anbar, A.D., 2008. Tracing the stepwise oxygenation of the Proterozoic ocean. *Nature* 452, 456–459.
- Scott, C., Planavsky, N.J., Dupont, C.L., Kendall, B., Gill, B.C., Robbins, L.J., Husband, K.F., Arnold, G.L., Wing, B.A., Poulton, S.W., Bekker, A., Anbar, A.D., Konhauser, K.O., Lyons, T.W., 2013. Bioavailability of zinc in marine systems through time. *Nature Geoscience* 6, 125–128.
- Severmann, S., Lyons, T., Anbar, A.D., McManus, J., Gordon, G., 2008. Modern iron isotope perspective on the benthic iron shuttle and the redox evolution of ancient oceans. *Geology* 36, 487–490.
- Sheldon, N.D., 2006. Precambrian paleosols and atmospheric CO₂ levels. *Precambrian Research* 147, 148–155.
- Shih, P.M., Hemp, J., Ward, L.M., Matzke, N.J., Fischer, W.W., 2016. Crown group Oxyphotobacteria postdate the rise of oxygen. *Geobiology* 15, 19–29.
- Siever, R., 1992. The silica cycle in the Precambrian. *Geochimica et Cosmochimica Acta* 56, 3265–3272.
- Simonson, B.M., 1985. Sedimentology of cherts in the Early Proterozoic Wishart Formation, Quebec-Newfoundland, Canada. *Sedimentology* 32, 23–40.

- Simonson, B.M., Goode, A.D.T., 1989. First discovery of ferruginous chert arenites in the early Precambrian Hamersley Group of Western Australia. *Geology* 17, 269-272.
- Smith, A.J.B., Beukes, N.J., 2016. Paleoproterozoic banded iron formation-hosted high grade hematite iron ore deposits of Transvaal Supergroup, South Africa. *Episodes* 39, 269–16.
- Solomon, E.I., Sundaram, U.M., Machonkin, T.E., 1996. Multicopper oxidases and oxygenases. *Chemical Reviews* 96, 2563-2605.
- Sposito, G., 1982. On the use of the Langmuir equation in the interpretation of “adsorption” phenomena. II. The “two-surface” Langmuir equation. *Soil Science Society of America Journal* 46, 1147-1152.
- Srinivasan, R., Shukla, M., Naqvi, S.M., Yadav, V.K., Venkatachala, B.S., Raj, B.U., Rao, D.V.S., 1989. Archaean stromatolites from the Chitradurga schist belt, Dharwar Craton, South India. *Precambrian Research* 43, 239–250.
- Steinboefel, G., von Blanckenburg, F., Horn, I., Konhauser, K.O., Beukes, N.J., Gutzmer, J., 2010. Deciphering formation processes of banded iron formations from the Transvaal and the Hamersley successions by combined Si and Fe isotope analysis using UV femtosecond laser ablation. *Geochimica et Cosmochimica Acta* 74, 2677-2696.
- Stüeken, E.E., Buick, R., Guy, B.M., Koehler, C., 2015. Isotopic evidence for nitrogen fixation by molybdenum-nitrogenase from 3.2 Gyr. *Nature* 520, 666-669.
- Stylo, M., Neubert, N., Wang, Y., Monga, N., Romaniello, S.J., Weyer, S., Bernier-Latmani, R., 2015. Uranium isotopes fingerprint biotic reduction. *Proceedings of the National Academy of Sciences* 112, 5619–5624.

- Sumner, D.Y., Grotzinger, J.P., 1996, Herringbone calcite: petrography and environmental significance. *Journal of Sedimentary Research* 66, 419–429.
- Sumner, D.Y., Grotzinger, J.P., 2000. Late Archean aragonite precipitation: petrography, facies associations, and environmental significance. *Carbonate Sedimentation and Diagenesis in the Evolving Precambrian World*. Society for Sedimentary Geology Special Publication 67, 123–144.
- Sun, S., Konhauser, K.O., Kappler, A., Li, Y.-L., 2015. Primary hematite in Neoproterozoic to Paleoproterozoic oceans. *Geological Society of America Bulletin* 127, 850–861.
- Swanner, E.D., Planavsky, N.J., Lalonde, S.V., Robbins, L.J., Bekker, A., Rouxel, O.J., Saito, M.A., Kappler, A., Mojzsis, S.J., Konhauser, K.O., 2014. Cobalt and marine redox evolution. *Earth and Planetary Science Letters* 390, 253-263.
- Swanner, E.D., Mloszewski, A.M., Cirpka, O.A., Schoenberg, R., Konhauser, K.O., Kappler, A., 2015. Modulation of oxygen production in Archean oceans by episodes of Fe (II) toxicity. *Nature Geoscience* 8, 126–130.
- Taylor, D., Dalstra, H., Harding, A., Broadbent, G., Barley, M.E., 2001. Genesis of high-grade hematite orebodies of the Hamersley Province, Western Australia. *Economic Geology* 96, 837–873.
- Taylor, S.R., McLennan, S.M. 1985. *The Continental Crust: its Composition and Evolution - An Examination of the Geochemical Record Preserved in Sedimentary Rocks*. Blackwell Scientific Publications, Oxford. pp 1-312.
- Thurston, P.C., 1980. Subaerial volcanism in the Archean Uchi-Confederation volcanic belt. *Precambrian Research* 12, 79–98.

- Tosca, N.J., Guggenheim, S., Pufahl, P.K., 2016. An authigenic origin for Precambrian greenalite: Implications for iron formation and the chemistry of ancient seawater. *Geological Society of America Bulletin* 128, 511–530.
- Trendall A.F., 1979. A revision of the Mount Bruce Supergroup. *Geological Survey of Western Australia Annual Report for 1978*, 63-71.
- Trendall, A.F., 2002. The significance of iron-formation in the Precambrian stratigraphic record. *Special Publications of the International Association of Sedimentologists* 33, 33-36.
- Trendall, A.F., Blockley, J.G., 1970. The iron formations of the Precambrian Hamersley Group, Western Australia with special reference to the associated crocidolite. *Geological Society of Western Australia Bulletin* 119, 1-366.
- Trivedi, P., Axe, L., 2001. Ni and Zn sorption to amorphous versus crystalline iron oxides: macroscopic studies. *Journal of Colloid and Interface Science* 244, 221–229.
- Turek, A., Sage, R.P., Van Schmus, W.R., 1992. Advances in the U–Pb zircon geochronology of the Michipicoten greenstone belt, Superior Province, Ontario. *Canadian Journal of Earth Sciences* 29, 1154–1165.
- Van Kranendonk, M.J., 2006. Volcanic degassing, hydrothermal circulation and the flourishing of early life on Earth: A review of the evidence from c. 3490-3240 Ma rocks of the Pilbara Supergroup, Pilbara Craton, Western Australia. *Earth-Science Reviews* 74, 197–240.
- Van Kranendonk, M.J., Mazumder, R., Precambrian, K.Y., 2015. Sedimentology of the Paleoproterozoic Kungarra Formation, Turee Creek Group, Western Australia: A

- conformable record of the transition from early to modern Earth. *Precambrian Res.* 256, 314–343.
- Van Kranendonk, M.J., Mazumder, R., 2015. Two Paleoproterozoic glacio-eustatic cycles in the Turee Creek Group, Western Australia. *Geological Society of America Bulletin* 127, 596–607.
- Veizer, J., Hoefs, J., Lowe, D.R., P.C. Thurston, 1989. Geochemistry of Precambrian carbonates: II. Archean greenstone belts and Archean sea water. *Geochimica et Cosmochimica Acta* 53, 859–871.
- Viehmann, S., Bau, M., Hoffmann, J.E., Münker, C., 2015. Geochemistry of the Krivoy Rog Banded Iron Formation, Ukraine, and the impact of peak episodes of increased global magmatic activity on the trace element composition of Precambrian seawater. *Precambrian Research* 270, 165–180.
- Vraspir, J.M., Butler, A., 2009. Chemistry of marine ligands and siderophores. *Annual Review of Marine Science* 1, 43–63.
- Walker, J.C.G., 1983. Possible limits on the composition of the Archaean ocean. *Astrobiology* 302, 518–520.
- Warchola, T., Lalonde, S.V., Pecoits, E., Gunten, K.V., Robbins, L.J., Alessi, D.S., Philippot, P., Konhauser, K.O., 2018. Petrology and Geochemistry of the Boolgeeda Iron Formation, Hamersley Basin, Western Australia. *Precambrian Research* 316, 155–173.
- Ward, L.M., Kirschvink, J.L., Fischer, W.W., 2016. Timescales of Oxygenation Following the Evolution of Oxygenic Photosynthesis. *Origins of Life and Evolution of Biospheres* 46, 51–65.

- Waldron, K.J., Tottey, S., Yanagisawa, S., Dennison, C., Robinson, N.J., 2007. A Periplasmic Iron-binding Protein Contributes toward Inward Copper Supply. *Journal of Biological Chemistry* 282, 3837-3846.
- Whitehouse, M.J., Fedo, C.M., 2007. Microscale heterogeneity of Fe isotopes in >3.71 Ga banded iron formation from the Isua Greenstone Belt, southwest Greenland. *Geology* 35, 719-722.
- Wilde, S.A., Valley, J.W., Peck, W.H., Graham, C.M., 2001. Evidence from detrital zircons for the existence of continental crust and oceans on the Earth 4.4 Gyr ago. *Astrobiology* 409, 175–178.
- Wilks, M.E., Nisbet, E.G., 1985. Archaean stromatolites from the Steep Rock Group, northwestern Ontario, Canada. *Canadian Journal of Earth Sciences* 22, 792–799.
- Wolery, T.J., Sleep, N.H., 1976. Hydrothermal Circulation and Geochemical Flux at Mid-Ocean Ridges. *The Journal Of Geology* 84, 249–275.
- Xu, Y., Shi, D., Aristilde, L., Morel, F., 2012. The effect of pH on the uptake of zinc and cadmium in marine phytoplankton: Possible role of weak complexes. *Limnology and Oceanography* 57, 293-304.
- Zegeye, A., Bonneville, S., Benning, L.G., Sturm, A., Fowle, D.A., Jones, C., Canfield, D.E., Ruby, C., MacLean, L.C., Nomosatryo, S., Crowe, S.A., Poulton, S.W., 2012. Green rust formation controls nutrient availability in a ferruginous water column. *Geology* 40, 599–602.
- Zerkle, A.L., House, C.H., Brantley, S.L., 2005. Biogeochemical signatures through time as inferred from whole microbial genomes. *American Journal of Science* 305, 467-502.

- Zhang, X., Sigman, D.M., Morel, F.M.M., Kraepiel, A.M.L., 2014. Nitrogen isotope fractionation by alternative nitrogenases and past ocean anoxia. *Proceedings of the National Academy of Sciences* 111, 4782-4787.
- Zhang, S., Wang, X., Wang, H., Bjerrum, C.J., Hammarlund, E.U., Costa, M.M., Connelly, J.N., Zhang, B., Su, J., Canfield, D.E., 2016. Sufficient oxygen for animal respiration 1,400 million years ago. . *Proceedings of the National Academy of Sciences* 113, 1731–1736.
- Zheng, X.-Y., Beard, B.L., Reddy, T.R., Roden, E.E., Johnson, C.M., 2016. Abiologic silicon isotope fractionation between aqueous Si and Fe(III)–Si gel in simulated Archean seawater: Implications for Si isotope records in Precambrian sedimentary rocks. *Geochimica et Cosmochimica Acta* 187, 102–122.

Appendix 1. Supplementary information for Chapter 2

A1.1 Sequence stratigraphy and iron formation mineralogy

Placing the occurrence of greenalite nanoparticles and the replacement of iron silicates by hematite in iron formations (IF) (as suggested by refs. Rasmussen et al., 2014, 2015, 2016, 2017; Rasmussen and Muhling, 2018, Johnson et al., 2018) into a proper stratigraphic and depositional context has thus far been lacking. This makes it challenging to assess potential sedimentological controls or the volumetric significance of these assumed replacement features.

Sequence stratigraphic, sedimentological and geochronological data have shown that there is a strong correlation between the Brockman and Weeli Wolli IF of the Hamersley Group of Australia and the Kuruman-Penge iron formations of the Transvaal Supergroup of South Africa (Appendix Fig. A1.1; Beukes and Gutzmer, 2008; Cheney, 1996). In addition to the Dales Gorge Member, the Kuruman Iron Formation has also been the focus of studies on greenalite nanoparticles in IF (Rasmussen et al., 2017). Although there are vertical variations in the cyclicity, texture and mineralogy of the iron formations, the cycles correlate across the Transvaal and Hamersley basins, making them laterally consistent over a combined strike length of approximately 1200 km (Cheney, 1996). The discussion here will focus on the Griqualand West region of South Africa, as it was subjected to lower burial temperatures and less metamorphism than the Hamersley Basin (Klein, 2005). In the Griqualand West region of the Transvaal Supergroup, the Kuruman Iron Formation appears to transition from shelf to deeper basin facies from NNE to SSW

(Klein and Beukes, 1989), with the latter basin facies showing the strongest correlation with the Hamersley Group IFs (Appendix Fig. A1.1; Beukes and Gutzmer, 2008).

Detailed vertical variations in the texture and mineralogy (hereafter collectively referred to as lithofacies) of the Kuruman Iron Formation have been well documented (Beukes, 1980, 1984; Klein and Beukes, 1989; Beukes and Gutzmer, 2008). The Kuruman Iron Formation conformably overlies the Campbellrand Subgroup, which is a deepening carbonate platform sequence (Appendix Fig. A1.1). The base of the Kuruman Iron Formation comprises less than 10 m of carbonate IF interbedded with shale, termed the Kliphuis Member. This is followed by a more than 100 m thick, chert-rich sequence of 15 to 16 stacked macrocycles of stilpnomelane lutite grading upwards into carbonate, carbonate-magnetite and magnetite-hematite micritic IF, termed the Stofbakkies-Buisvlei-Orange View Members (Appendix Fig. A1.1; Beukes, 1980; Klein and Beukes, 1989). Above the Stofbakkies-Buisvlei-Orange View Members, the Kuruman Iron Formation comprises approximately 80 to 100 m of greenalite-rich and chert-poor IF (Westerberg-Geduld Members), grading into intraclastic IF (Appendix Fig. A1.1; Klein and Beukes, 1989; Beukes and Gutzmer, 2008). The Kuruman Iron Formation is overlain by granular and conglomeratic units of the Griquatown Iron Formation.

The sequence stratigraphy clearly defines a major transgression at the base of the Stofbakkies Member, followed by repeat cycles of deep water IF deposition (Appendix Fig. A1.1). The lithofacies of each macrocycle are indicative of volcanic ash input (stilpnomelane lutite), followed by silica-, iron- and organic carbon-rich input from the volcanic source (chert-rich siderite and magnetite banded micritic IF), and ending in iron-rich but diminished silica and organic carbon input (magnetite and hematite banded micritic

IF). These macrocycles were followed by a major regression at the base of the Westerberg Member (Appendix Fig. A1.1), with deposition of chert-poor greenalite and siderite IF in a shallowing depositional setting, as indicated by increased wave reworking upwards in the sequence into the Westerberg Member. The deeper siderite-magnetite-hematite IFs contain distinct chert microbands, whereas the shallower greenalite-siderite IFs are chert-poor (Appendix Fig. A1.1; Beukes, 1984). This implies a different depositional setting and mechanism where iron and silica precipitation have become decoupled in deep water, while the iron and silica precipitation characteristic of the greenalite-siderite mineralogical facies suggest a shallower environment with unique Eh and pH conditions (Beukes and Gutzmer, 2008). There is, therefore, a strong link between the observed lithofacies and depositional setting, with the stilpnomelane-siderite-magnetite-hematite macrocycles changing to siderite-greenalite IF coinciding with shallowing (i.e. coastline distal to proximal) depositional conditions (Beukes and Gutzmer, 2008). This link between depositional setting and the lithofacies of IF, and the lateral consistency observed in these facies within the Transvaal-Hamersley succession, suggest the textural and mineralogical varieties observed are to a large extent controlled by depositional to early diagenetic processes, and cannot all be due to secondary overprinting of a homogenous precursor.

Greenalite-rich IF is, therefore, not disregarded completely, but rather, should be considered as a lithofacies subtype of IF, as opposed to the typical Superior type IF, with a distinct depositional setting. Critically, the lateral consistency of the lithofacies of the members of the Kuruman Iron Formation, make it highly unlikely that secondary processes could have extensively replaced the mineralogy and homogeneously changed the texture of the Stofbakkies-Buisvlei-Orange View Members (mostly devoid of greenalite with chert

microbands) in a lateral manner, without significantly affecting the overlying Westerberg-Geduld Members (greenalite-rich and chert-poor).

A1.2 References

- Beukes, N.J., 1980. Lithofacies and stratigraphy of the Kuruman and Griquatown iron-formations, Northern Cape Province, South Africa. *Transactions of the Geological Society of South Africa*. 83, 69-86.
- Beukes, N., 1984. Sedimentology of the Kuruman and Griquatown iron-formations, Transvaal supergroup, Griqualand West, South Africa. *Precambrian Research* 24, 47–84.
- Beukes, N.J., Gutzmer, J., 2008. Origin and paleoenvironmental significance of major iron formations at the Archean-Paleoproterozoic boundary. *Society of Economic Geologists Reviews* 15, 5–47.
- Cheney, E.S., 1996. Sequence stratigraphy and plate tectonic significance of the Transvaal succession of southern Africa and its equivalent in Western Australia. *Precambrian Research* 79, 3-24.
- Johnson, J.E., Muhling, J.R., Cosmidis, J., Rasmussen, B., Templeton, A.S., 2018. Low-Fe(III) Greenalite Was a Primary Mineral from Neoproterozoic Oceans. *Geophysical Research Letters* 45, 3182-3192.
- Klein, C., 2005. Some Precambrian banded iron-formations (BIFs) from around the world: Their age, geologic setting, mineralogy, metamorphism, geochemistry, and origins. *American Mineralogist* 90, 1473–1499.

- Klein, C., Beukes, N.J., 1989. Geochemistry and sedimentology of a facies transition from limestone to iron-formation in the early Proterozoic Transvaal Supergroup, South Africa. *Economic Geology* 84, 1733–1774.
- Rasmussen, B., Krapež, B., Muhling, J.R., Suvorova, A., 2015. Precipitation of iron silicate nanoparticles in early Precambrian oceans marks Earth's first iron age. *Geology* 43, 303–306.
- Rasmussen, B., Krapez, B., Meier, D.B., 2014. Replacement origin for hematite in 2.5 Ga banded iron formation: Evidence for postdepositional oxidation of iron-bearing minerals. *Geological Society of America Bulletin* 126, 438–446.
- Rasmussen, B., Muhling, J.R., 2018. Making magnetite late again: Evidence for widespread magnetite growth by thermal decomposition of siderite in Hamersley banded iron formations. *Precambrian Research* 306, 64–93.
- Rasmussen, B., Muhling, J.R., Suvorova, A., Krapez, B., 2017. Greenalite precipitation linked to the deposition of banded iron formations downslope from a late Archean carbonate platform. *Precambrian Research* 290, 49–62.
- Rasmussen, B., Muhling, J.R., Suvorova, A., Krapez, B., 2016. Dust to dust: Evidence for the formation of “primary” hematite dust in banded iron formations via oxidation of iron silicate nanoparticles. *Precambrian Research* 284, 49–63.

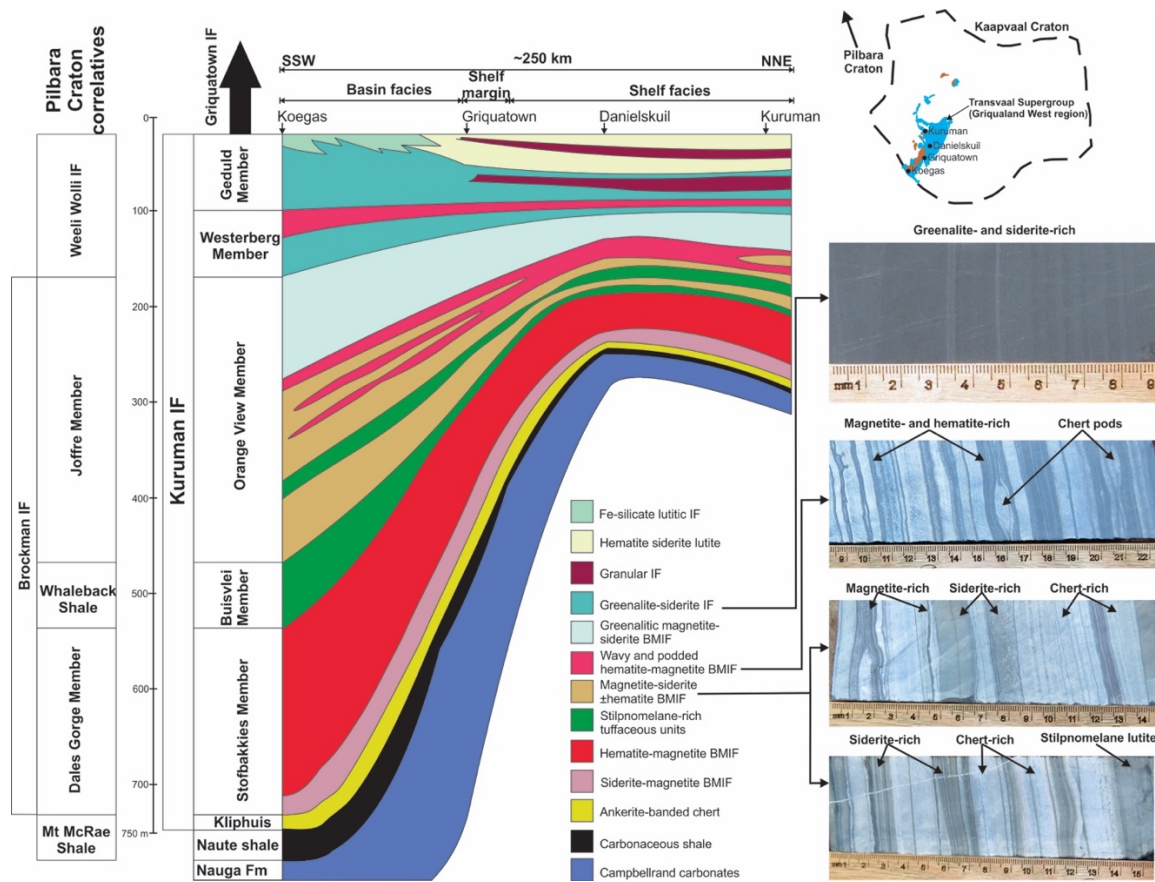


Figure A1.1. A SSW to NNE cross section of the Kuruman Iron Formation in the Griqualand West region of the Kaapvaal Craton with its Pilbara Craton correlatives also indicated to the left (adapted from Beukes and Gutzmer, 2008). Also included are photographs of drill core samples representative of the lithofacies occurring within the Kuruman Iron Formation. IF: Iron Formation.

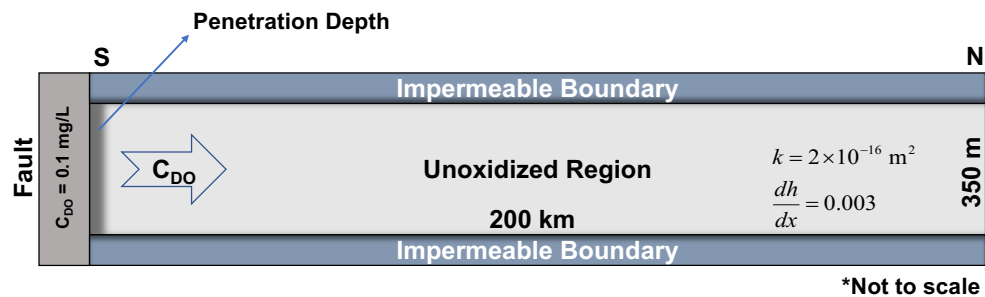


Figure A1.2. Schematic for realistic model to test the uniform penetration depth along the length of the 500 km long southern edge of the basin. Given a dissolved oxygen content of 0.1 mg/L, a hydraulic gradient of 0.003 m/m, and a permeability of $2 \times 10^{-16} \text{ m}^2$, the oxidation front penetrates the formation only $\sim 1 \text{ cm}$. This equates to $\sim 5.6 \times 10^9 \text{ kg}$ and represents only a very small fraction of the mass of BIF in the Hamersley basin. This highlights the difficulty in applying such a model for the post-depositional oxidation of BIF by groundwater over a large basin.

Appendix 2. Supplementary information for Chapter 3

Table A2.1. LA-HR-ICP-MS analyses for WW1-9 from the Weeli Wolli Iron Formation in Western Australia.

					Table A2.1 Continued					
Formation	Sample	Code	Shot	Method	Li	B	Mg	Ca	Ti	V
Weeli Wolli	WW1-9	S1	1	Mag		4.360E+04	5.645E+04	1.455E+06	2.021E+04	2.963E+04
Weeli Wolli	WW1-9	S1	2	Mag			3.224E+03	5.167E+05	7.245E+03	3.205E+04
Weeli Wolli	WW1-9	S1	3	Mag		3.712E+05	1.737E+04	1.193E+06	5.714E+02	2.787E+04
Weeli Wolli	WW1-9	S2	1	Mag	3.085E+05	1.099E+05	1.531E+05	3.384E+06	5.866E+04	3.455E+04
Weeli Wolli	WW1-9	S2	2	Mag	2.708E+05	5.300E+04	1.017E+05	1.479E+06	2.582E+04	3.038E+04
Weeli Wolli	WW1-9	S2	3	Mag	1.617E+05	1.024E+05	7.196E+04	2.692E+06	2.116E+05	3.121E+04
Weeli Wolli	WW1-9	S3	1	Mag			2.974E+03	1.424E+06	6.062E+02	2.862E+04
Weeli Wolli	WW1-9	S3	2	Mag			6.872E+03		2.675E+03	2.798E+04
Weeli Wolli	WW1-9	S3	3	Mag			3.043E+04	1.416E+06	1.224E+03	2.808E+04
Weeli Wolli	WW1-9	S4	1	Mag	4.641E+05		2.169E+05	1.797E+06	2.658E+03	3.007E+04
Weeli Wolli	WW1-9	S4	2	Mag	3.436E+05	6.985E+04	1.442E+05	3.270E+07	5.722E+03	2.907E+04
Weeli Wolli	WW1-9	S4	3	Mag	2.601E+05	4.008E+04	1.276E+05	5.321E+06	2.377E+03	2.969E+04
Weeli Wolli	WW1-9	S5	1	Mag	8.983E+04	5.772E+03	4.099E+04			2.375E+04
Weeli Wolli	WW1-9	S5	2	Mag	7.455E+05		3.345E+05	2.544E+06	1.639E+04	3.082E+04
Weeli Wolli	WW1-9	S5	3	Mag	1.463E+05		7.100E+04	2.632E+06	4.144E+03	2.600E+04
				Mean	3.100E+05	9.948E+04	9.195E+04	4.504E+06	2.571E+04	2.932E+04
				2*std dev	3.974E+05	2.298E+05	1.847E+05	1.712E+07	1.116E+05	5.090E+03
				count	9	8	15	13	14	15

Table A2.1 continued

Code	Shot	Method	Cr	Mn	Co	Ni	⁶⁵Cu	Zn	Ge	Rb
S1	1	Mag	3.148E+05	5.550E+04	5.030E+04	1.963E+05		3.078E+04	8.515E+05	6.205E+04
S1	2	Mag	2.969E+05	7.630E+03	4.131E+04	2.018E+05		8.716E+03	1.155E+06	5.026E+03
S1	3	Mag	2.697E+05	1.727E+04	4.512E+04	2.037E+05		1.419E+04		2.005E+05
S2	1	Mag		3.532E+04	7.092E+04	6.077E+05		6.689E+04	1.153E+06	7.675E+04
S2	2	Mag		2.018E+04	6.222E+04	5.221E+05		4.775E+04	8.493E+05	9.089E+04
S2	3	Mag		1.600E+04	5.516E+04	4.739E+05		3.539E+04	1.925E+06	5.292E+04
S3	1	Mag		5.766E+03	3.771E+04	1.003E+05		5.871E+03	6.069E+05	2.248E+03
S3	2	Mag		9.061E+03	3.962E+04			9.910E+03	9.131E+05	1.932E+04
S3	3	Mag	8.278E+04	1.085E+04	3.944E+04			1.689E+04		6.283E+03
S4	1	Mag	1.033E+05	3.376E+04	6.828E+04	3.342E+05		7.798E+04	1.418E+06	1.058E+05
S4	2	Mag	1.531E+05	4.634E+04	5.296E+04	2.460E+05		6.148E+04		1.446E+04
S4	3	Mag	1.598E+05	2.355E+04	5.138E+04	2.244E+05	1.193E+05	5.329E+04	1.258E+06	2.300E+04
S5	1	Mag	4.722E+04	8.102E+03	4.935E+04	1.420E+05	7.857E+02	1.524E+04	7.466E+05	
S5	2	Mag		5.729E+04	1.105E+05	3.878E+05		1.463E+05	1.468E+06	6.679E+05
S5	3	Mag	5.452E+04	1.595E+04	5.578E+04	1.938E+05		3.495E+04	1.216E+06	7.074E+03
		Mean	1.647E+05	2.417E+04	5.534E+04	2.949E+05	6.006E+04	4.171E+04	1.130E+06	9.530E+04
		2*std dev	2.093E+05	3.489E+04	3.662E+04	3.147E+05	1.676E+05	7.390E+04	7.333E+05	3.475E+05
		count	9	15	15	13	2	15	12	14

Table A2.1 continued

Code	Shot	Method	Sr	Y	Zr	Mo	Ba	La	Ce	Pr
S1	1	Mag	2.253E+03	6.896E+04	9.351E+04	2.844E+03	5.525E+03	1.180E+03	1.065E+04	6.372E+03
S1	2	Mag	1.218E+03	5.351E+03	2.275E+04	7.979E+02	2.761E+03	8.094E+02	1.130E+03	1.131E+03
S1	3	Mag	1.386E+04	2.071E+04	6.420E+04		3.684E+04	3.567E+03	4.006E+03	4.871E+03
S2	1	Mag	7.662E+03	4.437E+05	4.941E+05		2.469E+04	8.834E+03	1.710E+04	2.814E+04
S2	2	Mag	5.776E+03	1.302E+05	1.341E+05		3.537E+04	3.014E+03	5.890E+03	1.123E+04
S2	3	Mag	9.070E+03	1.068E+05	6.661E+04		1.953E+04	1.342E+04	1.705E+04	2.430E+04
S3	1	Mag	3.446E+03	6.903E+03	1.088E+04		4.486E+02	3.440E+03	3.095E+03	3.802E+03
S3	2	Mag	1.978E+03	3.499E+03	1.018E+04		7.951E+02	2.216E+03	2.095E+03	2.069E+03
S3	3	Mag	5.699E+03	3.360E+04	2.844E+04		9.488E+02	1.273E+05	1.245E+05	1.188E+05
S4	1	Mag	3.694E+03	2.949E+04	1.107E+05		4.690E+02	4.544E+03	3.807E+03	3.807E+03
S4	2	Mag	8.570E+04	1.317E+05	1.648E+05	1.170E+03	2.184E+03	7.071E+04	7.095E+04	7.189E+04
S4	3	Mag	1.581E+04	4.063E+04	4.081E+04		6.957E+02	2.134E+04	2.130E+04	2.229E+04
S5	1	Mag				4.200E+01				
S5	2	Mag	6.472E+03	1.313E+04	1.309E+04		1.707E+03	4.634E+03	5.774E+03	6.784E+03
S5	3	Mag	7.352E+03	2.041E+04	1.331E+04		6.982E+02	1.313E+04	1.385E+04	1.457E+04
		Mean	1.214E+04	7.537E+04	9.053E+04	1.214E+03	9.476E+03	1.987E+04	2.151E+04	2.286E+04
		2*std dev	4.318E+04	2.305E+05	2.527E+05	2.368E+03	2.712E+04	7.156E+04	6.907E+04	6.637E+04
		count	14	14	14	4	14	14	14	14

Table A2.1 continued

Code	Shot	Method	Nd	Sm	Eu	Tb	Gd	Dy	Ho	Er
S1	1	Mag	1.130E+04	2.924E+04	2.788E+04	4.638E+04	4.180E+04	5.556E+04	6.782E+04	8.121E+04
S1	2	Mag	1.492E+03						4.511E+03	6.985E+03
S1	3	Mag	5.987E+03	8.886E+03		8.845E+03	9.390E+03	8.294E+03	1.475E+04	2.480E+04
S2	1	Mag	4.658E+04	1.109E+05	1.337E+05	2.117E+05	1.828E+05	2.899E+05	4.041E+05	5.598E+05
S2	2	Mag	1.857E+04	4.561E+04	5.442E+04	7.177E+04	5.905E+04	8.313E+04	1.042E+05	1.323E+05
S2	3	Mag	3.217E+04	6.269E+04	7.105E+04	8.601E+04	7.823E+04	9.034E+04	9.928E+04	1.016E+05
S3	1	Mag	4.497E+03	5.203E+03		7.879E+03	7.707E+03	7.421E+03	7.624E+03	7.921E+03
S3	2	Mag	2.499E+03				3.655E+03	3.418E+03	3.372E+03	4.853E+03
S3	3	Mag	1.014E+05	5.330E+04	2.431E+04	2.531E+04	3.107E+04	2.009E+04	2.474E+04	2.982E+04
S4	1	Mag	3.756E+03	4.748E+03		6.106E+03	6.081E+03	9.476E+03	1.843E+04	3.530E+04
S4	2	Mag	7.428E+04	8.007E+04	6.649E+04	8.965E+04	9.113E+04	8.998E+04	1.084E+05	1.431E+05
S4	3	Mag	2.472E+04	2.794E+04	2.448E+04	3.069E+04	3.249E+04	3.097E+04	3.782E+04	4.103E+04
S5	1	Mag								
S5	2	Mag	7.359E+03	8.606E+03		9.654E+03	1.042E+04	8.842E+03	1.202E+04	1.185E+04
S5	3	Mag	1.460E+04	1.426E+04	9.594E+03	1.727E+04	1.823E+04	1.591E+04	1.865E+04	1.870E+04
		Mean	2.494E+04	3.762E+04	5.149E+04	5.094E+04	4.401E+04	5.487E+04	6.612E+04	8.567E+04
		2*std dev	6.006E+04	6.775E+04	7.982E+04	1.184E+05	1.009E+05	1.561E+05	2.093E+05	2.886E+05
		count	14	12	8	12	13	13	14	14

Table A2.1 continued

Code	Shot	Method	Yb	Lu	Hf	Pb	Th	U	Y/Ho	Ce/Ce* _{PAAS}
S1	1	Mag	1.066E+05	1.037E+05	6.284E+04	3.537E+04	8.705E+04	2.286E+04	1.017E+00	3.556E-01
S1	2	Mag	1.021E+04	1.688E+04	9.735E+03	4.876E+03	1.544E+04	3.426E+03	1.186E+00	1.903E-01
S1	3	Mag	4.021E+04	4.905E+04	3.208E+04	4.858E+04	2.437E+04	1.164E+04	1.404E+00	1.561E-01
S2	1	Mag	7.692E+05	8.540E+05	5.286E+05	2.965E+04	3.708E+05	1.906E+05	1.098E+00	1.257E-01
S2	2	Mag	1.591E+05	1.789E+05	1.151E+05	2.250E+04	7.301E+04	4.268E+04	1.250E+00	1.095E-01
S2	3	Mag	9.035E+04	7.521E+04	6.210E+04	1.498E+04	2.565E+04	2.248E+04	1.076E+00	1.381E-01
S3	1	Mag	9.615E+03		2.640E+03		1.415E+03	1.324E+03	9.055E-01	1.493E-01
S3	2	Mag				1.105E+04	1.711E+03	4.368E+03	1.037E+00	1.801E-01
S3	3	Mag	3.218E+04	4.211E+04	6.130E+03	1.120E+04	1.140E+05	1.047E+04	1.358E+00	1.864E-01
S4	1	Mag	7.789E+04	1.119E+05	2.571E+04	2.640E+04	4.887E+03	1.115E+04	1.600E+00	1.739E-01
S4	2	Mag	2.146E+05	2.862E+05	5.598E+04	6.410E+04	8.376E+04	6.603E+04	1.215E+00	1.784E-01
S4	3	Mag	5.531E+04	6.982E+04	1.247E+04	1.620E+04	2.116E+04	2.329E+04	1.074E+00	1.735E-01
S5	1	Mag			5.310E+02		4.190E+03			
S5	2	Mag	1.406E+04	1.390E+04		9.090E+03	6.774E+03	1.170E+04	1.093E+00	1.631E-01
S5	3	Mag	1.940E+04	1.433E+04		2.948E+04	3.667E+04	4.928E+04	1.094E+00	1.745E-01
		Mean	1.230E+05	1.513E+05	7.616E+04	2.488E+04	5.806E+04	3.367E+04	1.172E+00	1.753E-01
		2*std dev	4.077E+05	4.698E+05	2.930E+05	3.398E+04	1.876E+05	9.797E+04	3.635E-01	1.140E-01
		count	13	12	12	13	15	14	14	14

Table A2.1 continued

Code	Shot	Method	La/La* _{PAAS}	Pr/Pr* _{PAAS}	Eu/Eu* _{PAAS}	Pr/Yb* _{PAAS}	∑REE
S1	1	Mag	2.062E-02	3.089E+00	1.094E+00	1.909E-02	6.586E+05
S1	2	Mag	7.157E-02	4.398E+00		3.535E-02	4.851E+04
S1	3	Mag	7.173E-02	4.862E+00		3.869E-02	2.034E+05
S2	1	Mag	3.395E-02	4.011E+00	1.179E+00	1.168E-02	4.061E+06
S2	2	Mag	2.900E-02	4.092E+00	1.379E+00	2.255E-02	1.057E+06
S2	3	Mag	5.525E-02	4.733E+00	1.470E+00	8.591E-02	9.486E+05
S3	1	Mag	8.773E-02	5.020E+00		1.263E-01	7.511E+04
S3	2	Mag	1.044E-01	4.685E+00			2.768E+04
S3	3	Mag	9.696E-02	5.905E+00	1.297E+00	1.179E+00	7.884E+05
S4	1	Mag	1.110E-01	5.437E+00		1.561E-02	3.153E+05
S4	2	Mag	9.235E-02	5.282E+00	1.271E+00	1.070E-01	1.589E+06
S4	3	Mag	9.137E-02	5.066E+00	1.362E+00	1.287E-01	4.808E+05
S5	1	Mag					0.000E+00
S5	2	Mag	6.484E-02	5.306E+00		1.541E-01	1.270E+05
S5	3	Mag	8.404E-02	5.459E+00	9.667E-01	2.399E-01	2.229E+05
		Mean	7.249E-02	4.810E+00	1.252E+00	1.664E-01	7.069E+05
		2*std dev	5.722E-02	1.457E+00	3.291E-01	6.233E-01	2.073E+06
		count	14	14	8	13	15

Table A2.2. LA-HR-ICP-MS analyses for sample WW1-9b from the Weeli Wolli Iron Formation, Western Australia.

Formation	Sample	Code	Shot	Method	Li	B	Mg	Ca	Ti	V
Weeli Wolli	WW1-9b	S1	1.0	Hem	5.116E+01		5.433E+04		4.459E+02	1.522E+02
Weeli Wolli	WW1-9b	S1	2.0	Hem			3.950E+03	4.349E+04	2.749E+02	1.396E+02
Weeli Wolli	WW1-9b	S1	3.0	Hem			2.138E+03	1.086E+04	2.438E+02	1.369E+02
Weeli Wolli	WW1-9b	S2	1.0	Hem			1.064E+04	1.436E+04	4.775E+03	1.464E+02
Weeli Wolli	WW1-9b	S2	2.0	Hem	5.451E+01		5.106E+04	3.201E+04	6.291E+03	1.596E+02
Weeli Wolli	WW1-9b	S2	3.0	Hem			2.926E+04	3.474E+04	2.301E+04	1.607E+02
Weeli Wolli	WW1-9b	S3	1.0	Hem			5.594E+03	1.105E+04	6.229E+04	1.914E+02
Weeli Wolli	WW1-9b	S3	2.0	Hem	8.597E+01		6.704E+04	1.375E+04	1.729E+03	1.608E+02
Weeli Wolli	WW1-9b	S3	3.0	Hem		1.377E+01	1.980E+04	8.938E+04	9.687E+03	1.507E+02
Weeli Wolli	WW1-9b	S4	1.0	Hem			2.522E+04	1.120E+04	5.910E+02	1.375E+02
Weeli Wolli	WW1-9b	S4	2.0	Hem			6.240E+02		1.589E+02	1.336E+02
Weeli Wolli	WW1-9b	S4	3.0	Hem			1.443E+04	5.220E+03	6.173E+02	1.348E+02
Weeli Wolli	WW1-9b	TW1	1.0	Hem	1.296E+03	3.796E+02	9.958E+05	2.478E+05	1.268E+06	9.541E+03
Weeli Wolli	WW1-9b	TW2	1.0	Hem		6.614E+02	8.657E+04	5.795E+05	1.053E+07	5.540E+04
Weeli Wolli	WW1-9b	TW3	1.0	Hem	5.246E+02	1.133E+03	4.017E+05	1.209E+05	3.048E+06	1.142E+04
Weeli Wolli	WW1-9b	TW4	1.0	Hem		1.626E+03	9.828E+04	6.309E+05	3.512E+06	1.128E+04
Weeli Wolli	WW1-9b	TW5	1.0	Hem		3.683E+02	7.718E+04	3.502E+05	5.409E+06	4.061E+04
Weeli Wolli	WW1-9b	TW7	1.0	Hem	6.638E+02	1.085E+04	1.051E+06	2.834E+05	3.584E+04	7.661E+03
Weeli Wolli	WW1-9b	TW8	1.0	Hem	1.483E+03	5.613E+02	1.511E+06	3.558E+05	1.021E+06	1.195E+04
Weeli Wolli	WW1-9b	S5	1.0	Mag			5.926E+03	9.988E+03	1.235E+03	1.287E+02
Weeli Wolli	WW1-9b	S5	2.0	Mag			2.003E+04	1.530E+04	8.136E+02	1.317E+02
Weeli Wolli	WW1-9b	S5	3.0	Mag			3.396E+02	6.929E+03	2.084E+02	1.341E+02
Weeli Wolli	WW1-9b	TW6	1.0	Mag	1.287E+03	1.495E+02	1.260E+06		9.123E+04	9.677E+03
Weeli Wolli	WW1-9b	TW9	1.0	Mag	4.174E+02	2.663E+04	5.867E+05	1.929E+05	9.081E+03	9.178E+03
Weeli Wolli	WW1-9b	TW10	1.0	Mag		9.367E+02	1.518E+04	1.078E+05	4.957E+04	1.395E+04
Weeli Wolli	WW1-9b	TW11	1.0	Mag	4.871E+02	1.264E+02	5.784E+05	3.699E+05	2.125E+04	9.139E+03
Weeli Wolli	WW1-9b	TW12	1.0	Mag			5.415E+05	8.295E+04	7.148E+03	8.329E+03
Weeli Wolli	WW1-9b	TW13	1.0	Mag	4.581E+02	9.173E+02	7.262E+05	2.911E+05	1.070E+04	8.499E+03
			Hematite	average	5.943E+02	1.949E+03	2.371E+05	1.667E+05	1.312E+06	7.878E+03

	2*std dev	1.194E+03	7.263E+03	8.828E+05	4.122E+05	5.409E+06	3.015E+04
	count	7	8	19	17	19	19
Magnetite	average	6.623E+02	5.752E+03	4.149E+05	1.346E+05	2.125E+04	6.574E+03
	2*std dev	8.345E+02	2.336E+04	8.770E+05	2.754E+05	6.090E+04	1.022E+04
	count	4	5	9	8	9	9

Table A2.2 continued.

Code	Shot	Method	Cr	Mn	Co	Ni	⁶⁵ Cu	Zn	Ge	Rb
S1	1.0	Hem	2.955E+01	1.214E+03	3.992E+01	7.838E+01		1.271E+02		5.910E+01
S1	2.0	Hem	2.099E+01	2.373E+02	1.616E+01	2.726E+01				4.479E+00
S1	3.0	Hem	2.445E+01	1.252E+02	1.576E+01	3.316E+01				7.644E+00
S2	1.0	Hem	1.554E+01	2.091E+02	2.132E+01	6.131E+01		4.000E+01	1.755E+01	6.370E+01
S2	2.0	Hem		6.168E+02	2.874E+01	1.030E+02		1.109E+02		7.185E+01
S2	3.0	Hem	5.517E+01	4.857E+02	2.487E+01	9.198E+01		9.184E+01	5.575E+01	1.894E+02
S3	1.0	Hem		1.618E+02	2.155E+01	6.032E+01		2.824E+01	5.367E+01	2.797E+01
S3	2.0	Hem		7.757E+02	3.677E+01	1.385E+02		1.712E+02		7.400E+01
S3	3.0	Hem		2.901E+02	2.494E+01	9.385E+01		5.851E+01	8.928E+01	4.163E+01
S4	1.0	Hem	2.543E+01	7.932E+02	2.798E+01	2.728E+01		7.406E+01		2.450E+01
S4	2.0	Hem	4.243E+01	8.132E+01	1.882E+01	1.996E+01			9.836E+01	5.861E+00
S4	3.0	Hem	3.186E+01	2.546E+02	2.273E+01			5.049E+01	2.220E+02	7.528E+01
TW1	1.0	Hem		1.454E+04	1.264E+03	4.485E+03	1.909E+02	3.962E+03	1.177E+03	1.197E+03
TW2	1.0	Hem	7.854E+03	1.020E+04	8.516E+02	2.864E+03	9.313E+02	2.778E+03	1.358E+03	
TW3	1.0	Hem		9.976E+03	1.113E+03	3.618E+03	2.797E+02	2.354E+03	1.607E+03	3.887E+02
TW4	1.0	Hem		7.542E+03	1.206E+03	3.662E+03	8.419E+02	1.594E+03	1.979E+03	2.294E+02
TW5	1.0	Hem	4.019E+02	8.307E+03	8.604E+02	2.997E+03	1.292E+03	1.642E+03	1.292E+03	
TW7	1.0	Hem	1.807E+03	4.095E+04	5.220E+03	2.398E+03	7.797E+02	3.564E+03	3.814E+02	2.104E+03
TW8	1.0	Hem	1.599E+03	2.004E+04	1.353E+03	4.965E+03	1.364E+02	4.522E+03	1.349E+03	1.796E+03
S5	1.0	Mag	6.869E+01	2.871E+02	2.652E+01			2.091E+01		1.053E+01
S5	2.0	Mag	3.376E+01	9.986E+02	1.217E+02			6.739E+01	8.387E+00	3.597E+01
S5	3.0	Mag	3.071E+01	7.886E+01	2.276E+01					4.078E+00
TW6	1.0	Mag	4.005E+03	1.887E+04	1.516E+03	1.440E+03		4.466E+03	9.491E+02	2.722E+03
TW9	1.0	Mag	3.237E+03	1.718E+04	1.382E+03	1.149E+03		2.124E+03	7.961E+02	1.097E+03
TW10	1.0	Mag	2.896E+04	6.276E+03	1.124E+03	1.134E+03		8.477E+02	1.427E+03	3.703E+01
TW11	1.0	Mag	2.241E+03	2.017E+04	1.272E+03	1.166E+03		2.591E+03	6.799E+02	4.116E+03
TW12	1.0	Mag	8.794E+02	1.488E+04	1.127E+03	1.189E+03		2.237E+03	5.441E+02	2.312E+03
TW13	1.0	Mag	2.460E+03	3.155E+04	1.204E+03	1.316E+03	1.671E+02	2.762E+03	5.029E+02	2.690E+03
	Hematite	average	9.923E+02	6.148E+03	6.404E+02	1.429E+03	6.359E+02	1.323E+03	7.446E+02	3.741E+02
		2*std dev	4.507E+03	2.057E+04	2.452E+03	3.678E+03	8.773E+02	3.242E+03	1.441E+03	1.320E+03

	count	12	19	19	18	7	16	13	17
Magnetite	average	4.658E+03	1.225E+04	8.663E+02	1.232E+03	1.671E+02	1.889E+03	7.011E+02	1.447E+03
	2*std dev	1.847E+04	2.195E+04	1.239E+03	2.416E+02	#DIV/0!	3.020E+03	8.725E+02	3.106E+03
	count	9	9	9	6	1	8	7	9

Table A2.2 continued.

Code	Shot	Method	Sr	Y	Zr	Mo	Ba	La	Ce	Pr
S1	1.0	Hem	6.755E+01	1.024E+01	4.793E+02		2.264E+02	2.211E+00	4.288E+00	6.957E-01
S1	2.0	Hem	1.102E+02	3.523E+01	6.050E+02		3.383E+01	4.175E+00	9.575E+00	1.715E+00
S1	3.0	Hem	1.606E+01	7.657E+00	3.225E+02		2.071E+01		2.284E-01	
S2	1.0	Hem	5.130E+01	2.387E+01	2.287E+02		3.203E+02	2.253E+00	4.781E+00	9.742E-01
S2	2.0	Hem	1.022E+02	4.713E+01	4.281E+02		1.166E+02	5.055E+00	1.188E+01	2.181E+00
S2	3.0	Hem	1.400E+02	2.731E+01	1.953E+02		2.283E+02	7.261E+00	1.426E+01	2.275E+00
S3	1.0	Hem	4.114E+01	2.470E+01	1.598E+02		1.078E+02	6.869E+00	1.481E+01	2.408E+00
S3	2.0	Hem	3.316E+01	1.474E+01	1.511E+02		4.321E+02	6.604E-01	1.916E+00	4.603E-01
S3	3.0	Hem	3.364E+02	1.039E+02	2.047E+02		2.550E+02	1.017E+01	2.654E+01	5.570E+00
S4	1.0	Hem	1.761E+01	7.850E+00	2.143E+02		3.104E+01	9.758E-01	1.953E+00	2.870E-01
S4	2.0	Hem	6.520E+00	1.614E+00	4.755E+01		4.621E+00	1.869E-01	1.199E-01	
S4	3.0	Hem	9.173E+00	2.099E+00	6.575E+01		9.641E+00	2.887E-01	3.770E-01	
TW1	1.0	Hem	1.324E+03	1.034E+03	3.868E+03	3.059E+01	6.308E+03	2.181E+02	5.344E+02	8.075E+01
TW2	1.0	Hem	1.724E+03	6.503E+02	1.173E+04	6.342E+01	7.514E+02	1.807E+02	4.492E+02	6.040E+01
TW3	1.0	Hem	1.833E+03	1.054E+03	4.430E+03	8.509E+01	1.458E+03	3.574E+02	8.482E+02	1.146E+02
TW4	1.0	Hem	4.922E+03	1.048E+03	4.797E+03	1.126E+02	1.409E+03	2.304E+02	6.110E+02	9.302E+01
TW5	1.0	Hem	1.238E+03	2.592E+02	4.440E+03	3.526E+01	5.340E+02	7.992E+01	2.052E+02	2.985E+01
TW7	1.0	Hem	3.130E+03	4.279E+02	3.263E+03		2.877E+03	1.844E+02	4.143E+02	5.764E+01
TW8	1.0	Hem	1.750E+03	1.564E+03	9.170E+03	3.366E+01	8.221E+03	2.193E+02	5.793E+02	9.365E+01
S5	1.0	Mag	3.478E+01	4.744E+00	9.198E+01		2.167E+01	3.636E+00	6.475E+00	9.539E-01
S5	2.0	Mag	2.905E+01	1.049E+01	1.767E+02		5.618E+01	2.271E+00	4.212E+00	6.093E-01
S5	3.0	Mag	5.238E+01	9.743E-01	6.867E+01		7.882E+00	2.838E-01	5.892E-01	
TW6	1.0	Mag	2.051E+02	3.322E+01	8.227E+02		6.855E+02	3.449E+00	6.934E+00	9.660E-01
TW9	1.0	Mag	5.615E+03	1.124E+02	1.251E+03	3.691E+01	1.283E+03	3.255E+01	6.922E+01	9.743E+00
TW10	1.0	Mag	7.872E+02	1.009E+02	1.725E+03	2.794E+02	5.780E+02	2.302E+01	5.255E+01	6.785E+00
TW11	1.0	Mag	1.501E+03	2.764E+02	1.894E+03		1.128E+03	5.309E+01	1.454E+02	2.419E+01
TW12	1.0	Mag	3.308E+02	2.601E+01	8.636E+02		7.269E+02	5.403E+00	1.382E+01	2.253E+00
TW13	1.0	Mag	1.823E+03	1.591E+02	2.379E+03		3.776E+03	6.893E+01	1.428E+02	1.712E+01
	Hematite	average	8.870E+02	3.338E+02	2.358E+03	6.010E+01	1.229E+03	8.391E+01	1.964E+02	3.416E+01
		2*std dev	2.663E+03	9.770E+02	6.751E+03	6.678E+01	4.532E+03	2.291E+02	5.573E+02	8.379E+01
		count	19	19	19	6	19	18	19	16

Magnetite	average	1.153E+03	8.048E+01	1.030E+03	1.581E+02	9.182E+02	2.140E+01	4.910E+01	7.827E+00
	2*std dev	3.600E+03	1.846E+02	1.688E+03	3.429E+02	2.337E+03	5.048E+01	1.176E+02	1.750E+01
	count	9	9	9	2	9	9	9	8

Table A2.2 continued.

Code	Shot	Method	Nd	Sm	Eu	Tb	Gd	Dy	Ho	Er
S1	1.0	Hem	2.489E+00					9.144E-01	2.659E-01	1.388E+00
S1	2.0	Hem	1.090E+01	2.782E+00	6.742E-01	5.764E-01	3.992E+00	4.026E+00	9.931E-01	4.046E+00
S1	3.0	Hem							2.151E-01	1.126E+00
S2	1.0	Hem	6.136E+00	2.723E+00	6.024E-01	6.209E-01	3.636E+00	3.919E+00	7.524E-01	2.651E+00
S2	2.0	Hem	1.323E+01	4.843E+00	1.174E+00	9.114E-01	6.024E+00	6.744E+00	1.433E+00	4.983E+00
S2	3.0	Hem	1.159E+01	2.993E+00	8.128E-01	5.475E-01	4.142E+00	3.888E+00	8.752E-01	2.730E+00
S3	1.0	Hem	1.159E+01	3.160E+00	9.275E-01	6.119E-01	3.839E+00	4.192E+00	8.095E-01	2.090E+00
S3	2.0	Hem	3.631E+00	2.083E+00	4.863E-01	4.257E-01	2.384E+00	2.431E+00	5.407E-01	1.674E+00
S3	3.0	Hem	3.670E+01	1.321E+01	3.193E+00	2.312E+00	1.736E+01	1.646E+01	3.045E+00	9.111E+00
S4	1.0	Hem	1.383E+00	5.572E-01			6.048E-01	9.795E-01	2.935E-01	1.251E+00
S4	2.0	Hem								4.120E-01
S4	3.0	Hem	4.124E-01					4.171E-01		3.259E-01
TW1	1.0	Hem	4.189E+02	1.406E+02	3.906E+01	2.717E+01	1.636E+02	1.743E+02	3.572E+01	1.055E+02
TW2	1.0	Hem	2.666E+02	6.186E+01	1.920E+01	1.218E+01	7.525E+01	8.748E+01	2.161E+01	7.731E+01
TW3	1.0	Hem	5.287E+02	1.350E+02	3.908E+01	2.409E+01	1.514E+02	1.607E+02	3.483E+01	1.060E+02
TW4	1.0	Hem	4.535E+02	1.387E+02	5.323E+01	2.617E+01	1.578E+02	1.880E+02	3.732E+01	1.085E+02
TW5	1.0	Hem	1.313E+02	3.538E+01	1.055E+01	6.122E+00	3.745E+01	4.498E+01	9.730E+00	3.019E+01
TW7	1.0	Hem	2.761E+02	6.729E+01	1.489E+01	9.921E+00	7.117E+01	5.666E+01	1.570E+01	5.380E+01
TW8	1.0	Hem	5.101E+02	1.788E+02	5.093E+01	3.707E+01	2.127E+02	2.404E+02	5.009E+01	1.612E+02
S5	1.0	Mag	4.217E+00	7.983E-01			1.016E+00	8.929E-01	2.060E-01	5.375E-01
S5	2.0	Mag	2.768E+00				1.063E+00	1.564E+00	3.772E-01	1.366E+00
S5	3.0	Mag								
TW6	1.0	Mag	5.799E+00				2.287E+00	3.058E+00	9.604E-01	4.013E+00
TW9	1.0	Mag	5.019E+01	1.712E+01	3.939E+00	2.461E+00	1.813E+01	1.603E+01	3.955E+00	1.277E+01
TW10	1.0	Mag	3.244E+01	8.411E+00	2.744E+00	1.720E+00	9.461E+00	1.150E+01	2.975E+00	1.164E+01
TW11	1.0	Mag	1.401E+02	4.453E+01	9.541E+00	7.052E+00	5.424E+01	4.287E+01	9.593E+00	2.807E+01
TW12	1.0	Mag	1.353E+01				4.834E+00			
TW13	1.0	Mag	7.819E+01	1.502E+01	3.685E+00	2.779E+00	1.785E+01	2.028E+01	5.261E+00	2.016E+01
	Hematite	average	1.578E+02	5.266E+01	1.677E+01	1.062E+01	6.077E+01	5.861E+01	1.260E+01	3.549E+01
		2*std dev	4.074E+02	1.281E+02	4.022E+01	2.536E+01	1.483E+02	1.614E+02	3.359E+01	1.012E+02
		count	17	15	14	14	15	17	17	19

Magnetite	average	4.091E+01	1.718E+01	4.977E+00	3.503E+00	1.361E+01	1.374E+01	3.333E+00	1.122E+01
	2*std dev	9.615E+01	3.314E+01	6.171E+00	4.815E+00	3.568E+01	2.977E+01	6.711E+00	2.049E+01
	count	8	5	4	4	8	7	7	7

Table A2.2 continued.

Code	Shot	Method	Yb	Lu	Hf	Pb	Th	U	Y/Ho	Ce/Ce*_{PAAS}
S1	1.0	Hem	2.735E+00	4.881E-01	3.485E+00	1.604E+00	1.771E+00	4.162E-01	3.852E+01	7.883E-01
S1	2.0	Hem	6.255E+00	1.129E+00	6.468E+00	4.843E-01	1.620E+00	6.618E-01	3.547E+01	7.928E-01
S1	3.0	Hem	2.165E+00	4.703E-01	2.628E+00		5.740E-01	3.189E-01	3.559E+01	
S2	1.0	Hem	2.689E+00	4.477E-01	2.206E+00	2.653E+00	8.016E-01	2.728E-01	3.173E+01	7.096E-01
S2	2.0	Hem	5.880E+00	9.357E-01	5.551E+00	1.161E+00	1.910E+00	6.361E-01	3.288E+01	7.872E-01
S2	3.0	Hem	2.577E+00	4.299E-01	2.233E+00	2.760E+00	1.101E+00	3.140E-01	3.121E+01	8.000E-01
S3	1.0	Hem	1.715E+00	2.388E-01	1.844E+00	8.643E-01	5.101E-01	1.915E-01	3.051E+01	8.220E-01
S3	2.0	Hem	1.156E+00	2.118E-01	1.188E+00	8.443E-01	2.587E-01	1.643E-01	2.727E+01	6.935E-01
S3	3.0	Hem	7.141E+00	9.324E-01	3.867E+00	1.858E+00	1.357E+00	5.468E-01	3.412E+01	7.436E-01
S4	1.0	Hem	1.894E+00	4.232E-01	1.437E+00	2.761E+00	1.595E+00	4.884E-01	2.675E+01	8.454E-01
S4	2.0	Hem	4.573E-01		3.974E-01	1.973E+00	1.506E-01	7.952E-02		
S4	3.0	Hem			2.620E-01	7.648E+00	1.821E-01	7.328E-02		
TW1	1.0	Hem	9.968E+01	1.354E+01	9.835E+01	1.460E+02	4.884E+01	1.875E+01	2.894E+01	9.040E-01
TW2	1.0	Hem	1.040E+02	1.696E+01	2.263E+02	4.279E+02	4.890E+01	3.091E+01	3.009E+01	9.755E-01
TW3	1.0	Hem	1.138E+02	1.861E+01	1.544E+02	2.860E+02	4.495E+01	3.067E+01	3.025E+01	9.541E-01
TW4	1.0	Hem	9.587E+01	1.156E+01	1.375E+02	7.160E+02	5.150E+01	2.538E+01	2.807E+01	9.267E-01
TW5	1.0	Hem	3.321E+01	5.107E+00	8.817E+01	4.931E+01	2.612E+01	1.215E+01	2.664E+01	9.420E-01
TW7	1.0	Hem	6.417E+01	1.209E+01	7.189E+01	1.061E+03	1.578E+02	8.673E+01	2.726E+01	9.167E-01
TW8	1.0	Hem	1.779E+02	2.826E+01	1.914E+02	1.168E+02	1.177E+02	3.495E+01	3.123E+01	8.904E-01
S5	1.0	Mag	9.498E-01			2.986E+01	4.201E+00	1.749E+00	2.303E+01	8.006E-01
S5	2.0	Mag	1.491E+00	3.646E-01	1.169E+00	1.558E+01	2.587E+00	7.083E-01	2.782E+01	8.240E-01
S5	3.0	Mag			2.558E-01	6.130E-01	2.216E-01			
TW6	1.0	Mag	6.102E+00	1.158E+00	9.461E+00	1.916E+01	4.312E+00	1.840E+00	3.459E+01	8.725E-01
TW9	1.0	Mag	1.413E+01	2.796E+00	1.581E+01	1.238E+02	2.357E+01	8.029E+00	2.843E+01	8.895E-01
TW10	1.0	Mag	1.632E+01	2.716E+00	1.248E+01	5.636E+01	1.355E+01	4.202E+00	3.391E+01	9.629E-01
TW11	1.0	Mag	2.629E+01	4.967E+00	2.094E+01	4.819E+01	1.973E+01	5.808E+00	2.882E+01	8.848E-01
TW12	1.0	Mag				2.548E+01				8.753E-01
TW13	1.0	Mag	2.542E+01	5.348E+00	3.944E+01	1.137E+02	3.297E+01	1.389E+01	3.024E+01	9.581E-01
	Hematite	average	4.018E+01	6.578E+00	5.261E+01	1.571E+02	2.672E+01	1.283E+01	3.097E+01	8.432E-01
		2*std dev	1.094E+02	1.725E+01	1.496E+02	5.933E+02	8.862E+01	4.387E+01	6.908E+00	1.782E-01

	count	18	17	19	18	19	19	17	16
Magnetite	average	1.296E+01	2.892E+00	1.422E+01	4.809E+01	1.264E+01	5.175E+00	2.955E+01	8.834E-01
	2*std dev	2.111E+01	3.977E+00	2.677E+01	8.690E+01	2.366E+01	9.246E+00	7.837E+00	1.134E-01
	count	7	6	7	9	8	7	7	8

Table A2.2 continued.

Code	Shot	Method	La/La* _{PAAS}	Pr/Pr* _{PAAS}	Eu/Eu* _{PAAS}	Pr/Yb* _{PAAS}	∑REE
S1	1.0	Hem	6.463E-01	1.238E+00		8.125E-02	2.571E+01
S1	2.0	Hem	-1.803E+00	8.789E-01	1.069E+00	8.755E-02	8.607E+01
S1	3.0	Hem					1.186E+01
S2	1.0	Hem	-1.901E+00	9.153E-01	9.360E-01	1.157E-01	5.606E+01
S2	2.0	Hem	-3.355E+00	9.156E-01	1.113E+00	1.184E-01	1.124E+02
S2	3.0	Hem	2.126E+00	9.894E-01	1.262E+00	2.820E-01	8.169E+01
S3	1.0	Hem	1.335E+00	1.034E+00	1.333E+00	4.485E-01	7.795E+01
S3	2.0	Hem	-2.989E-01	7.948E-01	1.036E+00	1.272E-01	3.280E+01
S3	3.0	Hem	-9.750E-01	8.909E-01	1.142E+00	2.491E-01	2.556E+02
S4	1.0	Hem	1.605E+00	9.950E-01		4.838E-02	1.845E+01
S4	2.0	Hem					2.790E+00
S4	3.0	Hem					3.920E+00
TW1	1.0	Hem	2.096E+00	9.591E-01	1.262E+00	2.587E-01	3.085E+03
TW2	1.0	Hem	9.868E-01	1.013E+00	1.400E+00	1.856E-01	2.083E+03
TW3	1.0	Hem	1.207E+00	9.890E-01	1.358E+00	3.218E-01	3.686E+03
TW4	1.0	Hem	1.243E+00	1.001E+00	1.761E+00	3.099E-01	3.253E+03
TW5	1.0	Hem	8.736E-01	1.048E+00	1.416E+00	2.871E-01	9.182E+02
TW7	1.0	Hem	1.465E+00	9.780E-01	1.114E+00	2.868E-01	1.726E+03
TW8	1.0	Hem	3.333E+00	9.501E-01	1.257E+00	1.681E-01	4.104E+03
S5	1.0	Mag	1.264E+00	1.050E+00		3.207E-01	2.443E+01
S5	2.0	Mag	1.360E+00	1.026E+00		1.305E-01	2.658E+01
S5	3.0	Mag					1.847E+00
TW6	1.0	Mag	-6.473E+00	8.474E-01		5.055E-02	6.795E+01
TW9	1.0	Mag	2.440E+00	9.390E-01	1.168E+00	2.201E-01	3.655E+02
TW10	1.0	Mag	1.540E+00	9.504E-01	1.448E+00	1.328E-01	2.832E+02
TW11	1.0	Mag	-2.739E+01	9.191E-01	1.051E+00	2.938E-01	8.664E+02
TW12	1.0	Mag	-4.335E+00	8.912E-01			6.585E+01
TW13	1.0	Mag	1.499E+00	9.458E-01	1.135E+00	2.151E-01	5.819E+02
	Hematite	average	5.365E-01	9.743E-01	1.247E+00	2.110E-01	1.033E+03
		2*std dev	3.512E+00	1.916E-01	4.135E-01	2.218E-01	2.926E+03

	count	16	16	14	16	19
Magnetite	average	-3.762E+00	9.461E-01	1.201E+00	1.948E-01	2.537E+02
	2*std dev	2.017E+01	1.324E-01	3.442E-01	1.924E-01	6.057E+02
	count	8	8	4	7	9

Table A2.3. LA-HR-ICP-MS analyses for sample WW1-10 from the Weeli Wolli Iron Formation, Western Australia.

Formation	Sample	Code	Shot	Method	Li	B	Mg	Ca	Ti	V
Weeli Wolli	WW1-10	S6	2.1	Hem		4.044E+00	6.077E+03		3.464E+01	1.370E+01
Weeli Wolli	WW1-10	S6	2.2	Hem			2.174E+03		2.944E+01	1.380E+01
Weeli Wolli	WW1-10	S7	2.4	Hem		4.164E+01	1.986E+02	5.104E+04	5.198E+03	2.160E+01
Weeli Wolli	WW1-10	S7	2.5	Hem		3.662E+01	2.754E+02		5.082E+03	2.042E+01
Weeli Wolli	WW1-10	S7	2.6	Hem		4.053E+01	1.355E+02	1.541E+04	4.641E+03	1.895E+01
Weeli Wolli	WW1-10	S8	2.7	Hem	5.768E+00		3.499E+03	2.069E+03		1.430E+01
Weeli Wolli	WW1-10	S9	2.8	Hem		1.025E+01	7.995E+04	3.029E+03		1.305E+01
Weeli Wolli	WW1-10	S9	2.9	Hem	1.667E+01		5.098E+03		5.008E+03	1.498E+01
Weeli Wolli	WW1-10	S9	2.1	Hem	1.056E+01		1.584E+04	5.099E+03	3.527E+01	1.488E+01
Weeli Wolli	WW1-10	S6	3.2	Hem		3.714E+00	7.246E+03		9.361E+01	1.319E+01
Weeli Wolli	WW1-10	S1	1.0	Hem		2.806E+01	2.014E+02		2.411E+03	1.329E+01
Weeli Wolli	WW1-10	S3	2.0	Hem		3.635E+01	1.572E+02	1.518E+03	3.016E+03	1.493E+01
Weeli Wolli	WW1-10	S3	3.0	Hem		3.655E+01	3.483E+02		3.265E+03	1.514E+01
Weeli Wolli	WW1-10	S4	4.0	Hem	7.562E+00	5.219E+00	2.604E+04	2.337E+03		1.401E+01
Weeli Wolli	WW1-10	S4	5.0	Hem	1.369E+01		1.700E+03	1.576E+03	3.729E+02	1.674E+01
Weeli Wolli	WW1-10	S4	6.0	Hem	9.057E+00	1.919E+00	1.468E+03	1.909E+03	2.843E+01	1.431E+01
Weeli Wolli	WW1-10	S5	7.0	Hem	4.605E+00		1.484E+03	1.257E+03		1.398E+01
Weeli Wolli	WW1-10	S5	8.0	Hem			1.862E+03			1.381E+01
Weeli Wolli	WW1-10	S5	9.0	Hem	4.046E+00	2.931E+00	4.927E+03	2.042E+03	1.149E+02	1.402E+01
Weeli Wolli	WW1-10	TW1	1.0	Hem	4.731E+02	1.242E+02	1.324E+06	7.534E+04	2.740E+04	8.016E+02
Weeli Wolli	WW1-10	TW2	1.0	Hem	4.990E+02	8.265E+01	2.583E+05	6.624E+04	1.391E+04	7.581E+02
Weeli Wolli	WW1-10	TW5	1.0	Hem			5.750E+05	1.270E+05	6.587E+03	5.867E+02
Weeli Wolli	WW1-10	TW6	1.0	Hem			4.037E+05	6.962E+04	6.012E+03	6.086E+02
Weeli Wolli	WW1-10	TW7	1.0	Hem	9.800E+02		4.899E+05	1.174E+06	1.177E+04	6.437E+02
Weeli Wolli	WW1-10	TW8	1.0	Hem	1.115E+03		2.407E+05	6.661E+04	1.040E+05	7.384E+02
Weeli Wolli	WW1-10	TW9	1.0	Hem		9.853E+01	1.347E+06	5.648E+05	1.092E+04	5.605E+02
Weeli Wolli	WW1-10	TW11	1.0	Hem			4.761E+05	3.211E+04	1.254E+04	5.253E+02
Weeli Wolli	WW1-10	TW13	1.0	Hem			8.454E+04	2.739E+04	6.140E+03	5.421E+02
Weeli Wolli	WW1-10	S7	2.1	Mag	8.722E+00	4.829E+00	1.188E+03		5.687E+02	1.577E+01

Weeli Wolli	WW1-10	S8	2.2	Mag	1.279E+01		1.732E+03		3.542E+01	1.919E+01	
Weeli Wolli	WW1-10	S8	2.3	Mag		4.564E+00	2.243E+04		7.130E+01	1.505E+01	
Weeli Wolli	WW1-10	S1	2.0	Mag	1.034E+01		1.459E+03	1.359E+03	4.403E+01	1.421E+01	
Weeli Wolli	WW1-10	S2	3.0	Mag	1.139E+01		1.256E+03		3.286E+01	1.386E+01	
Weeli Wolli	WW1-10	S2	4.0	Mag	6.224E+00		7.395E+02		5.092E+01	1.423E+01	
Weeli Wolli	WW1-10	S2	5.0	Mag	5.279E+00		5.989E+02		1.680E+02	1.599E+01	
Weeli Wolli	WW1-10	S3	6.0	Mag	8.115E+00		3.515E+03	1.403E+03	7.659E+01	1.488E+01	
Weeli Wolli	WW1-10	TW3	1.0	Mag		2.137E+03	7.598E+04		2.302E+05	8.503E+02	
Weeli Wolli	WW1-10	TW4	1.0	Mag		1.472E+03	4.177E+04	7.213E+04	2.936E+05	7.918E+02	
Weeli Wolli	WW1-10	TW10	1.0	Mag		1.367E+03	1.435E+04	3.116E+04	1.783E+05	4.875E+02	
Weeli Wolli	WW1-10	TW12	1.0	Mag		1.454E+03	3.522E+04	3.294E+04	1.862E+05	5.632E+02	
				Hematite	average	2.616E+02	3.688E+01	1.914E+05	1.145E+05	9.939E+03	2.162E+02
					2*std dev	8.214E+02	7.541E+01	7.345E+05	5.573E+05	4.295E+04	6.051E+02
					count	12	15	28	20	23	28
				Magnetite	average	8.981E+00	1.073E+03	1.669E+04	2.780E+04	7.411E+04	2.347E+02
					2*std dev	5.436E+00	1.745E+03	4.728E+04	5.830E+04	2.254E+05	6.731E+02
					count	7	6	12	5	12	12

Table A2.3 continued

Code	Shot	Method	Cr	Mn	Co	Ni	⁶⁵ Cu	Zn	Ge	Rb
S6	2.1	Hem		1.031E+02	3.157E+00	9.918E+00		6.172E+00	3.667E+00	2.530E+01
S6	2.2	Hem		3.855E+01	2.775E+00	9.071E+00		4.242E+00	5.071E+00	1.041E+01
S7	2.4	Hem		1.665E+02						2.721E+00
S7	2.5	Hem		2.549E+01						2.074E+00
S7	2.6	Hem		2.977E+01			2.212E+01		4.997E+00	2.237E+00
S8	2.7	Hem	8.876E+00	7.822E+01	3.494E+00	7.897E+00	1.577E+00	4.544E+00	8.303E+00	1.022E+01
S9	2.8	Hem		1.008E+03	7.360E+00	1.291E+01		5.306E+01	7.564E+00	2.506E+02
S9	2.9	Hem	1.489E+01	8.792E+01	3.335E+00	8.798E+00	1.591E+00	6.692E+00	6.004E+01	1.058E+01
S9	2.1	Hem	1.552E+01	2.053E+02	3.897E+00	8.854E+00		1.436E+01	8.567E+00	5.024E+01
S6	3.2	Hem		1.015E+02	3.082E+00	9.684E+00		7.453E+00	6.134E+00	3.225E+01
S1	1.0	Hem		2.102E+01				1.707E+00	4.072E+00	2.650E+00
S3	2.0	Hem		4.701E+01					3.245E+00	2.509E+00
S3	3.0	Hem		2.181E+01					3.057E+00	2.633E+00
S4	4.0	Hem	1.492E+01	3.524E+02	1.383E+00	6.207E+00	1.950E+00	2.256E+01	4.418E+00	9.582E+01
S4	5.0	Hem	4.295E+01	5.409E+01		5.487E+00		5.348E+00	3.560E+01	4.262E-01
S4	6.0	Hem	2.056E+01	6.050E+01		4.664E+00	2.260E+00	3.141E+00	7.880E+00	1.101E+00
S5	7.0	Hem		5.946E+01		6.500E+00		3.850E+00	4.501E+00	4.855E+00
S5	8.0	Hem	1.298E+01	3.632E+01	1.314E+00	4.944E+00		3.119E+00	5.026E+00	5.565E+00
S5	9.0	Hem		5.627E+01	1.580E+00	8.282E+00		4.608E+00	4.317E+00	1.145E+01
TW1	1.0	Hem	3.620E+02	4.558E+03		2.484E+02		2.684E+02	4.143E+02	7.650E+02
TW2	1.0	Hem	2.165E+02	2.138E+03	6.456E+01	2.242E+02		1.604E+02	7.039E+02	3.154E+01
TW5	1.0	Hem	2.214E+02	2.290E+03	1.326E+02	3.448E+02	1.171E+02	2.052E+02	3.076E+02	3.363E+02
TW6	1.0	Hem	6.994E+02	2.143E+03	1.413E+02	3.374E+02			3.813E+02	1.963E+02
TW7	1.0	Hem	7.371E+02	2.926E+03	1.849E+02	4.826E+02			1.041E+03	2.808E+02
TW8	1.0	Hem	7.309E+02	2.099E+03	1.945E+02	4.605E+02		1.946E+02	1.878E+03	
TW9	1.0	Hem	2.938E+02	4.615E+03	4.872E+01	1.912E+02		2.839E+02	2.417E+02	8.918E+02
TW11	1.0	Hem	1.730E+02	2.265E+03	3.823E+01	1.507E+02		1.722E+02	2.139E+02	3.778E+02
TW13	1.0	Hem	1.052E+02	1.239E+03	4.145E+01	1.610E+02		1.321E+02	2.172E+02	
S7	2.1	Mag	1.180E+01	4.120E+01	2.545E+00	7.388E+00		2.754E+00	1.260E+01	1.788E+00
S8	2.2	Mag	8.726E+00	5.739E+01	2.938E+00	8.192E+00		4.521E+00	4.120E+01	1.374E+00
S8	2.3	Mag	1.266E+01	2.695E+02	4.150E+00	1.019E+01	2.804E+00	1.559E+01	6.405E+00	7.325E+01

S1	2.0	Mag		4.467E+01	1.468E+00	4.727E+00	2.820E+00	4.225E+00	8.053E+00	1.260E+00	
S2	3.0	Mag		7.820E+01	1.191E+00	4.462E+00	3.429E+00	4.677E+00	1.180E+01	2.353E-01	
S2	4.0	Mag		5.524E+01	1.064E+00	3.803E+00	1.959E+00	3.589E+00	5.555E+00	2.320E-01	
S2	5.0	Mag		2.995E+01		3.424E+00		3.293E+00	4.117E+00	3.156E-01	
S3	6.0	Mag	9.656E+00	6.678E+01	1.075E+00	5.402E+00	1.889E+00	4.500E+00	8.413E+00	1.002E+01	
TW3	1.0	Mag		1.354E+03					2.383E+02	8.576E+01	
TW4	1.0	Mag	1.384E+02	1.624E+03					1.706E+02	1.407E+02	
TW10	1.0	Mag		8.180E+02					9.683E+01	4.850E+01	
TW12	1.0	Mag	9.138E+01	9.568E+02					1.402E+02	5.678E+01	
Hematite		average		2.294E+02	9.580E+02	4.876E+01	1.229E+02	2.443E+01	7.418E+01	2.145E+02	1.309E+02
		2*std dev		5.372E+02	2.767E+03	1.343E+02	3.217E+02	9.223E+01	1.968E+02	8.467E+02	4.709E+02
		count		16	28	18	22	6	21	26	26
Magnetite		average		4.543E+01	4.497E+02	2.062E+00	5.949E+00	2.580E+00	5.393E+00	6.201E+01	3.502E+01
		2*std dev		1.116E+02	1.164E+03	2.372E+00	4.787E+00	1.301E+00	8.349E+00	1.607E+02	9.240E+01
		count		6	12	7	8	5	8	12	12

Table A2.3 continued

Code	Shot	Method	Sr	Y	Zr	Mo	Ba	La	Ce	Pr
S6	2.1	Hem	4.054E+00	1.551E+00			2.309E+01		1.634E-01	3.360E-02
S6	2.2	Hem		5.620E+00			1.418E+01	1.416E-01	4.466E-01	8.353E-02
S7	2.4	Hem	5.279E+02	8.613E+01			5.978E+01	6.704E+01	1.181E+02	1.407E+01
S7	2.5	Hem	2.312E+01	4.985E+01	1.262E+01		4.859E+01	5.398E+01	9.107E+01	1.043E+01
S7	2.6	Hem	4.255E+01	7.584E+01		8.623E-01	5.990E+01	6.464E+01	1.213E+02	1.459E+01
S8	2.7	Hem	7.907E+00	4.591E+00			1.546E+01	4.792E-01	1.237E+00	2.102E-01
S9	2.8	Hem	9.440E+00	6.807E+00			6.046E+02	7.774E-01	1.577E+00	1.737E-01
S9	2.9	Hem		3.313E+00	5.016E+00	9.196E-01	2.972E+01	9.107E-01	1.533E+00	2.203E-01
S9	2.1	Hem	1.520E+01	6.682E+00	3.017E+01		9.897E+01	5.397E-01	1.598E+00	3.224E-01
S6	3.2	Hem		1.386E+00			5.248E+00	6.101E-02	1.339E-01	2.224E-02
S1	1.0	Hem	1.914E+01	4.076E+01			5.613E+01	3.877E+01	6.508E+01	8.292E+00
S3	2.0	Hem	2.348E+01	4.791E+01			5.766E+01	4.867E+01	8.253E+01	1.047E+01
S3	3.0	Hem	2.290E+01	4.672E+01		4.737E-01	5.737E+01	4.689E+01	7.887E+01	9.867E+00
S4	4.0	Hem	2.297E+00	5.163E+00	2.578E+01		1.498E+02	5.531E-02	1.593E-01	
S4	5.0	Hem	1.999E+00	9.365E+00				3.810E+00	6.434E+00	8.789E-01
S4	6.0	Hem	2.459E+00	4.295E+00			1.270E+01	1.474E+00	2.454E+00	3.288E-01
S5	7.0	Hem	2.372E+00	2.099E+00			3.002E+01	3.116E-01	5.762E-01	8.192E-02
S5	8.0	Hem		1.138E+00		3.897E-01	1.596E+01	1.109E-01	2.196E-01	3.275E-02
S5	9.0	Hem	2.802E+00	8.659E+00		5.733E-01	3.275E+01	3.814E-01	6.249E-01	8.024E-02
TW1	1.0	Hem	2.170E+02	1.448E+02	9.252E+02		3.295E+03	1.207E+02	1.863E+02	2.227E+01
TW2	1.0	Hem	1.960E+02	1.444E+02	6.973E+02		2.645E+02	8.261E+01	1.312E+02	1.637E+01
TW5	1.0	Hem	3.450E+02	2.159E+02	7.379E+02		6.586E+02	5.429E+01	9.994E+01	1.454E+01
TW6	1.0	Hem	1.291E+02	1.102E+02	1.050E+03		5.727E+02	1.640E+01	2.817E+01	3.353E+00
TW7	1.0	Hem	2.966E+03	1.451E+03	6.917E+02		8.184E+02	1.028E+02	2.610E+02	5.094E+01
TW8	1.0	Hem	8.876E+01	3.570E+02	4.992E+02		7.210E+01	1.009E+02	1.574E+02	1.964E+01
TW9	1.0	Hem	1.392E+03	6.803E+02	1.228E+03		1.179E+03	1.366E+02	2.755E+02	4.286E+01
TW11	1.0	Hem	1.177E+02	9.249E+01	4.619E+02		1.529E+03	5.841E+01	8.827E+01	1.128E+01
TW13	1.0	Hem	6.522E+01	7.344E+01	3.166E+02		7.590E+01	2.716E+01	4.269E+01	5.646E+00
S7	2.1	Mag	3.965E+00	1.110E+01			6.695E+00	7.963E+00	1.363E+01	1.585E+00
S8	2.2	Mag		9.007E-01	7.819E+00		5.042E+00	3.635E-01	5.773E-01	8.794E-02
S8	2.3	Mag	2.019E+00	3.465E+00	6.632E+00	4.780E-01	1.569E+02	2.202E+00	4.554E+00	5.477E-01

S1	2.0	Mag	1.904E+00	8.462E+00	1.057E+01	3.466E-01	5.079E-01	2.978E+00	4.614E+00	5.625E-01
S2	3.0	Mag	3.346E+00	5.114E+00		4.730E-01		1.662E+00	2.877E+00	3.546E-01
S2	4.0	Mag	2.028E+00	1.868E+00				7.191E-01	1.221E+00	1.550E-01
S2	5.0	Mag	1.213E+00	2.531E+00	7.112E+00	4.068E-01	1.456E+00	2.167E+00	4.093E+00	4.934E-01
S3	6.0	Mag	2.261E+00	2.677E+00			6.813E+00	5.484E-01	1.100E+00	1.639E-01
TW3	1.0	Mag	1.359E+03	2.416E+03	6.067E+02	2.759E+01	3.411E+03	2.419E+03	4.395E+03	5.037E+02
TW4	1.0	Mag	1.295E+03	2.966E+03	8.324E+02	1.835E+01	2.756E+03	2.677E+03	4.372E+03	5.224E+02
TW10	1.0	Mag	9.523E+02	1.826E+03	4.540E+02	2.081E+01	2.584E+03	1.641E+03	2.782E+03	3.466E+02
TW12	1.0	Mag	1.006E+03	1.942E+03	4.080E+02	1.620E+01	2.517E+03	1.858E+03	3.231E+03	3.914E+02
Hematite		average	2.593E+02	1.313E+02	5.139E+02	6.437E-01	3.643E+02	3.811E+01	6.588E+01	9.522E+00
		2*std dev	1.295E+03	5.898E+02	8.379E+02	4.715E-01	1.411E+03	8.471E+01	1.605E+02	2.576E+01
		count	24	28	13	5	27	27	28	27
Magnetite		average	4.209E+02	7.655E+02	2.916E+02	1.058E+01	1.144E+03	7.178E+02	1.234E+03	1.473E+02
		2*std dev	1.183E+03	2.313E+03	6.561E+02	2.266E+01	2.918E+03	2.173E+03	3.733E+03	4.429E+02
		count	11	12	8	8	10	12	12	12

Table A2.3 continued

Code	Shot	Method	Sr	Y	Zr	Mo	Ba	La	Ce	Pr
S6	2.1	Hem	4.054E+00	1.551E+00			2.309E+01		1.634E-01	3.360E-02
S6	2.2	Hem		5.620E+00			1.418E+01	1.416E-01	4.466E-01	8.353E-02
S7	2.4	Hem	5.279E+02	8.613E+01			5.978E+01	6.704E+01	1.181E+02	1.407E+01
S7	2.5	Hem	2.312E+01	4.985E+01	1.262E+01		4.859E+01	5.398E+01	9.107E+01	1.043E+01
S7	2.6	Hem	4.255E+01	7.584E+01		8.623E-01	5.990E+01	6.464E+01	1.213E+02	1.459E+01
S8	2.7	Hem	7.907E+00	4.591E+00			1.546E+01	4.792E-01	1.237E+00	2.102E-01
S9	2.8	Hem	9.440E+00	6.807E+00			6.046E+02	7.774E-01	1.577E+00	1.737E-01
S9	2.9	Hem		3.313E+00	5.016E+00	9.196E-01	2.972E+01	9.107E-01	1.533E+00	2.203E-01
S9	2.1	Hem	1.520E+01	6.682E+00	3.017E+01		9.897E+01	5.397E-01	1.598E+00	3.224E-01
S6	3.2	Hem		1.386E+00			5.248E+00	6.101E-02	1.339E-01	2.224E-02
S1	1.0	Hem	1.914E+01	4.076E+01			5.613E+01	3.877E+01	6.508E+01	8.292E+00
S3	2.0	Hem	2.348E+01	4.791E+01			5.766E+01	4.867E+01	8.253E+01	1.047E+01
S3	3.0	Hem	2.290E+01	4.672E+01		4.737E-01	5.737E+01	4.689E+01	7.887E+01	9.867E+00
S4	4.0	Hem	2.297E+00	5.163E+00	2.578E+01		1.498E+02	5.531E-02	1.593E-01	
S4	5.0	Hem	1.999E+00	9.365E+00				3.810E+00	6.434E+00	8.789E-01
S4	6.0	Hem	2.459E+00	4.295E+00			1.270E+01	1.474E+00	2.454E+00	3.288E-01
S5	7.0	Hem	2.372E+00	2.099E+00			3.002E+01	3.116E-01	5.762E-01	8.192E-02
S5	8.0	Hem		1.138E+00		3.897E-01	1.596E+01	1.109E-01	2.196E-01	3.275E-02
S5	9.0	Hem	2.802E+00	8.659E+00		5.733E-01	3.275E+01	3.814E-01	6.249E-01	8.024E-02
TW1	1.0	Hem	2.170E+02	1.448E+02	9.252E+02		3.295E+03	1.207E+02	1.863E+02	2.227E+01
TW2	1.0	Hem	1.960E+02	1.444E+02	6.973E+02		2.645E+02	8.261E+01	1.312E+02	1.637E+01
TW5	1.0	Hem	3.450E+02	2.159E+02	7.379E+02		6.586E+02	5.429E+01	9.994E+01	1.454E+01
TW6	1.0	Hem	1.291E+02	1.102E+02	1.050E+03		5.727E+02	1.640E+01	2.817E+01	3.353E+00
TW7	1.0	Hem	2.966E+03	1.451E+03	6.917E+02		8.184E+02	1.028E+02	2.610E+02	5.094E+01
TW8	1.0	Hem	8.876E+01	3.570E+02	4.992E+02		7.210E+01	1.009E+02	1.574E+02	1.964E+01
TW9	1.0	Hem	1.392E+03	6.803E+02	1.228E+03		1.179E+03	1.366E+02	2.755E+02	4.286E+01
TW11	1.0	Hem	1.177E+02	9.249E+01	4.619E+02		1.529E+03	5.841E+01	8.827E+01	1.128E+01
TW13	1.0	Hem	6.522E+01	7.344E+01	3.166E+02		7.590E+01	2.716E+01	4.269E+01	5.646E+00
S7	2.1	Mag	3.965E+00	1.110E+01			6.695E+00	7.963E+00	1.363E+01	1.585E+00
S8	2.2	Mag		9.007E-01	7.819E+00		5.042E+00	3.635E-01	5.773E-01	8.794E-02
S8	2.3	Mag	2.019E+00	3.465E+00	6.632E+00	4.780E-01	1.569E+02	2.202E+00	4.554E+00	5.477E-01

S1	2.0	Mag	1.904E+00	8.462E+00	1.057E+01	3.466E-01	5.079E-01	2.978E+00	4.614E+00	5.625E-01
S2	3.0	Mag	3.346E+00	5.114E+00		4.730E-01		1.662E+00	2.877E+00	3.546E-01
S2	4.0	Mag	2.028E+00	1.868E+00				7.191E-01	1.221E+00	1.550E-01
S2	5.0	Mag	1.213E+00	2.531E+00	7.112E+00	4.068E-01	1.456E+00	2.167E+00	4.093E+00	4.934E-01
S3	6.0	Mag	2.261E+00	2.677E+00			6.813E+00	5.484E-01	1.100E+00	1.639E-01
TW3	1.0	Mag	1.359E+03	2.416E+03	6.067E+02	2.759E+01	3.411E+03	2.419E+03	4.395E+03	5.037E+02
TW4	1.0	Mag	1.295E+03	2.966E+03	8.324E+02	1.835E+01	2.756E+03	2.677E+03	4.372E+03	5.224E+02
TW10	1.0	Mag	9.523E+02	1.826E+03	4.540E+02	2.081E+01	2.584E+03	1.641E+03	2.782E+03	3.466E+02
TW12	1.0	Mag	1.006E+03	1.942E+03	4.080E+02	1.620E+01	2.517E+03	1.858E+03	3.231E+03	3.914E+02
Hematite		average	2.593E+02	1.313E+02	5.139E+02	6.437E-01	3.643E+02	3.811E+01	6.588E+01	9.522E+00
		2*std dev	1.295E+03	5.898E+02	8.379E+02	4.715E-01	1.411E+03	8.471E+01	1.605E+02	2.576E+01
		count	24	28	13	5	27	27	28	27
Magnetite		average	4.209E+02	7.655E+02	2.916E+02	1.058E+01	1.144E+03	7.178E+02	1.234E+03	1.473E+02
		2*std dev	1.183E+03	2.313E+03	6.561E+02	2.266E+01	2.918E+03	2.173E+03	3.733E+03	4.429E+02
		count	11	12	8	8	10	12	12	12

Table A2.3 continued

Code	Shot	Method	Yb	Lu	Hf	Pb	Th	U	Y/Ho	Ce/Ce*_{PAAS}
S6	2.1	Hem	2.230E-01		4.027E-01	3.186E-01	2.561E-01	2.677E-02	3.041E+01	
S6	2.2	Hem	9.905E-01	1.898E-01	5.075E-01	3.735E+00	4.108E+00	1.098E-01	3.388E+01	8.522E-01
S7	2.4	Hem	9.534E+00	1.830E+00	1.446E-01	6.947E+01	2.145E+01	7.068E+00	3.008E+01	8.866E-01
S7	2.5	Hem	6.544E+00	1.206E+00	1.105E-01	6.001E+01	1.865E+01	6.085E+00	2.828E+01	8.818E-01
S7	2.6	Hem	9.369E+00	1.617E+00		7.953E+01	2.097E+01	7.480E+00	2.693E+01	9.117E-01
S8	2.7	Hem	2.544E-01	4.502E-02		2.373E-01	1.015E-01	1.694E-02	3.200E+01	8.555E-01
S9	2.8	Hem	6.053E-01	1.023E-01	3.779E-01	2.571E-01	1.242E-01	3.439E-02	3.874E+01	9.900E-01
S9	2.9	Hem	2.941E-01	3.871E-02	2.249E-01	7.709E-02	1.224E-01		3.068E+01	7.893E-01
S9	2.1	Hem	4.181E-01	8.449E-02	2.036E-01	1.404E-01	2.284E-01	3.199E-02	3.527E+01	7.931E-01
S6	3.2	Hem	2.467E-01	5.313E-02	4.662E-01	3.582E-01	1.939E-01	2.925E-02	3.378E+01	8.171E-01
S1	1.0	Hem	4.994E+00	8.624E-01		3.972E+01	2.990E+00	6.764E+00	2.890E+01	8.369E-01
S3	2.0	Hem	6.596E+00	1.040E+00		5.225E+01	4.755E+00	8.661E+00	2.844E+01	8.432E-01
S3	3.0	Hem	5.948E+00	9.328E-01		4.694E+01	4.219E+00	7.717E+00	3.024E+01	8.452E-01
S4	4.0	Hem	1.163E+00	2.439E-01	8.224E-01	8.916E-02	3.622E-02	7.931E-02	3.569E+01	
S4	5.0	Hem	5.925E-01	6.723E-02	5.007E-02	2.491E-01	1.223E-01	1.267E-02	3.675E+01	8.113E-01
S4	6.0	Hem	3.508E-01	5.538E-02	4.584E-02	2.010E-01	1.188E-01	2.313E-02	3.558E+01	8.129E-01
S5	7.0	Hem		5.194E-02	8.480E-02	3.746E-01	8.048E-02	4.540E-02	2.557E+01	8.304E-01
S5	8.0	Hem	1.630E-01	3.356E-02		1.741E-01	1.205E-02		2.469E+01	8.346E-01
S5	9.0	Hem	6.353E-01	8.101E-02		2.382E-01	2.772E-02	3.807E-02	4.258E+01	8.233E-01
TW1	1.0	Hem	2.184E+01	3.843E+00		1.707E+02	1.455E+01	1.997E+01	2.585E+01	8.238E-01
TW2	1.0	Hem	1.674E+01	2.544E+00		6.863E+01	7.680E+00	1.086E+01	3.201E+01	8.209E-01
TW5	1.0	Hem	1.436E+01	2.189E+00	3.269E+00	3.425E+01	5.499E+00	2.007E+00	3.230E+01	8.184E-01
TW6	1.0	Hem	1.329E+01	2.138E+00	4.915E+00	6.465E+00	7.612E+00	1.812E+00	3.950E+01	8.750E-01
TW7	1.0	Hem	6.218E+01	9.708E+00	2.294E+00	9.300E+00	7.065E+00	1.642E+00	4.047E+01	7.750E-01
TW8	1.0	Hem	1.870E+01	2.869E+00	3.059E+00	5.578E+00	5.938E+00	8.447E-01	3.839E+01	8.123E-01
TW9	1.0	Hem	4.521E+01	7.760E+00	1.411E+01	1.815E+01	7.037E+00	3.964E+00	3.402E+01	8.211E-01
TW11	1.0	Hem	1.030E+01	1.924E+00		5.539E+01	5.385E+00	6.836E+00	3.001E+01	7.904E-01
TW13	1.0	Hem	6.905E+00	1.387E+00		2.289E+01	2.035E+00	2.790E+00	3.575E+01	7.943E-01
S7	2.1	Mag	8.931E-01	1.684E-01		6.477E+00	2.447E+00	7.894E-01	4.119E+01	8.828E-01
S8	2.2	Mag				1.603E-01	8.554E-02	1.725E-02	1.414E+01	7.447E-01

S8	2.3	Mag	2.973E-01	5.649E-02	3.234E-01	9.197E-01	4.144E-01	7.291E-02	2.749E+01	9.562E-01
S1	2.0	Mag	7.250E-01	8.985E-02		3.823E-01	5.627E-02		3.371E+01	8.184E-01
S2	3.0	Mag	3.695E-01	5.926E-02		1.560E-01	4.637E-02	6.578E-03	4.018E+01	8.641E-01
S2	4.0	Mag	1.744E-01	2.702E-02		2.305E-01	1.889E-02		2.994E+01	8.431E-01
S2	5.0	Mag	3.235E-01	4.858E-02		2.170E+00	1.719E-01	3.472E-01	3.429E+01	9.134E-01
S3	6.0	Mag	2.291E-01	3.465E-02	7.079E-02	2.946E-01	4.125E-02	4.035E-02	3.881E+01	8.394E-01
TW3	1.0	Mag	2.938E+02	5.156E+01	3.303E+00	2.724E+03	2.075E+02	4.560E+02	2.896E+01	9.174E-01
TW4	1.0	Mag	3.732E+02	6.606E+01	3.916E+00	2.558E+03	1.017E+03	3.050E+02	2.947E+01	8.499E-01
TW10	1.0	Mag	1.995E+02	3.769E+01	2.309E+00	1.845E+03	2.034E+02	2.739E+02	3.249E+01	8.501E-01
TW12	1.0	Mag	2.325E+02	4.027E+01	2.179E+00	1.962E+03	1.702E+02	3.290E+02	2.965E+01	8.733E-01
Hematite		average	9.572E+00	1.589E+00	1.829E+00	2.664E+01	5.049E+00	3.652E+00	3.274E+01	8.364E-01
		2*std dev	2.885E+01	4.658E+00	6.953E+00	7.749E+01	1.292E+01	9.586E+00	9.466E+00	9.045E-02
		count	27	27	17	28	28	26	28	26
Magnetite		average	1.002E+02	1.782E+01	2.017E+00	7.583E+02	1.335E+02	1.365E+02	3.169E+01	8.627E-01
		2*std dev	2.892E+02	5.126E+01	3.102E+00	2.282E+03	5.830E+02	3.638E+02	1.440E+01	1.078E-01
		count	11	11	6	12	12	10	12	12

Table A2.3 continued

Code	Shot	Method	La/La*_{PAAS}	Pr/Pr*_{PAAS}	Eu/Eu*_{PAAS}	Pr/Yb*_{PAAS}	∑REE
S6	2.1	Hem				4.812E-02	2.420E+00
S6	2.2	Hem	6.897E-01	1.106E+00		2.693E-02	9.851E+00
S7	2.4	Hem	1.381E+00	9.838E-01	1.167E+00	4.712E-01	4.045E+02
S7	2.5	Hem	1.402E+00	9.795E-01	1.134E+00	5.092E-01	2.869E+02
S7	2.6	Hem	1.390E+00	9.735E-01	1.192E+00	4.972E-01	4.018E+02
S8	2.7	Hem	-1.408E+00	8.546E-01	1.490E+00	2.639E-01	1.068E+01
S9	2.8	Hem	1.672E+00	9.100E-01		9.165E-02	1.293E+01
S9	2.9	Hem	1.178E+00	1.072E+00	1.250E+00	2.392E-01	8.846E+00
S9	2.1	Hem	-2.358E+00	9.380E-01	1.297E+00	2.462E-01	1.516E+01
S6	3.2	Hem	-8.442E-01	7.865E-01	1.799E+00	2.879E-02	2.682E+00
S1	1.0	Hem	1.599E+00	9.838E-01	1.114E+00	5.303E-01	2.216E+02
S3	2.0	Hem	1.446E+00	9.985E-01	1.073E+00	5.067E-01	2.749E+02
S3	3.0	Hem	1.416E+00	1.001E+00	1.197E+00	5.298E-01	2.598E+02
S4	4.0	Hem					8.706E+00
S4	5.0	Hem	1.366E+00	1.028E+00	1.590E+00	4.737E-01	2.924E+01
S4	6.0	Hem	1.631E+00	9.950E-01	1.514E+00	2.993E-01	1.253E+01
S5	7.0	Hem	1.946E+00	9.735E-01	1.071E+00		4.653E+00
S5	8.0	Hem	3.814E+00	9.340E-01		6.416E-02	2.309E+00
S5	9.0	Hem	-5.023E+00	8.086E-01		4.034E-02	1.332E+01
TW1	1.0	Hem	2.333E+00	9.262E-01	1.501E+00	3.257E-01	6.988E+02
TW2	1.0	Hem	1.699E+00	9.776E-01	1.288E+00	3.123E-01	5.490E+02
TW5	1.0	Hem	2.105E+00	9.721E-01	1.309E+00	3.233E-01	5.825E+02
TW6	1.0	Hem	3.278E+00	8.851E-01		8.055E-02	2.286E+02
TW7	1.0	Hem	-8.083E-01	8.486E-01	1.219E+00	2.617E-01	2.924E+03
TW8	1.0	Hem	2.269E+00	9.403E-01	1.341E+00	3.354E-01	9.022E+02
TW9	1.0	Hem	1.937E+00	9.887E-01	1.247E+00	3.028E-01	1.728E+03
TW11	1.0	Hem	1.753E+00	9.868E-01	1.432E+00	3.497E-01	3.615E+02
TW13	1.0	Hem	1.642E+00	9.999E-01	1.230E+00	2.611E-01	2.126E+02
S7	2.1	Mag	1.766E+00	9.411E-01	1.133E+00	5.668E-01	4.759E+01
S8	2.2	Mag	9.374E+00	9.186E-01			3.023E+00

S8	2.3	Mag	9.216E-01	1.043E+00	1.712E+00	5.883E-01	1.565E+01
S1	2.0	Mag	1.694E+00	9.762E-01	1.156E+00	2.478E-01	2.381E+01
S2	3.0	Mag	1.464E+00	9.852E-01	1.260E+00	3.064E-01	1.422E+01
S2	4.0	Mag	1.954E+00	9.528E-01	1.149E+00	2.839E-01	5.992E+00
S2	5.0	Mag	9.840E-01	1.050E+00	1.277E+00	4.870E-01	1.292E+01
S3	6.0	Mag	-1.668E+01	8.821E-01	1.262E+00	2.285E-01	7.173E+00
TW3	1.0	Mag	1.375E+00	9.689E-01	1.165E+00	5.475E-01	1.370E+04
TW4	1.0	Mag	1.504E+00	9.830E-01	1.115E+00	4.471E-01	1.492E+04
TW10	1.0	Mag	1.516E+00	9.856E-01	1.082E+00	5.549E-01	9.391E+03
TW12	1.0	Mag	1.716E+00	9.542E-01	1.092E+00	5.378E-01	1.067E+04
Hematite		average	1.058E+00	9.558E-01	1.307E+00	2.854E-01	3.632E+02
		2*std dev	3.648E+00	1.470E-01	3.733E-01	3.411E-01	1.254E+03
		count	26	26	21	26	28
Magnetite		average	6.322E-01	9.700E-01	1.218E+00	4.360E-01	4.068E+03
		2*std dev	1.183E+01	9.368E-02	3.550E-01	2.817E-01	1.227E+04
		count	12	12	11	11	12

Table A2.4. Bulk digestion and LA-HR-ICP-MS analyses for sample DD98-7 from the Joffre Member of the Brockman Iron Formation, Western Australia.

Formation	Sample	Code	Shot	Method	Li	B	Mg	Ca	Ti	V
Joffre	DD98-7	LR1-4	IF	Bulk	3.402E+00		7.629E+03	2.298E+02	1.399E+02	2.690E+01
Joffre	DD98-7	DD98-7*	IF	Bulk	1.393E+02				6.432E+02	3.678E+01
Joffre	DD98-7	S1	1	Hem		4.892E+01	3.777E+03	8.016E+03	4.050E+02	6.136E+01
Joffre	DD98-7	S1	2	Hem		4.842E+01	4.363E+03	6.899E+03	3.219E+02	5.837E+01
Joffre	DD98-7	S1	3	Hem		5.906E+01	8.236E+03	6.183E+03	3.231E+02	6.221E+01
Joffre	DD98-7	S2	1	Hem		5.182E+01	3.333E+03	3.911E+03	3.542E+02	6.102E+01
Joffre	DD98-7	S2	2	Hem		4.629E+01	3.556E+03	5.060E+03	3.687E+02	6.291E+01
Joffre	DD98-7	S2	3	Hem		5.423E+01	3.116E+03	5.980E+03	3.580E+02	5.985E+01
Joffre	DD98-7	S3	1	Hem		5.949E+01	3.525E+03	5.428E+03	3.404E+02	6.243E+01
Joffre	DD98-7	S3	2	Hem		5.852E+01	2.897E+03	6.759E+03	3.969E+02	6.176E+01
Joffre	DD98-7	S3	3	Hem		5.164E+01	3.053E+03	6.403E+03	3.705E+02	6.146E+01
Joffre	DD98-7	S4	1	Hem		4.662E+01	8.024E+03	7.632E+03	4.552E+02	6.295E+01
Joffre	DD98-7	S4	2	Hem		4.862E+01	9.559E+03	4.468E+03	3.529E+02	5.719E+01
Joffre	DD98-7	S4	3	Hem		4.816E+01	4.336E+03	4.866E+03	3.128E+02	5.427E+01
Joffre	DD98-7	S5	1	Hem		3.877E+01	2.532E+03	6.387E+03	3.032E+02	5.495E+01
Joffre	DD98-7	S5	2	Hem		4.332E+01	4.326E+03	9.737E+03	3.405E+02	5.336E+01
Joffre	DD98-7	S5	3	Hem		4.089E+01	4.565E+03		2.646E+02	5.420E+01
Joffre	DD98-7	S6	1	Hem		8.577E+01	1.542E+04	1.431E+04	5.571E+02	5.636E+01
Joffre	DD98-7	S6	2	Hem		6.424E+01	8.531E+03	1.686E+04	5.287E+02	5.384E+01
Joffre	DD98-7	S6	3	Hem		6.665E+01	8.554E+03	2.174E+04	4.779E+02	5.338E+01
Joffre	DD98-7	S7	1	Hem		4.480E+01	1.393E+03	6.127E+03	2.220E+02	4.719E+01
Joffre	DD98-7	S7	2	Hem		5.506E+01	1.453E+03	7.133E+03	3.079E+02	5.070E+01
Joffre	DD98-7	S7	3	Hem		4.535E+01	2.041E+03	9.917E+03	3.315E+02	4.878E+01
			Bulk	average	7.135E+01		7.629E+03	2.298E+02	3.916E+02	3.184E+01
				2*std dev	1.922E+02				7.117E+02	1.398E+01
				count	2	0	1	1	2	2
			Hematite	average		5.270E+01	5.076E+03	8.191E+03	3.663E+02	5.707E+01
				2*std dev		2.116E+01	6.872E+03	9.027E+03	1.636E+02	9.740E+00
				count	0	21	21	20	21	21

Table A2.4 continued

Code	Shot	Method	Cr	Mn	Co	Ni	⁶⁵ Cu	Zn	Ge	Rb
LR1-4	IF	Bulk	1.943E+01	1.464E+02	2.144E+00	9.700E+00	4.325E+00	8.049E+00	4.118E+01	1.735E+01
DD98-7*	IF	Bulk	6.010E+00	1.368E+02	3.174E+01	6.404E+00	1.766E+01	1.283E+01		2.140E+01
S1	1	Hem		8.778E+01	6.378E+00					1.850E+01
S1	2	Hem		1.020E+02	4.692E+00			1.338E+01		2.271E+01
S1	3	Hem		2.011E+02	4.361E+00					3.190E+01
S2	1	Hem		8.093E+01	4.599E+00					1.488E+01
S2	2	Hem		9.197E+01						1.482E+01
S2	3	Hem		7.932E+01						1.466E+01
S3	1	Hem		8.114E+01	3.808E+00					1.515E+01
S3	2	Hem		7.204E+01	3.262E+00					1.278E+01
S3	3	Hem		7.409E+01	4.439E+00					1.396E+01
S4	1	Hem		1.431E+02	4.817E+00		5.531E+01	1.110E+01		1.229E+01
S4	2	Hem		1.611E+02	5.109E+00		5.290E+01			1.858E+01
S4	3	Hem		1.100E+02	4.931E+00		3.640E+01			9.886E+00
S5	1	Hem		6.876E+01	5.062E+00		8.379E+01			1.014E+01
S5	2	Hem		9.468E+01			7.005E+01			1.511E+01
S5	3	Hem		7.740E+01	4.756E+00		5.505E+01			1.166E+01
S6	1	Hem		3.145E+02	1.344E+01					7.658E+01
S6	2	Hem		1.859E+02	1.094E+01		3.068E+01			3.984E+01
S6	3	Hem		2.013E+02					6.500E+00	4.671E+01
S7	1	Hem		4.757E+01	5.874E+00		7.413E+01			5.578E+00
S7	2	Hem		4.974E+01	7.481E+00		9.774E+01			7.311E+00
S7	3	Hem		6.274E+01	1.153E+01		9.052E+01			8.789E+00
	Bulk	average	1.272E+01	1.416E+02	1.694E+01	8.052E+00	1.099E+01	1.044E+01	4.118E+01	1.938E+01
		2*std dev	1.898E+01	1.354E+01	4.186E+01	4.661E+00	1.886E+01	6.756E+00		5.718E+00
		count	2	2	2	2	2	2	1	2
	Hematite	average		1.137E+02	6.205E+00		6.466E+01	1.224E+01	6.500E+00	2.009E+01
		2*std dev		1.316E+02	5.892E+00		4.482E+01	3.222E+00		3.317E+01
		count	0	21	17	0	10	2	1	21

Table A2.4 continued

Code	Shot	Method	Sr	Y	Zr	Mo	Ba	La	Ce	Pr
LR1-4	IF	Bulk	1.992E+00	3.268E+00	1.154E+01	2.488E-01	6.691E+01	2.484E+00	4.586E+00	5.181E-01
DD98-7*	IF	Bulk	2.184E+00	3.966E+00	1.435E+01	9.555E-02	6.289E+01	3.436E+00	6.005E+00	6.222E-01
S1	1	Hem	1.148E+01	2.124E+00	8.524E+01		7.342E+01	6.499E-01	9.694E-01	1.378E-01
S1	2	Hem	1.184E+01	2.190E+00	7.296E+01		7.640E+01	6.960E-01	9.815E-01	1.521E-01
S1	3	Hem	1.053E+01	5.371E+00	6.011E+01		1.202E+02	1.031E+00	1.793E+00	3.129E-01
S2	1	Hem	8.362E+00	2.886E+00	6.192E+01		8.273E+01	9.202E-01	1.417E+00	1.930E-01
S2	2	Hem	7.564E+00	3.072E+00	5.022E+01		9.374E+01	9.958E-01	1.544E+00	1.845E-01
S2	3	Hem	9.078E+00	2.863E+00	4.728E+01		8.577E+01	1.960E+00	2.627E+00	3.196E-01
S3	1	Hem	9.877E+00	2.844E+00	6.820E+01		9.211E+01	1.095E+00	1.640E+00	2.021E-01
S3	2	Hem	9.400E+00	3.392E+00	5.825E+01		9.419E+01	1.161E+00	1.968E+00	2.359E-01
S3	3	Hem	7.551E+00	3.039E+00	5.120E+01		8.415E+01	9.210E-01	1.475E+00	2.207E-01
S4	1	Hem	1.169E+01	5.274E+01	7.067E+01		1.802E+02	5.117E+00	8.104E+00	1.055E+00
S4	2	Hem	1.099E+01	2.980E+01	6.070E+01		1.442E+02	5.005E+00	7.042E+00	7.093E-01
S4	3	Hem	1.002E+01	5.606E+00	5.608E+01		1.654E+02	1.843E+00	2.729E+00	3.194E-01
S5	1	Hem	1.198E+01	1.063E+02	7.503E+01		1.395E+02	1.440E+00	2.516E+00	4.069E-01
S5	2	Hem	1.263E+01	1.191E+02	6.382E+01		1.596E+02	3.303E-01	5.954E-01	1.271E-01
S5	3	Hem	1.181E+01	4.900E+01	7.383E+01		1.275E+02	6.117E-01	1.195E+00	1.926E-01
S6	1	Hem	2.109E+01	8.381E+00	2.050E+02		1.864E+02	6.566E+00	1.224E+01	1.716E+00
S6	2	Hem	1.960E+01	1.961E+00	1.792E+02		1.252E+02	5.214E-01	8.250E-01	
S6	3	Hem	2.706E+01	1.145E+00	2.213E+02		1.380E+02	1.112E+00	1.792E+00	
S7	1	Hem	1.184E+01	9.490E+01	7.669E+01		1.722E+02	5.791E-01	1.235E+00	2.042E-01
S7	2	Hem	1.208E+01	2.177E+01	6.256E+01		1.625E+02	2.106E-01	5.361E-01	1.039E-01
S7	3	Hem	1.418E+01	2.650E+02	9.988E+01		1.374E+02		8.488E-01	1.383E-01
	Bulk	average	2.088E+00	3.617E+00	1.294E+01	1.722E-01	6.490E+01	2.960E+00	5.296E+00	5.702E-01
		2*std dev	2.719E-01	9.872E-01	3.973E+00	2.167E-01	5.688E+00	1.346E+00	2.007E+00	1.473E-01
		count	2	2	2	2	2	2	2	2
	Hematite	average	1.241E+01	3.731E+01	8.572E+01		1.258E+02	1.638E+00	2.575E+00	3.648E-01
		2*std dev	9.475E+00	1.282E+02	1.010E+02		7.379E+01	3.541E+00	5.882E+00	8.004E-01
		count	21	21	21	0	21	20	21	19

Table A2.4 continued

Code	Shot	Method	Nd	Sm	Eu	Tb	Gd	Dy	Ho	Er
LR1-4	IF	Bulk	2.085E+00	3.998E-01	1.541E-01	7.163E-02	4.626E-01	4.506E-01	9.691E-02	3.525E-01
DD98-7*	IF	Bulk	2.589E+00	4.504E-01	1.871E-01	8.118E-02	6.111E-01	5.274E-01	1.267E-01	4.302E-01
S1	1	Hem	7.276E-01							
S1	2	Hem	6.859E-01						9.174E-02	
S1	3	Hem	1.482E+00				6.282E-01		1.742E-01	5.102E-01
S2	1	Hem	1.055E+00				4.395E-01	5.230E-01	1.213E-01	3.402E-01
S2	2	Hem	1.011E+00				5.599E-01	6.518E-01	1.363E-01	
S2	3	Hem	1.335E+00					5.706E-01	1.313E-01	4.062E-01
S3	1	Hem	1.068E+00				4.929E-01		1.257E-01	4.650E-01
S3	2	Hem	1.397E+00	5.199E-01			4.884E-01	6.749E-01	1.365E-01	4.472E-01
S3	3	Hem	1.105E+00	3.553E-01		9.213E-02	5.047E-01	6.142E-01	1.216E-01	
S4	1	Hem	4.529E+00	1.086E+00	5.201E-01	4.856E-01	2.926E+00	5.072E+00	1.366E+00	4.621E+00
S4	2	Hem	3.239E+00	1.329E+00	1.034E+00	1.485E+00	7.458E+00	1.656E+01	4.879E+00	1.743E+01
S4	3	Hem	1.564E+00	3.919E-01			5.271E-01	7.295E-01	1.675E-01	6.213E-01
S5	1	Hem	2.729E+00	1.554E+00	1.115E+00	9.551E-01	4.878E+00	9.192E+00	2.719E+00	1.063E+01
S5	2	Hem	1.029E+00	1.286E+00	9.110E-01	1.067E+00	5.246E+00	1.084E+01	2.826E+00	1.020E+01
S5	3	Hem	1.325E+00	1.027E+00	5.731E-01	6.102E-01	3.215E+00	5.867E+00	1.496E+00	5.190E+00
S6	1	Hem	7.681E+00	1.844E+00	6.239E-01		2.267E+00	1.751E+00	2.888E-01	
S6	2	Hem	7.265E-01							
S6	3	Hem	1.158E+00							
S7	1	Hem	1.491E+00	1.093E+00	1.003E+00	1.038E+00	4.491E+00	7.578E+00	2.022E+00	6.581E+00
S7	2	Hem	6.531E-01	7.456E-01	5.355E-01	5.698E-01	2.688E+00	5.802E+00	1.231E+00	3.606E+00
S7	3	Hem	1.562E+00	1.703E+00	2.564E+00	3.153E+00	1.532E+01	3.730E+01	1.095E+01	3.812E+01
	Bulk	average	2.337E+00	4.251E-01	1.706E-01	7.641E-02	5.369E-01	4.890E-01	1.118E-01	3.913E-01
		2*std dev	7.121E-01	7.158E-02	4.679E-02	1.350E-02	2.099E-01	1.086E-01	4.219E-02	1.098E-01
		count	2	2	2	2	2	2	2	2
	Hematite	average	1.788E+00	1.078E+00	9.867E-01	1.051E+00	3.258E+00	6.914E+00	1.610E+00	7.083E+00
		2*std dev	3.284E+00	9.960E-01	1.272E+00	1.772E+00	7.749E+00	1.932E+01	5.367E+00	2.059E+01
		count	21	12	9	9	16	15	18	14

Table A2.4 continued

Code	Shot	Method	Yb	Lu	Hf	Pb	Th	U	Y/Ho	Ce/Ce* _{PAAS}
LR1-4	IF	Bulk	3.930E-01	8.383E-02	1.865E-01	1.546E+00	4.847E-01	1.648E-01	3.373E+01	9.315E-01
DD98-7*	IF	Bulk	5.595E-01	1.085E-01	2.839E-01	2.467E+00	8.492E-01	2.200E-01	3.129E+01	9.406E-01
S1	1	Hem	4.059E-01			5.737E+00	3.323E-01	1.657E-01		7.466E-01
S1	2	Hem				5.706E+00	3.267E-01	2.004E-01	2.387E+01	6.957E-01
S1	3	Hem	6.688E-01		1.794E-01	7.674E+00	5.006E-01	2.651E-01	3.084E+01	7.217E-01
S2	1	Hem	3.112E-01		5.233E-02	6.306E+00	3.326E-01	1.646E-01	2.379E+01	7.748E-01
S2	2	Hem		1.092E-01		5.992E+00	3.389E-01	1.876E-01	2.254E+01	8.262E-01
S2	3	Hem	4.911E-01		7.319E-02	6.281E+00	3.204E-01	1.592E-01	2.180E+01	7.541E-01
S3	1	Hem	5.089E-01			7.496E+00	2.933E-01	1.857E-01	2.263E+01	7.995E-01
S3	2	Hem	4.711E-01			7.031E+00	3.157E-01	1.415E-01	2.484E+01	8.659E-01
S3	3	Hem				6.806E+00	3.243E-01	1.437E-01	2.499E+01	7.547E-01
S4	1	Hem	4.606E+00	7.751E-01		1.682E+01	6.832E-01	2.103E-01	3.860E+01	8.036E-01
S4	2	Hem	1.363E+01	2.199E+00	2.294E-01	1.375E+01	8.051E-01	2.484E-01	6.108E+00	8.371E-01
S4	3	Hem	6.566E-01	1.610E-01		1.479E+01	4.735E-01	2.145E-01	3.346E+01	8.122E-01
S5	1	Hem	8.384E+00	1.301E+00		1.206E+01	4.619E-01	4.207E-01	3.912E+01	7.548E-01
S5	2	Hem	1.041E+01	1.728E+00		1.251E+01	6.495E-01	4.582E-01	4.214E+01	6.494E-01
S5	3	Hem	4.689E+00	6.858E-01	2.085E-01	9.456E+00	4.744E-01	3.033E-01	3.276E+01	7.938E-01
S6	1	Hem			1.061E+00	5.192E+00	1.978E+00	5.947E-01	2.902E+01	8.397E-01
S6	2	Hem			7.320E-01	4.619E+00	8.602E-01	4.162E-01		
S6	3	Hem	3.608E-01			4.165E+00	7.564E-01	4.104E-01		
S7	1	Hem	6.262E+00	8.600E-01		1.593E+01	5.194E-01	2.686E-01	4.693E+01	8.104E-01
S7	2	Hem	3.330E+00	4.710E-01		1.557E+01	2.396E-01	3.872E-01	1.768E+01	7.794E-01
S7	3	Hem	3.221E+01	4.367E+00	1.062E-01	3.023E+01	1.697E+00	5.279E-01	2.419E+01	
	Bulk	average	4.762E-01	9.618E-02	2.352E-01	2.006E+00	6.670E-01	1.924E-01	3.251E+01	9.360E-01
		2*std dev	2.355E-01	3.495E-02	1.377E-01	1.302E+00	5.154E-01	7.798E-02	3.439E+00	1.287E-02
		count	2	2	2	2	2	2	2	2
	Hematite	average	5.462E+00	1.266E+00	3.302E-01	1.020E+01	6.040E-01	2.892E-01	2.807E+01	7.789E-01
		2*std dev	1.649E+01	2.550E+00	7.316E-01	1.238E+01	9.009E-01	2.723E-01	1.944E+01	1.085E-01
		count	16	10	8	21	21	21	18	18

Table A2.4 continued

Code	Shot	Method	La/La* _{PAAS}	Pr/Pr* _{PAAS}	Eu/Eu* _{PAAS}	Pr/Yb* _{PAAS}	∑REE
LR1-4	IF	Bulk	1.227E+00	9.851E-01	1.805E+00	4.210E-01	1.541E+01
DD98-7*	IF	Bulk	1.533E+00	9.284E-01	1.941E+00	3.552E-01	1.970E+01
S1	1	Hem	4.364E+00	9.279E-01		1.084E-01	5.014E+00
S1	2	Hem	1.625E+00	1.058E+00			4.797E+00
S1	3	Hem	1.432E+00	1.070E+00		1.494E-01	1.197E+01
S2	1	Hem	7.193E+00	8.938E-01		1.981E-01	8.207E+00
S2	2	Hem	8.593E+00	8.490E-01			8.265E+00
S2	3	Hem	1.719E+00	1.000E+00		2.079E-01	1.070E+01
S3	1	Hem	5.078E+00	8.783E-01		1.268E-01	8.441E+00
S3	2	Hem		8.103E-01		1.599E-01	1.089E+01
S3	3	Hem	2.462E+00	9.778E-01			8.449E+00
S4	1	Hem	1.471E+00	1.015E+00	1.414E+00	7.311E-02	9.300E+01
S4	2	Hem	2.628E+00	8.730E-01	1.193E+00	1.662E-02	1.118E+02
S4	3	Hem	2.968E+00	8.996E-01		1.554E-01	1.532E+01
S5	1	Hem	-1.656E+00	8.221E-01	1.721E+00	1.550E-02	1.542E+02
S5	2	Hem	-4.925E-01	7.606E-01	1.369E+00	3.901E-03	1.657E+02
S5	3	Hem	-1.258E+00	8.065E-01	1.369E+00	1.312E-02	7.568E+01
S6	1	Hem	1.323E+00	1.022E+00			4.336E+01
S6	2	Hem					4.034E+00
S6	3	Hem					5.568E+00
S7	1	Hem	-8.151E-01	7.773E-01	1.599E+00	1.041E-02	1.293E+02
S7	2	Hem	-1.712E+00	9.053E-01	1.475E+00	9.966E-03	4.225E+01
S7	3	Hem		5.521E-01	1.513E+00	1.371E-03	4.132E+02
	Bulk	average	1.380E+00	9.568E-01	1.873E+00	3.881E-01	1.755E+01
		2*std dev	4.322E-01	8.010E-02	1.933E-01	9.312E-02	6.072E+00
		count	2	2	2	2	2
	Hematite	average	2.054E+00	8.894E-01	1.457E+00	8.333E-02	6.334E+01
		2*std dev	5.920E+00	2.489E-01	3.206E-01	1.553E-01	1.929E+02
		count	17	19	8	15	21

Table A2.5. Bulk digestion and LA-HR-ICP-MS analyses for sample DD98-12 from the Joffre Member of the Brockman Iron Formation, Western Australia.

Formation	Sample	Code	Shot	Method	Li	B	Mg	Ca	Ti	V
Joffre	DD98-12	LR1-6	IF	Bulk	7.645E+00		1.295E+04	1.103E+03	5.016E+01	5.390E+00
Joffre	DD98-12	DD98-12*	IF	Bulk	5.364E+02				2.025E+02	7.041E+00
Joffre	DD98-12	S2	5.0	Hem		6.428E+01	1.556E+04		1.054E+02	2.068E+01
Joffre	DD98-12	S3	7.0	Hem		7.846E+01	2.183E+04	2.344E+04		1.732E+01
Joffre	DD98-12	S3	9.0	Hem		9.686E+01	1.328E+04			1.783E+01
Joffre	DD98-12	S4	10.0	Hem		7.570E+01	7.961E+03		7.884E+01	2.524E+01
Joffre	DD98-12	S4	12.0	Hem		8.518E+01	1.112E+04		4.626E+01	2.796E+01
Joffre	DD98-12	S5	13.0	Hem		7.976E+01	1.048E+04	2.157E+03	4.018E+01	1.422E+01
Joffre	DD98-12	S5	15.0	Hem		4.810E+01	8.826E+03	2.540E+03		8.706E+00
Joffre	DD98-12	S6	16.0	Hem		7.509E+01	1.430E+04	2.367E+03		1.134E+01
Joffre	DD98-12	S6	18.0	Hem		7.822E+01	1.870E+03			1.108E+01
Joffre	DD98-12	S7	19.0	Hem		7.745E+01	1.170E+03	8.126E+02		9.314E+00
Joffre	DD98-12	S7	21.0	Hem		6.358E+01	1.313E+03		2.962E+01	1.277E+01
Joffre	DD98-12	S8	24.0	Hem		6.388E+01	6.377E+02	2.079E+03	3.341E+01	9.110E+00
Joffre	DD98-12	S1	1.0	Mag		2.172E+01	6.593E+04	6.315E+03		1.315E+00
Joffre	DD98-12	S1	2.0	Mag		1.422E+01	6.980E+04	6.548E+03		
Joffre	DD98-12	S1	3.0	Mag		1.354E+01	6.804E+04	2.648E+03		
Joffre	DD98-12	S4	4.0	Mag		5.027E+00	1.094E+03		1.242E+01	6.355E+00
Joffre	DD98-12	S2	6.0	Mag		3.967E+00	9.490E+01			8.071E+00
Joffre	DD98-12	S3	8.0	Mag		1.706E+01			2.364E+01	1.111E+01
Joffre	DD98-12	S4	11.0	Mag		7.628E+00	3.965E+03	1.993E+03		6.698E+00
Joffre	DD98-12	S5	14.0	Mag		8.434E+00	2.441E+03		1.807E+01	5.511E+00
Joffre	DD98-12	S6	17.0	Mag		1.127E+01	1.908E+03			6.377E+00
Joffre	DD98-12	S7	20.0	Mag		4.380E+01	8.260E+03			8.419E+00
Joffre	DD98-12	S8	22.0	Mag		3.995E+01	2.189E+04			1.113E+01
Joffre	DD98-12	S8	23.0	Mag		1.564E+01	3.626E+03		3.918E+01	6.710E+00
			Bulk	average	2.720E+02		1.295E+04	1.103E+03	1.263E+02	6.215E+00
				2*std dev	7.478E+02				2.154E+02	2.334E+00
				count	2	0	1	1	2	2

Hematite	average		7.388E+01	9.030E+03	5.566E+03	5.562E+01	1.546E+01
	2*std dev		2.494E+01	1.353E+04	1.755E+04	6.008E+01	1.289E+01
	count	0	12	12	6	6	12
Magnetite	average		16.8547	22458.3423	4375.9050	23.3258	7.1695
	2*std dev		25.5542	59620.6802	4780.2319	23.0371	5.6697
	count	0	12	11	4	4	10

Table A2.5 continued

Code	Shot	Method	Cr	Mn	Co	Ni	⁶⁵ Cu	Zn	Ge	Rb
LR1-6	IF	Bulk	4.513E+01	1.917E+02	2.506E+00	6.018E+00	2.198E+00	1.120E+01	3.859E+01	4.841E+00
DD98-12*	IF	Bulk	2.908E+00	4.512E+02	1.441E+01	3.915E+00	3.167E+00	1.979E+01		1.328E+01
S2	5.0	Hem		1.383E+03	4.941E+00			1.290E+01		1.878E+01
S3	7.0	Hem		1.386E+03				1.532E+01	4.882E+00	5.041E+01
S3	9.0	Hem		9.490E+02	2.033E+00			1.892E+01	5.149E+00	7.677E+01
S4	10.0	Hem		4.872E+02	1.914E+00			7.539E+00	4.788E+00	2.011E+01
S4	12.0	Hem		5.444E+01			1.214E+01	1.539E+01	8.166E+00	6.324E+00
S5	13.0	Hem		1.480E+02	6.728E-01			1.431E+01	1.103E+01	6.743E+00
S5	15.0	Hem		4.070E+02	1.088E+00			9.802E+00	5.143E+00	1.663E+01
S6	16.0	Hem		1.418E+03	6.199E+00	8.034E+00		9.361E+00		3.548E+00
S6	18.0	Hem		3.256E+02	1.244E+01	1.532E+01	1.138E+01			2.419E+00
S7	19.0	Hem		6.260E+01	1.053E+00				4.312E+00	3.978E+00
S7	21.0	Hem		1.347E+02	9.464E+00	1.274E+01	1.574E+01	2.020E+00	2.711E+00	1.819E+00
S8	24.0	Hem		2.756E+01	3.240E+00		6.782E+00		2.835E+00	2.528E+00
S1	1.0	Mag		9.506E+03				2.100E+01		2.793E+01
S1	2.0	Mag		8.526E+03				2.227E+01		1.807E+01
S1	3.0	Mag		1.003E+04				1.850E+01		1.789E+01
S4	4.0	Mag		3.820E+01				3.271E+00	3.505E+01	2.546E+00
S2	6.0	Mag		7.515E+00					1.295E+01	3.314E-01
S3	8.0	Mag		7.906E+00	5.369E-01				1.160E+01	
S4	11.0	Mag		2.103E+01				5.965E+00	1.344E+01	1.191E+00
S5	14.0	Mag		3.066E+02	1.135E+00				1.020E+01	3.061E+00
S6	17.0	Mag		5.465E+01	7.664E-01				6.856E+00	2.527E+00
S7	20.0	Mag		7.723E+01	6.919E-01			1.035E+01	6.986E+00	7.416E+00
S8	22.0	Mag		1.192E+02	1.113E+01	1.399E+01	8.672E+00	2.598E+01	1.286E+01	9.687E-01
S8	23.0	Mag	8.026E+00	1.698E+01	1.116E+00			5.804E+00	6.067E+00	6.932E-01
	Bulk	average	2.402E+01	3.214E+02	8.456E+00	4.967E+00	2.683E+00	1.550E+01	3.859E+01	9.063E+00
		2*std dev	5.970E+01	3.671E+02	1.683E+01	2.974E+00	1.371E+00	1.214E+01		1.194E+01
		count	2	2	2	2	2	2	1	2

Hematite	average		5.653E+02	4.305E+00	1.203E+01	1.151E+01	1.173E+01	5.446E+00	1.750E+01
	2*std dev		1.123E+03	7.970E+00	7.387E+00	7.361E+00	1.018E+01	5.248E+00	4.640E+01
	count	0	12	10	3	4	9	9	12
Magnetite	average	8.0255	2392.6825	2.5629	13.9892	8.6720	14.1428	12.8921	7.5110
	2*std dev		8422.8214	8.4096			17.5839	17.5796	18.8280
	count	1	12	6	1	1	8	9	11

Table A2.5 continued

Code	Shot	Method	Sr	Y	Zr	Mo	Ba	La	Ce	Pr
LR1-6	IF	Bulk	4.653E+00	5.280E+00	7.854E+00	3.976E-01	2.860E+01	2.768E+00	4.561E+00	5.303E-01
DD98-12*	IF	Bulk	3.143E+01	1.250E+01	6.137E+00	1.647E-01	5.210E+01	2.290E+00	4.121E+00	5.326E-01
S2	5.0	Hem	1.986E+00	9.837E+00			9.229E+01	2.765E+01	4.239E+01	4.657E+00
S3	7.0	Hem	3.444E+01	1.295E+01			9.014E+01	3.152E+00	5.095E+00	6.056E-01
S3	9.0	Hem	1.444E+00	1.048E+01			8.469E+01	1.796E+00	3.236E+00	4.308E-01
S4	10.0	Hem	4.920E+00	9.505E+00			1.234E+02	4.529E+00	6.725E+00	7.649E-01
S4	12.0	Hem	1.880E+00	1.020E+01	1.076E+01		1.562E+02	1.925E+00	3.355E+00	4.530E-01
S5	13.0	Hem	2.150E+00	5.921E+00			1.354E+02	1.431E+00	2.006E+00	2.236E-01
S5	15.0	Hem	1.459E+00	4.226E+00			8.598E+01	1.113E+00	1.654E+00	1.822E-01
S6	16.0	Hem	1.073E+00	6.937E+00			1.617E+02	1.971E+00	2.607E+00	2.809E-01
S6	18.0	Hem	1.670E+00	5.145E+00	1.111E+01		1.918E+02	2.026E+00	3.064E+00	5.092E-01
S7	19.0	Hem		2.401E+00		7.924E-01	2.063E+02	9.117E-01	1.151E+00	1.135E-01
S7	21.0	Hem	1.897E+00	3.944E+00			1.782E+02	7.773E-01	1.287E+00	1.598E-01
S8	24.0	Hem	7.032E+00	1.979E+01	9.153E+00	9.936E-01	1.772E+02	5.661E+00	9.734E+00	1.347E+00
S1	1.0	Mag		3.879E+00			1.912E+01	2.307E-01	4.222E-01	6.100E-02
S1	2.0	Mag		2.000E+00			1.385E+01	1.598E-01	2.647E-01	3.832E-02
S1	3.0	Mag	2.100E+00	3.713E+00			1.665E+01	2.564E-01	3.794E-01	4.357E-02
S4	4.0	Mag		6.436E-01			1.842E+00	6.622E-02	1.398E-01	2.193E-02
S2	6.0	Mag	6.016E-01	7.781E-01			2.479E+01	2.157E-01	4.083E-01	6.894E-02
S3	8.0	Mag	9.145E-01	6.470E+00			4.556E+01	4.428E+00	7.664E+00	8.938E-01
S4	11.0	Mag		9.119E-01			1.067E+01	1.090E-01	1.968E-01	
S5	14.0	Mag		2.068E+00			2.189E+01	4.293E-01	8.861E-01	1.119E-01
S6	17.0	Mag		6.631E-01			1.910E+01	1.960E-01	2.911E-01	3.534E-02
S7	20.0	Mag		2.402E+00			6.487E+01	4.863E-01	6.762E-01	8.408E-02
S8	22.0	Mag	2.046E+00	6.777E+00			1.353E+01	6.223E-01	1.373E+00	2.166E-01
S8	23.0	Mag	5.757E-01	1.141E+00			5.626E+01	6.964E-01	8.680E-01	7.925E-02
	Bulk	average	1.804E+01	8.890E+00	6.995E+00	2.812E-01	4.035E+01	2.529E+00	4.341E+00	5.315E-01
		2*std dev	3.787E+01	1.021E+01	2.427E+00	3.294E-01	3.323E+01	6.769E-01	6.226E-01	3.283E-03
		count	2	2	2	2	2	2	2	2
	Hematite	average	5.450E+00	8.444E+00	1.034E+01	8.930E-01	1.403E+02	4.412E+00	6.858E+00	8.106E-01

	2*std dev	1.956E+01	9.598E+00	2.088E+00	2.845E-01	8.882E+01	1.493E+01	2.293E+01	2.517E+00
	count	11	12	3	2	12	12	12	12
Magnetite	average	1.2476	2.6207			25.6766	0.6580	1.1308	0.1504
	2*std dev	1.5309	4.3423			38.7539	2.4081	4.1767	0.5045
	count	5	12	0	0	12	12	12	11

Table A2.5 continued

Code	Shot	Method	Nd	Sm	Eu	Tb	Gd	Dy	Ho	Er
LR1-6	IF	Bulk	2.335E+00	4.794E-01	2.036E-01	9.661E-02	6.317E-01	5.889E-01	1.440E-01	4.934E-01
DD98-12*	IF	Bulk	2.836E+00	6.924E-01	3.210E-01	1.619E-01	1.075E+00	1.170E+00	3.121E-01	1.135E+00
S2	5.0	Hem	1.709E+01	2.234E+00	6.371E-01	2.039E-01	1.443E+00	1.271E+00	3.148E-01	1.261E+00
S3	7.0	Hem	2.903E+00	6.832E-01	2.009E-01	1.704E-01	8.933E-01	1.489E+00	4.412E-01	1.580E+00
S3	9.0	Hem	1.752E+00	4.706E-01	1.698E-01	1.342E-01	6.668E-01	1.232E+00	3.792E-01	1.600E+00
S4	10.0	Hem	3.356E+00	6.366E-01	2.264E-01	1.466E-01	8.628E-01	1.251E+00	3.295E-01	1.391E+00
S4	12.0	Hem	1.912E+00	4.566E-01	1.535E-01	1.317E-01	7.253E-01	1.186E+00	3.196E-01	1.270E+00
S5	13.0	Hem	8.476E-01			5.733E-02	4.375E-01	6.533E-01	1.861E-01	8.671E-01
S5	15.0	Hem	8.927E-01	3.437E-01	1.035E-01	6.974E-02	4.034E-01	5.676E-01	1.687E-01	5.252E-01
S6	16.0	Hem	1.167E+00		2.045E-01	9.257E-02	5.813E-01	7.608E-01	2.056E-01	8.643E-01
S6	18.0	Hem	1.476E+00	4.615E-01	1.620E-01	9.757E-02	6.681E-01	7.203E-01	1.391E-01	5.241E-01
S7	19.0	Hem	4.475E-01			3.783E-02	1.798E-01	3.099E-01	8.665E-02	3.415E-01
S7	21.0	Hem	8.408E-01	2.649E-01	1.111E-01	6.618E-02	3.732E-01	3.803E-01	1.186E-01	3.971E-01
S8	24.0	Hem	6.843E+00	1.806E+00	6.645E-01	3.294E-01	2.467E+00	2.512E+00	5.034E-01	1.420E+00
S1	1.0	Mag	3.605E-01			3.219E-02	1.440E-01	3.477E-01	1.001E-01	6.417E-01
S1	2.0	Mag		8.373E-02		2.323E-02			5.226E-02	3.094E-01
S1	3.0	Mag	2.844E-01			3.061E-02	1.212E-01	2.351E-01	9.779E-02	7.010E-01
S4	4.0	Mag			2.337E-02					1.361E-01
S2	6.0	Mag	2.051E-01						3.301E-02	9.901E-02
S3	8.0	Mag	3.979E+00	6.946E-01	2.396E-01	1.083E-01	8.123E-01	6.518E-01	1.804E-01	5.746E-01
S4	11.0	Mag	1.590E-01					1.293E-01	3.560E-02	1.685E-01
S5	14.0	Mag	6.790E-01		6.400E-02	3.610E-02	2.479E-01	2.603E-01	7.103E-02	2.473E-01
S6	17.0	Mag					5.867E-02	9.777E-02		1.269E-01
S7	20.0	Mag	3.175E-01	9.748E-02		3.015E-02	1.790E-01	2.947E-01	7.276E-02	4.208E-01
S8	22.0	Mag	1.319E+00	4.535E-01	1.516E-01	1.010E-01	5.787E-01	7.008E-01	2.155E-01	8.655E-01
S8	23.0	Mag	3.630E-01			2.872E-02	1.412E-01	1.849E-01	4.779E-02	1.432E-01
	Bulk	average	2.585E+00	5.859E-01	2.623E-01	1.292E-01	8.533E-01	8.792E-01	2.281E-01	8.143E-01
		2*std dev	7.089E-01	3.013E-01	1.660E-01	9.226E-02	6.267E-01	8.212E-01	2.377E-01	9.077E-01
		count	2	2	2	2	2	2	2	2
	Hematite	average	3.293E+00	8.174E-01	2.633E-01	1.281E-01	8.085E-01	1.028E+00	2.660E-01	1.003E+00

	2*std dev	9.360E+00	1.404E+00	4.159E-01	1.607E-01	1.228E+00	1.213E+00	2.688E-01	9.443E-01
	count	12	9	10	12	12	12	12	12
Magnetite	average	0.8518	0.3323	0.1196	0.0488	0.2854	0.3225	0.0906	0.3695
	2*std dev	2.4509	0.5920	0.1924	0.0695	0.5321	0.4308	0.1232	0.5296
	count	9	4	4	8	8	9	10	12

Table A2.5 continued

Code	Shot	Method	Yb	Lu	Hf	Pb	Th	U	Y/Ho	Ce/Ce* _{PAAS}
LR1-6	IF	Bulk	7.205E-01	1.550E-01	4.307E-02	1.447E+00	1.223E-01	2.838E-02	3.666E+01	8.648E-01
DD98-12*	IF	Bulk	1.688E+00	2.932E-01	1.301E-01	4.216E-01	3.730E-01	6.552E-02	4.005E+01	8.610E-01
S2	5.0	Hem	1.579E+00	2.464E-01		2.220E+00	7.700E-01	1.599E-01	3.125E+01	8.511E-01
S3	7.0	Hem	1.943E+00	3.308E-01	1.246E-01	7.176E-01	4.316E-01	2.673E-01	2.935E+01	8.473E-01
S3	9.0	Hem	1.890E+00	3.128E-01		1.142E+00	4.294E-01	3.045E-01	2.763E+01	8.488E-01
S4	10.0	Hem	1.582E+00	2.609E-01	8.853E-02	1.215E+00	5.366E-01	1.857E-01	2.885E+01	8.234E-01
S4	12.0	Hem	2.019E+00	3.445E-01	2.429E-01	4.737E-01	3.802E-01	1.109E-01	3.191E+01	8.291E-01
S5	13.0	Hem	1.299E+00	2.412E-01	6.332E-02	3.774E-01	3.755E-01	9.214E-02	3.182E+01	8.025E-01
S5	15.0	Hem	9.118E-01	1.586E-01	5.750E-02	5.229E-01	2.635E-01	1.393E-01	2.505E+01	8.347E-01
S6	16.0	Hem	1.439E+00	2.088E-01		3.445E+00	2.929E-01	5.767E-02	3.375E+01	7.852E-01
S6	18.0	Hem	5.944E-01	8.932E-02	5.031E-02	5.821E+00	1.968E-01	8.473E-02	3.698E+01	6.955E-01
S7	19.0	Hem	3.223E-01	5.428E-02		1.538E+00	2.857E-01	7.201E-02	2.771E+01	7.878E-01
S7	21.0	Hem	3.561E-01	7.445E-02	5.114E-02	1.417E+01	1.208E-01	9.224E-02	3.325E+01	8.409E-01
S8	24.0	Hem	1.175E+00	1.774E-01		1.547E+00	3.420E-01	8.390E-02	3.931E+01	8.132E-01
S1	1.0	Mag	1.620E+00	2.640E-01			3.172E-02	5.346E-02	3.875E+01	8.193E-01
S1	2.0	Mag	9.562E-01	1.811E-01					3.828E+01	7.803E-01
S1	3.0	Mag	1.722E+00	2.998E-01				8.315E-03	3.796E+01	8.185E-01
S4	4.0	Mag		3.036E-02			7.135E-02	2.212E-02		8.328E-01
S2	6.0	Mag	1.324E-01	2.878E-02		1.614E-01	6.262E-02	1.913E-02	2.357E+01	7.625E-01
S3	8.0	Mag	5.564E-01	8.591E-02	5.205E-02	2.047E-01	2.226E-01	4.946E-02	3.587E+01	8.868E-01
S4	11.0	Mag	3.976E-01	8.536E-02		2.319E-01	4.719E-02		2.562E+01	
S5	14.0	Mag	2.165E-01	4.196E-02		3.736E-01	3.861E-02	2.570E-02	2.912E+01	9.309E-01
S6	17.0	Mag	2.445E-01	6.093E-02		9.706E-01		2.459E-02		8.007E-01
S7	20.0	Mag	7.208E-01	1.573E-01	6.885E-02	1.159E+00	1.055E-01	5.962E-02	3.302E+01	7.635E-01
S8	22.0	Mag	2.528E+00	5.666E-01		1.155E+01	1.998E-01	2.787E-02	3.144E+01	8.451E-01
S8	23.0	Mag	3.359E-01	6.435E-02	6.099E-02	5.787E-01	1.512E-01	1.383E-02	2.388E+01	8.017E-01
	Bulk	average	1.204E+00	2.241E-01	8.659E-02	9.341E-01	2.476E-01	4.695E-02	3.836E+01	8.629E-01
		2*std dev	1.368E+00	1.955E-01	1.231E-01	1.450E+00	3.546E-01	5.252E-02	4.791E+00	5.330E-03
		count	2	2	2	2	2	2	2	2

Hematite	average	1.259E+00	2.083E-01	9.690E-02	2.766E+00	3.688E-01	1.375E-01	3.140E+01	8.133E-01
	2*std dev	1.198E+00	1.991E-01	1.393E-01	7.824E+00	3.371E-01	1.580E-01	8.133E+00	8.707E-02
	count	12	12	7	12	12	12	12	12
Magnetite	average	0.8573	0.1555	0.0606	1.9037	0.1034	0.0304	31.7506	0.8220
	2*std dev	1.5536	0.3156	0.0168	7.8299	0.1432	0.0351	11.9662	0.1026
	count	11	12	3	8	9	10	10	11

Table A2.5 continued

Code	Shot	Method	La/La* _{PAAS}	Pr/Pr* _{PAAS}	Eu/Eu* _{PAAS}	Pr/Yb* _{PAAS}	ΣREE
LR1-6	IF	Bulk	1.708E+00	9.520E-01	1.897E+00	2.351E-01	1.899E+01
DD98-12*	IF	Bulk	4.391E+00	8.908E-01	1.940E+00	1.008E-01	2.913E+01
S2	5.0	Hem	1.261E+00	1.018E+00	1.654E+00	9.416E-01	1.108E+02
S3	7.0	Hem	2.391E+00	9.167E-01	1.194E+00	9.954E-02	3.244E+01
S3	9.0	Hem	1.093E+00	1.057E+00	1.372E+00	7.279E-02	2.455E+01
S4	10.0	Hem	1.917E+00	9.442E-01	1.498E+00	1.544E-01	3.157E+01
S4	12.0	Hem	1.226E+00	1.041E+00	1.271E+00	7.164E-02	2.445E+01
S5	13.0	Hem	1.443E+00	1.009E+00		5.496E-02	1.417E+01
S5	15.0	Hem	3.154E+00	8.761E-01	1.340E+00	6.382E-02	1.132E+01
S6	16.0	Hem	1.940E+00	9.473E-01		6.237E-02	1.732E+01
S6	18.0	Hem	6.169E-01	1.406E+00	1.536E+00	2.736E-01	1.568E+01
S7	19.0	Hem	1.965E+00	9.290E-01		1.124E-01	6.357E+00
S7	21.0	Hem	4.334E+00	8.836E-01	1.701E+00	1.433E-01	9.150E+00
S8	24.0	Hem	2.743E+00	9.414E-01	1.711E+00	3.663E-01	5.443E+01
S1	1.0	Mag	-1.111E+01	8.669E-01		1.203E-02	8.103E+00
S1	2.0	Mag				1.280E-02	4.069E+00
S1	3.0	Mag	-3.394E+00	7.501E-01		8.083E-03	7.883E+00
S4	4.0	Mag					1.061E+00
S2	6.0	Mag	4.988E-01	1.397E+00		1.663E-01	1.969E+00
S3	8.0	Mag	1.682E+00	9.476E-01	1.702E+00	5.131E-01	2.734E+01
S4	11.0	Mag					2.193E+00
S5	14.0	Mag	-5.535E+00	8.136E-01		1.651E-01	5.360E+00
S6	17.0	Mag				4.617E-02	1.774E+00
S7	20.0	Mag	1.294E+00	1.066E+00		3.725E-02	5.939E+00
S8	22.0	Mag	-3.846E+00	8.735E-01	1.429E+00	2.735E-02	1.647E+01
S8	23.0	Mag	3.311E+00	8.304E-01		7.535E-02	4.094E+00
	Bulk	average	3.049E+00	9.214E-01	1.918E+00	1.679E-01	2.406E+01
		2*std dev	3.794E+00	8.652E-02	6.083E-02	1.899E-01	1.434E+01
		count	2	2	2	2	2

Hematite	average	2.007E+00	9.974E-01	1.475E+00	2.014E-01	2.935E+01
	2*std dev	2.061E+00	2.831E-01	3.827E-01	5.035E-01	5.768E+01
	count	12	12	9	12	12
Magnetite	average	-2.1369	0.9431	1.5657	0.1063	7.1879
	2*std dev	9.5464	0.4128	0.3854	0.3094	15.2164
	count	8	8	2	10	12

Note: * indicates a sample that was previously analyzed by bulk digestion but included here.

Table A2.6. Bulk digestion and laser ablation data for sample DD98-21a from the Joffre Member of the Brockman Iron Formation, Western Australia.

Formation	Sample	Code	Shot	Method	Li	B	Mg	Ca	Ti	V
Joffre	DD98-21a	DD98-21A*	IF	Bulk	1.307E+02				8.482E+02	1.188E+01
Joffre	DD98-21a	DD98-21B*	IF	Bulk	3.233E+02				3.348E+02	6.029E+00
Joffre	DD98-21a	S7	2.4	Hem		8.976E+01	2.718E+03	9.620E+02	7.208E+01	1.353E+01
Joffre	DD98-21a	S7	2.5	Hem		7.083E+01	1.625E+03		1.736E+02	9.695E+00
Joffre	DD98-21a	S8	2.7	Hem		6.405E+01	1.534E+04	3.608E+04	9.035E+01	7.390E+00
Joffre	DD98-21a	S8	2.8	Hem		6.704E+01	5.747E+03	2.321E+03	8.663E+01	1.016E+01
Joffre	DD98-21a	S9	2.1	Hem		5.166E+00	2.305E+03	6.707E+02		6.062E+00
Joffre	DD98-21a	S9	2.1	Hem		5.103E+01	1.912E+04		8.214E+01	6.931E+00
Joffre	DD98-21a	TW1	1.0	Hem		2.353E+02	1.035E+04	3.873E+04	1.219E+03	1.841E+02
Joffre	DD98-21a	TW2	1.0	Hem		1.597E+02	4.242E+03	2.326E+04	1.052E+03	2.454E+02
Joffre	DD98-21a	TW3	1.0	Hem		2.518E+02	2.955E+04	5.026E+04	2.152E+03	3.838E+02
Joffre	DD98-21a	TW4	1.0	Hem		3.104E+02	9.741E+04	8.239E+04	5.288E+03	3.725E+02
Joffre	DD98-21a	TW7	1.0	Hem		1.014E+03		2.402E+05		2.075E+03
Joffre	DD98-21a	TW8	1.0	Hem		1.215E+04				
Joffre	DD98-21a	S1	1.0	Mag		6.744E+00	1.529E+03	5.170E+02		7.083E+00
Joffre	DD98-21a	S1	2.0	Mag		6.425E+00	3.402E+02			5.898E+00
Joffre	DD98-21a	S1	3.0	Mag		1.005E+01	2.666E+02		1.794E+01	7.388E+00
Joffre	DD98-21a	S2	4.0	Mag		9.625E+00	3.854E+02			4.512E+00
Joffre	DD98-21a	S2	5.0	Mag		1.062E+01	8.151E+02	8.888E+02		6.123E+00
Joffre	DD98-21a	S2	6.0	Mag		8.637E+00				4.988E+00
Joffre	DD98-21a	S3	7.0	Mag		8.095E+00				2.013E+01
Joffre	DD98-21a	S3	8.0	Mag		1.034E+01	4.645E+02		2.187E+01	1.184E+01
Joffre	DD98-21a	S3	9.0	Mag		1.141E+01	2.823E+03	7.300E+03	1.387E+01	1.300E+01
Joffre	DD98-21a	S4	10.0	Mag		9.801E+00				8.105E+00
Joffre	DD98-21a	S4	11.0	Mag		1.249E+01	2.338E+02			1.208E+01
Joffre	DD98-21a	S4	12.0	Mag		1.053E+01		9.181E+02	2.135E+01	8.406E+00
Joffre	DD98-21a	S5	13.0	Mag		9.644E+00				7.702E+00
Joffre	DD98-21a	S5	14.0	Mag		8.275E+00		1.019E+03	1.376E+01	8.997E+00
Joffre	DD98-21a	S5	15.0	Mag		8.505E+00		6.831E+02		8.287E+00
Joffre	DD98-21a	S6	2.1	Mag		1.214E+01	3.448E+03			1.178E+01
Joffre	DD98-21a	S6	2.2	Mag		1.006E+01	3.999E+03	1.205E+03		8.870E+00
Joffre	DD98-21a	S6	2.3	Mag		4.229E+00	1.103E+04	2.942E+04	4.155E+01	8.088E+00

Joffre	DD98-21a	S7	2.6	Mag	1.215E+01	1.518E+02			8.600E+00
Joffre	DD98-21a	S8	2.9	Mag	7.051E+00	4.152E+02			8.140E+00
Joffre	DD98-21a	S9	2.1	Mag	1.077E+01	1.267E+04	2.242E+04	4.026E+01	6.314E+00
Joffre	DD98-21a	TW5	1.0	Mag	4.808E+03	1.234E+06	8.537E+04	2.617E+04	8.309E+02
Joffre	DD98-21a	TW6	1.0	Mag	5.564E+03		1.812E+05		7.584E+02
		Bulk	average		2.270E+02			5.915E+02	8.955E+00
			2*std dev		2.723E+02			7.261E+02	8.274E+00
			count		2	0	0	0	2
		Hematite	average		1.206E+03	1.884E+04	5.276E+04	1.135E+03	3.013E+02
			2*std dev		6.914E+03	5.807E+04	1.505E+05	3.439E+03	1.214E+03
			count		0	12	10	9	9
		Magnetite	average		4.596E+02	8.483E+04	3.009E+04	3.293E+03	7.720E+01
			2*std dev		2.991E+03	6.358E+05	1.124E+05	1.849E+04	4.534E+02
			count		0	23	15	11	8

Table A2.6 continued

Code	Shot	Method	Cr	Mn	Co	Ni	⁶⁵Cu	Zn	Ge	Rb
DD98-21A*	IF	Bulk	9.947E+00	9.522E+02	1.281E+01	4.694E+00	2.836E+00	8.950E+00		9.474E+01
DD98-21B*	IF	Bulk	1.323E+00	1.967E+02	4.297E+00	1.220E+00	1.338E+00	6.493E+00		2.373E+01
S7	2.4	Hem		4.705E+01	7.188E-01		7.873E+00			7.434E+00
S7	2.5	Hem		2.789E+01	1.211E+00			2.635E+00		3.048E+01
S8	2.7	Hem		4.423E+02	4.312E+00			6.777E+00		1.276E+02
S8	2.8	Hem		1.051E+02				4.588E+00		8.780E+01
S9	2.1	Hem		4.336E+01					1.822E+01	5.270E-01
S9	2.1	Hem		6.566E+01				1.555E+01		3.239E+02
TW1	1.0	Hem		2.689E+02					4.644E+02	1.211E+02
TW2	1.0	Hem		3.725E+02	2.767E+01	1.080E+02			6.600E+02	4.475E+01
TW3	1.0	Hem	2.876E+02	5.684E+02		9.956E+01			5.790E+02	2.290E+02
TW4	1.0	Hem	9.085E+02	5.571E+02		3.100E+02			5.692E+02	2.376E+02
TW7	1.0	Hem	2.106E+03	5.668E+03		9.998E+02			4.792E+03	4.649E+02
TW8	1.0	Hem					1.862E+04		5.366E+03	
S1	1.0	Mag		2.576E+01					9.326E+00	3.029E+00
S1	2.0	Mag	6.117E+00	7.600E+00					8.901E+00	4.502E+00
S1	3.0	Mag		1.999E+01					1.028E+01	9.388E-01
S2	4.0	Mag		1.192E+01					1.273E+01	3.842E+00
S2	5.0	Mag	9.292E+00	1.718E+01	6.441E-01				9.387E+00	2.033E+01
S2	6.0	Mag		8.680E+00					1.320E+01	9.803E-01
S3	7.0	Mag	2.933E+01	1.978E+01	1.265E+00	4.977E+00			9.836E+00	8.229E-01
S3	8.0	Mag	8.514E+00	1.102E+01	9.834E-01	5.149E+00			8.291E+00	4.519E+00
S3	9.0	Mag	7.308E+00	9.597E+01	1.557E+00				1.010E+01	1.827E+00
S4	10.0	Mag		9.247E+00	8.059E-01				1.280E+01	1.762E+00
S4	11.0	Mag		1.762E+01	1.018E+00				1.335E+01	2.394E+00
S4	12.0	Mag		1.097E+01	8.366E-01				1.346E+01	2.182E+00
S5	13.0	Mag		1.148E+01	9.097E-01				1.525E+01	2.026E+00
S5	14.0	Mag		1.445E+01	7.678E-01				1.926E+01	1.660E+00
S5	15.0	Mag		1.148E+01	1.194E+00				1.426E+01	3.086E+00
S6	2.1	Mag		4.440E+01	2.987E+00				1.185E+01	2.464E+00
S6	2.2	Mag		5.214E+01	1.843E+00	7.884E+00			1.617E+01	1.048E+01

S6	2.3	Mag		3.549E+02	1.403E+00				1.388E+01	1.390E+00
S7	2.6	Mag		1.825E+01	6.552E-01				1.696E+01	2.599E+00
S8	2.9	Mag		7.210E+00					1.515E+01	1.856E+00
S9	2.1	Mag		2.745E+02				6.345E+00	1.528E+01	7.703E+01
TW5	1.0	Mag	2.863E+02	1.076E+03	1.002E+02	1.762E+02	4.763E+02			3.525E+02
TW6	1.0	Mag	1.079E+03	3.035E+03		4.703E+02	6.740E+02			1.565E+03
	Bulk	average	5.635E+00	5.745E+02	8.554E+00	2.957E+00	2.087E+00	7.722E+00		5.923E+01
		2*std dev	1.220E+01	1.069E+03	1.204E+01	4.912E+00	2.118E+00	3.474E+00		1.004E+02
		count	2	2	2	2	2	2	0	2
	Hematite	average	1.101E+03	7.424E+02	8.478E+00	3.794E+02	9.314E+03	7.387E+00	1.778E+03	1.523E+02
		2*std dev	1.849E+03	3.294E+03	2.579E+01	8.498E+02	2.632E+04	1.139E+01	4.541E+03	2.943E+02
		count	3	11	4	4	2	4	7	11
	Magnetite	average	2.037E+02	2.242E+02	7.806E+00	1.329E+02	5.751E+02	6.345E+00	1.284E+01	8.989E+01
		2*std dev	7.987E+02	1.310E+03	5.115E+01	4.050E+02	2.796E+02		5.914E+00	6.599E+02
		count	7	23	15	5	2	1	21	23

Table A2.6 continued

Code	Shot	Method	Sr	Y	Zr	Mo	Ba	La	Ce	Pr
DD98-21A*	IF	Bulk	7.264E+01	2.036E+01	3.062E+01	2.326E-01	1.391E+02	7.282E+00	1.425E+01	1.740E+00
DD98-21B*	IF	Bulk	4.788E+00	3.455E+00	4.187E+00	1.130E-01	7.484E+01	1.965E+00	3.333E+00	3.618E-01
S7	2.4	Hem	4.387E+00	1.121E+01		1.127E+00	1.722E+02	2.066E+00	3.718E+00	5.236E-01
S7	2.5	Hem	4.303E+00	2.173E+01	1.563E+01	3.112E+00	1.455E+02	2.231E+00	4.109E+00	5.429E-01
S8	2.7	Hem	1.064E+02	1.264E+01			1.131E+02	3.011E+00	4.066E+00	5.042E-01
S8	2.8	Hem	1.272E+01	3.939E+01	1.032E+01		9.539E+01	1.911E+01	1.498E+01	1.174E+00
S9	2.1	Hem		3.455E-01			8.044E+00	5.089E-02	8.351E-02	
S9	2.1	Hem	1.201E+00	8.861E+00	1.457E+01		5.495E+01	1.320E+02	1.708E+02	2.146E+01
TW1	1.0	Hem	5.050E+01	3.836E+02	3.023E+02	2.796E+01	5.123E+02	1.811E+01	4.270E+01	5.739E+00
TW2	1.0	Hem	3.592E+01	1.814E+01	2.294E+02	1.259E+01	4.148E+02	3.584E+01	7.165E+01	8.663E+00
TW3	1.0	Hem	6.010E+01	7.957E+00	5.074E+02		5.049E+02	1.564E+01	3.316E+01	4.218E+00
TW4	1.0	Hem	9.893E+01	2.267E+01	8.966E+02		9.063E+02	2.429E+00	4.648E+00	7.064E-01
TW7	1.0	Hem	2.533E+02	7.691E+02	2.063E+03		4.235E+03	3.932E+01	7.366E+01	8.218E+00
TW8	1.0	Hem		1.772E+05				3.298E+05		
S1	1.0	Mag		9.706E-01			1.205E+01	2.862E-01	4.436E-01	5.123E-02
S1	2.0	Mag	1.328E+00	4.347E-01	1.284E+01		1.167E+01	2.912E-01	5.598E-01	6.267E-02
S1	3.0	Mag	1.302E+00	1.778E+00	9.955E+00		2.031E+01	1.363E+00	2.237E+00	2.475E-01
S2	4.0	Mag		8.750E-01		6.349E-01	1.865E+01	3.933E-01	6.501E-01	8.400E-02
S2	5.0	Mag		2.927E-01	1.371E+01	8.095E-01	2.048E+01		9.225E-02	
S2	6.0	Mag	6.456E-01	6.748E-01			2.076E+01	1.715E-01	2.638E-01	
S3	7.0	Mag		3.509E-01			1.470E+01	2.554E-01	4.318E-01	6.116E-02
S3	8.0	Mag		5.559E+00	7.469E+00		1.639E+01	1.106E+01	2.054E+01	2.543E+00
S3	9.0	Mag	2.591E+01	1.255E+00			1.662E+01	4.813E-01	9.318E-01	1.376E-01
S4	10.0	Mag	4.371E-01	8.994E-01			1.331E+01	6.755E-01	1.034E+00	1.534E-01
S4	11.0	Mag		6.100E-01	4.406E+00		1.841E+01	2.124E+00	3.968E+00	5.125E-01
S4	12.0	Mag	7.604E-01	5.571E-01			1.507E+01	3.157E+00	5.548E+00	6.921E-01
S5	13.0	Mag		2.238E-01			9.963E+00	1.132E+00	2.118E+00	2.862E-01
S5	14.0	Mag		5.297E-01			1.400E+01	2.206E+00	3.956E+00	4.627E-01
S5	15.0	Mag		4.375E-01	6.232E+00		1.414E+01	2.768E-01	6.096E-01	7.806E-02
S6	2.1	Mag	1.005E+00	3.422E-01			1.884E+01	3.985E-01	6.892E-01	7.982E-02
S6	2.2	Mag	5.770E-01	5.393E-01			1.438E+01	2.023E-01	3.450E-01	4.160E-02

S6	2.3	Mag	1.070E+02	1.962E+00			7.375E+00	1.248E-01	3.159E-01	6.714E-02
S7	2.6	Mag	5.496E+00	1.309E+00	3.851E+00		2.016E+01	1.052E-01	1.905E-01	4.160E-02
S8	2.9	Mag		3.522E+00	3.022E+00		1.561E+01	1.813E-01	1.892E-01	2.425E-02
S9	2.1	Mag	6.305E+01	1.891E+00			1.412E+01	2.936E-01	3.950E-01	7.555E-02
TW5	1.0	Mag	4.518E+02	4.793E+02	8.227E+02	6.724E+01	1.084E+04	7.341E+01	1.488E+02	1.993E+01
TW6	1.0	Mag	7.812E+02	6.136E+02	2.633E+03	1.154E+02	1.918E+04	1.128E+02	2.399E+02	3.001E+01
	Bulk	average	3.872E+01	1.191E+01	1.740E+01	1.728E-01	1.070E+02	4.623E+00	8.794E+00	1.051E+00
		2*std dev	9.596E+01	2.391E+01	3.738E+01	1.691E-01	9.093E+01	7.519E+00	1.544E+01	1.949E+00
		count	2	2	2	2	2	2	2	2
	Hematite	average	6.277E+01	1.488E+04	5.049E+02	1.120E+01	6.511E+02	2.751E+04	3.851E+01	5.175E+00
		2*std dev	1.542E+02	1.023E+05	1.398E+03	2.449E+01	2.438E+03	1.904E+05	1.032E+02	1.314E+01
		count	10	12	8	4	11	12	11	10
	Magnetite	average	1.108E+02	4.861E+01	3.517E+02	4.602E+01	1.319E+03	9.609E+00	1.888E+01	2.650E+00
		2*std dev	4.729E+02	3.168E+02	1.683E+03	1.117E+02	8.999E+03	5.560E+01	1.144E+02	1.522E+01
		count	13	23	10	4	23	22	23	21

Table A2.6 continued

Code	Shot	Method	Nd	Sm	Eu	Tb	Gd	Dy	Ho	Er
DD98-21A*	IF	Bulk	8.145E+00	2.105E+00	8.658E-01	4.211E-01	2.861E+00	2.585E+00	5.710E-01	1.537E+00
DD98-21B*	IF	Bulk	1.587E+00	3.288E-01	1.521E-01	6.303E-02	4.639E-01	4.084E-01	9.786E-02	3.517E-01
S7	2.4	Hem	2.568E+00	6.681E-01	2.198E-01	1.616E-01	1.163E+00	1.440E+00	3.460E-01	1.202E+00
S7	2.5	Hem	2.726E+00	5.679E-01	1.965E-01	1.883E-01	1.166E+00	1.726E+00	4.395E-01	1.567E+00
S8	2.7	Hem	2.638E+00	6.136E-01	2.703E-01	1.855E-01	1.279E+00	1.394E+00	3.441E-01	1.267E+00
S8	2.8	Hem	4.923E+00	1.064E+00	4.470E-01	4.398E-01	2.610E+00	3.485E+00	8.715E-01	2.683E+00
S9	2.1	Hem							1.940E-02	
S9	2.1	Hem	1.008E+02	1.410E+01	3.268E+00	5.714E-01	8.856E+00	1.888E+00	2.721E-01	8.214E-01
TW1	1.0	Hem	3.039E+01	1.088E+01	6.079E+00	1.078E+01	5.390E+01	1.119E+02	3.161E+01	1.090E+02
TW2	1.0	Hem	3.857E+01	6.446E+00	1.579E+00	4.173E-01	4.083E+00	2.794E+00	5.516E-01	
TW3	1.0	Hem	1.688E+01	3.798E+00					4.136E-01	
TW4	1.0	Hem					2.720E+00	3.279E+00	6.888E-01	
TW7	1.0	Hem	3.864E+01	1.633E+01		7.797E+00	4.590E+01	7.060E+01	1.679E+01	6.458E+01
TW8	1.0	Hem	4.634E+04	2.145E+04	7.298E+03	1.842E+03	1.544E+04	2.079E+04	3.090E+03	1.167E+04
S1	1.0	Mag	2.885E-01			2.247E-02			4.641E-02	
S1	2.0	Mag	2.863E-01							
S1	3.0	Mag	1.210E+00	2.524E-01	8.592E-02	7.832E-02	4.368E-01	5.363E-01	1.593E-01	5.535E-01
S2	4.0	Mag	3.810E-01						4.630E-02	2.020E-01
S2	5.0	Mag								
S2	6.0	Mag	2.471E-01				1.179E-01	1.660E-01	3.778E-02	1.367E-01
S3	7.0	Mag	3.912E-01	8.090E-02						
S3	8.0	Mag	1.197E+01	1.844E+00	4.159E-01	1.302E-01	1.342E+00	8.088E-01	1.595E-01	5.691E-01
S3	9.0	Mag	7.078E-01		7.408E-02			2.456E-01	4.715E-02	2.009E-01
S4	10.0	Mag	7.454E-01	2.143E-01		2.494E-02			3.379E-02	
S4	11.0	Mag	2.288E+00	4.409E-01	1.083E-01		3.356E-01		3.614E-02	
S4	12.0	Mag	2.935E+00	5.101E-01	1.222E-01		3.725E-01			
S5	13.0	Mag	1.214E+00	2.200E-01						
S5	14.0	Mag	1.881E+00	2.938E-01			2.339E-01		1.908E-02	7.421E-02
S5	15.0	Mag	3.481E-01						3.402E-02	8.223E-02
S6	2.1	Mag	4.706E-01							
S6	2.2	Mag	2.324E-01						1.792E-02	

S6	2.3	Mag	3.854E-01			7.040E-02	3.004E-01	3.839E-01	8.122E-02	2.355E-01
S7	2.6	Mag	2.450E-01	9.675E-02			1.438E-01	1.697E-01	3.492E-02	1.320E-01
S8	2.9	Mag					1.072E-01	3.063E-01	7.402E-02	2.805E-01
S9	2.1	Mag	3.280E-01					2.553E-01		
TW5	1.0	Mag	8.704E+01	2.038E+01	8.970E+00	6.754E+00	3.747E+01	5.561E+01	1.360E+01	5.081E+01
TW6	1.0	Mag	1.293E+02	3.387E+01	1.055E+01	8.835E+00	5.669E+01	7.717E+01	1.893E+01	6.804E+01
	Bulk	average	4.866E+00	1.217E+00	5.089E-01	2.421E-01	1.662E+00	1.497E+00	3.344E-01	9.444E-01
		2*std dev	9.274E+00	2.512E+00	1.009E+00	5.064E-01	3.390E+00	3.078E+00	6.690E-01	1.676E+00
		count	2	2	2	2	2	2	2	2
	Hematite	average	4.657E+03	2.150E+03	9.137E+02	2.070E+02	1.557E+03	2.099E+03	2.619E+02	1.481E+03
		2*std dev	2.929E+04	1.356E+04	5.159E+03	1.226E+03	9.759E+03	1.313E+04	1.782E+03	8.234E+03
		count	10	10	8	9	10	10	12	8
	Magnetite	average	1.157E+01	5.290E+00	2.904E+00	2.274E+00	8.868E+00	1.357E+01	2.085E+00	1.011E+01
		2*std dev	6.580E+01	2.243E+01	9.417E+00	7.638E+00	3.875E+01	5.660E+01	1.124E+01	4.665E+01
		count	21	11	7	7	11	10	16	12

Table A2.6 continued

Code	Shot	Method	Yb	Lu	Hf	Pb	Th	U	Y/Ho	Ce/Ce* _{PAAS}
DD98-21A*	IF	Bulk	1.123E+00	1.568E-01	1.044E+00	2.141E+00	2.799E+00	4.094E-01	3.566E+01	9.238E-01
DD98-21B*	IF	Bulk	6.171E-01	1.157E-01	8.836E-02	3.844E-01	3.658E-01	1.508E-01	3.530E+01	9.063E-01
S7	2.4	Hem	1.229E+00	2.251E-01	1.005E-01	1.146E+00	4.975E-01	1.323E-01	3.240E+01	8.238E-01
S7	2.5	Hem	1.420E+00	2.145E-01	2.369E-01	1.849E+00	9.411E-01	1.449E-01	4.944E+01	8.611E-01
S8	2.7	Hem	1.320E+00	2.807E-01		2.020E+00	3.441E-01	9.965E-02	3.672E+01	7.514E-01
S8	2.8	Hem	2.450E+00	4.217E-01	1.621E-01	9.194E-01	4.876E-01	1.082E-01	4.519E+01	5.945E-01
S9	2.1	Hem			2.094E-02		1.680E-02		1.781E+01	
S9	2.1	Hem	9.919E-01	2.559E-01	4.024E-01	1.123E+00	6.530E+00	2.123E-01	3.256E+01	7.291E-01
TW1	1.0	Hem	9.624E+01	1.453E+01		9.879E+00	1.059E+00	2.541E-01	1.213E+01	9.543E-01
TW2	1.0	Hem				7.182E+00	8.611E-01	2.672E-01	3.289E+01	9.380E-01
TW3	1.0	Hem			2.544E+00	1.266E+01	2.031E+00	4.681E-01	1.924E+01	9.395E-01
TW4	1.0	Hem			5.432E+00	2.810E+01	8.768E+00		3.291E+01	8.133E-01
TW7	1.0	Hem	5.460E+01	7.913E+00	1.660E+01	1.178E+02	3.612E+01	3.955E+00	4.582E+01	9.443E-01
TW8	1.0	Hem	9.870E+03	1.341E+03			8.064E+02		5.735E+01	
S1	1.0	Mag	1.353E-01			2.695E-01	2.044E-02		2.092E+01	8.385E-01
S1	2.0	Mag				2.488E-01	1.336E-02	9.087E-03		9.555E-01
S1	3.0	Mag	4.803E-01	7.070E-02		2.597E-01	1.879E-01	4.855E-03	1.116E+01	8.825E-01
S2	4.0	Mag	1.680E-01			2.109E-01		1.050E-02	1.890E+01	8.246E-01
S2	5.0	Mag	4.919E-02		6.999E-02	6.692E-01	6.627E-02	2.388E-02		
S2	6.0	Mag				3.250E-01	7.543E-03		1.786E+01	
S3	7.0	Mag				3.793E-01		9.726E-03		7.972E-01
S3	8.0	Mag	4.604E-01		8.196E-02	5.991E-01	5.017E-01	3.291E-02	3.485E+01	8.934E-01
S3	9.0	Mag	1.841E-01			6.972E-01	3.667E-02		2.661E+01	8.306E-01
S4	10.0	Mag	8.804E-02		3.272E-02	4.507E-01	3.271E-02	1.450E-02	2.662E+01	7.411E-01
S4	11.0	Mag				3.499E-01	5.117E-02	1.494E-02	1.688E+01	8.773E-01
S4	12.0	Mag				3.355E-01	8.128E-02			8.656E-01
S5	13.0	Mag				2.578E-01				8.578E-01
S5	14.0	Mag				2.940E-01	4.172E-02	1.487E-02	2.776E+01	9.024E-01
S5	15.0	Mag	5.814E-02			5.958E-01	2.983E-02	1.010E-02	1.286E+01	9.521E-01
S6	2.1	Mag				1.259E+00	9.133E-02			8.892E-01

S6	2.2	Mag				5.382E-01	1.277E-01	1.876E-02	3.009E+01	8.663E-01
S6	2.3	Mag	3.529E-01	7.706E-02		4.911E-01	3.324E-02	7.071E-03	2.415E+01	7.301E-01
S7	2.6	Mag	8.986E-02	2.126E-02		6.560E-01	1.747E-01	2.054E-02	3.749E+01	6.411E-01
S8	2.9	Mag	3.229E-01	5.240E-02	5.199E-02		7.162E-02		4.758E+01	6.344E-01
S9	2.1	Mag	3.314E-01	1.128E-01	1.239E-01		1.146E-01	3.868E-02		6.110E-01
TW5	1.0	Mag	5.276E+01	8.498E+00	3.643E+00	1.550E+02	2.129E+01	7.495E+00	3.525E+01	8.945E-01
TW6	1.0	Mag	7.074E+01	1.120E+01	1.577E+01	2.234E+02	8.960E+01	1.200E+01	3.242E+01	9.488E-01
	Bulk	average	8.702E-01	1.362E-01	5.662E-01	1.262E+00	1.583E+00	2.801E-01	3.548E+01	9.151E-01
		2*std dev	7.158E-01	5.809E-02	1.351E+00	2.483E+00	3.442E+00	3.656E-01	5.102E-01	2.469E-02
		count	2	2	2	2	2	2	2	2
	Hematite	average	1.253E+03	1.707E+02	3.188E+00	1.827E+01	7.201E+01	6.269E-01	3.454E+01	8.349E-01
		2*std dev	6.963E+03	9.462E+02	1.148E+01	7.196E+01	4.630E+02	2.507E+00	2.709E+01	2.357E-01
		count	8	8	8	10	12	9	12	10
	Magnetite	average	9.016E+00	2.862E+00	2.825E+00	1.845E+01	5.629E+00	1.233E+00	2.634E+01	8.302E-01
		2*std dev	4.524E+01	9.676E+00	1.172E+01	1.156E+02	4.065E+01	6.849E+00	1.962E+01	2.054E-01
		count	14	7	7	21	20	16	16	21

Table A2.6 continued

Code	Shot	Method	La/La* _{PAAS}	Pr/Pr* _{PAAS}	Eu/Eu* _{PAAS}	Pr/Yb* _{PAAS}	∑REE
DD98-21A*	IF	Bulk	1.722E+00	9.399E-01	1.842E+00	4.947E-01	6.401E+01
DD98-21B*	IF	Bulk	1.755E+00	9.240E-01	2.108E+00	1.872E-01	1.330E+01
S7	2.4	Hem	2.049E+00	9.685E-01	1.355E+00	1.361E-01	2.674E+01
S7	2.5	Hem	2.474E+00	9.313E-01	1.215E+00	1.221E-01	3.882E+01
S8	2.7	Hem	5.027E+00	8.861E-01	1.625E+00	1.220E-01	2.981E+01
S8	2.8	Hem	4.616E+00	7.974E-01	1.301E+00	1.530E-01	9.404E+01
S9	2.1	Hem					4.993E-01
S9	2.1	Hem	2.570E+00	9.496E-01	1.559E+00	6.909E+00	4.649E+02
TW1	1.0	Hem	3.015E+00	9.073E-01	9.420E-01	1.905E-02	9.255E+02
TW2	1.0	Hem	1.406E+00	9.627E-01	1.531E+00		1.887E+02
TW3	1.0	Hem	9.362E-01	1.045E+00			8.206E+01
TW4	1.0	Hem					3.714E+01
TW7	1.0	Hem	2.008E+00	9.013E-01		4.807E-02	1.213E+03
TW8	1.0	Hem			2.003E+00		6.462E+05
S1	1.0	Mag	1.956E+01	8.238E-01		1.210E-01	2.244E+00
S1	2.0	Mag	1.732E+00	9.171E-01			1.635E+00
S1	3.0	Mag	2.812E+00	8.785E-01	1.239E+00	1.645E-01	9.488E+00
S2	4.0	Mag	1.700E+00	9.803E-01		1.597E-01	2.800E+00
S2	5.0	Mag					4.341E-01
S2	6.0	Mag					1.816E+00
S3	7.0	Mag	-2.905E+00	8.165E-01			1.571E+00
S3	8.0	Mag	1.835E+00	9.426E-01	1.386E+00	1.764E+00	5.741E+01
S3	9.0	Mag	2.518E+00	9.567E-01		2.387E-01	4.265E+00
S4	10.0	Mag	2.172E+00	9.934E-01		5.565E-01	3.869E+00
S4	11.0	Mag	1.422E+00	9.891E-01			1.042E+01
S4	12.0	Mag	1.334E+00	1.003E+00			1.389E+01
S5	13.0	Mag	1.157E+00	1.038E+00			5.194E+00
S5	14.0	Mag	1.248E+00	9.964E-01			9.657E+00
S5	15.0	Mag	1.211E+00	9.863E-01		4.288E-01	1.924E+00
S6	2.1	Mag	-1.619E+01	8.021E-01			1.980E+00

S6	2.2	Mag	1.247E+01	8.422E-01			1.378E+00
S6	2.3	Mag	4.532E+01	9.915E-01		6.076E-02	4.356E+00
S7	2.6	Mag	-8.683E+00	9.796E-01		1.479E-01	2.580E+00
S8	2.9	Mag				2.398E-02	5.060E+00
S9	2.1	Mag	1.217E+00	1.169E+00		7.280E-02	3.683E+00
TW5	1.0	Mag	1.173E+00	1.018E+00	1.546E+00	1.207E-01	1.063E+03
TW6	1.0	Mag	1.149E+00	9.957E-01	1.238E+00	1.355E-01	1.482E+03
	Bulk	average	1.739E+00	9.320E-01	1.975E+00	3.410E-01	3.865E+01
		2*std dev	4.699E-02	2.251E-02	3.762E-01	4.349E-01	7.171E+01
		count	2	2	2	2	2
	Hematite	average	2.678E+00	9.276E-01	1.441E+00	1.073E+00	5.411E+04
		2*std dev	2.733E+00	1.358E-01	6.320E-01	5.148E+00	3.729E+05
		count	9	9	8	7	12
	Magnetite	average	3.613E+00	9.560E-01	1.352E+00	3.073E-01	1.170E+02
		2*std dev	2.392E+01	1.768E-01	2.937E-01	9.250E-01	7.404E+02
		count	20	20	4	13	23

Note: * indicates a sample that was previously analyzed by bulk digestion but included here.

Table A2.7. Bulk digestion and LA-ICP-MS analyses for sample DD98-26 from the Dales Gorge Member of the Brockman Iron Formation, Western Australia.

Formation	Sample	Code	Shot	Method	Li	B	Mg	Ca	Ti	V
Dales Gorge	DD98-26	DD98-26A*	IF	Bulk	6.876E+01				1.177E+02	4.978E+00
Dales Gorge	DD98-26	DD98-26B*	IF	Bulk	1.075E+02				3.045E+02	1.559E+01
Dales Gorge	DD98-26	S1	3	Hem		6.015E+00			1.313E+01	6.115E+00
Dales Gorge	DD98-26	S1	3	Hem		1.001E+01	2.206E+02	7.084E+02		6.622E+00
Dales Gorge	DD98-26	S1	3	Hem		2.376E+01	1.628E+02			7.760E+00
Dales Gorge	DD98-26	S2	3	Hem		1.075E+01	3.735E+02			4.252E+00
Dales Gorge	DD98-26	S2	4	Hem		4.150E+01			2.121E+01	5.328E+00
Dales Gorge	DD98-26	S2	4	Hem		2.847E+00				6.165E+00
Dales Gorge	DD98-26	S3	4	Hem		1.112E+01	1.278E+02	1.860E+03		5.599E+00
Dales Gorge	DD98-26	S3	4	Hem		1.358E+01			1.962E+01	1.570E+00
Dales Gorge	DD98-26	S3	4	Hem		8.024E+00	8.342E+02			7.131E+00
Dales Gorge	DD98-26	S4	3	Hem		1.447E+01	2.059E+03	1.065E+04		6.023E+00
Dales Gorge	DD98-26	S4	3	Hem		1.110E+01	1.045E+02	2.328E+03		6.144E+00
Dales Gorge	DD98-26	S4	3	Hem		4.441E+00				6.824E+00
Dales Gorge	DD98-26	S5	3	Hem		1.705E+01	2.820E+03	2.871E+04		6.589E+00
Dales Gorge	DD98-26	S5	3	Hem		1.065E+01	1.437E+02	1.213E+04	1.993E+01	5.641E+00
Dales Gorge	DD98-26	S5	3	Hem		1.051E+01	1.551E+02	2.355E+03		5.024E+00
Dales Gorge	DD98-26	S6	3	Hem		1.382E+01		2.186E+03		5.523E+00
Dales Gorge	DD98-26	S6	3	Hem		2.858E+01		1.471E+03		5.483E+00
Dales Gorge	DD98-26	S6	3	Hem		5.169E+00		2.051E+03	1.629E+01	5.919E+00
			Bulk	average	8.811E+01				2.111E+02	1.028E+01
				2*std dev	5.473E+01				2.642E+02	1.500E+01
				count	2	0	0	0	2	2
			Hematite	average		1.35E+01	7.00E+02	6.45E+03	1.80E+01	5.76E+00
				2*std dev		1.90E+01	1.92E+03	1.76E+04	6.58E+00	2.64E+00
				count	0	18	10	10	5	18

Table A2.7 continued

Code	Shot	Method	Cr	Mn	Co	Ni	⁶⁵ Cu	Zn	Ge	Rb
DD98-26A*	IF	Bulk	1.058E+00	5.183E+02	3.044E+00	7.649E-01	2.787E+00	5.603E+00		1.863E+01
DD98-26B*	IF	Bulk	3.030E+00	5.246E+02	9.333E+00	2.428E+00	1.256E+00	1.133E+01		2.865E+01
S1	3	Hem		1.996E+01					4.358E+01	1.179E+00
S1	3	Hem		1.623E+01					4.770E+01	9.276E-01
S1	3	Hem		2.437E+01					5.164E+01	7.079E-01
S2	3	Hem		3.162E+01					4.280E+01	6.267E-01
S2	4	Hem		4.344E+01				2.894E+00	3.282E+01	1.921E+00
S2	4	Hem		7.815E+00					3.723E+01	
S3	4	Hem	1.868E+01	1.245E+01					4.379E+01	8.360E-01
S3	4	Hem		1.799E+01				2.381E+00	3.764E+01	5.998E-01
S3	4	Hem		1.520E+01					4.493E+01	3.619E+00
S4	3	Hem		1.246E+02					3.218E+01	1.167E+00
S4	3	Hem		1.618E+01					3.624E+01	2.030E+00
S4	3	Hem		1.112E+01					3.918E+01	4.341E-01
S5	3	Hem		1.004E+02				2.800E+00	3.484E+01	1.118E+01
S5	3	Hem		4.519E+01					3.103E+01	1.256E+00
S5	3	Hem		6.505E+01					2.599E+01	1.194E+00
S6	3	Hem		3.556E+01					3.026E+01	9.571E-01
S6	3	Hem		3.075E+01					2.112E+01	1.237E+00
S6	3	Hem		1.214E+01					3.173E+01	2.453E-01
	Bulk	average	2.044E+00	5.214E+02	6.189E+00	1.596E+00	2.022E+00	8.466E+00		2.364E+01
		2*std dev	2.788E+00	8.947E+00	8.894E+00	2.352E+00	2.165E+00	8.099E+00		1.416E+01
		count	2	2	2	2	2	2	0	2
	Hematite	average	1.87E+01	3.50E+01				2.69E+00	3.69E+01	1.77E+00
		2*std dev		6.41E+01				5.46E-01	1.57E+01	5.09E+00
		count	1	18	0	0	0	3	18	17

Table A2.7 continued

Code	Shot	Method	Sr	Y	Zr	Mo	Ba	La	Ce	Pr
DD98-26A*	IF	Bulk	3.620E+01	1.186E+01	9.061E+00	5.177E-01	1.942E+01	4.730E+00	7.426E+00	8.176E-01
DD98-26B*	IF	Bulk	3.991E+01	1.502E+01	2.001E+01	1.097E+00	1.719E+01	6.073E+00	1.206E+01	1.379E+00
S1	3	Hem		7.872E-01			9.060E+00	2.018E-01	2.964E-01	5.361E-02
S1	3	Hem	7.185E-01	8.917E-01			1.459E+01	1.552E-01	2.270E-01	2.787E-02
S1	3	Hem	1.537E+00	9.490E-01			4.044E+01	2.911E-01	4.140E-01	4.946E-02
S2	3	Hem		2.939E+00			1.981E+01	1.004E+00	1.807E+00	2.489E-01
S2	4	Hem	2.437E+00	1.440E+00	4.870E+00		8.840E+01	6.438E-01	8.999E-01	1.233E-01
S2	4	Hem		2.147E-01			1.373E+01	6.555E-02	7.816E-02	
S3	4	Hem		5.387E-01			2.388E+01	1.338E-01	1.466E-01	
S3	4	Hem	1.712E+00	9.394E-01			3.736E+01	2.572E-01	3.742E-01	4.139E-02
S3	4	Hem		2.337E-01			1.555E+01	5.050E-02	6.473E-02	
S4	3	Hem	7.919E+00	7.554E+00			3.458E+01	2.383E+00	3.698E+00	4.865E-01
S4	3	Hem	1.043E+00	4.752E-01			2.668E+01	1.623E-01	2.220E-01	3.009E-02
S4	3	Hem	1.013E+00	2.205E-01		6.982E-01	9.497E+00	4.167E-02	5.660E-02	
S5	3	Hem	9.827E+01	8.446E+01		2.084E+00	3.547E+01	2.188E+01	3.542E+01	4.472E+00
S5	3	Hem	6.046E+01	6.257E+01		3.131E+00	2.710E+01	1.573E+01	2.249E+01	2.698E+00
S5	3	Hem	8.194E+00	7.467E+00		3.921E+00	2.151E+01	2.067E+00	2.972E+00	3.584E-01
S6	3	Hem	2.077E+00	5.612E+00		1.739E+00	2.498E+01	1.556E+00	2.320E+00	2.888E-01
S6	3	Hem	2.981E+00	8.480E-01	4.234E+00		6.850E+01	2.592E-01	3.417E-01	4.724E-02
S6	3	Hem	4.940E+00	4.105E+00			7.780E+00	1.034E+00	1.665E+00	2.037E-01
	Bulk	average	3.806E+01	1.344E+01	1.453E+01	8.074E-01	1.831E+01	5.401E+00	9.744E+00	1.098E+00
		2*std dev	5.243E+00	4.478E+00	1.548E+01	8.193E-01	3.147E+00	1.900E+00	6.556E+00	7.934E-01
		count	2	2	2	2	2	2	2	2
	Hematite	average	1.49E+01	1.01E+01	4.55E+00	2.31E+00	2.88E+01	2.66E+00	4.08E+00	6.52E-01
		2*std dev	5.95E+01	4.70E+01	9.01E-01	2.50E+00	4.17E+01	1.20E+01	1.88E+01	2.60E+00
		count	13	18	2	5	18	18	18	14

Table A2.7 continued

Code	Shot	Method	Nd	Sm	Eu	Tb	Gd	Dy	Ho	Er
DD98-26A*	IF	Bulk	3.869E+00	7.825E-01	3.405E-01	1.680E-01	1.210E+00	1.040E+00	2.911E-01	9.160E-01
DD98-26B*	IF	Bulk	6.138E+00	1.240E+00	4.883E-01	2.544E-01	1.924E+00	1.430E+00	3.446E-01	9.641E-01
S1	3	Hem	2.145E-01					1.136E-01	2.811E-02	1.043E-01
S1	3	Hem	1.253E-01					5.415E-02		
S1	3	Hem	1.947E-01					1.171E-01	2.773E-02	1.404E-01
S2	3	Hem	1.313E+00	2.693E-01	1.014E-01	5.838E-02	4.111E-01	4.878E-01	1.071E-01	3.732E-01
S2	4	Hem	5.981E-01				1.278E-01	1.781E-01	5.175E-02	1.399E-01
S2	4	Hem	6.115E-02						9.717E-03	
S3	4	Hem		6.234E-02						7.998E-02
S3	4	Hem	1.846E-01				8.724E-02		2.859E-02	1.146E-01
S3	4	Hem	4.394E-02							
S4	3	Hem	2.391E+00	5.099E-01	2.022E-01	1.217E-01	7.433E-01	8.605E-01	1.897E-01	6.414E-01
S4	3	Hem				9.851E-03		7.204E-02	1.969E-02	
S4	3	Hem	3.624E-02							
S5	3	Hem	2.183E+01	4.720E+00	2.106E+00	1.096E+00	7.223E+00	7.751E+00	1.929E+00	5.901E+00
S5	3	Hem	1.234E+01	2.597E+00	1.125E+00	6.760E-01	4.191E+00	5.198E+00	1.389E+00	4.419E+00
S5	3	Hem	1.540E+00	3.777E-01	1.433E-01	7.299E-02	6.053E-01	5.744E-01	1.674E-01	4.579E-01
S6	3	Hem	1.360E+00	2.749E-01	1.359E-01	6.596E-02	4.913E-01	4.796E-01	1.298E-01	5.033E-01
S6	3	Hem	1.730E-01				9.721E-02		2.354E-02	1.326E-01
S6	3	Hem	1.073E+00	2.611E-01	1.189E-01	5.802E-02	3.863E-01	4.099E-01	1.021E-01	3.491E-01
	Bulk	average	5.004E+00	1.011E+00	4.144E-01	2.112E-01	1.567E+00	1.235E+00	3.178E-01	9.400E-01
		2*std dev	3.209E+00	6.464E-01	2.090E-01	1.221E-01	1.010E+00	5.515E-01	7.570E-02	6.808E-02
		count	2	2	2	2	2	2	2	2
	Hematite	average	2.72E+00	1.13E+00	5.62E-01	2.70E-01	1.44E+00	1.36E+00	3.00E-01	1.03E+00
		2*std dev	1.18E+01	3.33E+00	1.55E+00	7.95E-01	4.74E+00	4.93E+00	1.18E+00	3.73E+00
		count	16	8	7	8	10	12	14	13

Table A2.7 continued

Code	Shot	Method	Yb	Lu	Hf	Pb	Th	U	Y/Ho	Ce/Ce* _{PAAS}
DD98-26A*	IF	Bulk	1.028E+00	1.613E-01	1.201E-01	3.288E-01	3.675E-01	6.952E-02	4.073E+01	8.622E-01
DD98-26B*	IF	Bulk	9.511E-01	1.401E-01	1.535E-01	2.731E-01	3.760E-01	6.882E-02	4.359E+01	9.618E-01
S1	3	Hem	1.335E-01			7.818E+00	6.443E-02		2.800E+01	6.559E-01
S1	3	Hem	1.147E-01			2.543E-01	4.582E-02	1.059E-02		7.901E-01
S1	3	Hem	1.655E-01	2.841E-02		4.948E-01	5.094E-02	1.405E-02	3.422E+01	7.868E-01
S2	3	Hem	3.412E-01	5.028E-02		2.599E-01	3.886E-02		2.745E+01	8.338E-01
S2	4	Hem	2.073E-01	4.060E-02	7.748E-02	5.227E-01	7.521E-02	1.892E-02	2.783E+01	7.338E-01
S2	4	Hem		1.622E-02		5.168E-01		4.604E-03	2.209E+01	
S3	4	Hem			2.890E-02	2.817E-01	4.097E-02			
S3	4	Hem	2.485E-01	4.172E-02		3.896E-01	1.494E-02		3.286E+01	8.233E-01
S3	4	Hem			4.081E-02		3.878E-02	1.800E-02		
S4	3	Hem	5.726E-01	8.451E-02		4.387E-01	2.054E-01	2.667E-02	3.982E+01	7.910E-01
S4	3	Hem				3.400E-01		2.749E-02	2.414E+01	7.287E-01
S4	3	Hem	4.087E-02			3.577E-01		2.597E-02		
S5	3	Hem	5.136E+00	7.639E-01	3.985E-02	3.307E-01	3.742E-01	6.120E-02	4.379E+01	8.246E-01
S5	3	Hem	4.094E+00	6.205E-01		5.330E-01	4.470E-01	2.874E-02	4.505E+01	7.876E-01
S5	3	Hem	5.812E-01	8.090E-02		3.154E-01	5.992E-02	1.364E-02	4.459E+01	7.886E-01
S6	3	Hem	3.407E-01	6.594E-02		2.155E-01	4.122E-02	1.148E-02	4.325E+01	7.938E-01
S6	3	Hem	1.809E-01		2.269E-02	3.283E-01		1.752E-02	3.603E+01	7.074E-01
S6	3	Hem	3.193E-01	4.829E-02			2.417E-02		4.022E+01	8.340E-01
	Bulk	average	9.896E-01	1.507E-01	1.368E-01	3.010E-01	3.717E-01	6.917E-02	4.216E+01	9.120E-01
		2*std dev	1.088E-01	2.989E-02	4.715E-02	7.876E-02	1.204E-02	9.813E-04	4.046E+00	1.408E-01
		count	2	2	2	2	2	2	2	2
	Hematite	average	8.91E-01	1.67E-01	4.19E-02	8.37E-01	1.09E-01	2.15E-02	3.50E+01	7.77E-01
		2*std dev	3.20E+00	5.24E-01	4.25E-02	3.73E+00	2.73E-01	2.81E-02	1.60E+01	1.05E-01
		count	14	11	5	16	14	13	14	14

Table A2.7 continued

Code	Shot	Method	La/La* _{PAAS}	Pr/Pr* _{PAAS}	Eu/Eu* _{PAAS}	Pr/Yb* _{PAAS}	∑REE
DD98-26A*	IF	Bulk	2.501E+00	8.927E-01	1.891E+00	2.540E-01	3.464E+01
DD98-26B*	IF	Bulk	1.496E+00	9.388E-01	1.746E+00	4.629E-01	4.841E+01
S1	3	Hem	9.502E-01	1.208E+00		1.283E-01	1.933E+00
S1	3	Hem	1.958E+00	9.639E-01		7.763E-02	1.596E+00
S1	3	Hem	1.433E+00	1.024E+00		9.547E-02	2.377E+00
S2	3	Hem	3.706E+00	9.175E-01	1.630E+00	2.330E-01	9.512E+00
S2	4	Hem	2.557E+00	9.644E-01		1.899E-01	4.451E+00
S2	4	Hem					4.455E-01
S3	4	Hem					9.614E-01
S3	4	Hem	2.123E+00	9.239E-01		5.319E-02	2.317E+00
S3	4	Hem					3.928E-01
S4	3	Hem	2.575E+00	9.419E-01	1.643E+00	2.713E-01	2.044E+01
S4	3	Hem					9.911E-01
S4	3	Hem					3.959E-01
S5	3	Hem	2.475E+00	9.302E-01	1.872E+00	2.781E-01	2.047E+02
S5	3	Hem	2.187E+00	9.450E-01	1.723E+00	2.104E-01	1.401E+02
S5	3	Hem	1.751E+00	9.807E-01	1.724E+00	1.970E-01	1.747E+01
S6	3	Hem	2.275E+00	9.445E-01	2.043E+00	2.707E-01	1.362E+01
S6	3	Hem	1.161E+00	1.139E+00		8.339E-02	2.103E+00
S6	3	Hem	4.605E+00	8.776E-01	1.949E+00	2.037E-01	1.013E+01
	Bulk	average	1.999E+00	9.158E-01	1.818E+00	3.584E-01	4.152E+01
		2*std dev	1.421E+00	6.521E-02	2.059E-01	2.955E-01	1.948E+01
		count	2	2	2	2	2
	Hematite	average	2.29E+00	9.82E-01	1.80E+00	1.76E-01	2.41E+01
		2*std dev	1.98E+00	1.86E-01	3.18E-01	1.60E-01	1.11E+02
		count	13	13	7	13	18

Note: * indicates a sample that was previously analyzed by bulk digestion but included here.

Table A2.8. Bulk digestion and LA-HR-ICP-MS data for sample DD98-27 from the Dales Gorge Member of the Brockman Iron Formation, Western Australia.

Formation	Sample	Code	Shot	Method	Li	B	Mg	Ca	Ti	V
Dales Gorge	DD98-27	LR1-9	IF	Bulk	1.282E+01		1.158E+04	6.298E+02	5.820E+00	2.089E+00
Dales Gorge	DD98-27	LR1-23	IF	Bulk	1.324E+01		1.129E+04	6.497E+02	1.261E+01	2.171E+00
Dales Gorge	DD98-27	DD98-27*	IF	Bulk	9.978E+01				5.830E+01	1.635E+00
Dales Gorge	DD98-27	TW1	1	Hem		9.835E+02	7.223E+04	7.006E+04	2.046E+03	8.328E+01
Dales Gorge	DD98-27	TW2	1	Hem		1.773E+02	3.507E+03	4.363E+04	1.176E+03	5.730E+01
Dales Gorge	DD98-27	TW3	1	Hem			1.540E+03	3.546E+04	1.069E+03	4.836E+01
Dales Gorge	DD98-27	TW4	1	Hem		1.160E+03	4.130E+03	3.523E+04	1.044E+03	1.212E+02
Dales Gorge	DD98-27	TW5	1	Hem		9.839E+01	1.991E+03	2.537E+04	9.018E+02	4.543E+01
Dales Gorge	DD98-27	TW8	1	Hem		1.049E+03	3.553E+03	2.782E+04	8.860E+02	7.421E+01
Dales Gorge	DD98-27	TW11	1	Hem			1.513E+03	1.664E+04	5.192E+02	3.047E+01
Dales Gorge	DD98-27	TW12	1	Hem		5.254E+01	1.609E+03	1.746E+04	4.110E+02	2.654E+01
Dales Gorge	DD98-27	TW6	1	Mag		3.246E+03	1.830E+04	4.976E+04	1.632E+03	1.063E+02
Dales Gorge	DD98-27	TW7	1	Mag		3.695E+03	1.505E+04	3.802E+04	1.450E+03	1.084E+02
Dales Gorge	DD98-27	TW9	1	Mag	6.882E+03	1.526E+03	1.385E+06			1.144E+02
Dales Gorge	DD98-27	TW10	1	Mag	6.618E+03	1.396E+03	1.429E+06	1.377E+05	2.802E+03	1.141E+02
Dales Gorge	DD98-27	TW13	1	Mag		3.233E+03	1.960E+04	2.637E+04	1.007E+03	8.608E+01
			Bulk	average	4.195E+01		1.144E+04	6.398E+02	2.558E+01	1.965E+00
				2*std dev	1.002E+02		4.163E+02	2.816E+01	5.708E+01	5.769E-01
				count	3	0	2	2	3	3
			Hematite	average		5.867E+02	1.126E+04	3.396E+04	1.007E+03	6.085E+01
				2*std dev		1.055E+03	4.932E+04	3.451E+04	9.947E+02	6.250E+01
				count	0	6	8	8	8	8
			Magnetite	average	6.750E+03	2.619E+03	5.734E+05	6.297E+04	1.723E+03	1.059E+02
				2*std dev	3.734E+02	2.149E+03	1.522E+06	1.015E+05	1.531E+03	2.324E+01
				count	2	5	5	4	4	5

Table A2.8 continued

Code	Shot	Method	Cr	Mn	Co	Ni	⁶⁵ Cu	Zn	Ge	Rb
LR1-9	IF	Bulk	2.391E+01	6.086E+01	1.918E-01	2.973E+00	8.537E-01	5.307E+00	4.920E+01	2.266E+00
LR1-23	IF	Bulk	2.314E+01	5.951E+01	1.957E-01	2.786E+00	7.153E-01	5.172E+00	5.327E+01	2.207E+00
DD98-27*	IF	Bulk	4.630E-01	1.901E+02	1.783E+00	6.688E-01	1.053E+00			1.806E+01
TW1	1	Hem		8.630E+02					3.380E+02	3.492E+01
TW2	1	Hem		7.872E+02					5.522E+02	
TW3	1	Hem		6.776E+02					5.665E+02	
TW4	1	Hem		1.286E+03					2.589E+02	3.516E+01
TW5	1	Hem		5.671E+02					3.547E+02	
TW8	1	Hem		1.162E+03				4.561E+01	2.571E+02	3.032E+01
TW11	1	Hem		5.126E+02					3.949E+02	
TW12	1	Hem		4.560E+02				3.053E+01	4.027E+02	1.547E+01
TW6	1	Mag		1.919E+03			8.163E+01		1.313E+02	2.789E+02
TW7	1	Mag		2.396E+03					1.770E+02	1.480E+02
TW9	1	Mag		4.682E+03				8.545E+02	5.990E+02	
TW10	1	Mag		4.846E+03				7.057E+02	5.088E+02	
TW13	1	Mag		9.977E+02			4.125E+01		1.483E+02	1.107E+02
	Bulk	average	1.584E+01	1.035E+02	7.234E-01	2.143E+00	8.739E-01	5.240E+00	5.124E+01	7.511E+00
		2*std dev	2.664E+01	1.500E+02	1.835E+00	2.560E+00	3.391E-01	1.906E-01	5.753E+00	1.827E+01
		count	3	3	3	3	3	2	2	3
	Hematite	average		7.889E+02				3.807E+01	3.906E+02	2.897E+01
		2*std dev		6.050E+02				2.132E+01	2.348E+02	1.854E+01
		count	0	8	0	0	0	2	8	4
	Magnetite	average		2.968E+03			6.144E+01	7.801E+02	3.129E+02	1.792E+02
		2*std dev		3.431E+03			5.711E+01	2.105E+02	4.458E+02	1.767E+02
		count	0	5	0	0	2	2	5	3

Table A2.8 continued

Code	Shot	Method	Sr	Y	Zr	Mo	Ba	La	Ce	Pr
LR1-9	IF	Bulk	3.209E+00	2.534E+00	5.544E+00	3.529E-01	3.429E+01	1.922E+00	2.952E+00	3.250E-01
LR1-23	IF	Bulk	3.088E+00	2.686E+00	8.776E+00	3.194E-01	3.746E+01	2.166E+00	3.328E+00	3.654E-01
DD98-27*	IF	Bulk	1.919E+01	1.326E+00	2.580E+00	1.811E-01	3.115E+01	9.379E-01	1.264E+00	1.256E-01
TW1	1	Hem	1.052E+02	7.948E+01	7.035E+02		2.113E+03	8.152E+01	1.345E+02	1.390E+01
TW2	1	Hem	3.952E+01	5.843E+00	2.842E+02		3.898E+02	8.469E-01	1.849E+00	2.811E-01
TW3	1	Hem	3.786E+01		3.543E+02		8.904E+01			
TW4	1	Hem	1.435E+02	1.589E+02	3.522E+02	1.246E+01	2.927E+03	1.610E+01	3.036E+01	4.147E+00
TW5	1	Hem	3.474E+01	3.332E+00	2.446E+02		2.584E+02	1.062E+00	1.978E+00	2.917E-01
TW8	1	Hem	8.357E+01	2.604E+01	3.008E+02	2.108E+01	2.557E+03	1.140E+01	1.867E+01	2.458E+00
TW11	1	Hem	2.658E+01	9.506E-01	2.259E+02		7.432E+01		6.136E-01	
TW12	1	Hem	1.449E+01	8.889E-01	1.071E+02		1.082E+02			
TW6	1	Mag	2.153E+02	8.903E+01	3.880E+02		8.232E+03	2.802E+01	4.625E+01	5.883E+00
TW7	1	Mag	2.098E+02	9.194E+01	3.542E+02		8.204E+03	2.932E+01	4.375E+01	4.938E+00
TW9	1	Mag	1.372E+02	2.191E+02			4.357E+02	6.755E+00	1.554E+01	2.822E+00
TW10	1	Mag	1.302E+02	2.232E+02	7.818E+02		4.506E+02	8.812E+00	2.087E+01	3.301E+00
TW13	1	Mag	1.640E+02	1.343E+02	2.635E+02	9.039E+00	5.934E+03	2.198E+01	3.557E+01	4.175E+00
	Bulk	average	8.497E+00	2.182E+00	5.633E+00	2.844E-01	3.430E+01	1.675E+00	2.515E+00	2.720E-01
		2*std dev	1.853E+01	1.491E+00	6.197E+00	1.822E-01	6.310E+00	1.300E+00	2.198E+00	2.568E-01
		count	3	3	3	3	3	3	3	3
	Hematite	average	6.068E+01	3.935E+01	3.216E+02	1.677E+01	1.065E+03	2.219E+01	3.134E+01	4.216E+00
		2*std dev	9.042E+01	1.196E+02	3.471E+02	1.220E+01	2.478E+03	6.764E+01	1.039E+02	1.131E+01
		count	8	7	8	2	8	5	6	5
	Magnetite	average	1.713E+02	1.515E+02	4.469E+02	9.039E+00	4.651E+03	1.898E+01	3.240E+01	4.224E+00
		2*std dev	7.950E+01	1.322E+02	4.588E+02	#DIV/0!	7.906E+03	2.123E+01	2.735E+01	2.466E+00
		count	5	5	4	1	5	5	5	5

Table A2.8 continued

Code	Shot	Method	Nd	Sm	Eu	Tb	Gd	Dy	Ho	Er
LR1-9	IF	Bulk	1.338E+00	2.092E-01	8.158E-02	4.054E-02	2.737E-01	2.625E-01	7.026E-02	2.936E-01
LR1-23	IF	Bulk	1.475E+00	2.244E-01	9.057E-02	4.402E-02	3.037E-01	2.747E-01	7.656E-02	3.142E-01
DD98-27*	IF	Bulk	5.440E-01	8.244E-02	4.336E-02	1.746E-02	1.327E-01	1.225E-01	3.299E-02	1.222E-01
TW1	1	Hem	5.246E+01	7.172E+00		8.744E-01	6.442E+00	7.318E+00	1.318E+00	5.198E+00
TW2	1	Hem	1.622E+00							
TW3	1	Hem								
TW4	1	Hem	2.400E+01	6.258E+00	2.974E+00	1.668E+00	1.020E+01	1.127E+01	2.735E+00	7.604E+00
TW5	1	Hem								
TW8	1	Hem	1.098E+01	2.748E+00		5.062E-01	2.774E+00	3.347E+00	8.863E-01	3.261E+00
TW11	1	Hem								
TW12	1	Hem								
TW6	1	Mag	2.743E+01	6.375E+00	3.020E+00	1.620E+00	9.972E+00	1.127E+01	2.898E+00	9.980E+00
TW7	1	Mag	2.033E+01	4.315E+00	1.956E+00	1.435E+00	7.484E+00	1.150E+01	2.725E+00	1.033E+01
TW9	1	Mag	1.610E+01			2.823E+00	1.168E+01	1.852E+01	5.667E+00	2.905E+01
TW10	1	Mag	1.935E+01	7.466E+00	3.479E+00	2.250E+00	1.267E+01	2.007E+01	5.865E+00	2.870E+01
TW13	1	Mag	1.768E+01	4.337E+00	2.114E+00	1.634E+00	8.026E+00	1.250E+01	3.198E+00	1.152E+01
	Bulk	average	1.119E+00	1.720E-01	7.184E-02	3.401E-02	2.367E-01	2.199E-01	5.994E-02	2.433E-01
		2*std dev	1.005E+00	1.559E-01	5.014E-02	2.887E-02	1.827E-01	1.691E-01	4.709E-02	2.108E-01
		count	3	3	3	3	3	3	3	3
	Hematite	average	2.227E+01	5.393E+00	2.974E+00	1.016E+00	6.471E+00	7.312E+00	1.646E+00	5.354E+00
		2*std dev	4.425E+01	4.671E+00		1.188E+00	7.424E+00	7.923E+00	1.934E+00	4.351E+00
		count	4	3	1	3	3	3	3	3
	Magnetite	average	2.018E+01	5.623E+00	2.642E+00	1.952E+00	9.967E+00	1.477E+01	4.071E+00	1.791E+01
		2*std dev	8.728E+00	3.125E+00	1.457E+00	1.152E+00	4.493E+00	8.381E+00	3.117E+00	2.004E+01
		count	5	4	4	5	5	5	5	5

Table A2.8 continued

Code	Shot	Method	Yb	Lu	Hf	Pb	Th	U	Y/Ho	Ce/Ce* _{PAAS}
LR1-9	IF	Bulk	4.783E-01	9.729E-02		2.087E-01	2.585E-02	1.227E-02	3.606E+01	8.514E-01
LR1-23	IF	Bulk	5.101E-01	1.020E-01		1.965E-01	3.046E-02	1.457E-02	3.509E+01	8.525E-01
DD98-27*	IF	Bulk	1.817E-01	3.765E-02	3.711E-02	1.176E-01	1.316E-01	2.361E-02	4.019E+01	8.194E-01
TW1	1	Hem		9.809E-01		4.574E+00	1.236E+00		6.031E+01	9.115E-01
TW2	1	Hem				2.653E+00				8.605E-01
TW3	1	Hem				2.641E+00				
TW4	1	Hem	6.201E+00	9.729E-01		7.833E+00	5.025E-01	2.044E-01	5.810E+01	8.560E-01
TW5	1	Hem								8.169E-01
TW8	1	Hem	2.474E+00	4.145E-01		5.170E+00	5.210E-01		2.938E+01	8.133E-01
TW11	1	Hem								
TW12	1	Hem				8.048E-01				
TW6	1	Mag	1.185E+01	1.921E+00		1.236E+01	2.247E+00	4.005E-01	3.072E+01	8.301E-01
TW7	1	Mag	1.105E+01	1.821E+00		1.030E+01	2.455E+00	3.781E-01	3.374E+01	8.284E-01
TW9	1	Mag	5.112E+01	1.028E+01		1.069E+01	1.590E+00	2.065E+00	3.866E+01	7.865E-01
TW10	1	Mag	5.189E+01	9.983E+00		1.071E+01	1.446E+00	7.775E-01	3.806E+01	8.676E-01
TW13	1	Mag	1.221E+01	2.370E+00		9.207E+00	9.677E-01	4.430E-01	4.198E+01	8.527E-01
	Bulk	average	3.901E-01	7.897E-02	3.711E-02	1.743E-01	6.262E-02	1.682E-02	3.711E+01	8.411E-01
		2*std dev	3.622E-01	7.173E-02		9.891E-02	1.195E-01	1.199E-02	5.420E+00	3.766E-02
		count	3	3	1	3	3	3	3	3
	Hematite	average	4.338E+00	7.894E-01		3.946E+00	7.530E-01	2.044E-01	4.927E+01	8.516E-01
		2*std dev	5.270E+00	6.495E-01		4.919E+00	8.361E-01		3.451E+01	7.974E-02
		count	2	3	0	6	3	1	3	5
	Magnetite	average	2.763E+01	5.274E+00		1.065E+01	1.741E+00	8.127E-01	3.663E+01	8.331E-01
		2*std dev	4.361E+01	8.877E+00		2.269E+00	1.214E+00	1.437E+00	8.834E+00	6.141E-02
		count	5	5	0	5	5	5	5	5

Table A2.8 continued

Code	Shot	Method	La/La* _{PAAS}	Pr/Pr* _{PAAS}	Eu/Eu* _{PAAS}	Pr/Yb* _{PAAS}	∑REE
LR1-9	IF	Bulk	1.598E+00	9.616E-01	1.770E+00	2.170E-01	1.088E+01
LR1-23	IF	Bulk	1.527E+00	9.700E-01	1.823E+00	2.287E-01	1.196E+01
DD98-27*	IF	Bulk	2.323E+00	8.907E-01	2.299E+00	2.207E-01	4.971E+00
TW1	1	Hem	1.310E+00	9.726E-01			3.912E+02
TW2	1	Hem	-1.197E+02	8.957E-01			1.044E+01
TW3	1	Hem					0.000E+00
TW4	1	Hem	-6.147E+01	8.624E-01	1.869E+00	2.136E-01	2.834E+02
TW5	1	Hem					6.664E+00
TW8	1	Hem	1.592E+00	9.970E-01		3.172E-01	8.596E+01
TW11	1	Hem					1.564E+00
TW12	1	Hem					8.889E-01
TW6	1	Mag	1.929E+00	9.585E-01	1.906E+00	1.585E-01	2.555E+02
TW7	1	Mag	1.605E+00	9.731E-01	1.590E+00	1.427E-01	2.429E+02
TW9	1	Mag	2.056E+01	9.536E-01		1.763E-02	3.895E+02
TW10	1	Mag	-1.167E+01	8.977E-01	1.722E+00	2.032E-02	4.180E+02
TW13	1	Mag	1.533E+00	9.764E-01	1.594E+00	1.092E-01	2.716E+02
	Bulk	average	1.816E+00	9.408E-01	1.964E+00	2.221E-01	9.270E+00
		2*std dev	8.806E-01	8.712E-02	5.829E-01	1.201E-02	7.524E+00
		count	3	3	3	3	3
	Hematite	average	-4.456E+01	9.319E-01	1.869E+00	2.654E-01	9.752E+01
		2*std dev	1.164E+02	1.267E-01		1.465E-01	3.069E+02
		count	4	4	1	2	8
	Magnetite	average	2.792E+00	9.519E-01	1.703E+00	8.966E-02	3.155E+02
		2*std dev	2.299E+01	6.351E-02	2.974E-01	1.339E-01	1.636E+02
		count	5	5	4	5	5

Note: * indicates a sample that was previously analyzed by bulk digestion but included here.

Table A2.9. Bulk digestion and LA--HRICP-MS analyses for sample 090709-4b2 from the Nuvvuagittuq Supracrustal Belt, Québec, Canada.

Formation	Sample	Code	Shot	Method	Li	B	Mg	Ca	Ti	V
Nuvvuagittuq	090709-4b2	LR1-11	IF	Bulk	5.477E-01		1.588E+04	6.234E+03	5.031E+01	2.970E+00
Nuvvuagittuq	090709-4b2	S1	1	Hem			3.254E+02	1.774E+03	1.440E+02	5.206E+00
Nuvvuagittuq	090709-4b2	S1	2	Hem			6.380E+01	1.562E+03	1.372E+02	5.468E+00
Nuvvuagittuq	090709-4b2	S1	3	Hem			2.414E+02	1.783E+03	1.342E+02	5.273E+00
Nuvvuagittuq	090709-4b2	S2	1	Hem				2.056E+03	1.425E+02	5.779E+00
Nuvvuagittuq	090709-4b2	S2	2	Hem				1.796E+03	1.362E+02	4.618E+00
Nuvvuagittuq	090709-4b2	S2	3	Hem				2.164E+03	1.567E+02	5.570E+00
Nuvvuagittuq	090709-4b2	S3	1	Hem				2.026E+03	1.622E+02	7.238E+00
Nuvvuagittuq	090709-4b2	S3	2	Hem				1.471E+03	1.729E+02	7.393E+00
Nuvvuagittuq	090709-4b2	S3	3	Hem				1.887E+03	1.732E+02	7.295E+00
Nuvvuagittuq	090709-4b2	S4	1	Hem				1.789E+03	1.321E+02	5.106E+00
Nuvvuagittuq	090709-4b2	S4	2	Hem				3.008E+03	1.538E+02	5.143E+00
Nuvvuagittuq	090709-4b2	S4	3	Hem				1.625E+03	1.329E+02	5.175E+00
Nuvvuagittuq	090709-4b2	S5	1	Hem			1.345E+04	3.591E+03	1.538E+02	5.790E+00
Nuvvuagittuq	090709-4b2	S5	2	Hem				2.837E+03	1.539E+02	6.994E+00
Nuvvuagittuq	090709-4b2	S5	3	Hem			1.302E+02	1.520E+03	1.600E+02	6.587E+00
			Bulk	average	5.477E-01		1.588E+04	6.234E+03	5.031E+01	2.970E+00
				2*std dev						
				count		1 0	1	1	1	1
			Hematite	average			2.842E+03	2.059E+03	1.497E+02	5.909E+00
				2*std dev			1.186E+04	1.227E+03	2.782E+01	1.867E+00
				count		0 0	5	15	15	15

Table A2.9 continued

Code	Shot	Method	Cr	Mn	Co	Ni	⁶⁵ Cu	Zn	Ge	Rb
LR1-11	IF	Bulk	1.484E+01	1.095E+03	6.775E+00	4.635E+01	3.324E+00	6.430E+01	6.623E+01	1.893E-01
S1	1	Hem	2.011E+01	1.250E+02	6.502E+00	7.017E+01		3.890E+01	1.529E+01	
S1	2	Hem	2.207E+01	9.909E+01	6.813E+00	7.151E+01		2.416E+01	1.605E+01	
S1	3	Hem	1.990E+01	1.138E+02	6.696E+00	6.870E+01		3.715E+01	1.805E+01	
S2	1	Hem	1.831E+01	9.616E+01	6.744E+00	6.562E+01		2.562E+01	1.663E+01	
S2	2	Hem	3.496E+00	1.020E+02	6.910E+00	6.404E+01		3.983E+01	1.877E+01	
S2	3	Hem	1.060E+01	6.924E+01	6.155E+00	5.850E+01	5.436E+00	1.785E+01	1.750E+01	
S3	1	Hem	8.728E+00	8.623E+01	5.769E+00	5.328E+01		2.440E+01	2.058E+01	
S3	2	Hem	9.557E+00	9.105E+01	5.805E+00	5.529E+01		1.443E+01	2.245E+01	
S3	3	Hem	6.681E+00	9.650E+01	6.089E+00	5.533E+01		1.896E+01	2.314E+01	
S4	1	Hem	8.805E+00	1.119E+02	7.053E+00	6.578E+01		4.085E+01	2.021E+01	
S4	2	Hem	1.073E+01	1.138E+02	6.758E+00	6.811E+01		9.078E+00	2.271E+01	
S4	3	Hem	1.133E+01	1.128E+02	7.158E+00	6.447E+01		4.703E+01	1.999E+01	
S5	1	Hem	1.272E+01	1.350E+03	8.609E+00	7.141E+01		1.131E+02	3.238E+01	
S5	2	Hem	1.713E+01	1.185E+02	7.480E+00	6.731E+01		2.611E+01	2.404E+01	
S5	3	Hem	1.606E+01	1.140E+02	7.151E+00	6.585E+01		2.872E+01	2.847E+01	
	Bulk	average	1.484E+01	1.095E+03	6.775E+00	4.635E+01	3.324E+00	6.430E+01	6.623E+01	1.893E-01
		2*std dev								
		count	1	1	1	1	1	1	1	1
	Hematite	average	1.308E+01	1.867E+02	6.780E+00	6.436E+01	5.436E+00	3.374E+01	2.108E+01	
		2*std dev	1.104E+01	6.445E+02	1.428E+00	1.199E+01	#DIV/0!	4.892E+01	9.380E+00	
		count	15	15	15	15	1	15	15	0

Table A2.9 continued

Code	Shot	Method	Sr	Y	Zr	Mo	Ba	La	Ce	Pr
LR1-11	IF	Bulk	3.994E+00	1.015E+01	5.594E+00	7.692E-01	2.919E-01	1.777E+00	3.365E+00	3.920E-01
S1	1	Hem		9.363E-02		1.883E+00	1.080E+00		1.611E-02	
S1	2	Hem	2.505E+00	1.163E-01	2.413E+01	1.778E+00	1.847E+00		3.118E-02	
S1	3	Hem	2.304E+00	5.628E-01	2.038E+01	2.141E+00	1.734E+00	1.340E-01	1.728E-01	2.438E-02
S2	1	Hem	5.606E+00		2.538E+01	2.090E+00	2.091E+00	3.879E-01	7.105E-01	6.751E-02
S2	2	Hem	2.417E+00		2.392E+01	2.157E+00	1.801E+00			
S2	3	Hem	5.864E+00	6.457E-01	1.761E+01	2.010E+00	1.384E+00	9.642E-01	1.719E+00	1.889E-01
S3	1	Hem	1.992E+00		1.969E+01	2.282E+00	1.630E+00			
S3	2	Hem	2.060E+00	1.075E-01	1.806E+01	2.447E+00	1.767E+00	2.251E-02	3.249E-02	
S3	3	Hem	2.432E+00	3.226E-01	2.041E+01	1.838E+00	1.644E+00		5.931E-02	1.370E-02
S4	1	Hem	1.633E+00			1.748E+00	1.236E+00			
S4	2	Hem	3.709E+00	1.031E+01	2.243E+01	1.709E+00	1.906E+00	5.395E-01	1.260E+00	1.836E-01
S4	3	Hem	2.780E+00		2.506E+01	1.872E+00	1.962E+00			
S5	1	Hem	2.170E+00	2.645E+00	1.941E+01	1.940E+00	1.618E+00	1.029E-01	2.432E-01	3.890E-02
S5	2	Hem	2.272E+00	2.790E-01	2.217E+01	1.720E+00	1.902E+00		8.094E-02	2.239E-02
S5	3	Hem	2.829E+00	5.397E-01	2.403E+01	1.889E+00	1.951E+00	7.749E-02	1.515E-01	2.904E-02
	Bulk	average	3.994E+00	1.015E+01	5.594E+00	7.692E-01	2.919E-01	1.777E+00	3.365E+00	3.920E-01
		2*std dev								
		count	1	1	1	1	1	1	1	1
	Hematite	average	2.898E+00	1.563E+00	2.174E+01	1.967E+00	1.703E+00	3.184E-01	4.070E-01	7.104E-02
		2*std dev	2.590E+00	6.331E+00	5.306E+00	4.355E-01	5.655E-01	6.816E-01	1.157E+00	1.458E-01
		count	14	10	13	15	15	7	11	8

Table A2.9 continued

Code	Shot	Method	Nd	Sm	Eu	Tb	Gd	Dy	Ho	Er
LR1-11	IF	Bulk	1.613E+00	3.908E-01	2.446E-01	1.307E-01	6.474E-01	9.982E-01	2.609E-01	9.076E-01
S1	1	Hem								
S1	2	Hem								
S1	3	Hem								
S2	1	Hem	1.889E-01							
S2	2	Hem								1.686E-02
S2	3	Hem	7.316E-01	1.825E-01	8.883E-02	3.233E-02	1.447E-01	2.049E-01	3.252E-02	8.703E-02
S3	1	Hem								
S3	2	Hem								
S3	3	Hem							1.708E-02	
S4	1	Hem								
S4	2	Hem	1.073E+00	4.061E-01	3.005E-01	1.582E-01	1.016E+00	1.305E+00	3.436E-01	1.159E+00
S4	3	Hem								
S5	1	Hem	2.287E-01	1.014E-01			1.890E-01	2.746E-01	7.715E-02	3.197E-01
S5	2	Hem	1.054E-01							
S5	3	Hem	2.027E-01						2.304E-02	6.057E-02
	Bulk	average	1.613E+00	3.908E-01	2.446E-01	1.307E-01	6.474E-01	9.982E-01	2.609E-01	9.076E-01
		2*std dev								
		count	1	1	1	1	1	1	1	1
	Hematite	average	4.217E-01	2.300E-01	1.946E-01	9.526E-02	4.500E-01	5.948E-01	9.868E-02	3.287E-01
		2*std dev	7.796E-01	3.156E-01	2.993E-01	1.780E-01	9.817E-01	1.232E+00	2.779E-01	9.579E-01
		count	6	3	2	2	3	3	5	5

Table A2.9 continued

Code	Shot	Method	Yb	Lu	Hf	Pb	Th	U	Y/Ho	Ce/Ce* _{PAAS}
LR1-11	IF	Bulk	1.034E+00	1.942E-01		2.511E-01	6.546E-02	9.888E-03	3.891E+01	9.301E-01
S1	1	Hem					3.075E-03			
S1	2	Hem					9.993E-03	1.876E-03		
S1	3	Hem	5.360E-02							6.927E-01
S2	1	Hem					3.417E-02	1.301E-02		1.003E+00
S2	2	Hem								
S2	3	Hem	8.958E-02				1.436E-01	4.267E-02	1.985E+01	9.262E-01
S3	1	Hem			2.906E-02	7.544E+00				
S3	2	Hem				8.281E+00				
S3	3	Hem			3.827E-02	1.969E-01			1.889E+01	
S4	1	Hem				6.046E-01				
S4	2	Hem	6.795E-01	8.933E-02	1.212E-01		4.798E-02	8.834E-03	3.001E+01	9.068E-01
S4	3	Hem								
S5	1	Hem	7.335E-01	1.557E-01			8.294E-02	7.581E-03	3.428E+01	8.608E-01
S5	2	Hem			5.088E-02	4.175E-01	7.984E-02	9.932E-03		
S5	3	Hem	5.905E-02				1.134E-02	3.490E-03	2.343E+01	7.159E-01
	Bulk	average	1.034E+00	1.942E-01		2.511E-01	6.546E-02	9.888E-03	3.891E+01	9.301E-01
		2*std dev								
		count	1	1	0	1	1	1	1	1
	Hematite	average	3.231E-01	1.225E-01	5.986E-02	3.409E+00	5.161E-02	1.248E-02	2.529E+01	8.509E-01
		2*std dev	7.017E-01	9.391E-02	8.377E-02	8.244E+00	9.640E-02	2.768E-02	1.331E+01	2.453E-01
		count	5	2	4	5	8	7	5	6

Table A2.9 continued

Code	Shot	Method	La/La* _{PAAS}	Pr/Pr* _{PAAS}	Eu/Eu* _{PAAS}	Pr/Yb* _{PAAS}	∑REE
LR1-11	IF	Bulk	1.222E+00	9.883E-01	2.188E+00	1.211E-01	2.211E+01
S1	1	Hem					1.097E-01
S1	2	Hem					1.475E-01
S1	3	Hem				1.453E-01	9.476E-01
S2	1	Hem	8.610E-01	1.055E+00			1.355E+00
S2	2	Hem					1.686E-02
S2	3	Hem	1.202E+00	9.908E-01	2.290E+00	6.733E-01	5.112E+00
S3	1	Hem					0.000E+00
S3	2	Hem					1.625E-01
S3	3	Hem					4.126E-01
S4	1	Hem					0.000E+00
S4	2	Hem	-1.497E+01	8.756E-01	2.373E+00	8.627E-02	1.883E+01
S4	3	Hem					0.000E+00
S5	1	Hem	-9.739E+00	8.989E-01		1.694E-02	5.110E+00
S5	2	Hem		1.229E+00			4.878E-01
S5	3	Hem	-9.707E-01	8.346E-01		1.571E-01	1.143E+00
	Bulk	average	1.222E+00	9.883E-01	2.188E+00	1.211E-01	2.211E+01
		2*std dev					
		count	1	1	1	1	1
	Hematite	average	-4.724E+00	9.806E-01	2.331E+00	2.158E-01	2.255E+00
		2*std dev	1.451E+01	2.915E-01	1.169E-01	5.235E-01	9.782E+00
		count	5	6	2	5	15

Table A2.10. Bulk digestion and LA-HR-ICP-MS analyses for sample 090709-5 from the Nuvvuagittuq Supracrustal Belt, Québec, Canada.

Formation	Sample	Code	Shot	Method	Li	B	Mg	Ca	Ti	V
Nuvvuagittuq	090709-5	LR1-3	IF	Bulk	5.385E-01		7.334E+03	1.006E+03	3.860E+01	2.596E+00
Nuvvuagittuq	090709-5	LR1-24	IF	Bulk	3.487E-01		7.004E+03	8.763E+02	3.720E+01	2.338E+00
Nuvvuagittuq	090709-5	S1	1	Hem	8.494E+00			3.283E+03	1.150E+02	2.614E+00
Nuvvuagittuq	090709-5	S1	2	Hem	4.419E+00			3.573E+03	7.094E+01	2.771E+00
Nuvvuagittuq	090709-5	S1	3	Hem	4.492E+00			2.501E+03	6.746E+01	2.739E+00
Nuvvuagittuq	090709-5	S2	1	Hem	3.992E+00				6.701E+01	2.856E+00
Nuvvuagittuq	090709-5	S2	2	Hem	1.999E+00		1.083E+02	3.715E+03	1.238E+02	2.778E+00
Nuvvuagittuq	090709-5	S2	3	Hem	1.345E+00			3.470E+03	1.120E+02	2.957E+00
Nuvvuagittuq	090709-5	S3	1	Hem	1.044E+00			3.586E+03	1.403E+02	3.628E+00
Nuvvuagittuq	090709-5	S3	2	Hem	2.336E-01			2.444E+03	1.335E+02	3.777E+00
Nuvvuagittuq	090709-5	S3	3	Hem				2.446E+03	1.391E+02	3.081E+00
Nuvvuagittuq	090709-5	S4	1	Hem			7.842E+03	3.420E+03	1.269E+02	5.640E+00
Nuvvuagittuq	090709-5	S4	2	Hem				3.192E+03	1.610E+02	6.787E+00
Nuvvuagittuq	090709-5	S4	3	Hem		8.562E+00	4.508E+03	3.217E+03	1.934E+02	5.823E+00
Nuvvuagittuq	090709-5	S5	1	Hem			6.460E+02	2.117E+03	2.163E+02	9.910E+00
Nuvvuagittuq	090709-5	S5	2	Hem					2.539E+02	1.035E+01
Nuvvuagittuq	090709-5	S5	3	Hem				2.108E+03	2.369E+02	1.067E+01
Nuvvuagittuq	090709-5	TW1	1	Hem			3.665E+03	6.156E+04	1.110E+04	6.979E+02
Nuvvuagittuq	090709-5	TW2	1	Hem			6.233E+03	5.002E+04	5.557E+03	3.049E+02
Nuvvuagittuq	090709-5	TW3	1	Hem			4.040E+03		4.445E+03	2.836E+02
Nuvvuagittuq	090709-5	TW4	1	Hem			3.019E+03	5.595E+04	9.505E+03	6.100E+02
Nuvvuagittuq	090709-5	TW5	1	Hem			5.260E+03	6.163E+04	1.464E+04	1.097E+03
Nuvvuagittuq	090709-5	TW6	1	Hem			2.465E+03	4.396E+04	1.152E+04	8.238E+02
Nuvvuagittuq	090709-5	TW7	1	Hem			2.829E+03	8.384E+04	1.068E+04	8.542E+02
Nuvvuagittuq	090709-5	TW8	1	Hem			4.482E+03	6.238E+04	9.366E+03	7.468E+02
Nuvvuagittuq	090709-5	TW9	1	Hem			6.009E+03	4.401E+04	1.044E+04	8.981E+02
Nuvvuagittuq	090709-5	TW10	1	Hem			2.906E+03	5.967E+04	1.021E+04	9.809E+02
Nuvvuagittuq	090709-5	TW11	1	Hem			4.370E+03	6.427E+04	2.833E+03	2.235E+02
Nuvvuagittuq	090709-5	TW12	1	Hem			2.593E+03	4.556E+04	3.925E+03	2.801E+02
Nuvvuagittuq	090709-5	TW13	1	Hem			9.640E+03	5.572E+04	4.549E+03	2.658E+02

Nuvvuagittuq	090709-5	TW14	1	Hem			8.167E+03	7.625E+03	9.310E+02		
Nuvvuagittuq	090709-5	TW15	1	Hem	2.260E+07	1.380E+05			3.647E+06		
Nuvvuagittuq	090709-5	TW16	1	Hem				8.783E+04			
Nuvvuagittuq	090709-5	TW17	1	Hem							
Nuvvuagittuq	090709-5	TW18	1	Hem							
Nuvvuagittuq	090709-5	TW19	1	Hem							
Nuvvuagittuq	090709-5	TW20	1	Mag							
Nuvvuagittuq	090709-5	TW21	1	Mag							
Nuvvuagittuq	090709-5	TW22	1	Mag					3.572E+00		
Nuvvuagittuq	090709-5	TW23	1	Mag							
Nuvvuagittuq	090709-5	TW24	1	Mag							
Nuvvuagittuq	090709-5	TW25	1	Mag							
Nuvvuagittuq	090709-5	TW26	1	Mag							
				Bulk	average	4.436E-01	7.169E+03	9.412E+02	3.790E+01	2.467E+00	
					2*std dev	2.684E-01	4.669E+02	1.836E+02	1.991E+00	3.650E-01	
					count	2	0	2	2	2	
				Hematite	average	2.511E+06	6.902E+04	4.377E+03	2.911E+04	6.880E+03	1.219E+05
					2*std dev	1.507E+07	1.952E+05	5.017E+03	5.748E+04	3.200E+04	1.331E+06
					count	9	2	18	25	30	30
				magnetite	average						3.572E+00
					2*std dev						
					count	0	0	0	0	0	1

Table A2.10 continued

Code	Shot	Method	Cr	Mn	Co	Ni	⁶⁵Cu	Zn	Ge	Rb
LR1-3	IF	Bulk	1.652E+01	6.393E+02	7.494E+00	4.160E+01	5.996E+00	4.730E+01	4.571E+01	4.437E-01
LR1-24	IF	Bulk	1.535E+01	5.588E+02	6.619E+00	3.884E+01	5.907E+00	4.546E+01	6.010E+01	4.286E-01
S1	1	Hem	4.559E+00	6.632E+01	9.173E+00	1.239E+02		3.445E+01		
S1	2	Hem	6.259E+00	9.727E+01	8.761E+00	1.285E+02		2.816E+01		
S1	3	Hem	6.555E+00	7.782E+01	9.816E+00	1.297E+02		5.670E+01		
S2	1	Hem	5.443E+00	6.845E+01	6.542E+00	1.532E+02		2.953E+01		
S2	2	Hem		1.679E+02	1.020E+01	1.719E+02		6.169E+01		
S2	3	Hem	7.265E+00	8.562E+01	7.319E+00	2.660E+02		5.620E+01		
S3	1	Hem	6.859E+00	5.997E+01	8.193E+00			2.662E+01		
S3	2	Hem		7.901E+01	7.046E+00			2.087E+01		
S3	3	Hem	4.596E+00	5.191E+01	7.994E+00	3.105E+01		4.838E+01	1.250E+00	
S4	1	Hem	1.259E+01	9.355E+02	1.084E+01	5.677E+01		1.290E+02	4.337E+00	
S4	2	Hem	2.166E+01	6.071E+01	7.510E+00	6.220E+01		3.924E+01	4.790E+00	
S4	3	Hem	1.369E+01	6.127E+02	1.093E+01	7.227E+01		1.097E+02	8.253E+00	1.969E+00
S5	1	Hem	9.985E+00	9.888E+01	7.892E+00	6.282E+01		5.198E+01	1.094E+01	
S5	2	Hem	1.034E+01	6.820E+01	7.514E+00	7.751E+01		4.767E+01	1.419E+01	
S5	3	Hem	1.764E+01	6.830E+01	8.099E+00	7.468E+01		2.423E+01	1.516E+01	
TW1	1	Hem	5.250E+02	4.560E+03	4.695E+02	6.353E+03		2.065E+03	1.486E+03	
TW2	1	Hem	8.270E+02	4.103E+03	4.754E+02	7.057E+03		6.768E+03	2.033E+03	
TW3	1	Hem	3.633E+02	5.458E+03	6.982E+02	6.671E+03		3.061E+03	1.740E+03	
TW4	1	Hem	5.386E+02	4.267E+03	6.061E+02	6.911E+03		1.416E+03	1.633E+03	
TW5	1	Hem	2.102E+03	3.688E+03	5.613E+02	6.230E+03		4.176E+03	1.310E+03	
TW6	1	Hem	1.002E+03	4.467E+03	5.731E+02	6.084E+03		5.738E+03	1.444E+03	
TW7	1	Hem	6.854E+02	3.764E+03	4.411E+02	6.806E+03		2.624E+03	1.867E+03	
TW8	1	Hem	2.042E+02	3.288E+03	4.543E+02	6.807E+03		1.728E+03	1.724E+03	
TW9	1	Hem	1.529E+03	4.298E+03	5.903E+02	6.455E+03		3.550E+03	1.623E+03	
TW10	1	Hem	5.469E+02	2.943E+03	3.286E+02	5.812E+03		2.263E+03	1.422E+03	
TW11	1	Hem	5.858E+02	7.897E+03	7.409E+02	6.518E+03		1.628E+03	1.929E+03	
TW12	1	Hem	2.990E+02	3.714E+03	4.947E+02	5.279E+03		5.232E+03	1.421E+03	
TW13	1	Hem	8.188E+02	4.375E+03	4.808E+02	5.486E+03		3.224E+03	1.357E+03	
TW14	1	Hem	1.708E+03	1.943E+04	2.118E+03	1.502E+04		1.282E+04	2.195E+03	

TW15	1	Hem			4.857E+06		7.849E+06	3.260E+06	7.324E+05	
TW16	1	Hem					8.092E+02	2.796E+03	3.328E+01	
TW17	1	Hem					2.423E+01	7.056E+03	9.419E+00	
TW18	1	Hem					1.501E+01	7.893E+03		
TW19	1	Hem					1.136E+01	1.150E+04	1.999E+00	
TW20	1	Mag	1.027E+00					2.069E+04		
TW21	1	Mag					8.829E+00	3.230E+04		
TW22	1	Mag	5.948E+00				1.745E-01	8.303E+04		
TW23	1	Mag					3.304E+01			
TW24	1	Mag								
TW25	1	Mag								
TW26	1	Mag								
<hr/>										
	Bulk	average	1.593E+01	5.991E+02	7.056E+00	4.022E+01	5.951E+00	4.638E+01	5.290E+01	4.361E-01
		2*std								
		dev	1.661E+00	1.138E+02	1.237E+00	3.900E+00	1.256E-01	2.607E+00	2.035E+01	2.141E-02
		count	2	2	2	2	2	2	2	2
	Hematite	average	4.393E+02	2.719E+03	1.622E+05	3.663E+03	1.570E+06	1.968E+03	1.274E+05	1.465E+05
		2*std								
		dev	1.161E+03	7.847E+03	1.773E+06	7.749E+03	7.020E+06	5.757E+03	1.278E+06	6.551E+05
		count	27	29	30	27	5	29	26	5
	magnetite	average	3.488E+00				1.401E+01		4.534E+04	
		2*std								
		dev	6.959E+00				3.407E+01		6.630E+04	
		count	2	0	0	0	3	0	3	0
<hr/>										

Table A2.10 continued

Code	Shot	Method	Sr	Y	Zr	Mo	Ba	La	Ce	Pr
LR1-3	IF	Bulk	3.432E-01	6.291E+00	6.061E+00	8.476E-01	1.944E-01	1.205E+00	1.913E+00	2.085E-01
LR1-24	IF	Bulk	3.537E-01	7.235E+00	6.460E+00	6.786E-01	1.935E-01	1.154E+00	1.844E+00	2.034E-01
S1	1	Hem	3.095E+00		2.578E+01	1.823E+00	2.173E+00			
S1	2	Hem	2.732E+00	1.679E+00	3.274E+01		2.984E+00	1.496E-01	4.198E-01	7.877E-02
S1	3	Hem	3.104E+00		2.788E+01	1.757E+00	2.691E+00			
S2	1	Hem								
S2	2	Hem	4.251E+00		3.592E+01		3.910E+00			
S2	3	Hem	3.107E+00	5.896E-01	2.579E+01		2.493E+00	4.904E-02	1.377E-01	3.613E-02
S3	1	Hem	3.396E+00		3.061E+01		2.834E+00			
S3	2	Hem	3.206E+00		3.400E+01	1.661E+00	2.456E+00			
S3	3	Hem	3.071E+00	2.115E+00	2.471E+01	1.998E+00	1.874E+00	1.897E-01	4.943E-01	7.390E-02
S4	1	Hem	3.675E+00	4.016E+00	3.033E+01		3.138E+00	3.475E-01	5.326E-01	5.272E-02
S4	2	Hem	3.012E+00		2.504E+01	1.869E+00	3.065E+00			
S4	3	Hem	3.041E+00	2.000E+00	2.693E+01		2.470E+00	1.260E+00	1.240E+00	9.851E-02
S5	1	Hem	3.313E+00	4.449E-01	2.620E+01		2.570E+00	4.726E-02	8.394E-02	
S5	2	Hem	2.628E+00	3.647E-01	2.672E+01	1.968E+00	2.312E+00			
S5	3	Hem	3.404E+00	4.367E-01	2.254E+01	1.707E+00	2.501E+00	3.077E-02	8.236E-02	
TW1	1	Hem	5.943E+01		6.442E+02	1.455E+02	4.608E+01	9.920E-01		
TW2	1	Hem	4.896E+01	1.169E+01	5.322E+02	1.492E+02	3.822E+01	1.473E+00	3.189E+00	4.901E-01
TW3	1	Hem	3.746E+01		3.762E+02	1.256E+02				
TW4	1	Hem	4.018E+01		3.952E+02	1.403E+02	3.117E+01			
TW5	1	Hem	4.995E+01	1.189E+01	4.793E+02	1.248E+02	3.588E+01	8.170E+00	7.082E+00	
TW6	1	Hem	4.041E+01	1.032E+01	4.559E+02	1.139E+02	3.129E+01	7.061E+00	6.104E+00	5.303E-01
TW7	1	Hem	5.451E+01		5.775E+02	1.423E+02	4.505E+01		7.908E-01	
TW8	1	Hem	5.465E+01	8.826E+00	5.671E+02	1.417E+02	4.174E+01	1.017E+00	3.346E+00	5.685E-01
TW9	1	Hem	4.211E+01	3.645E+00	4.684E+02	1.398E+02	3.255E+01		8.712E-01	
TW10	1	Hem	7.118E+01		6.061E+02	1.189E+02	4.925E+01			
TW11	1	Hem	4.469E+01		4.528E+02	1.295E+02	4.470E+01			
TW12	1	Hem	5.832E+01	3.360E+00	5.773E+02	1.083E+02	4.467E+01	5.759E+00	5.138E+00	
TW13	1	Hem	6.516E+01	8.232E+00	6.795E+02	1.037E+02	5.745E+01	9.593E-01	2.059E+00	4.432E-01
TW14	1	Hem		2.076E+01		4.090E+02		2.331E+01	2.959E+01	2.481E+00
TW15	1	Hem							6.827E+04	

TW16	1	Hem								
TW17	1	Hem								4.060E-02
TW18	1	Hem								
TW19	1	Hem								4.115E-02
TW20	1	Mag								
TW21	1	Mag								
TW22	1	Mag								
TW23	1	Mag								
TW24	1	Mag								
TW25	1	Mag								
TW26	1	Mag								
	Bulk	average	3.485E-01	6.763E+00	6.260E+00	7.631E-01	1.939E-01	1.180E+00	1.878E+00	2.059E-01
		2*std								
		dev	1.481E-02	1.334E+00	5.639E-01	2.390E-01	1.262E-03	7.189E-02	9.730E-02	7.221E-03
		count	2	2	2	2	2	2	2	2
	Hematite	average	2.637E+01	5.647E+00	2.669E+02	1.002E+02	2.060E+01	3.388E+00	4.020E+03	4.112E-01
		2*std								
		dev	5.097E+01	1.159E+01	5.208E+02	1.881E+02	4.088E+01	1.228E+01	3.311E+04	1.375E+00
		count	27	16	27	21	26	15	17	12
	magnetite	average								
		2*std								
		dev								
		count	0	0	0	0	0	0	0	0

Table A2.10 continued

Code	Shot	Method	Nd	Sm	Eu	Tb	Gd	Dy	Ho	Er
LR1-3	IF	Bulk	8.625E-01	2.542E-01	2.239E-01	9.211E-02	4.133E-01	7.447E-01	2.005E-01	7.253E-01
LR1-24	IF	Bulk	8.290E-01	2.452E-01	2.143E-01	9.546E-02	4.352E-01	7.583E-01	2.013E-01	7.335E-01
S1	1	Hem								
S1	2	Hem	4.116E-01	1.185E-01	1.067E-01	4.548E-02	2.557E-01	3.150E-01	6.791E-02	2.198E-01
S1	3	Hem								
S2	1	Hem								
S2	2	Hem								
S2	3	Hem	1.272E-01	6.903E-02					2.296E-02	8.107E-02
S3	1	Hem								
S3	2	Hem								
S3	3	Hem	3.969E-01	1.714E-01	1.198E-01	4.515E-02	4.556E-01	4.513E-01	7.712E-02	2.489E-01
S4	1	Hem				3.466E-02	1.705E-01	3.644E-01	1.175E-01	4.992E-01
S4	2	Hem								
S4	3	Hem	3.255E-01	9.971E-02		2.054E-02		1.874E-01	5.808E-02	3.206E-01
S5	1	Hem								
S5	2	Hem								2.041E-02
S5	3	Hem						6.031E-02	1.935E-02	6.860E-02
TW1	1	Hem								
TW2	1	Hem								
TW3	1	Hem								
TW4	1	Hem								
TW5	1	Hem								
TW6	1	Hem	2.564E+00						4.009E-01	2.448E+00
TW7	1	Hem	1.071E+00							
TW8	1	Hem								
TW9	1	Hem								
TW10	1	Hem								
TW11	1	Hem								
TW12	1	Hem								
TW13	1	Hem								
TW14	1	Hem								
TW15	1	Hem			4.468E+05			1.387E+05	2.097E+04	

TW16	1	Hem				2.220E-01		2.043E+00		
TW17	1	Hem	7.637E-01	3.788E-01			9.419E-02	2.773E-01	2.454E-02	
TW18	1	Hem								
TW19	1	Hem	1.536E-01	1.867E-01				1.048E-01		4.035E-03
TW20	1	Mag								
TW21	1	Mag								
TW22	1	Mag								
TW23	1	Mag								
TW24	1	Mag								
TW25	1	Mag								
TW26	1	Mag								
	Bulk	average	8.457E-01	2.497E-01	2.191E-01	9.378E-02	4.243E-01	7.515E-01	2.009E-01	7.294E-01
		2*std								
		dev	4.740E-02	1.274E-02	1.353E-02	4.738E-03	3.095E-02	1.926E-02	1.042E-03	1.157E-02
		count	2	2	2	2	2	2	2	2
	Hematite	average	8.160E-01	2.293E-01	8.936E+04	7.357E-02	2.440E-01	1.541E+04	2.330E+03	4.345E-01
		2*std								
		dev	1.828E+00	5.287E-01	3.996E+05	1.672E-01	3.114E-01	9.247E+04	1.398E+04	1.544E+00
		count	6	6	5	5	4	9	9	9
	magnetite	average								
		2*std								
		dev								
		count	0	0	0	0	0	0	0	0

Table A2.10 continued

Code	Shot	Method	Yb	Lu	Hf	Pb	Th	U	Y/Ho	Ce/Ce* _{PAAS}
LR1-3	IF	Bulk	8.872E-01	1.652E-01		7.574E-02	5.351E-02	1.646E-02	3.137E+01	8.712E-01
LR1-24	IF	Bulk	8.927E-01	1.669E-01		7.957E-02	6.107E-02	1.883E-02	3.595E+01	8.700E-01
S1	1	Hem			2.767E-02					
S1	2	Hem	1.653E-01		3.036E-02		6.626E-03	1.285E-02	2.472E+01	8.216E-01
S1	3	Hem								
S2	1	Hem								
S2	2	Hem			2.685E-02					
S2	3	Hem							2.568E+01	6.436E-01
S3	1	Hem			2.776E-02					
S3	2	Hem			2.313E-02					
S3	3	Hem	1.932E-01	3.750E-02			6.360E-03	1.410E-02	2.743E+01	9.313E-01
S4	1	Hem	1.134E+00	2.317E-01	2.373E-02		2.937E-02	1.933E-02	3.419E+01	8.882E-01
S4	2	Hem								
S4	3	Hem	4.648E-01	9.789E-02				6.218E-03	3.443E+01	7.057E-01
S5	1	Hem					4.907E-03			
S5	2	Hem		8.640E-03	1.774E-02		1.503E-02	3.927E-03		
S5	3	Hem					3.925E-02		2.256E+01	
TW1	1	Hem						4.389E-01		
TW2	1	Hem						6.442E-01		8.519E-01
TW3	1	Hem						3.159E-01		
TW4	1	Hem								
TW5	1	Hem	4.592E+00							
TW6	1	Hem		7.068E-01					2.574E+01	6.262E-01
TW7	1	Hem								
TW8	1	Hem								9.239E-01
TW9	1	Hem								
TW10	1	Hem								
TW11	1	Hem								
TW12	1	Hem								
TW13	1	Hem					1.238E+00	6.940E-01		6.869E-01
TW14	1	Hem			5.189E+00					8.344E-01

TW15	1	Hem			6.618E+05	6.437E+05		7.077E+03		
TW16	1	Hem		3.689E-01			1.350E+00			
TW17	1	Hem		1.084E-01		1.420E-01				
TW18	1	Hem								
TW19	1	Hem	8.354E-02			1.085E-01	3.208E-02	3.522E-03		
TW20	1	Mag								
TW21	1	Mag					1.444E-02			
TW22	1	Mag								
TW23	1	Mag			1.069E-01	2.237E-01	1.880E-02			
TW24	1	Mag					1.575E-03			
TW25	1	Mag								
TW26	1	Mag								
	Bulk	average	8.900E-01	1.661E-01		7.765E-02	5.729E-02	1.764E-02	3.366E+01	8.706E-01
		2*std								
		dev	7.805E-03	2.413E-03		5.416E-03	1.070E-02	3.358E-03	6.467E+00	1.741E-03
		count	2	2	0	2	2	2	2	2
	Hematite	average	1.105E+00	2.228E-01	7.353E+04	2.146E+05	3.024E-01	6.435E+02	2.782E+01	7.914E-01
		2*std								
		dev	3.501E+00	4.930E-01	4.412E+05	7.432E+05	1.126E+00	4.267E+03	9.328E+00	2.313E-01
		count	6	7	9	3	9	11	7	10
	magnetite	average			1.069E-01	2.237E-01	1.160E-02			
		2*std								
		dev					1.791E-02			
		count	0	0	1	1	3	0	0	0

Table A2.10 continued

Code	Shot	Method	La/La* _{PAAS}	Pr/Pr* _{PAAS}	Eu/Eu* _{PAAS}	Pr/Yb* _{PAAS}	∑REE
LR1-3	IF	Bulk	1.581E+00	9.546E-01	2.944E+00	7.505E-02	1.419E+01
LR1-24	IF	Bulk	1.496E+00	9.674E-01	2.804E+00	7.276E-02	1.501E+01
S1	1	Hem					0.000E+00
S1	2	Hem	1.579E+00	1.025E+00	2.912E+00	1.522E-01	4.033E+00
S1	3	Hem					0.000E+00
S2	1	Hem					0.000E+00
S2	2	Hem					0.000E+00
S2	3	Hem	2.692E-01	1.493E+00			1.113E+00
S3	1	Hem					0.000E+00
S3	2	Hem					0.000E+00
S3	3	Hem	2.936E+00	9.342E-01	2.765E+00	1.221E-01	5.070E+00
S4	1	Hem				1.484E-02	7.501E+00
S4	2	Hem					0.000E+00
S4	3	Hem	2.313E+00	8.861E-01		6.769E-02	6.173E+00
S5	1	Hem					5.761E-01
S5	2	Hem					3.938E-01
S5	3	Hem					6.981E-01
TW1	1	Hem					9.920E-01
TW2	1	Hem					1.684E+01
TW3	1	Hem					0.000E+00
TW4	1	Hem					0.000E+00
TW5	1	Hem					3.173E+01
TW6	1	Hem	6.401E+00	7.885E-01			3.014E+01
TW7	1	Hem					1.861E+00
TW8	1	Hem					1.376E+01
TW9	1	Hem					4.516E+00
TW10	1	Hem					0.000E+00
TW11	1	Hem					0.000E+00
TW12	1	Hem					1.426E+01
TW13	1	Hem					1.169E+01
TW14	1	Hem					7.613E+01

TW15	1	Hem					6.747E+05
TW16	1	Hem					2.633E+00
TW17	1	Hem					1.687E+00
TW18	1	Hem					0.000E+00
TW19	1	Hem			1.573E-01		5.738E-01
TW20	1	Mag					0.000E+00
TW21	1	Mag					0.000E+00
TW22	1	Mag					0.000E+00
TW23	1	Mag					0.000E+00
TW24	1	Mag					0.000E+00
TW25	1	Mag					0.000E+00
TW26	1	Mag					0.000E+00
	Bulk	average	1.539E+00	9.610E-01	2.874E+00	7.390E-02	1.460E+01
		2*std					
		dev	1.201E-01	1.819E-02	1.986E-01	3.239E-03	1.162E+00
		count	2	2	2	2	2
	Hematite	average	2.700E+00	1.025E+00	2.838E+00	1.028E-01	1.985E+04
		2*std					
		dev	4.590E+00	5.496E-01	2.077E-01	1.214E-01	2.314E+05
		count	5	5	2	5	34
	magnetite	average					0.000E+00
		2*std					
		dev					0.000E+00
		count	0	0	0	0	7

Table A2.11. Bulk digestion and LA-HR-ICP-MS analyses for sample 090710-2 from the Nuvvuagittuq Supracrustal Belt, Québec, Canada.

Formation	Sample	Code	Shot	Method	Li	B	Mg	Ca	Ti	V
Nuvvuagittuq	090710-2	LR1-7	IF	Bulk	8.634E-01		2.124E+04	2.503E+03	1.009E+02	7.246E+00
Nuvvuagittuq	090710-2	LR1-10	IF	Bulk	3.347E-01		1.560E+04	6.956E+03	2.613E+01	1.711E+00
Nuvvuagittuq	090710-2	S1	1	Hem				2.034E+03	1.250E+02	5.070E+00
Nuvvuagittuq	090710-2	S1	2	Hem			6.380E+01	2.064E+03	1.211E+02	5.020E+00
Nuvvuagittuq	090710-2	S1	3	Hem			5.573E+01	2.282E+03	1.190E+02	5.144E+00
Nuvvuagittuq	090710-2	S2	1	Hem			4.017E+02	2.044E+03	1.239E+02	5.370E+00
Nuvvuagittuq	090710-2	S2	2	Hem			6.591E+01	2.009E+03	1.199E+02	5.130E+00
Nuvvuagittuq	090710-2	S2	3	Hem			8.339E+01	2.305E+03	1.230E+02	4.983E+00
Nuvvuagittuq	090710-2	S3	1	Hem			5.911E+01	1.805E+03	1.145E+02	5.674E+00
Nuvvuagittuq	090710-2	S3	2	Hem			6.626E+01	1.743E+03	1.183E+02	5.572E+00
Nuvvuagittuq	090710-2	S3	3	Hem			4.073E+02	2.036E+03	1.100E+02	5.141E+00
Nuvvuagittuq	090710-2	S4	1	Hem		3.291E+00	1.626E+04	3.067E+03	9.049E+01	4.108E+00
Nuvvuagittuq	090710-2	S4	2	Hem		5.891E+00	2.611E+04	1.083E+05	1.233E+02	4.139E+00
Nuvvuagittuq	090710-2	S4	3	Hem				1.508E+03	9.027E+01	5.024E+00
Nuvvuagittuq	090710-2	S5	1	Hem			4.228E+02	1.760E+03	1.076E+02	4.482E+00
Nuvvuagittuq	090710-2	S5	2	Hem		1.600E+01	2.819E+04	4.115E+03	8.882E+01	3.147E+00
Nuvvuagittuq	090710-2	S5	3	Hem		2.992E+00	7.927E+03	2.363E+03	1.039E+02	4.071E+00
Nuvvuagittuq	090710-2	S6	1	Hem			4.507E+01	1.362E+03	9.857E+01	4.171E+00
Nuvvuagittuq	090710-2	S6	2	Hem			8.173E+01	1.317E+03	9.686E+01	4.081E+00
Nuvvuagittuq	090710-2	S6	3	Hem			6.973E+01	1.168E+03	9.944E+01	4.257E+00
Nuvvuagittuq	090710-2	TW1	1	Hem			2.195E+03	5.840E+04	6.332E+03	4.872E+02
Nuvvuagittuq	090710-2	TW2	1	Hem			4.471E+03	7.003E+04	6.313E+03	4.292E+02
Nuvvuagittuq	090710-2	TW3	1	Hem			7.578E+04	6.003E+05	6.277E+03	3.621E+02
Nuvvuagittuq	090710-2	TW4	1	Hem			1.244E+03		3.560E+03	2.585E+02
Nuvvuagittuq	090710-2	TW5	1	Hem			2.149E+03	4.306E+04	3.626E+03	2.043E+02
Nuvvuagittuq	090710-2	TW6	1	Hem			3.497E+03	9.438E+04	3.794E+03	1.891E+02
Nuvvuagittuq	090710-2	TW7	1	Hem			7.255E+03	5.669E+04	3.002E+03	1.481E+02
Nuvvuagittuq	090710-2	TW8	1	Hem			3.119E+03	4.048E+04	2.873E+03	1.590E+02
Nuvvuagittuq	090710-2	TW9	1	Hem			1.849E+03		2.433E+03	1.472E+02
Nuvvuagittuq	090710-2	TW10	1	Hem			3.190E+03	5.184E+04	2.616E+03	1.410E+02

Nuvvuagittuq	090710-2	TW11	1	Hem	5.516E+01	1.626E+05	4.658E+04	2.890E+03	1.754E+02
Nuvvuagittuq	090710-2	TW12	1	Hem		1.785E+03		3.514E+03	2.300E+02
Nuvvuagittuq	090710-2	TW13	1	Hem		2.627E+03	6.302E+04	3.165E+03	1.361E+02
Nuvvuagittuq	090710-2	TW14	1	Hem	5.995E+02	6.984E+06	2.347E+07	3.234E+03	
Nuvvuagittuq	090710-2	TW16	1	Hem		6.930E+03	7.893E+04	7.849E+03	4.845E+02
Nuvvuagittuq	090710-2	TW18	1	Hem		4.209E+04	1.077E+05	8.671E+03	5.101E+02
Nuvvuagittuq	090710-2	TW21	1	Hem		8.441E+03	1.510E+06	9.363E+03	5.848E+02
Nuvvuagittuq	090710-2	TW22	1	Hem		1.625E+04	1.620E+05	1.152E+04	6.937E+02
Nuvvuagittuq	090710-2	TW23	1	Hem		3.243E+05	2.710E+05	1.480E+04	1.107E+03
Nuvvuagittuq	090710-2	TW25	1	Hem			1.123E+06	2.939E+04	2.429E+03
Nuvvuagittuq	090710-2	TW17	1	Mag		5.988E+06	5.510E+05		5.563E+01
Nuvvuagittuq	090710-2	TW24	1	Mag	1.222E+04	2.782E+08	3.566E+06		
Nuvvuagittuq	090710-2	TW26	1	Mag	2.447E+04		6.671E+07	2.394E+04	3.973E+03
		Bulk		average	5.991E-01	1.842E+04	4.729E+03	6.349E+01	4.478E+00
				2*std dev	7.476E-01	7.969E+03	6.297E+03	1.057E+02	7.828E+00
				count	2	0	2	2	2
		Hematite		average	1.138E+02	2.210E+05	7.999E+05	3.610E+03	2.422E+02
				2*std dev	4.775E+02	2.357E+06	7.917E+06	1.127E+04	8.922E+02
				count	0	6	35	35	38
		Magnetite		average	1.835E+04	1.421E+08	2.361E+07	2.394E+04	2.014E+03
				2*std dev	1.733E+04	3.849E+08	7.471E+07		5.540E+03
				count	0	2	2	3	1

Table A2.11 continued

Code	Shot	Method	Cr	Mn	Co	Ni	⁶⁵Cu	Zn	Ge	Rb
LR1-7	IF	Bulk	2.134E+01	3.567E+03	1.971E+01	8.229E+01	5.633E+01	5.165E+01	2.559E+01	2.979E-01
LR1-10	IF	Bulk	1.588E+01	1.271E+03	7.598E+00	3.067E+01	8.138E-01	5.718E+01	6.156E+01	1.676E-01
S1	1	Hem	1.024E+01	1.076E+02	7.951E+00	5.022E+01		3.091E+01	2.049E+01	
S1	2	Hem	7.972E+00	1.226E+02	8.552E+00	5.077E+01		3.862E+01	1.943E+01	
S1	3	Hem	1.162E+01	1.130E+02	8.242E+00	5.037E+01		2.933E+01	1.906E+01	
S2	1	Hem	1.009E+01	1.311E+02	7.986E+00	5.128E+01		3.099E+01	2.031E+01	
S2	2	Hem	1.162E+01	1.039E+02	6.879E+00	4.912E+01		3.286E+01	1.891E+01	
S2	3	Hem	1.031E+01	1.258E+02	6.550E+00	5.042E+01		3.558E+01	1.857E+01	
S3	1	Hem	1.109E+01	1.256E+02	8.198E+00	4.963E+01	1.668E+01	4.547E+01	1.944E+01	
S3	2	Hem	1.351E+01	1.296E+02	7.924E+00	4.862E+01		2.586E+01	1.846E+01	
S3	3	Hem	1.043E+01	1.529E+02	6.553E+00	4.790E+01	2.224E+01	1.941E+01	2.018E+01	
S4	1	Hem	1.431E+01	2.034E+03	1.003E+01	4.930E+01		9.586E+01	2.561E+01	4.480E-01
S4	2	Hem	1.032E+01	1.451E+03	1.211E+01	5.470E+01		6.085E+01	2.651E+01	
S4	3	Hem	1.942E+01	1.168E+02	7.740E+00	4.769E+01		2.502E+01	1.828E+01	
S5	1	Hem	1.040E+01	1.637E+02	6.854E+00	4.765E+01		4.882E+01	2.007E+01	
S5	2	Hem	5.106E+00	2.896E+03	1.351E+01	5.035E+01	4.006E+00	1.750E+02	3.068E+01	6.543E-01
S5	3	Hem	8.018E+00	8.846E+02	8.796E+00	4.777E+01		4.170E+01	2.120E+01	3.337E-01
S6	1	Hem	7.334E+00	1.371E+02	7.200E+00	4.611E+01		3.324E+01	1.679E+01	
S6	2	Hem	9.051E+00	1.460E+02	7.322E+00	4.755E+01		2.481E+01	1.819E+01	
S6	3	Hem	7.001E+00	1.301E+02	7.637E+00	4.710E+01		3.288E+01	1.816E+01	
TW1	1	Hem	8.632E+02	4.705E+03	3.702E+02	2.845E+03		2.188E+03	1.252E+03	
TW2	1	Hem	9.775E+02	5.853E+03	3.800E+02	2.586E+03		9.657E+02	1.222E+03	
TW3	1	Hem	1.168E+03	9.271E+03	3.168E+02	2.294E+03		1.089E+03	1.086E+03	
TW4	1	Hem	5.484E+02	4.308E+03	3.266E+02	2.089E+03		1.141E+03	1.015E+03	
TW5	1	Hem	4.036E+02	5.909E+03	3.203E+02	1.891E+03		1.509E+03	9.850E+02	
TW6	1	Hem	3.526E+02	3.668E+03	2.490E+02	1.621E+03		7.656E+02	8.269E+02	
TW7	1	Hem	2.228E+02	3.496E+03	2.464E+02	1.640E+03		1.005E+03	9.049E+02	
TW8	1	Hem	3.134E+02	3.449E+03	2.191E+02	1.472E+03		7.156E+02	8.450E+02	
TW9	1	Hem	2.314E+02	4.510E+03	2.299E+02	1.504E+03		1.260E+03	8.240E+02	
TW10	1	Hem	2.529E+02	3.213E+03	2.231E+02	1.424E+03		7.081E+02	8.837E+02	
TW11	1	Hem	4.723E+02	2.435E+04	2.333E+02	1.707E+03		1.304E+03	9.924E+02	

TW12	1	Hem	4.092E+02	4.791E+03	2.794E+02	1.791E+03		1.595E+03	9.082E+02	
TW13	1	Hem	2.246E+02	4.202E+03	2.327E+02	1.378E+03		8.730E+02	8.107E+02	
TW14	1	Hem		2.869E+05	1.245E+03	4.648E+03	7.904E+02	7.493E+03	2.989E+03	
TW16	1	Hem	1.667E+03	6.365E+03	3.463E+02	2.981E+03		2.154E+03	1.347E+03	
TW18	1	Hem	8.094E+02	8.146E+03	2.970E+02	3.316E+03		1.362E+03	1.481E+03	
TW21	1	Hem	1.062E+03	1.441E+04	8.379E+02	5.402E+03		5.305E+03	2.259E+03	
TW22	1	Hem	1.213E+03	1.659E+04	1.027E+03	6.045E+03		4.664E+03	2.301E+03	
TW23	1	Hem	2.119E+03	3.288E+04	1.217E+03	8.537E+03		6.417E+03	2.108E+03	
TW25	1	Hem	4.432E+03	8.276E+04	4.237E+03	1.744E+04			3.406E+03	
TW17	1	Mag		2.949E+05	1.990E+03	1.049E+04		2.363E+04	1.624E+03	
TW24	1	Mag		2.323E+06	7.634E+03	1.408E+04		1.851E+05	4.026E+03	5.305E+02
TW26	1	Mag	4.159E+03	2.998E+07	6.893E+04	4.003E+04			7.462E+03	5.850E+03
	Bulk	average	1.861E+01	2.419E+03	1.366E+01	5.648E+01	2.857E+01	5.441E+01	4.358E+01	2.328E-01
		2*std								
		dev	7.722E+00	3.247E+03	1.713E+01	7.301E+01	7.852E+01	7.818E+00	5.086E+01	1.843E-01
		count	2	2	2	2	2	2	2	2
	Hematite	average	4.846E+02	1.418E+04	3.417E+02	1.934E+03	2.083E+02	1.171E+03	7.584E+02	4.787E-01
		2*std								
		dev	1.694E+03	9.537E+04	1.454E+03	6.491E+03	7.762E+02	3.692E+03	1.799E+03	3.250E-01
		count	37	38	38	38	4	37	38	3
	Magnetite	average	4.159E+03	1.086E+07	2.618E+04	2.153E+04		1.044E+05	4.371E+03	3.190E+03
		2*std								
		dev		3.316E+07	7.425E+04	3.224E+04		2.284E+05	5.869E+03	7.524E+03
		count	1	3	3	3	0	2	3	2

Table A2.11 continued

Code	Shot	Method	Sr	Y	Zr	Mo	Ba	La	Ce	Pr
LR1-7	IF	Bulk	4.314E-01	1.512E+01	9.333E+00	5.026E-01	1.012E+00	7.813E+00	1.479E+01	2.044E+00
LR1-10	IF	Bulk	1.879E+00	6.957E+00	5.254E+00	7.570E-01	1.568E-01	1.498E+00	2.229E+00	2.427E-01
S1	1	Hem	3.626E+00		1.688E+01	1.711E+00	1.848E+00		3.049E-02	
S1	2	Hem	1.611E+00	1.377E+00	1.359E+01	2.078E+00	1.247E+00	2.073E-01	5.395E-01	7.931E-02
S1	3	Hem	2.928E+00		1.793E+01	1.861E+00	1.721E+00			
S2	1	Hem	2.475E+00		2.492E+01	1.847E+00	2.148E+00			
S2	2	Hem	2.156E+00	8.481E-02	1.944E+01	1.805E+00	1.884E+00	6.395E-02	7.399E-02	8.961E-03
S2	3	Hem	1.791E+00		1.576E+01	1.959E+00	1.571E+00	1.096E-02	1.803E-02	
S3	1	Hem	1.995E+00	7.039E-02	1.834E+01	2.226E+00	1.482E+00	8.094E-02	5.690E-02	
S3	2	Hem	1.884E+00	1.468E-01	1.300E+01	2.198E+00	1.695E+00	4.016E-02	7.500E-02	
S3	3	Hem	5.487E+00	2.080E-01	1.908E+01	1.859E+00	1.677E+00	8.840E-02	9.751E-02	1.791E-02
S4	1	Hem	2.361E+00	3.519E+00	1.478E+01	1.666E+00	1.538E+00	6.401E-01	7.794E-01	8.868E-02
S4	2	Hem	2.380E+01	2.758E+01	2.704E+01	1.490E+00	2.767E+00	3.714E+00	6.473E+00	9.109E-01
S4	3	Hem	1.563E+00		1.332E+01	2.155E+00	1.267E+00		4.764E-02	
S5	1	Hem	2.297E+00	4.578E-01	1.821E+01	1.645E+00	1.730E+00	1.701E+00	1.672E+00	1.566E-01
S5	2	Hem	2.776E+00	9.995E+00	1.582E+01	1.636E+00	1.964E+00	2.042E+00	3.367E+00	4.484E-01
S5	3	Hem	1.808E+00	2.086E+00	1.409E+01	1.629E+00	1.608E+00	8.525E-01	1.037E+00	1.176E-01
S6	1	Hem	2.425E+00	1.270E-01	1.958E+01	1.973E+00	1.834E+00	1.171E-01	1.176E-01	
S6	2	Hem	2.050E+00		1.868E+01	1.769E+00	1.569E+00	1.970E-02	2.220E-02	
S6	3	Hem	1.943E+00		1.751E+01	1.942E+00	1.836E+00		1.478E-02	
TW1	1	Hem	5.261E+01		5.698E+02	8.835E+01	4.680E+01	1.671E+00	1.681E+00	
TW2	1	Hem	5.586E+01	4.125E+00	4.653E+02	8.946E+01	3.997E+01	1.018E+00	1.987E+00	
TW3	1	Hem	7.190E+02	2.295E+03	5.582E+02	6.933E+01	5.417E+01	1.339E+03	1.379E+03	1.588E+02
TW4	1	Hem				7.320E+01	2.020E+01			
TW5	1	Hem	3.375E+01		3.580E+02	6.268E+01	3.039E+01		5.871E-01	
TW6	1	Hem	5.521E+01	1.057E+01	5.379E+02	6.313E+01	4.149E+01	2.056E+00	4.821E+00	8.565E-01
TW7	1	Hem	3.666E+01	5.695E+00	3.079E+02	5.635E+01	2.822E+01	2.260E+00	2.883E+00	3.944E-01
TW8	1	Hem	4.874E+01	2.880E+00	4.285E+02	5.035E+01	3.217E+01	1.719E+00	2.000E+00	
TW9	1	Hem	2.895E+01	3.761E+01	2.885E+02	5.275E+01	2.104E+01	1.460E+01	1.632E+01	1.931E+00
TW10	1	Hem	3.946E+01	2.185E+00	3.717E+02	5.144E+01	2.774E+01	8.431E-01	1.032E+00	
TW11	1	Hem	2.913E+01	5.423E+01	2.521E+02	5.217E+01	2.095E+01	1.134E+01	1.545E+01	2.037E+00

TW12	1	Hem			1.905E+02	5.217E+01				
TW13	1	Hem	3.755E+01		3.968E+02	4.370E+01	2.898E+01			
TW14	1	Hem	4.153E+03	7.856E+03	1.001E+03		9.129E+01	1.050E+03	2.466E+03	3.660E+02
TW16	1	Hem	8.017E+01	2.622E+01	6.062E+02	9.901E+01	5.101E+01	8.279E+00	9.001E+00	1.016E+00
TW18	1	Hem	1.282E+02	2.247E+01	9.944E+02	1.202E+02	9.631E+01	9.576E+00	1.098E+01	2.146E+00
TW21	1	Hem	2.059E+03	5.994E+03	1.121E+03	2.173E+02	1.126E+02	2.304E+03	3.005E+03	3.074E+02
TW22	1	Hem	1.674E+02		1.467E+03	2.598E+02	1.397E+02			
TW23	1	Hem	2.521E+02	1.521E+02	2.139E+03	4.082E+02	2.080E+02	3.476E+01	6.660E+01	9.606E+00
TW25	1	Hem	8.776E+02	7.805E+01	4.931E+03	1.890E+03	7.172E+02	5.682E+01	7.304E+01	7.903E+00
TW17	1	Mag		4.261E+02				1.104E+01	1.137E+01	1.329E+00
TW24	1	Mag		4.195E+03				9.743E+02	1.118E+03	1.196E+02
TW26	1	Mag	3.887E+03	7.042E+03	8.100E+03		4.840E+03	1.053E+04	1.176E+04	1.234E+03
	Bulk	average	1.155E+00	1.104E+01	7.294E+00	6.298E-01	5.845E-01	4.655E+00	8.509E+00	1.143E+00
		2*std								
		dev	2.047E+00	1.154E+01	5.769E+00	3.598E-01	1.210E+00	8.931E+00	1.776E+01	2.548E+00
		count	2	2	2	2	2	2	2	2
	Hematite	average	2.478E+02	6.634E+02	4.676E+02	1.036E+02	4.972E+01	1.731E+02	2.210E+02	4.526E+01
		2*std								
		dev	1.538E+03	3.914E+03	1.783E+03	6.267E+02	2.433E+02	1.045E+03	1.412E+03	2.186E+02
		count	36	25	37	37	37	28	32	19
	Magnetite	average	3.887E+03	3.888E+03	8.100E+03		4.840E+03	3.839E+03	4.295E+03	4.517E+02
		2*std								
		dev		6.637E+03				1.163E+04	1.297E+04	1.361E+03
		count	1	3	1	0	1	3	3	3

Table A2.11 continued

Code	Shot	Method	Nd	Sm	Eu	Tb	Gd	Dy	Ho	Er
LR1-7	IF	Bulk	8.222E+00	1.884E+00	6.467E-01	3.529E-01	2.183E+00	2.080E+00	4.783E-01	1.463E+00
LR1-10	IF	Bulk	1.040E+00	2.930E-01	2.170E-01	9.305E-02	4.811E-01	6.849E-01	1.746E-01	5.964E-01
S1	1	Hem							3.225E-03	
S1	2	Hem	4.665E-01	1.430E-01	8.740E-02	3.603E-02	2.691E-01	2.580E-01	5.826E-02	1.768E-01
S1	3	Hem				5.523E-03				
S2	1	Hem				3.567E-03				
S2	2	Hem		1.999E-02				2.173E-02		2.191E-02
S2	3	Hem								
S3	1	Hem							3.700E-03	
S3	2	Hem						5.128E-02	5.276E-03	
S3	3	Hem	6.081E-02							
S4	1	Hem	4.435E-01	1.068E-01	8.687E-02	3.783E-02	2.282E-01	2.824E-01	8.487E-02	3.579E-01
S4	2	Hem	4.458E+00	1.561E+00	1.178E+00	4.635E-01	2.648E+00	3.256E+00	7.251E-01	2.243E+00
S4	3	Hem								
S5	1	Hem	5.372E-01	1.068E-01			1.004E-01	1.002E-01	1.725E-02	5.417E-02
S5	2	Hem	2.272E+00	6.548E-01	3.923E-01	1.817E-01	1.033E+00	1.194E+00	2.954E-01	9.810E-01
S5	3	Hem	4.378E-01	1.332E-01	7.443E-02	3.131E-02	2.299E-01	2.549E-01	5.838E-02	2.414E-01
S6	1	Hem								
S6	2	Hem								
S6	3	Hem								
TW1	1	Hem								
TW2	1	Hem								
TW3	1	Hem	6.565E+02	1.378E+02	7.741E+01	2.884E+01	1.994E+02	2.077E+02	5.068E+01	1.695E+02
TW4	1	Hem								
TW5	1	Hem								
TW6	1	Hem	3.551E+00				2.245E+00	2.526E+00	4.828E-01	
TW7	1	Hem								
TW8	1	Hem								
TW9	1	Hem	8.915E+00			5.474E-01	4.114E+00	4.173E+00	9.340E-01	2.902E+00
TW10	1	Hem								
TW11	1	Hem	9.249E+00	3.508E+00	2.386E+00	8.547E-01	5.468E+00	6.562E+00	1.618E+00	4.933E+00

TW12	1	Hem									
TW13	1	Hem									
TW14	1	Hem	1.737E+03	5.603E+02	4.072E+02	1.454E+02	8.992E+02	1.027E+03	2.127E+02	6.346E+02	
TW16	1	Hem								1.598E+00	
TW18	1	Hem	4.813E+00						7.429E-01		
TW21	1	Hem	1.391E+03	3.428E+02	1.987E+02	9.369E+01	5.938E+02	6.697E+02	1.447E+02	4.494E+02	
TW22	1	Hem									
TW23	1	Hem	4.189E+01	1.632E+01		5.198E+00	2.183E+01	2.390E+01	5.967E+00	1.789E+01	
TW25	1	Hem									
TW17	1	Mag	7.157E+00			2.708E+00	9.015E+00	2.733E+01	8.553E+00	4.253E+01	
TW24	1	Mag	5.089E+02	1.586E+02	1.199E+02	4.586E+01	2.604E+02	3.781E+02	1.072E+02	4.471E+02	
TW26	1	Mag	2.945E+03	8.199E+02	8.086E+02	1.645E+02	7.341E+02	7.554E+02	1.943E+02	7.929E+02	
	Bulk	average	4.631E+00	1.088E+00	4.318E-01	2.230E-01	1.332E+00	1.383E+00	3.265E-01	1.030E+00	
		2*std									
		dev	1.016E+01	2.250E+00	6.077E-01	3.675E-01	2.407E+00	1.973E+00	4.295E-01	1.226E+00	
		count	2	2	2	2	2	2	2	2	
	Hematite	average	2.575E+02	8.862E+01	7.640E+01	2.118E+01	1.331E+02	1.298E+02	2.465E+01	9.178E+01	
		2*std									
		dev	1.120E+03	3.600E+02	2.818E+02	9.121E+01	5.689E+02	6.082E+02	1.209E+02	3.984E+02	
		count	15	12	9	13	13	15	17	14	
	Magnetite	average	1.154E+03	4.892E+02	4.642E+02	7.102E+01	3.345E+02	3.869E+02	1.033E+02	4.275E+02	
		2*std									
		dev	3.143E+03	9.352E+02	9.740E+02	1.675E+02	7.363E+02	7.282E+02	1.858E+02	7.511E+02	
		count	3	2	2	3	3	3	3	3	

Table A2.11 continued

Code	Shot	Method	Yb	Lu	Hf	Pb	Th	U	Y/Ho	Ce/Ce* _{PAAS}
LR1-7	IF	Bulk	1.203E+00	2.037E-01	2.070E-01	1.302E+00	7.371E-01	2.205E-01	3.160E+01	8.523E-01
LR1-10	IF	Bulk	6.592E-01	1.274E-01	2.542E-02	1.213E-01	3.768E-02	8.493E-03	3.984E+01	8.397E-01
S1	1	Hem					4.112E-03			
S1	2	Hem	8.183E-02		1.914E-02		7.850E-03	7.170E-03	2.364E+01	9.407E-01
S1	3	Hem			1.054E-02					
S2	1	Hem								
S2	2	Hem	2.590E-02				2.654E-03			6.914E-01
S2	3	Hem	1.873E-02							
S3	1	Hem			2.479E-02	3.609E-01		4.822E-02	1.902E+01	
S3	2	Hem			1.083E-02		4.780E-03	3.394E-03	2.783E+01	
S3	3	Hem	2.597E-02		2.140E-02			3.023E-03		5.642E-01
S4	1	Hem	5.571E-01	9.697E-02	3.016E-02			9.368E-03	4.147E+01	7.307E-01
S4	2	Hem	2.545E+00	5.188E-01	1.067E-01	7.733E-01	3.675E-03	7.965E-03	3.803E+01	8.116E-01
S4	3	Hem								
S5	1	Hem						7.675E-03	2.654E+01	6.748E-01
S5	2	Hem	1.053E+00	1.870E-01				2.444E-01	3.384E+01	8.116E-01
S5	3	Hem	2.690E-01	5.075E-02	4.289E-02			2.499E-02	3.573E+01	7.310E-01
S6	1	Hem			1.833E-02			2.534E-03		
S6	2	Hem		8.174E-03	2.712E-02					
S6	3	Hem			1.965E-02			2.438E-03		
TW1	1	Hem								
TW2	1	Hem			1.672E+00					
TW3	1	Hem	1.701E+02	2.685E+01		2.770E+00	4.261E-01	7.039E-01	4.528E+01	6.534E-01
TW4	1	Hem								
TW5	1	Hem								
TW6	1	Hem							2.190E+01	8.031E-01
TW7	1	Hem								6.975E-01
TW8	1	Hem								
TW9	1	Hem		3.093E-01					4.027E+01	6.821E-01
TW10	1	Hem						2.320E-01		

TW11	1	Hem	7.545E+00	1.322E+00	6.636E-01		2.646E-01	1.704E-01	3.352E+01	7.362E-01
TW12	1	Hem								
TW13	1	Hem								
TW14	1	Hem	5.770E+02	1.097E+02	4.937E+00	1.470E+02		1.701E+00	3.693E+01	8.988E-01
TW16	1	Hem								6.817E-01
TW18	1	Hem							3.025E+01	5.586E-01
TW21	1	Hem	3.651E+02	4.973E+01				9.199E-01	4.143E+01	7.936E-01
TW22	1	Hem								
TW23	1	Hem							2.549E+01	8.375E-01
TW25	1	Hem						3.983E+00		7.702E-01
TW17	1	Mag	6.486E+01	1.159E+01					4.982E+01	6.501E-01
TW24	1	Mag	7.320E+02	1.407E+02					3.914E+01	7.197E-01
TW26	1	Mag	1.359E+03	2.701E+02			4.008E+01	8.218E+01	3.625E+01	7.109E-01
	Bulk	average	9.311E-01	1.656E-01	1.162E-01	7.114E-01	3.874E-01	1.145E-01	3.572E+01	8.460E-01
		2*std								
		dev	7.688E-01	1.079E-01	2.568E-01	1.669E+00	9.891E-01	2.998E-01	1.164E+01	1.787E-02
		count	2	2	2	2	2	2	2	2
	Hematite	average	9.370E+01	1.887E+01	5.431E-01	3.773E+01	1.020E-01	4.748E-01	3.257E+01	7.405E-01
		2*std								
		dev	3.765E+02	7.198E+01	2.689E+00	1.457E+02	3.454E-01	2.026E+00	1.576E+01	1.998E-01
		count	12	10	14	4	7	17	16	19
	Magnetite	average	7.186E+02	1.408E+02			4.008E+01	8.218E+01	4.174E+01	6.935E-01
		2*std								
		dev	1.294E+03	2.585E+02					1.430E+01	7.578E-02
		count	3	3	0	0	1	1	3	3

Table A2.11 continued

Code	Shot	Method	La/La* _{PAAS}	Pr/Pr* _{PAAS}	Eu/Eu* _{PAAS}	Pr/Yb* _{PAAS}	∑REE
LR1-7	IF	Bulk	9.768E-01	1.081E+00	1.580E+00	5.427E-01	5.848E+01
LR1-10	IF	Bulk	1.860E+00	9.367E-01	2.662E+00	1.176E-01	1.529E+01
S1	1	Hem					3.371E-02
S1	2	Hem	-9.434E+00	8.747E-01	2.469E+00	3.095E-01	3.781E+00
S1	3	Hem					5.523E-03
S2	1	Hem					3.567E-03
S2	2	Hem				1.105E-01	3.212E-01
S2	3	Hem					4.772E-02
S3	1	Hem					2.119E-01
S3	2	Hem					3.185E-01
S3	3	Hem	9.265E-01	1.344E+00		2.202E-01	4.986E-01
S4	1	Hem	4.225E+00	8.782E-01	2.754E+00	5.084E-02	7.310E+00
S4	2	Hem	2.092E+00	9.694E-01	2.811E+00	1.143E-01	5.827E+01
S4	3	Hem					4.764E-02
S5	1	Hem	2.071E+00	9.622E-01			4.903E+00
S5	2	Hem	2.923E+00	9.290E-01	2.309E+00	1.360E-01	2.410E+01
S5	3	Hem	1.581E+00	1.027E+00	2.332E+00	1.396E-01	5.874E+00
S6	1	Hem					3.616E-01
S6	2	Hem					5.007E-02
S6	3	Hem					1.478E-02
TW1	1	Hem					3.352E+00
TW2	1	Hem					7.130E+00
TW3	1	Hem	2.303E+00	9.803E-01	2.468E+00	2.982E-01	6.896E+03
TW4	1	Hem					0.000E+00
TW5	1	Hem					5.871E-01
TW6	1	Hem	6.603E-01	1.174E+00			2.711E+01
TW7	1	Hem					1.123E+01
TW8	1	Hem					6.599E+00
TW9	1	Hem	2.937E+00	9.348E-01			9.236E+01
TW10	1	Hem					4.060E+00

TW11	1	Hem	2.027E+00	9.880E-01	2.791E+00	8.622E-02	1.265E+02
TW12	1	Hem					0.000E+00
TW13	1	Hem					0.000E+00
TW14	1	Hem	1.256E+00	1.008E+00	2.895E+00	2.026E-01	1.805E+04
TW16	1	Hem					4.611E+01
TW18	1	Hem	5.632E-01	1.737E+00			5.072E+01
TW21	1	Hem	2.696E+00	8.838E-01	2.251E+00	2.689E-01	1.591E+04
TW22	1	Hem					0.000E+00
TW23	1	Hem	1.149E+00	1.050E+00			3.961E+02
TW25	1	Hem					2.158E+02
TW17	1	Mag	9.883E+00	8.504E-01		6.544E-03	6.236E+02
TW24	1	Mag	2.407E+00	9.318E-01	2.853E+00	5.216E-02	9.305E+03
TW26	1	Mag	1.122E+00	1.192E+00	4.412E+00	2.901E-01	3.941E+04
	Bulk	average	1.418E+00	1.009E+00	2.121E+00	3.301E-01	3.689E+01
		2*std					
		dev	1.249E+00	2.039E-01	1.530E+00	6.012E-01	6.108E+01
		count	2	2	2	2	2
	Hematite	average	1.198E+00	1.049E+00	2.564E+00	1.761E-01	1.104E+03
		2*std					
		dev	6.207E+00	4.517E-01	4.964E-01	1.775E-01	7.921E+03
		count	15	15	9	11	38
	Magnetite	average	4.471E+00	9.914E-01	3.633E+00	1.163E-01	1.645E+04
		2*std					
		dev	9.462E+00	3.569E-01	2.205E+00	3.045E-01	4.071E+04
		count	3	3	2	3	3

Table A2.12. Bulk digestion and LA-HR-ICP-MS analyses for the sample 090710-4 from the Nuvvuagittuq Supracrustal Belt, Québec, Canada.

Formation	Sample	Code	Shot	Method	Li	B	Mg	Ca	Ti	V
Nuvvuagittuq	090710-4	LR1-2	IF	Bulk	8.324E-01		1.401E+04	4.984E+03	6.795E+01	4.021E+00
Nuvvuagittuq	090710-4	LR1-12	IF	Bulk	6.131E-01		1.488E+04	4.023E+03	7.914E+01	4.273E+00
Nuvvuagittuq	090710-4	S1	1	Hem				1.932E+03	2.448E+02	1.113E+01
Nuvvuagittuq	090710-4	S1	2	Hem				2.065E+03	2.452E+02	1.107E+01
Nuvvuagittuq	090710-4	S1	3	Hem			8.820E+01	1.936E+03	2.583E+02	1.159E+01
Nuvvuagittuq	090710-4	S2	1	Hem				2.588E+03	1.573E+02	5.440E+00
Nuvvuagittuq	090710-4	S2	2	Hem				1.862E+03	1.382E+02	5.235E+00
Nuvvuagittuq	090710-4	S2	3	Hem			9.499E+03	3.365E+03	1.443E+02	4.777E+00
Nuvvuagittuq	090710-4	S3	1	Hem			1.470E+02	3.147E+03	2.110E+02	9.003E+00
Nuvvuagittuq	090710-4	S3	2	Hem			1.180E+02	2.980E+03	2.357E+02	9.112E+00
Nuvvuagittuq	090710-4	S3	3	Hem				2.400E+03	2.180E+02	9.088E+00
Nuvvuagittuq	090710-4	S4	1	Hem			7.048E+01	2.336E+03	3.505E+02	1.646E+01
Nuvvuagittuq	090710-4	S4	2	Hem				2.457E+03	3.699E+02	1.745E+01
Nuvvuagittuq	090710-4	S4	3	Hem				2.478E+03	3.652E+02	1.668E+01
Nuvvuagittuq	090710-4	TW1	1	Hem			5.072E+03	1.586E+05	7.111E+03	3.238E+02
Nuvvuagittuq	090710-4	TW2	1	Hem			3.182E+03	5.846E+04	6.332E+03	3.649E+02
Nuvvuagittuq	090710-4	TW3	1	Hem			7.261E+03		9.840E+03	7.903E+02
Nuvvuagittuq	090710-4	TW4	1	Hem			2.239E+05	7.661E+04	1.011E+04	7.643E+02
Nuvvuagittuq	090710-4	TW5	1	Hem			3.455E+03	5.929E+04	9.649E+03	6.222E+02
Nuvvuagittuq	090710-4	TW6	1	Hem			2.778E+03	4.955E+04	5.150E+03	2.935E+02
Nuvvuagittuq	090710-4	TW7	1	Hem			2.336E+03		1.179E+04	6.360E+02
Nuvvuagittuq	090710-4	TW8	1	Hem			2.049E+03		1.122E+04	8.380E+02
Nuvvuagittuq	090710-4	TW9	1	Hem			3.010E+03	5.582E+04	1.086E+04	6.760E+02
Nuvvuagittuq	090710-4	TW10	1	Hem			3.232E+03	7.539E+04	6.796E+03	3.902E+02
Nuvvuagittuq	090710-4	TW11	1	Hem			3.317E+03	3.131E+04	4.869E+03	2.488E+02
Nuvvuagittuq	090710-4	TW12	1	Hem			2.683E+03	4.467E+04	5.075E+03	2.188E+02
Nuvvuagittuq	090710-4	TW13	1	Hem			2.078E+03	3.790E+04	3.897E+03	2.002E+02
			Bulk	average	7.227E-01		1.444E+04	4.503E+03	7.354E+01	4.147E+00
				2*std dev	3.102E-01		1.231E+03	1.359E+03	1.582E+01	3.557E-01

	count	2	0	2	2	2	2
Hematite	average			1.524E+04	3.078E+04	4.226E+03	2.598E+02
	2*std dev			1.043E+05	7.910E+04	8.732E+03	5.917E+02
	count	0	0	18	22	25	25

Table A2.12 continued

Code	Shot	Method	Cr	Mn	Co	Ni	⁶⁵Cu	Zn	Ge	Rb
LR1-2	IF	Bulk	1.479E+01	1.370E+03	9.853E+00	4.572E+01	5.753E+00	2.963E+01	5.239E+01	1.852E-01
LR1-12	IF	Bulk	2.110E+01	1.120E+03	8.674E+00	4.770E+01	1.003E+01	2.825E+01	7.270E+01	1.678E-01
S1	1	Hem	1.477E+01	1.114E+02	8.449E+00	7.753E+01		1.141E+01	2.338E+01	
S1	2	Hem	1.478E+01	1.176E+02	9.334E+00	7.577E+01		6.722E+00	2.175E+01	
S1	3	Hem	1.898E+01	1.129E+02	8.513E+00	8.165E+01		8.176E+00	2.510E+01	
S2	1	Hem	1.664E+01	9.824E+01	9.599E+00	8.010E+01		1.996E+01	2.399E+01	
S2	2	Hem	1.455E+01	9.849E+01	9.600E+00	7.995E+01		2.096E+01	2.151E+01	
S2	3	Hem	1.380E+01	1.157E+03	1.201E+01	7.830E+01		4.102E+01	2.546E+01	
S3	1	Hem	1.355E+01	1.161E+02	9.680E+00	7.679E+01		2.866E+01	2.277E+01	
S3	2	Hem	1.816E+01	9.839E+01	9.032E+00	7.808E+01		2.186E+01	2.081E+01	
S3	3	Hem	1.214E+01	1.149E+02	1.004E+01	7.912E+01		2.309E+01	2.074E+01	
S4	1	Hem	4.060E+01	1.216E+02	8.477E+00	7.378E+01		1.643E+01	1.956E+01	
S4	2	Hem	3.756E+01	1.329E+02	9.564E+00	7.577E+01		1.560E+01	1.911E+01	
S4	3	Hem	5.278E+01	1.357E+02	8.882E+00	7.647E+01		7.625E+00	1.754E+01	
TW1	1	Hem	9.991E+02	6.429E+03	5.405E+02	5.008E+03		1.690E+03	1.448E+03	
TW2	1	Hem	8.196E+02	6.274E+03	6.044E+02	5.158E+03		1.535E+03	1.541E+03	
TW3	1	Hem	1.335E+03	5.244E+03	5.254E+02	5.154E+03		9.382E+02	1.554E+03	
TW4	1	Hem	2.249E+03	3.094E+04	4.255E+02	5.100E+03		9.213E+02	1.294E+03	
TW5	1	Hem	1.729E+03	5.861E+03	4.566E+02	4.126E+03		8.259E+02	1.070E+03	
TW6	1	Hem	8.538E+02	4.708E+03	4.420E+02	3.960E+03		6.045E+02	1.047E+03	
TW7	1	Hem	1.921E+02	5.210E+03	3.441E+02	3.282E+03		3.243E+02	8.422E+02	
TW8	1	Hem	1.923E+03	4.755E+03	4.229E+02	3.789E+03		6.857E+02	1.103E+03	
TW9	1	Hem	2.139E+03	4.050E+03	3.764E+02	3.320E+03		3.242E+02	9.181E+02	
TW10	1	Hem	1.538E+03	3.507E+03	3.591E+02	3.055E+03		1.250E+03	9.242E+02	
TW11	1	Hem	3.462E+02	3.235E+03	2.910E+02	3.158E+03		6.723E+02	9.362E+02	
TW12	1	Hem	4.947E+02	3.822E+03	3.281E+02	2.815E+03		7.617E+02	7.843E+02	
TW13	1	Hem	5.287E+02	3.929E+03	3.476E+02	2.978E+03		3.817E+02	7.301E+02	
	Bulk	average	1.794E+01	1.245E+03	9.264E+00	4.671E+01	7.894E+00	2.894E+01	6.255E+01	1.765E-01
		2*std dev	8.921E+00	3.534E+02	1.667E+00	2.804E+00	6.054E+00	1.954E+00	2.872E+01	2.457E-02
		count	2	2	2	2	2	2	2	2

Hematite	average	6.167E+02	3.615E+03	2.231E+02	2.074E+03	4.454E+02	5.782E+02	
	2*std dev	1.530E+03	1.235E+04	4.390E+02	4.119E+03	1.037E+03	1.162E+03	
	count	25	25	25	25	0	25	25

Table A2.12 continued

Code	Shot	Method	Sr	Y	Zr	Mo	Ba	La	Ce	Pr
LR1-2	IF	Bulk	1.015E+00	8.642E+00	6.723E+00	1.058E+00	1.811E-01	7.431E-01	1.801E+00	2.538E-01
LR1-12	IF	Bulk	1.003E+00	1.047E+01	7.488E+00	9.089E-01	1.876E-01	8.116E-01	1.939E+00	2.722E-01
S1	1	Hem	2.408E+00	5.985E-01	2.562E+01	1.749E+00	1.789E+00	1.299E-01	2.480E-01	4.772E-02
S1	2	Hem	2.341E+00		2.459E+01	1.780E+00	1.853E+00			
S1	3	Hem	2.623E+00	2.553E-01	2.810E+01	1.691E+00	2.070E+00	4.558E-02	7.980E-02	
S2	1	Hem	2.110E+00	9.816E-02	2.146E+01	1.907E+00	1.820E+00		4.345E-02	
S2	2	Hem	2.023E+00	2.142E-01	1.916E+01	1.916E+00	1.595E+00	4.758E-02	6.523E-02	
S2	3	Hem	2.300E+00	3.723E+00	1.966E+01	1.351E+00	1.721E+00	8.379E-02	1.530E-01	2.626E-02
S3	1	Hem	2.944E+00	1.498E+00	2.714E+01	1.913E+00	1.879E+00	2.872E-01	5.299E-01	7.435E-02
S3	2	Hem	2.918E+00	5.512E-01	3.203E+01	1.688E+00	2.785E+00	9.024E-02	1.425E-01	
S3	3	Hem	2.882E+00	1.778E-01	2.356E+01	1.780E+00	1.966E+00	4.319E-02	6.562E-02	
S4	1	Hem	2.317E+00	5.644E-01	2.299E+01	1.495E+00	2.103E+00	8.343E-02	1.780E-01	3.723E-02
S4	2	Hem	2.222E+00		2.366E+01	1.686E+00	2.117E+00		3.860E-02	
S4	3	Hem	2.129E+00		2.198E+01	1.799E+00	1.966E+00			
TW1	1	Hem	8.574E+01	2.436E+00	8.871E+02	1.377E+02	7.847E+01	1.298E+00	2.222E+00	
TW2	1	Hem	4.738E+01		4.575E+02	1.257E+02		1.303E+00	1.862E+00	6.862E-01
TW3	1	Hem	4.874E+01	4.621E+01	4.063E+02	1.217E+02	4.040E+01	7.504E+00	1.573E+01	1.645E+00
TW4	1	Hem	9.239E+01	1.141E+02	5.761E+02	9.813E+01	5.183E+01	2.625E+00	5.539E+00	1.064E+00
TW5	1	Hem	4.499E+01		4.242E+02	1.012E+02	3.337E+01			
TW6	1	Hem	4.211E+01		3.911E+02	9.052E+01	3.770E+01	7.118E-01	6.314E-01	
TW7	1	Hem	2.609E+01		2.341E+02	6.647E+01				
TW8	1	Hem		4.174E+00		9.606E+01		2.554E+00	2.766E+00	
TW9	1	Hem	4.182E+01	1.485E+00	3.449E+02	8.660E+01	3.761E+01	7.998E-01	9.234E-01	
TW10	1	Hem	7.024E+01	2.575E+00	6.084E+02	6.861E+01	5.333E+01	1.754E+00	2.739E+00	3.449E-01
TW11	1	Hem	2.400E+01	3.874E+00	1.912E+02	9.081E+01	1.702E+01	8.379E-01	1.710E+00	
TW12	1	Hem	4.592E+01		4.299E+02	5.652E+01	3.193E+01		6.586E-01	
TW13	1	Hem	3.156E+01		2.929E+02	6.981E+01	2.472E+01			
	Bulk	average	1.009E+00	9.557E+00	7.105E+00	9.832E-01	1.843E-01	7.773E-01	1.870E+00	2.630E-01
		2*std dev	1.647E-02	2.588E+00	1.082E+00	2.103E-01	9.270E-03	9.697E-02	1.960E-01	2.605E-02
		count	2	2	2	2	2	2	2	2

Hematite	average	2.626E+01	1.141E+01	2.306E+02	4.922E+01	1.955E+01	1.188E+00	1.816E+00	4.907E-01
	2*std dev	5.729E+01	5.918E+01	4.949E+02	9.939E+01	4.542E+01	3.679E+00	7.119E+00	1.198E+00
	count	24	16	24	25	22	17	20	8

Table A2.12 continued

Code	Shot	Method	Nd	Sm	Eu	Tb	Gd	Dy	Ho	Er
LR1-2	IF	Bulk	1.209E+00	3.574E-01	2.586E-01	1.164E-01	5.300E-01	9.262E-01	2.472E-01	8.834E-01
LR1-12	IF	Bulk	1.303E+00	3.957E-01	2.888E-01	1.367E-01	6.381E-01	1.048E+00	2.771E-01	9.670E-01
S1	1	Hem	1.991E-01				1.005E-01		1.966E-02	
S1	2	Hem								
S1	3	Hem								
S2	1	Hem							7.263E-03	
S2	2	Hem					3.587E-02		6.768E-03	2.923E-02
S2	3	Hem	1.487E-01		3.937E-02	3.380E-02		3.121E-01	1.142E-01	5.165E-01
S3	1	Hem	4.023E-01			2.597E-02	1.681E-01	2.098E-01	3.504E-02	1.395E-01
S3	2	Hem	1.029E-01							6.212E-02
S3	3	Hem						3.962E-02		2.232E-02
S4	1	Hem	1.717E-01				9.677E-02		1.887E-02	6.302E-02
S4	2	Hem								
S4	3	Hem								
TW1	1	Hem								
TW2	1	Hem								
TW3	1	Hem	7.130E+00			5.554E-01	3.545E+00	5.512E+00	1.283E+00	4.654E+00
TW4	1	Hem	5.511E+00			1.344E+00	6.305E+00	1.196E+01	3.508E+00	1.257E+01
TW5	1	Hem								
TW6	1	Hem								
TW7	1	Hem								
TW8	1	Hem								
TW9	1	Hem								
TW10	1	Hem								
TW11	1	Hem								
TW12	1	Hem								
TW13	1	Hem								
	Bulk	average	1.256E+00	3.766E-01	2.737E-01	1.266E-01	5.840E-01	9.872E-01	2.621E-01	9.252E-01
		2*std dev	1.324E-01	5.422E-02	4.267E-02	2.874E-02	1.529E-01	1.727E-01	4.242E-02	1.181E-01
		count	2	2	2	2	2	2	2	2

Hematite	average	1.952E+00		3.937E-02	4.899E-01	1.709E+00	3.607E+00	6.241E-01	2.257E+00
	2*std dev	6.044E+00			1.242E+00	5.281E+00	1.042E+01	2.490E+00	8.919E+00
	count	7	0	1	4	6	5	8	8

Table A2.12 continued

Code	Shot	Method	Yb	Lu	Hf	Pb	Th	U	Y/Ho	Ce/Ce* _{PAAS}
LR1-2	IF	Bulk	1.039E+00	1.945E-01	3.531E-02	1.019E-01	6.401E-02	9.835E-03	3.497E+01	9.388E-01
LR1-12	IF	Bulk	1.103E+00	2.031E-01		8.583E-02	8.563E-02	1.776E-02	3.778E+01	9.357E-01
S1	1	Hem					8.256E-02	4.574E-03	3.045E+01	7.077E-01
S1	2	Hem								
S1	3	Hem	3.746E-02				1.494E-02			
S2	1	Hem					7.641E-03		1.352E+01	
S2	2	Hem			4.256E-02				3.165E+01	
S2	3	Hem	7.916E-01	1.674E-01	4.661E-02				3.261E+01	7.439E-01
S3	1	Hem	1.313E-01				5.599E-02	4.850E-03	4.277E+01	8.354E-01
S3	2	Hem					3.085E-02			
S3	3	Hem					8.824E-03	3.137E-03		
S4	1	Hem	4.977E-02				1.326E-01	3.604E-03	2.991E+01	6.987E-01
S4	2	Hem			2.539E-02		5.539E-03			
S4	3	Hem								
TW1	1	Hem								
TW2	1	Hem								4.184E-01
TW3	1	Hem	4.484E+00	7.232E-01	2.221E+00				3.602E+01	1.033E+00
TW4	1	Hem	1.547E+01	3.049E+00			1.179E+00	2.487E-01	3.252E+01	7.354E-01
TW5	1	Hem								
TW6	1	Hem			8.805E-01					
TW7	1	Hem			1.200E+00					
TW8	1	Hem						2.900E-01		
TW9	1	Hem								
TW10	1	Hem								8.098E-01
TW11	1	Hem								
TW12	1	Hem								
TW13	1	Hem								
	Bulk	average	1.071E+00	1.988E-01	3.531E-02	9.388E-02	7.482E-02	1.380E-02	3.637E+01	9.373E-01
		2*std dev	9.031E-02	1.222E-02		2.276E-02	3.056E-02	1.121E-02	3.985E+00	4.416E-03
		count	2	2	1	2	2	2	2	2

Hematite	average	3.494E+00	1.313E+00	7.360E-01		1.687E-01	9.247E-02	3.118E+01	7.477E-01
	2*std dev	1.222E+01	3.057E+00	1.767E+00		7.626E-01	2.752E-01	1.649E+01	3.426E-01
	count	6	3	6	0	9	6	8	8

Table A2.12 continued

Code	Shot	Method	La/La* _{PAAS}	Pr/Pr* _{PAAS}	Eu/Eu* _{PAAS}	Pr/Yb* _{PAAS}	∑REE
LR1-2	IF	Bulk	1.307E+00	9.861E-01	2.566E+00	7.798E-02	1.720E+01
LR1-12	IF	Bulk	1.360E+00	9.818E-01	2.505E+00	7.880E-02	1.986E+01
S1	1	Hem	7.605E-01	1.203E+00			1.343E+00
S1	2	Hem					0.000E+00
S1	3	Hem					4.181E-01
S2	1	Hem					1.489E-01
S2	2	Hem					3.989E-01
S2	3	Hem	1.474E+01	9.428E-01		1.059E-02	6.109E+00
S3	1	Hem	4.922E+00	9.091E-01		1.808E-01	3.502E+00
S3	2	Hem					9.491E-01
S3	3	Hem					3.485E-01
S4	1	Hem	8.668E-01	1.155E+00		2.389E-01	1.263E+00
S4	2	Hem					3.860E-02
S4	3	Hem					0.000E+00
TW1	1	Hem					5.956E+00
TW2	1	Hem					3.851E+00
TW3	1	Hem	1.421E+00	9.133E-01		1.171E-01	9.898E+01
TW4	1	Hem	1.886E+00	1.038E+00		2.197E-02	1.830E+02
TW5	1	Hem					0.000E+00
TW6	1	Hem					1.343E+00
TW7	1	Hem					0.000E+00
TW8	1	Hem					9.493E+00
TW9	1	Hem					3.209E+00
TW10	1	Hem					7.412E+00
TW11	1	Hem					6.423E+00
TW12	1	Hem					6.586E-01
TW13	1	Hem					0.000E+00
	Bulk	average	1.334E+00	9.840E-01	2.535E+00	7.839E-02	1.853E+01
		2*std dev	7.545E-02	6.013E-03	8.546E-02	1.159E-03	3.753E+00
		count	2	2	2	2	2

Hematite	average	4.099E+00	1.027E+00		1.139E-01	1.339E+01
	2*std dev	1.086E+01	2.551E-01		1.981E-01	8.074E+01
	count	6	6	0	5	25

Table A2.13. Bulk digestion and LA-HR-ICP-MS data for sample 090710-12 from the Nuvvuagittuq Supracrustal Belt, Québec, Canada.

Formation	Sample	Code	Shot	Method	Li	B	Mg	Ca	Ti	V
Nuvvuagittuq	090710-12	LR1-39	IF	Bulk	9.123E-01		1.674E+04	1.657E+03	1.148E+02	5.869E+00
Nuvvuagittuq	090710-12	S1	1	Hem			5.321E+02	5.970E+03	5.368E+02	9.189E+01
Nuvvuagittuq	090710-12	S1	2	Hem			8.592E+02	9.156E+03	8.419E+02	1.027E+02
Nuvvuagittuq	090710-12	S1	3	Hem				3.871E+03	6.770E+02	9.412E+01
Nuvvuagittuq	090710-12	S2	1	Hem			4.851E+02	4.122E+03	8.421E+02	6.964E+01
Nuvvuagittuq	090710-12	S2	2	Hem			2.196E+02	4.582E+03	1.064E+03	6.924E+01
Nuvvuagittuq	090710-12	S2	3	Hem			2.349E+02	6.315E+03	1.168E+03	6.586E+01
Nuvvuagittuq	090710-12	S3	1	Hem			1.438E+02		9.210E+02	5.422E+01
Nuvvuagittuq	090710-12	S3	2	Hem			1.816E+02		9.615E+02	5.526E+01
Nuvvuagittuq	090710-12	S3	3	Hem					9.486E+02	5.826E+01
Nuvvuagittuq	090710-12	S4	1	Hem					1.037E+03	4.328E+01
Nuvvuagittuq	090710-12	S4	2	Hem			6.413E+02	5.422E+03	1.001E+03	4.257E+01
Nuvvuagittuq	090710-12	S4	3	Hem			8.275E+02	4.665E+03	1.098E+03	4.487E+01
Nuvvuagittuq	090710-12	S5	1	Hem				4.617E+03	5.991E+02	3.657E+01
Nuvvuagittuq	090710-12	S5	2	Hem				3.638E+03	5.715E+02	3.622E+01
Nuvvuagittuq	090710-12	S5	3	Hem				3.992E+03	5.725E+02	3.621E+01
Nuvvuagittuq	090710-12	S6	1	Hem				3.219E+03	3.789E+02	2.498E+01
Nuvvuagittuq	090710-12	S6	2	Hem				2.786E+03	3.450E+02	2.834E+01
Nuvvuagittuq	090710-12	S6	3	Hem			7.156E+04	1.060E+04	2.613E+02	1.647E+01
Nuvvuagittuq	090710-12	S7	1	Hem				3.603E+03	3.064E+02	2.179E+01
Nuvvuagittuq	090710-12	S7	2	Hem				2.815E+03	3.035E+02	2.194E+01
Nuvvuagittuq	090710-12	S7	3	Hem				2.508E+03	3.131E+02	2.264E+01
			Bulk	average	9.123E-01		1.674E+04	1.657E+03	1.148E+02	5.869E+00
				2*std dev						
				count		1 0	1	1	1	1
			Hematite	average			7.569E+03	4.816E+03	7.023E+02	4.938E+01
				2*std dev			4.497E+04	4.395E+03	6.143E+02	5.066E+01
				count		0 0	10	17	21	21

Table A2.13 continued

Code	Shot	Method	Cr	Mn	Co	Ni	⁶⁵Cu	Zn	Ge	Rb
LR1-39	IF	Bulk	1.258E+01	2.892E+03	2.645E+01	9.209E+01	1.137E+02	4.804E+01	5.989E+01	3.686E-01
S1	1	Hem	4.015E+01	2.389E+02	1.338E+01	9.234E+01		4.501E+01	1.527E+01	
S1	2	Hem	3.808E+01	3.059E+02	1.510E+01	1.087E+02		1.017E+02		
S1	3	Hem	3.270E+01	2.899E+02	1.389E+01	1.038E+02		2.728E+02	1.284E+01	
S2	1	Hem		2.989E+02	1.186E+01	1.080E+02		9.857E+01	1.397E+01	
S2	2	Hem		3.142E+02	1.221E+01	9.775E+01		6.990E+01	1.391E+01	
S2	3	Hem		3.253E+02	1.294E+01	9.941E+01		1.037E+02	1.426E+01	
S3	1	Hem		2.751E+02	1.092E+01	8.736E+01		3.340E+01	1.267E+01	
S3	2	Hem		3.010E+02	1.151E+01	8.671E+01		4.250E+01	1.243E+01	
S3	3	Hem	1.236E+01	2.975E+02	1.183E+01	9.219E+01		5.318E+01		
S4	1	Hem		3.062E+02	1.064E+01	7.491E+01		2.458E+02	1.708E+01	
S4	2	Hem		4.361E+02	1.110E+01	7.871E+01		1.039E+02		
S4	3	Hem		4.616E+02	1.169E+01	7.744E+01		1.680E+02		
S5	1	Hem	1.392E+01	3.047E+02	1.276E+01	6.586E+01		4.641E+01		
S5	2	Hem	1.696E+01	2.800E+02	1.251E+01	6.651E+01		3.821E+01		
S5	3	Hem	1.532E+01	2.893E+02	1.217E+01	6.785E+01		4.646E+01		
S6	1	Hem		2.102E+02	1.399E+01	7.926E+01		9.706E+01		
S6	2	Hem		2.126E+02	1.402E+01	8.338E+01		1.260E+02		
S6	3	Hem		1.622E+04	5.149E+01	1.894E+02		2.688E+02		
S7	1	Hem	1.080E+01	2.496E+02	1.109E+01	5.982E+01		4.143E+01		
S7	2	Hem	9.932E+00	2.510E+02	1.074E+01	6.663E+01		3.516E+01		
S7	3	Hem	8.917E+00	2.292E+02	9.141E+00	5.915E+01		4.606E+01		
	Bulk	average	1.258E+01	2.892E+03	2.645E+01	9.209E+01	1.137E+02	4.804E+01	5.989E+01	3.686E-01
		2*std dev								
		count	1	1	1	1	1	1	1	1
	Hematite	average	1.991E+01	1.052E+03	1.405E+01	8.787E+01		9.924E+01	1.405E+01	
		2*std dev	2.431E+01	6.950E+03	1.738E+01	5.573E+01		1.542E+02	3.094E+00	
		count	10	21	21	21	0	21	8	0

Table A2.13 continued

Code	Shot	Method	Sr	Y	Zr	Mo	Ba	La	Ce	Pr
LR1-39	IF	Bulk	3.350E-01	7.194E+00	7.907E+00	1.024E+00	8.504E-01	1.016E+00	1.923E+00	2.231E-01
S1	1	Hem	7.026E+00	1.247E+00	8.589E+01		6.012E+00	7.698E-01	2.118E+00	3.205E-01
S1	2	Hem	1.132E+01	7.830E+00	1.359E+02		8.905E+00	2.308E+00	5.631E+00	7.464E-01
S1	3	Hem	4.047E+00		5.749E+01		3.169E+00			
S2	1	Hem	4.529E+00	2.379E+00	5.041E+01		3.476E+00	7.551E-01	1.816E+00	2.750E-01
S2	2	Hem	3.990E+00	4.118E-01	5.412E+01		3.788E+00	1.042E-01	2.578E-01	4.021E-02
S2	3	Hem	4.363E+00	1.561E+00	5.055E+01		3.508E+00	4.821E-01	1.338E+00	2.173E-01
S3	1	Hem	4.438E+00	2.084E+01	5.290E+01		3.232E+00	4.002E+00	8.340E+00	1.286E+00
S3	2	Hem	2.974E+00	1.996E-01	3.243E+01	1.111E+00	1.707E+00	6.473E-02	1.208E-01	2.389E-02
S3	3	Hem	3.727E+00		4.739E+01				4.779E-02	
S4	1	Hem				1.534E+00				
S4	2	Hem	5.599E+00	8.270E-01	6.384E+01		4.134E+00	1.730E-01	3.807E-01	5.864E-02
S4	3	Hem	4.955E+00	9.892E-01	5.750E+01		4.586E+00	2.115E-01	4.626E-01	6.741E-02
S5	1	Hem	4.086E+00		4.617E+01		3.378E+00		6.048E-02	
S5	2	Hem	4.345E+00		4.285E+01		3.279E+00			
S5	3	Hem	3.317E+00		4.787E+01		3.758E+00			
S6	1	Hem	4.616E+00	4.573E-01	4.707E+01		3.487E+00	2.179E-01	4.098E-01	5.627E-02
S6	2	Hem	4.151E+00		3.977E+01		3.135E+00			
S6	3	Hem	7.184E+00	3.254E+01	6.438E+01		6.021E+00	3.560E-01	7.206E-01	1.229E-01
S7	1	Hem	5.195E+00		4.272E+01		3.696E+00			
S7	2	Hem	3.450E+00		3.178E+01		2.648E+00			
S7	3	Hem	3.296E+00		2.737E+01		2.476E+00			
	Bulk	average	3.350E-01	7.194E+00	7.907E+00	1.024E+00	8.504E-01	1.016E+00	1.923E+00	2.231E-01
		2*std dev								
		count	1	1	1	1	1	1	1	1
	Hematite	average	4.830E+00	6.299E+00	5.392E+01	1.323E+00	3.915E+00	8.586E-01	1.669E+00	2.922E-01
		2*std dev	3.769E+00	2.126E+01	4.655E+01	5.980E-01	3.188E+00	2.441E+00	5.024E+00	7.810E-01
		count	20	11	20	2	19	11	13	11

Table A2.13 continued

Code	Shot	Method	Nd	Sm	Eu	Tb	Gd	Dy	Ho	Er
LR1-39	IF	Bulk	9.226E-01	3.040E-01	1.347E-01	1.162E-01	5.507E-01	8.190E-01	2.002E-01	6.387E-01
S1	1	Hem	1.310E+00	2.992E-01		5.695E-02	4.181E-01			
S1	2	Hem	3.593E+00	9.571E-01	3.919E-01	2.338E-01	1.863E+00	1.411E+00	2.312E-01	7.441E-01
S1	3	Hem								
S2	1	Hem	1.474E+00	4.769E-01	1.458E-01	7.355E-02	4.311E-01	3.491E-01	8.198E-02	
S2	2	Hem	2.119E-01							
S2	3	Hem	7.558E-01	2.776E-01				3.128E-01	7.066E-02	2.231E-01
S3	1	Hem	6.956E+00	2.892E+00	1.038E+00	5.868E-01	4.248E+00	3.578E+00	7.543E-01	2.331E+00
S3	2	Hem								
S3	3	Hem								
S4	1	Hem								
S4	2	Hem	3.645E-01				2.512E-01		4.109E-02	
S4	3	Hem	3.427E-01					2.127E-01	4.242E-02	
S5	1	Hem								
S5	2	Hem								
S5	3	Hem								
S6	1	Hem	2.662E-01							
S6	2	Hem								
S6	3	Hem	6.711E-01	5.244E-01	2.862E-01	3.818E-01	1.849E+00	3.565E+00	8.865E-01	3.014E+00
S7	1	Hem								
S7	2	Hem								
S7	3	Hem								
	Bulk	average	9.226E-01	3.040E-01	1.347E-01	1.162E-01	5.507E-01	8.190E-01	2.002E-01	6.387E-01
		2*std dev								
		count	1	1	1	1	1	1	1	1
	Hematite	average	1.594E+00	9.046E-01	4.656E-01	2.666E-01	1.510E+00	1.571E+00	3.012E-01	1.578E+00
		2*std dev	4.277E+00	2.008E+00	7.899E-01	4.451E-01	3.056E+00	3.219E+00	7.251E-01	2.623E+00
		count	10	6	4	5	6	6	7	4

Table A2.13 continued

Code	Shot	Method	Yb	Lu	Hf	Pb	Th	U	Y/Ho	Ce/Ce* _{PAAS}
LR1-39	IF	Bulk	5.786E-01	1.024E-01	6.588E-02	2.094E+00	9.795E-03	4.187E-02	3.594E+01	9.315E-01
S1	1	Hem						9.756E-02		9.426E-01
S1	2	Hem	7.092E-01			1.705E+00	1.651E-01	1.629E-01	3.386E+01	9.759E-01
S1	3	Hem						9.631E-03		
S2	1	Hem					7.382E-02	9.329E-02	2.902E+01	8.959E-01
S2	2	Hem						1.935E-02		8.895E-01
S2	3	Hem					4.571E-02	4.658E-02	2.210E+01	9.029E-01
S3	1	Hem	1.708E+00	2.455E-01			5.164E-02	1.799E-01	2.763E+01	8.371E-01
S3	2	Hem						9.824E-03		6.895E-01
S3	3	Hem								
S4	1	Hem								
S4	2	Hem						4.164E-02	2.013E+01	8.565E-01
S4	3	Hem		3.190E-02				4.129E-02	2.332E+01	8.827E-01
S5	1	Hem				8.591E-01				
S5	2	Hem								
S5	3	Hem								
S6	1	Hem				5.291E-01		3.301E-02		8.526E-01
S6	2	Hem								
S6	3	Hem	3.334E+00	5.595E-01		6.832E-01		9.735E-02	3.671E+01	7.791E-01
S7	1	Hem								
S7	2	Hem								
S7	3	Hem								
	Bulk	average	5.786E-01	1.024E-01	6.588E-02	2.094E+00	9.795E-03	4.187E-02	3.594E+01	9.315E-01
		2*std dev								
		count	1	1	1	1	1	1	1	1
	Hematite	average	1.917E+00	2.790E-01		9.442E-01	8.406E-02	6.936E-02	2.754E+01	8.640E-01
		2*std dev	2.650E+00	5.308E-01		1.050E+00	1.107E-01	1.146E-01	1.235E+01	1.559E-01
		count	3	3	0	4	4	12	7	11

Table A2.13 continued

Code	Shot	Method	La/La* _{PAAS}	Pr/Pr* _{PAAS}	Eu/Eu* _{PAAS}	Pr/Yb* _{PAAS}	ΣREE
LR1-39	IF	Bulk	1.246E+00	9.835E-01	1.436E+00	1.231E-01	1.472E+01
S1	1	Hem	6.370E-01	1.113E+00			6.539E+00
S1	2	Hem	1.451E+00	9.567E-01	1.679E+00	3.362E-01	2.665E+01
S1	3	Hem					0.000E+00
S2	1	Hem	3.036E+00	9.400E-01	1.515E+00		8.257E+00
S2	2	Hem	2.355E+00	9.597E-01			1.026E+00
S2	3	Hem	4.317E-01	1.259E+00			5.238E+00
S3	1	Hem	3.972E+00	9.394E-01	1.599E+00	2.404E-01	5.881E+01
S3	2	Hem					4.090E-01
S3	3	Hem					4.779E-02
S4	1	Hem					0.000E+00
S4	2	Hem	-2.859E+00	8.549E-01			2.096E+00
S4	3	Hem	2.062E+00	9.590E-01			2.360E+00
S5	1	Hem					6.048E-02
S5	2	Hem					0.000E+00
S5	3	Hem					0.000E+00
S6	1	Hem	1.671E+00	9.804E-01			1.407E+00
S6	2	Hem					0.000E+00
S6	3	Hem	4.296E+00	9.651E-01	1.161E+00	1.177E-02	4.881E+01
S7	1	Hem					0.000E+00
S7	2	Hem					0.000E+00
S7	3	Hem					0.000E+00
	Bulk	average	1.246E+00	9.835E-01	1.436E+00	1.231E-01	1.472E+01
		2*std dev					
		count	1	1	1	1	1
	Hematite	average	1.705E+00	9.927E-01	1.488E+00	1.961E-01	7.701E+00
		2*std dev	4.101E+00	2.253E-01	4.565E-01	3.333E-01	3.304E+01
		count	10	10	4	3	21

Appendix 3. Supplementary Information for Chapter 4

A3.1 Excluded species from phase diagrams and rational

Several possible mineral phases were excluded from consideration in the thermodynamic phase diagrams and are listed below. Similar to Halevy et al. (2017), mineral phases were excluded for one of several reasons, either (i) minerals are characteristic of igneous or metamorphic processes, or mantle phases, and therefore uncharacteristic of authigenic precipitates (e.g., Hedenbergite, Minnesotaite, $\text{FeO}_{(c)}$), (ii) are incompatible with the deposition of banded iron formations (e.g., pyrite), (iii) minerals are crystalline phases that are unlikely to be primary precipitates (e.g., hematite), or (iv) are unlikely to form substantial deposits due to low concentrations of sulfate (e.g., schwertmannite, green rust sulfate as in ref. 8). Excluded mineral phases include: Andradite, Fayalite, $\text{Fe}(\text{OH})_{2(\text{ppd})}$, $\text{FeO}_{(c)}$, Ferrite-2-Ca, Ferrite-Ca, Ferrite-Cu, Ferrite-Mg, Ferrite-Zn, Ferrosilite, Goethite, Hedenbergite, Hematite, Minnesotaite, Pyrite, Schwertmannite, and Strengite.

A3.2 References

Abell, P.I., McClory, J., Martin, A., Nisbet, E.G., and Kyser, T.K., 1985, Petrography and stable isotope ratios from Archaean stromatolites, Mushandike Formation, Zimbabwe: *Precambrian Research*, v. 27, no. 4, p. 385–398, doi: 10.1016/0301-9268(85)90095-6.

- Awramik, S.M., and Buchheim, H.P., 2009, A giant, Late Archean lake system: The Meentheena Member (Tumbiana Formation; Fortescue Group), Western Australia: *Precambrian Research*, v. 174, no. 3-4, p. 215–240, doi: 10.1016/j.precamres.2009.07.005.
- Bolhar, R., Hofmann, A., Woodhead, J., Hergt, J., and Dirks, P., 2002, Pb- and Nd-isotope systematics of stromatolitic limestones from the 2.7 Ga Ngezi Group of the Belingwe Greenstone Belt: constraints on timing of deposition and provenance: *Precambrian Research*, v. 114, no. 3-4, p. 277–294, doi: 10.1016/s0301-9268(01)00229-7.
- Bolhar, R., and Van Kranendonk, M.J., 2007, A non-marine depositional setting for the northern Fortescue Group, Pilbara Craton, inferred from trace element geochemistry of stromatolitic carbonates: *Precambrian Research*, v. 155, no. 3-4, p. 229–250, doi: 10.1016/j.precamres.2007.02.002.
- Buck, S.G., 1980, Stromatolite and ooid deposits within the fluvial and lacustrine sediments of the Precambrian Ventersdorp Supergroup of South Africa: *Precambrian Research*, v. 12, no. 1-4, p. 311–330, doi: 10.1016/0301-9268(80)90033-9.
- Bruland KW, Middag R, Lohan MC (2014) Controls of Trace Metals in Seawater *in* *Treatise on Geochemistry*. Holland HD, Turekian K (eds.) Second Edition. Elsevier Ltd. Volume 8: 19-51.

- Corfu, F., and Wallace, H., 1986, U–Pb zircon ages for magmatism in the Red Lake greenstone belt, northwestern Ontario: *Canadian Journal of Earth Sciences*, v. 23, no. 1, p. 27–42, doi: 10.1139/e86-004.
- Crowe SA, et al. (2014) Sulfate was a trace constituent of Archean seawater. *Science*, 346(6210):735–739.
- Devaney, J.R., 2001, *Sedimentology and Volcanology of Selected Tectonized Stratigraphic Units, Southern Birch–Uchi Greenstone Belt, Uchi Subprovince: Ontario Geological Survey Open File Report 6031*, p. 1–47.
- Fralick, P., Hollings, P., and King, D., 2008, Stratigraphy, geochemistry, and depositional environments of Mesoarchean sedimentary units in western Superior Province: Implications for generation of early crust, *in* Condie, K.C. and Pease, V. eds., *When Did Plate Tectonics Begin on Planet Earth, Special Paper 440: When Did Plate Tectonics Begin on Planet Earth?*, p. 77–96.
- Green, M.G., 2001, Early Archaean crustal evolution: evidence from ~3.5 billion year old greenstone successions in the Pilgangoora Belt, Pilbara Craton, Australia: 277 p.
- Halevy, I., Alesker, M., Schuster, E.M., Popovitz-Biro, R., and Feldman, Y., 2017, A key role for green rust in the Precambrian oceans and the genesis of iron formations: *Nature*, v. 10, no. 2, p. 135–139, doi: 10.1038/ngeo2878.
- Harnmeijer, J., 2010, Squeezing blood from a stone: Inferences into the life and depositional environments of the Early Archaean. p. 1-609.

- Hegner, E., Kröner, A., and Hunt, P., 1994, A precise U-Pb zircon age for the Archaean Pongola Supergroup volcanics in Swaziland: *Journal of African Earth Sciences*, v. 18, no. 4, p. 339–341, doi: 10.1016/0899-5362(94)90072-8.
- Henderson, J.B., 1975, Archean Stromatolites in the Northern Slave Province, Northwest Territories, Canada: *Canadian Journal of Earth Sciences*, v. 12, no. 9, p. 1619–1630, doi: 10.1139/e75-144.
- Hofmann, A., Dirks, P.H.G.M., and Jelsma, H.A., 2004, Shallowing-Upward Carbonate Cycles in the Belingwe Greenstone Belt, Zimbabwe: A Record of Archean Sea-Level Oscillations: *Journal of Sedimentary Research*, v. 74, no. 1, p. 64–81, doi: 10.1306/052903740064.
- Jones C, Nomosatryo S, Crowe SA, Bjerrum CJ, Canfield DE (2015) Iron oxides, divalent cations, silica, and the early earth phosphorus crisis. *Geology* 43:135–138.
- Kamber, B.S., Bolhar, R., and Webb, G.E., 2004, Geochemistry of late Archaean stromatolites from Zimbabwe: evidence for microbial life in restricted epicontinental seas: *Precambrian Research*, v. 132, no. 4, p. 379–399, doi: 10.1016/j.precamres.2004.03.006.
- Lambert, M.B., 1998, Stromatolites of the late Archaean Back River stratovolcano, Slave structural province, Northwest Territories, Canada: *Canadian Journal of Earth Sciences*, v. 35, no. 3, p. 290–301, doi: 10.1139/e97-115.
- Langmuir D (1997) *Aqueous Environmental Geochemistry* (Prentice Hall, Upper Saddle River, New Jersey), pp. 1-600.

- Lowe, D.R., L. P. Knauth, 1977, Sedimentology of the Onverwacht Group (3.4 Billion Years), Transvaal, South Africa, and Its Bearing on the Characteristics and Evolution of the Early Earth: *The Journal of Geology*, v. 85, no. 6, p. 699–723, doi: 10.1086/628358.
- Lowe, D.R., and Byerly, G.R., 2007, An Overview of the Geology of the Barberton Greenstone Belt and Vicinity: Implications for Early Crustal Development, *in* Van Kranendonk, M.J., Smithies, R.H., and Bennett, V.C. eds., *Earth's Oldest Rocks, Developments in Precambrian Geology*, Elsevier, p. 481–526.
- Martin, A., Nisbet, E.G., and Bickle, M.J., 1980, Archaean stromatolites of the Belingwe Greenstone Belt, Zimbabwe (Rhodesia): *Precambrian Research*, v. 13, no. 4, p. 337–362, doi: 10.1016/0301-9268(80)90049-2.
- Mason, T.R., and Brunn, Von, V., 1977, 3-Gyr-old stromatolites from South Africa: *Nature*, v. 266, p. 47–49, doi: 10.1038/266047a0.
- Murphy, M.A., and Sumner, D.Y., 2008, Tube structures of probable microbial origin in the Neoproterozoic Carawine Dolomite, Hamersley Basin, Western Australia: *Geobiology*, v. 6, p. 83–93, doi: 10.1111/j.1472-4669.2007.00114.x.
- Russell, J., Chadwick, B., Rao, B.K., and Vasudev, V.N., 1996, Whole-rock Pb/Pb isotopic ages of Late Archaean limestones, Karnataka, India: *Precambrian Research*, v. 78, no. 4, p. 261–272, doi: 10.1016/0301-9268(95)00082-8.
- Schopf, J., 2006, Fossil evidence of Archaean life: *Philosophical Transactions of the Royal Society B: Biological Sciences*, v. 361, no. 1470, p. 869–885.

- Schröder, S., Beukes, N.J., and Sumner, D.Y., 2009, Microbialite–sediment interactions on the slope of the Campbellrand carbonate platform (Neoproterozoic, South Africa): *Precambrian Research*, v. 169, no. 1-4, p. 68–79, doi: 10.1016/j.precamres.2008.10.014.
- Siever, R., 1992. The silica cycle in the Precambrian. *Geochimica et Cosmochimica Acta* 56, 3265–3272.
- Srinivasan, R., Shukla, M., Naqvi, S.M., Yadav, V.K., Venkatachala, B.S., Raj, B.U., and Rao, D.V.S., 1989, Archaean stromatolites from the Chitradurga schist belt, Dharwar Craton, South India: *Precambrian Research*, v. 43, no. 3, p. 239–250, doi: 10.1016/0301-9268(89)90058-2.
- Sumner, D.Y., and Grotzinger, J.P., 2000, Late Archean aragonite precipitation: petrography, facies associations, and environmental significance: *Carbonate Sedimentation and Diagenesis in the Evolving Precambrian World*, p. 123–144, doi: 10.2110/pec.00.67.0123.
- Thurston, P.C., 1980, Subaerial volcanism in the Archean Uchi-Confederation volcanic belt: *Precambrian Research*, v. 12, no. 1-4, p. 79–98, doi: 10.1016/0301-9268(80)90024-8.
- Turek, A., Sage, R.P., and Van Schmus, W.R., 1992, Advances in the U–Pb zircon geochronology of the Michipicoten greenstone belt, Superior Province, Ontario: *Canadian Journal of Earth Sciences*, v. 29, no. 6, p. 1154–1165, doi: 10.1139/e92-093.

- Van Kranendonk, M.J., 2006, Volcanic degassing, hydrothermal circulation and the flourishing of early life on Earth: A review of the evidence from c. 3490-3240 Ma rocks of the Pilbara Supergroup, Pilbara Craton, Western Australia: *Earth-Science Reviews*, v. 74, no. 3-4, p. 197–240, doi: 10.1016/j.earscirev.2005.09.005.
- Veizer, J., Hoefs, J., Lowe, D.R., P.C. Thurston, 1989, Geochemistry of Precambrian carbonates: II. Archean greenstone belts and Archean sea water: *Geochimica et Cosmochimica Acta*, v. 53, no. 4, p. 859–871, doi: 10.1016/0016-7037(89)90031-8.
- Wilks, M.E., and Nisbet, E.G., 1985, Archaean stromatolites from the Steep Rock Group, northwestern Ontario, Canada: *Canadian Journal of Earth Sciences*, v. 22, no. 5, p. 792–799, doi: 10.1139/e85-086.

Appendix Table A3.1. Activity coefficients for correcting carbonate system concentrations calculated using the Tuesdell-Jones equation for an ionic strength of 0.7 M; the activity coefficient for carbonic acid was determined using the Setchenow equation (Langmuir, 1997).

Ion	Charge	$\log \gamma$	γ
Ca^{2+}	+2	-0.602	0.250
HCO_3^-	-1	-0.171	0.674
CO_3^{2-}	-2	-0.686	0.206
H_2CO_3	0	0.162	1.451

Appendix Table A3.2. Molar concentrations and corresponding activity inputs for thermodynamic phase diagrams generated in Geochemists' Workbench. Concentrations were selected to simulated Paleoproterozoic seawater wherever possible, or set at modern values (Na⁺, Cl⁻).

Component	Concentration (M)	Activity Coefficients* (γ)	Activity (α)	log α	Reference
low Fe ²⁺	1.00E-09	0.252	2.52E-10	-9.599	
High Fe ²⁺	1.79E-02	0.252	4.50E-03	-2.346	
Ca ²⁺	0.03	0.250	7.49E-03	-2.125	Jones et al. (2015)
Mg ²⁺	3.00E-02	0.289	8.68E-03	-2.062	Jones et al. (2015)
SiO ₂ ^o	2.20E-03	1.138	2.50E-03	-2.602	Siever (1992)
SO ₄ ²⁻	2.00E-06	0.179	3.59E-07	-6.445	Crowe et al. (2014)
HPO ₄ ²⁻	1.30E-07	0.179	2.33E-08	-7.632	Jones et al. (2015)
Cl ⁻	0.546	0.625	3.41E-01	-0.467	Bruland et al. (2014)
Na ⁺	0.468	0.707	3.31E-01	-0.480	Bruland et al. (2014)

*Activity coefficients were calculated using the Truesdell-Jones equation and coefficients (Langmuir, 1997) at an ionic strength of 0.7 M, equivalent to seawater. A coefficient could not be calculated for phosphate due to the absence of constants for the Truesdell-Jones equation, so the activity coefficient was assumed to be equivalent to sulfate.

Appendix Table A3.3. Paleoproterozoic to Neoproterozoic carbonate succession thickness and associated references.

Age Range (Ma)	Plot Age (Ma)	Stratigraphic Thickness (m)	Formation, unit, or bed	Group, craton	Locality	References
2597-2504	2550.5	475	Wittenoom Fm.; Paraburdoo member	Hamersley Group; Mount Bruce Supergroup	Australia	Murphy and Sumner (2008)
2600-2520	2560	1900	Campbellrand Subgroup (including Monteville and Nauga formation basin facies and Ghaap Plateau facies)	Transvaal Supergroup	South Africa	Schröder et al. (2009)
-	2600	24	Huntsman Limestone	Bulawayo Belt	Zimbabwe	Sumner and Grotzinger (2000)
-	2630	225	Carawine Dolomite	Hamersley Group; Mount Bruce Supergroup	Australia	Murphy and Sumner (2008)
-	2639	80	Vanivilas Formation	Chitradurga Group; Dharwar Supergroup	India	Srinivasan et al. (1989); Russell et al. (1996)
-	2650	60	Cheshire Fm.	Belingwe Belt	Zimbabwe	Hofmann et al. (2004); Bolhar et al. (2002)
-	2650	40	Snowfield Lake	High Lake Volcanic Belt; Yellowknife Supergroup; Slave Province	Canada	Henderson (1975); Schopf (2006)

-	2692	5	Back River volcanic complex dolomite			Lambert (1998)
-	2700	50	Manjeri Fm.	Ngezi Group; Bulawayan Supergroup	Zimbabwe	Martin et al. (1980); Bolhar et al. (2002)
2721- 2709	2715	2		Ventersdorp Supergroup	South Africa	Buck (1980); Armstrong et al. (1991)
-	2720	50	Meentheena Carbonate Member; Tumbiana Formation	Fortescue Group; Pilbara Craton	Australia	Bolhar and Van Kranendonk (2007); Awramik and Buchheim (2009)
-	2729	50	Goudreau Lake area	Wawa Greenstone Belt; Superior Province	Canada	Veizer et al. (1989); Turek et al. (1992)
2828- 2780	2804	500		Steep Rock Group	Canada	Wilks and Nisbet (1985); Fralick et al. (2008)
2839 or 2817	2828	200	Mushandike Fm.		Zimbabwe	Abell et al. (1985); Kamber et al. (2004)
-	2840	60	Woman Lake	Birch-Uchi Greenstone Belt	Canada	Devaney (2001); Thurston (1980)
2980- 2870	2975	30	White Mfolozi Formation	Nsuze Group; Pongola Supergroup	South Africa	Mason and von Brunn (1977); Hegner et al. (1994)
2940- 2925	2932.5	400	Ball assemblage	Red Lake Greenstone Belt	Canada	Corfu and Wallace (1986)
-	3400	8	Strelley Pool Formation	Pilbara Craton	Australia	Van Kranendonk (2006)

-	3435	30	Kromberg Formation	Onverwacht Group	South Africa	Lowe and Knauth (1977); Lowe and Byerly (2007)
-	3490	10	Dresser carbonate	Pilbara Craton	Australia	Van Kranendonk (2006)
-	3517	1	ferroan calcite horizon	Coonterunha Group; Pilgangoora Belt; Pilbara Craton	Australia	Harnmeijer (2010); Green (2001)